LOCALISED STATES IN NATURAL DOUBLY DIFFUSIVE CONVECTION

JOANNA TUMELTY

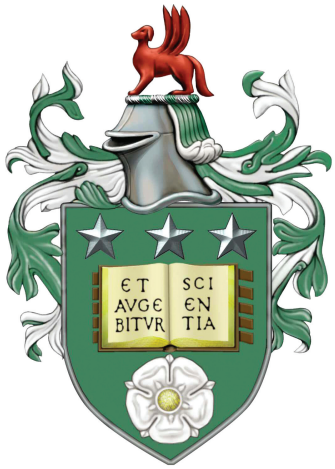

Submitted in accordance with the requirements for
the degree of Doctor of Philosophy

THE UNIVERSITY OF LEEDS
SCHOOL OF MATHEMATICS

APRIL 2022

The candidate confirms that the work submitted is her own, except where work which has formed part of jointly authored publications has been included. The contribution of the candidate and the other authors to this work has been explicitly indicated below. The candidate confirms that appropriate credit has been given within the thesis where reference has been made to the work of others.

Chapter 4 is based on work from the jointly authored publication:

> C. Beaume, A. M. Rucklidge, and J. Tumelty. Near-onset dynamics in natural doubly diffusive convection. *Journal of Fluid Mechanics*, 934:A42, 2022

The candidate performed the research under the supervision of the other authors. JT and CB wrote the initial draft of the manuscript and all authors were involved in revising the manuscript for publication.

ACKNOWLEDGEMENTS

Firstly, I would like to thank my supervisors, Cédric Beaume and Alastair Rucklidge, not only for providing me with code that I used to generate the majority of the results presented in this thesis, but more importantly for their patience, guidance and continued enthusiasm towards this research.

I am also incredibly grateful to my family for their support and generosity, particularly during the first lockdown. Finally, I would like to thank Luis for helping me to stay positive over the past couple of months.

This work was supported by the Leeds-York Natural Environment Research Council (NERC) Doctoral Training Partnership (DTP) SPHERES under grant NE/L002574/1.

ABSTRACT

Fluids subject to both thermal and compositional variations can undergo doubly diffusive convection when these properties both affect the fluid density and diffuse at different rates. This phenomenon can lead to the formation of a variety of patterns, including salt fingers and thermohaline staircases, which have been identified throughout the world's oceans. In this thesis, we consider natural doubly diffusive convection driven by opposing thermal and solutal gradients in the horizontal direction and aim to determine how states in this system are affected by the physical parameters that characterise the strength of the thermal gradients, the balance between thermal and solutal gradients, and ratios between thermal, solutal and viscous diffusivities.

In the particular case when the imposed thermal and solutal gradients balance, a motionless conduction state exists but destabilises when the gradients are sufficiently large. We determine the nature of the associated primary bifurcation using a weakly nonlinear analysis and extend the resulting primary convection branches using numerical continuation to find that large-amplitude steady convection states can coexist with the stable conduction state for both sub- and supercritical bifurcations. We proceed by considering vertically extended domains where spatially localised states, known as convectons, have been found to lie on a pair of secondary branches that intertwine when the onset of convection is subcritical. This process is known as homoclinic snaking and is usually associated with bistability. Here, we show that convectons persist into parameter regimes where the primary bifurcation is supercritical and there is no bistability. We finally consider how the system changes when the imposed thermal and solutal gradients do not balance and the motionless conduction state does not exist. We focus on how the form

of convectons change with increasing imbalance and how these localised states cease to exist in sufficiently thermally dominated flows.

CONTENTS

LIST OF FIGURES

LIST OF TABLES

ABBREVIATIONS

NON-DIMENSIONAL PARAMETERS

Le	Lewis number
Ra	Rayleigh number
Pr	Prandtl number
Gr	Grashof number
N	Buoyancy ratio

NUMERICAL TERMS

ODE	Ordinary differential equation
PDE	Partial differential equation
ETD	Exponential time differencing

BIFURCATIONS AND STATES

(R)PO	(Relative) periodic orbits
TW	Travelling wave
SOC	Steady overturning convection
SN	Saddle-node bifurcation
SNIPER	Saddle node infinite period bifurcation

BRANCHES OF STEADY STATES

PN	Primary branches of spatially periodic states with N rolls
L^- ($\tilde{L}^-$)	Branches of (hybrid) convectons with an even number of central rolls
L^+ ($\tilde{L}^+$)	Branch of (hybrid) convectons with an odd number of central rolls
A, $\tilde{A}$	Branches of anticonvectons

1 | INTRODUCTION

1.1 DOUBLY DIFFUSIVE CONVECTION

Upon heating, fluids tend to expand and become less dense. This provides an upward buoyancy force, which can lead to convective motion when the heating is sufficiently strong. Such behaviour is widespread and occurs across a range of scales, from heating a saucepan of water to controlling the motion of tectonic plates. Many natural fluids, however, also exhibit variations in the concentration of a solute that affects the fluid density and that diffuses at a different rate to temperature. This can lead to a range of more complex fluid dynamics and instabilities, even when the fluid is stably stratified. This phenomenon is known as doubly diffusive convection and has been the subject of a vast number of studies over the past six decades, e.g., see the reviews [68, 87, 143, 158, 178, 179].

Doubly diffusive convection has perhaps been most widely studied in oceanography, where the presence of icebergs, river and ocean outflows or evaporation at the ocean's surface, for example, can all lead to variations in both temperature and salinity. Indeed, You [192] previously estimated that approximately 44% of the world's oceans could undergo this phenomenon based on data from the 1994 Levitus climatological atlas [111, 112]. Despite this relatively high percentage, doubly diffusive convection has recently been shown to only provide a small contribution to the global ocean circulation energy budget [183]. However, this phenomenon can lead to pronounced regional effects [143] for fluid mixing [132, 156, 158] and heat, salt or nutrient transport [74, 97, 197]. These effects arise owing to the patterns that form as a direct result of doubly diffusive

Figure 1.1: Experimental observation of the salt-fingering instability in fluid that has a stable temperature stratification and salt solution poured on top. From [87].

convection and vary with both the strength and orientation of the driving temperature and salinity gradients.

Tropical and subtropical oceans at low latitudes contain warm and salty waters overlying colder and fresher waters. This configuration is prone to salt-fingering instabilities, like that shown in figure 1.1(a), where many thin, vertical channels transport warm and salty fluid downwards or cold and fresh fluid upwards. These oceans can also feature thermohaline staircases [159, 160, 171, 183, 192, 197], where the flow is characterised by well-mixed horizontal layers interspersed with interfaces displaying sharp variations in temperature and salinity. These can be large-scale coherent structures that, in some locations, retain their identity over decadal time-scales. For example, staircases containing mixed layers of up to 400m thick that extend over 150km in the horizontal have been found in the Tyrrhenian Sea throughout a 40-year period [65, 197].

Polar oceans at high latitudes have a contrasting configuration, with cold and fresh waters overlying hotter and saltier waters. Nevertheless, these oceans can also admit large-scale staircase structures that form via a type of doubly diffusive convection known as diffusive layering [97, 136, 140]. The steps in these staircases tend to be smaller than those in the previous configuration, however, owing to the smaller temperature difference [143]. Diffusive staircases, like that shown in figure 1.2(a), are widespread across the central Arctic Ocean; for example, they have been found within 80% of the Canada basin [164], and allow heat to be transported from the warm Atlantic waters below

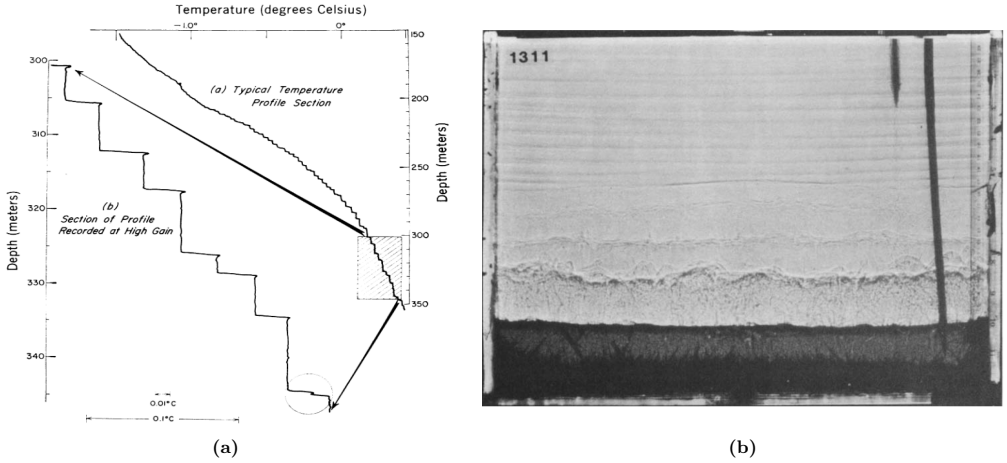

Figure 1.2: (a) Temperature profile of a diffusive staircase in the Arctic Ocean. From [133]. (b) Experimental observation of the diffusive layering in a stratified potassium carbonate solution to model layering in a magma chamber. From [87].

the staircases upwards through the mixed layers towards the surface. Indeed, Turner [180] considered this mechanism amongst others to explain the increased melting rate of Arctic sea ice and found that it gave a substantial contribution.

Layering due to doubly diffusive processes can also occur in geological and astrophysical flows: in magmas (e.g., see the experimental model in figure 1.2(b)), where the additional process of crystallisation can increase the thermal and compositional gradients required for layering [85]; at the core-mantle boundary, where melting subducting plates and minerals undergoing phase transitions can provide temperature and compositional variations between the core and mantle [77, 104]; and in stellar interiors [69, 168] or in planetary interiors, where the thermal and compositional profiles resulting from doubly diffusive convection may impact planet formation and cooling properties [105].

The systems of doubly diffusive convection described above tend to have thermal and solutal gradients parallel to gravity, where the kinetic energy required to sustain fluid motion can be extracted from the potential energy of the stably stratified field. However, there are further systems where these gradients are either inclined to each other or to gravity, which undergo different types of doubly diffusive convection.

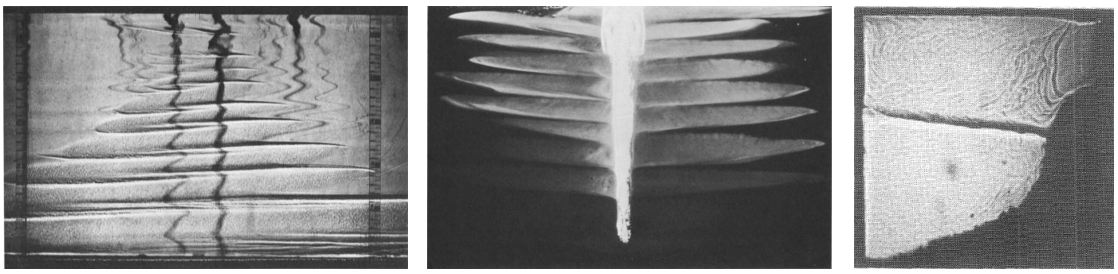

(a) (b) (c)

Figure 1.3: (a) Doubly diffusive intrusions between stratified sugar (left) and salt (right) solutions. From [148]. (b) Formation of horizontal layers when ice melts in a stratified salt solution. From [87]. (c) Doubly diffusive convection during the solidification of ammonium chloride solution when the right sidewall is cooled. Light (dark) regions mostly indicate fluid (solid), except for the upward plumes from the interface and the nearly horizontal diffusive interface between convecting layers. From [18]

Within oceanography, lateral gradients exist near fronts between water masses with different physical properties. This can lead to the formation of interleaving thermohaline intrusions that may extend up to several hundred kilometres laterally (see [146] and references therein). The laboratory experiment by Ruddick et al. [147, 148], shown in figure 1.3(a), illustrates intrusions on a smaller scale when a barrier between stably stratified sugar (left) and salt (right) solutions is removed. We see that interleaving layers form and extend away from the centre, with the width and height of the layers increasing with depth and lateral variation in sugar concentration, which Ruddick and Turner [147] explained using the energetics of the system. One might also observe similar upward-tilting intrusions that spread outwards into the surrounding fluid in the vicinity of a melting ice-block [84, 86] (see figure 1.3(b)).

Solidification during crystal growth is another system where lateral gradients are important [17, 18, 31, 83, 181]. This process is illustrated in figure 1.3(c), which depicts an experimental snapshot by Beckermann and Viskanta [18] of an ammonium chloride solution that is cooled from the right. The solution solidifies near the colder right sidewall to form solid dendrites with a higher ammonium chloride concentration than the surrounding fluid. Water is rejected during this process, which results in the fluid in the mushy layer—the multiphase porous media between the purely solid and liquid

regions—being relatively less dense and rising upwards (see upward plumes in figure 1.3(c)). The fluid within the liquid region is subject to doubly diffusive convection, which can lead to sharp interfaces separating distinct layers of convective motion. The resulting convection may further affect the shape of the mushy layer since the local solidification rates are influenced by the local fluid temperature and solute concentration. This is particularly important since the shape of the interface can affect the trajectory of convective jets (plumes), which affect where freckles, or defects, in the solid occur [48].

The configuration where both the thermal and solutal gradients are perpendicular to the buoyancy force is typically referred to as natural doubly diffusive convection and is the configuration of interest in this thesis. In particular, we will consider a domain that is bounded in the horizontal direction and impose the driving gradients by fixing the temperature and solutal concentration on the sidewalls.

1.2 GOVERNING EQUATIONS

One of the two key properties that allows a fluid to undergo doubly diffusive convection is that both thermal and solutal variations affect the density of the fluid. We assume that this dependence is linear in both temperature and solutal concentrations, so that the fluid density satisfies

$$\rho^* = \rho_0 + \rho_T(T^* - T_0) + \rho_C(C^* - C_0), \tag{1.1}$$

where ρ_0 is the density of the fluid at temperature T_0 and concentration C_0 and ρ_T (resp. ρ_C) is the thermal (resp. solutal) expansion coefficient, with $\rho_T < 0$ and $\rho_C > 0$. The imposed thermal and solutal variations are also assumed to be sufficiently small so that the Boussinesq approximation can be applied, whereby density variations are neglected except when they appear in buoyancy terms.

Systems of doubly diffusive convection are governed by four equations: the Navier–Stokes equation for fluid momentum, the incompressibility condition and advection-

diffusion equations for both the temperature and the concentration. The governing equations therefore read:

$$\rho_0 \left(\frac{\partial \mathbf{u}^*}{\partial t^*} + \mathbf{u}^* \cdot \nabla^* \mathbf{u}^* \right) = -\nabla^* p^* + \nu \rho_0 \nabla^{*2} \mathbf{u}^* + (\rho_0 - \rho^*) g \hat{\mathbf{z}}, \tag{1.2}$$

$$\nabla^* \cdot \mathbf{u}^* = 0, \tag{1.3}$$

$$\frac{\partial T^*}{\partial t^*} + \mathbf{u}^* \cdot \nabla^* T^* = \kappa \nabla^{*2} T^*, \tag{1.4}$$

$$\frac{\partial C^*}{\partial t^*} + \mathbf{u}^* \cdot \nabla^* C^* = D \nabla^{*2} C^*, \tag{1.5}$$

where $\hat{\mathbf{z}}$ is the vertical ascending unit vector, κ is the rate of thermal diffusivity, D is the rate of solutal diffusivity and ν is the kinematic viscosity. Cross-diffusion effects, where either the solute concentration diffuses owing to a temperature gradient, in a process known as the Soret effect, or temperature diffuses owing to a solutal concentration gradient, in a process known as the Dufour effect, may also play a role in the dynamics. However, their effect will be neglected here since a suitable linear transformation can transform the system into one equivalent to (1.2–1.5) without cross-diffusion effects when suitable thermal and solutal boundary conditions are applied [98].

We introduce the non-dimensional quantities:

$$\mathbf{x} = \frac{\mathbf{x}^*}{L}, \quad t = \frac{t^*}{L^2/\kappa}, \quad \mathbf{u} = \frac{\mathbf{u}^*}{\kappa/L}, \quad T = \frac{T^* - T_0}{\Delta T}, \quad C = \frac{C^* - C_0}{\Delta C}, \quad p = \frac{p^*}{\rho_0 \kappa \nu / L^2}, \tag{1.6}$$

where L is a relevant length scale and ΔT and ΔC are appropriate temperature and solutal concentration differences within the system. The non-dimensional governing equations for the fluid velocity $\mathbf{u} = u\hat{\mathbf{x}} + v\hat{\mathbf{y}} + w\hat{\mathbf{z}}$, the pressure p, the temperature T

and the concentration C thus read:

$$\frac{1}{Pr}\left(\frac{\partial \mathbf{u}}{\partial t} + \mathbf{u}\cdot\nabla\mathbf{u}\right) = -\nabla p + \nabla^2\mathbf{u} + Ra\,(T + NC)\,\hat{\mathbf{z}}, \tag{1.7}$$

$$\nabla\cdot\mathbf{u} = 0, \tag{1.8}$$

$$\frac{\partial T}{\partial t} + \mathbf{u}\cdot\nabla T = \nabla^2 T, \tag{1.9}$$

$$\frac{\partial C}{\partial t} + \mathbf{u}\cdot\nabla C = \frac{1}{Le}\nabla^2 C, \tag{1.10}$$

where we have introduced the following dimensionless parameters. The Prandtl number:

$$Pr = \frac{\nu}{\kappa}, \tag{1.11}$$

represents the ratio of momentum to thermal diffusivity and therefore quantifies inertial effects; the Rayleigh number:

$$Ra = \frac{gL^3|\rho_T|\Delta T}{\rho_0 \nu\kappa}, \tag{1.12}$$

provides a measure of the imposed temperature difference; the buoyancy ratio:

$$N = \frac{\rho_C \Delta C}{\rho_T \Delta T}, \tag{1.13}$$

represents the ratio of solutal to thermal contributions to the fluid density; and the Lewis number:

$$Le = \frac{\kappa}{D}, \tag{1.14}$$

represents the ratio of thermal to solutal diffusivities. Analogous non-dimensionalisations, e.g., where the kinematic viscosity or the rate of solutal diffusivity are used in place of the rate of thermal diffusivity, are possible and may introduce alter-

native dimensionless parameters:

$$\text{the Schmidt number} \quad Sc = \frac{\nu}{D} = PrLe, \tag{1.15}$$

$$\text{the solutal Rayleigh number} \quad Ra_S = \frac{gL^3|\rho_C|\Delta C}{\rho_0 \nu D} = Ra|N|Le, \tag{1.16}$$

$$\text{the Grashof number} \quad Gr = \frac{gL^3|\rho_T|\Delta T}{\rho_0 \nu^2} = \frac{Ra}{Pr}, \tag{1.17}$$

$$\text{and the solutal Grashof number} \quad Gr_S = \frac{gL^3|\rho_C|\Delta C}{\rho_0 \nu^2} = \frac{Ra|N|}{Pr}, \tag{1.18}$$

into the formulation. These parameters will not be considered in this thesis, but have been included in reference to other literature on doubly diffusive convection.

1.3 PHYSICAL PARAMETERS

Values for the physical parameters vary significantly across the astrophysical and geophysical flows in which doubly diffusive convection occurs. For example, variations across Prandtl (1.11) and Lewis (1.14) numbers are summarised by the grey regions in figure 1.4, which illustrate parameter values from Schmitt [157]. One might expect for the behaviour of the system to differ between systems where the Prandtl number is large (e.g., 0.4–5×10^3 in magmas) and inertia is negligible meaning that an infinite-Prandtl number approximation may be made [78], and those where the Prandtl number is small (e.g., 10^{-6} in stellar interiors) and inertia plays an important role [68]. Despite this wide range, early studies of natural doubly diffusive convection with opposing driving gradients only considered a much smaller range of parameter values as evidenced by the blue and red regions in figure 1.4, which represent parameter values used in numerical and experimental studies respectively. In particular, we note the cluster of values shown in the right panel, which are associated with horizontal crystal-growth processes that frequently motivated these early studies.

The Lewis number (1.14) characterises the extent to which heat and solutal concentration have different rates of diffusion, with $Le > 1$ ($Le < 1$) indicating that temperature

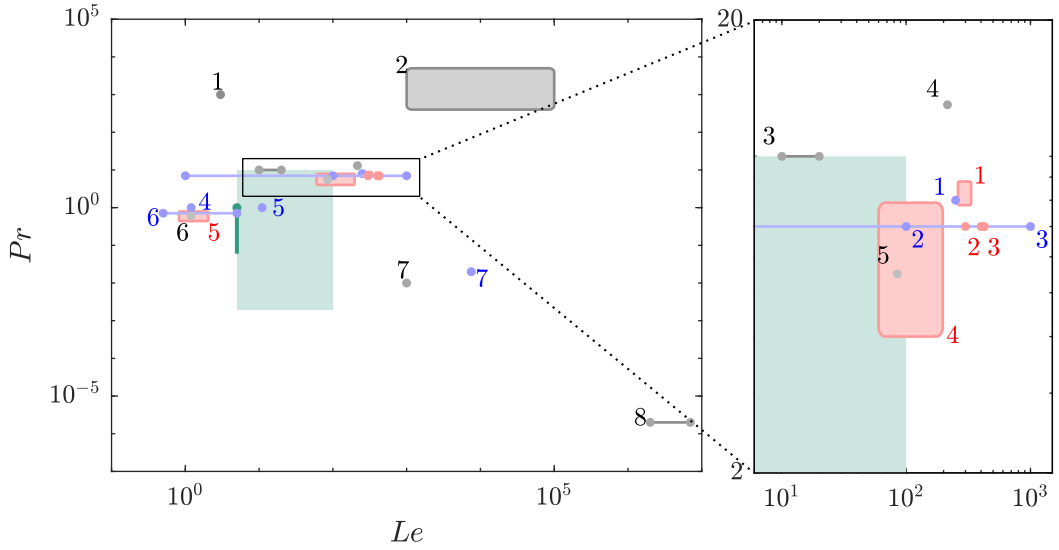

Physical

[1]Salt/sugar
[2]Magmas
[3]Oxide semiconductors
[4]Heat/salt at 0°C
[5]Heat/salt at 30°C
[6]Humidity/heat
[7]Liquid metals
[8]Stellar interiors

Experimental

[1]Copper sulphate solution [75]
[2]Copper sulphate solution [92]
[3]Copper sulphate solution [90]
[4]Salt-water solution [106]
[5]Binary gases [189]

Numerical

[1]Han and Kuehn [76]
[2]Lee and Hyun, [88, 108]
[3]Bennacer and Gobin, [20, 72]
[4]Xin et al. [191]
[5]Convectons [12, 14, 23, 24]
[6]Beghein et al. [19]
[7]Bergman and Hyun [27]

Figure 1.4: Parameter values of the Prandtl and Lewis numbers for a selection of physical (grey), numerical (blue) and experimental (red) systems of doubly diffusive convection. Physical values were taken from [157] and many of the experimental and numerical results were taken from the summary in Ghorayeb and Mojtabi [70]. The green region, line and point indicate the parameter values that we consider in Chapters 4, 5 and 6, respectively.

(solutal concentration) is the faster diffusing component. Taking $Le \neq 1$, i.e., imposing that the rates of thermal and solutal diffusion differ, is essential for the system to undergo doubly diffusive convection, since otherwise a transformation $\hat{T} = T + NC$ reduces (1.7–1.10) to a system for single-component convection.

The buoyancy ratio (1.13) characterises the contributions of solutal variations to the total fluid density compared to contributions from thermal variations. In particular, the sign of this parameter indicates whether the imposed thermal and solutal gradients provide cooperating ($N > 0$) or opposing ($N < 0$) effects on the total fluid density. It is also helpful to note the particular limits: $N = -1$, which indicates the balanced system where the imposed thermal and solutal gradients balance; $N = 0$, which indicates purely thermal convection; and $N \to \pm\infty$, which represent the limits of purely solutal convection.

Early experimental works on natural doubly diffusive convection with opposing gradients showed that the buoyancy ratio separates regimes of unicellular and multicellular flow [106] or regimes where the flow is steady or exhibits oscillatory behaviour [90, 92]. Later numerical studies considered the latter observation in more detail by finding ranges of buoyancy ratios where the flow was steady, periodic, quasiperiodic or chaotic [113, 114, 135, 196] and determining the difference between the associated dynamics in two- and three-dimensional domains [162]. These studies, however, tended to consider large Rayleigh numbers, well beyond the onset of convection, where one typically expects a range of complicated dynamics [165].

1.4 BIFURCATION ANALYSIS

In the balanced system of natural doubly diffusive convection when $N = -1$, a motionless conduction state with linear temperature and solutal profiles exists for all Rayleigh numbers. This trivial state is stable to all linear perturbations at sufficiently low Rayleigh numbers but will destabilise to an increasing number of linear modes as the Rayleigh number increases. The Rayleigh number at which the conduction state first destabilises to a stationary mode, where the growth rate of the perturbation is purely real, is referred

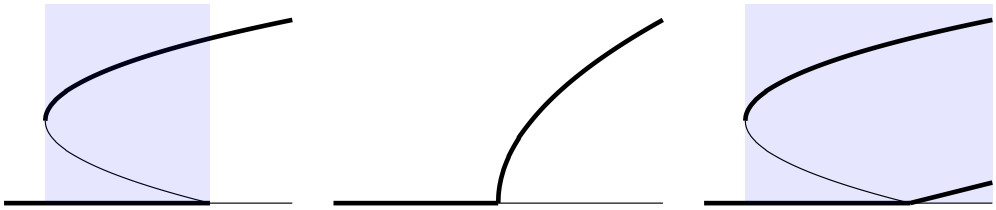

(a) Subcritical pitchfork bifurcation

(b) Supercritical pitchfork bifurcation

(c) Transcritical bifurcation

Figure 1.5: Sketches depicting (a) subcritical and (b) supercritical pitchfork bifurcations and (c) a transcritical bifurcation of the trivial state, together with typical nonlinear behaviour. Thick (thin) lines indicate stable (unstable) steady solutions. The blue shaded regions in (a) and (c) indicate the region of bistability between a pair of stable steady states.

to as the critical Rayleigh number and its value depends on both the Lewis number and the geometry of the domain; for example, Ghorayeb and Mojtabi [70] showed that in the limit of infinite aspect ratio the critical Rayleigh number converges on the value it takes when periodic boundary conditions are imposed in the vertical direction:

$$Ra_c \approx \frac{6509}{|1 - Le|}, \tag{1.19}$$

which we note tends to infinity in the limit $Le \to 1$.

A pair of branches consisting of convection states bifurcate at each stationary instability of the conduction state. The resulting branches are referred to as primary branches and bifurcate either subcritically, towards lower values of the Rayleigh number as in figure 1.5(a), or supercritically, towards higher Rayleigh numbers as in figure 1.5(b). Both subcritical and supercritical branches have been found in closed domains of natural doubly diffusive convection since the conduction state can destabilise in transcritical bifurcations, like that shown in figure 1.5(c), as well as pitchfork bifurcations [25, 70]. With periodic boundary conditions in the vertical direction, however, the conduction state has only been found to destabilise in subcritical pitchfork bifurcations for the parameters values considered in previous studies [23, 24, 191].

Subcritical branches are of particular interest since, while these initially head towards lower parameter values, they often turn around at a subcritical saddle-node bifurcation

where they regain stability and proceed to extend towards larger parameter values, as evidenced by the nonlinear behaviour in figures 1.5(a) and (c). This leads to a region below the linear onset of convection where multiple steady states coexist with the stable trivial state. Further, when the non-trivial steady states undergo no additional instabilities, the system will exhibit a region of bistability where at least two stable states coexist, which are indicated by the blue shading in figure 1.5. Bistability has often been viewed as an important property for pattern formation, including for localised states, which typically consist of a region of one stable pattern embedded within a background of a second stable pattern and whose study across a range of physical systems has been an active field of research over the past 15 years.

1.5 CONVECTONS

Ghorayeb and Mojtabi [70] first identified spatially localised states in natural doubly diffusive convection at low Rayleigh numbers as one of a number of stable coexisting states in sufficiently large domains. Bergeon and Knobloch [23, 24] later studied localised states in larger domains, where they found that these states consist of a number of convection rolls within a background of quiescent fluid, as depicted in figure 1.6(b). Such localised states are typically referred to as convectons, after Blanchflower [30] first described similar states in magnetoconvection. Since then, convectons have been studied across a range of other coupled convective systems, including: binary fluid convection [7, 129, 130, 186, 187] (in a porous medium [116, 119]), where a solutal concentration gradient develops from the Soret effect applied to an imposed temperature gradient; and in rotating convection [11, 50] or magnetoconvection [30, 50, 54, 117, 118].

Bergeon and Knobloch [23, 24] were the first to elucidate the snaking structure of the branches associated with convectons in two-dimensional natural doubly diffusive convection, which we have depicted in figure 1.6(a). They found that a pair of secondary branches, L1 and L2, bifurcate from the subcritical primary branch P1 when a small-amplitude periodic state undergoes an Eckhaus, or modulational, instability, where the

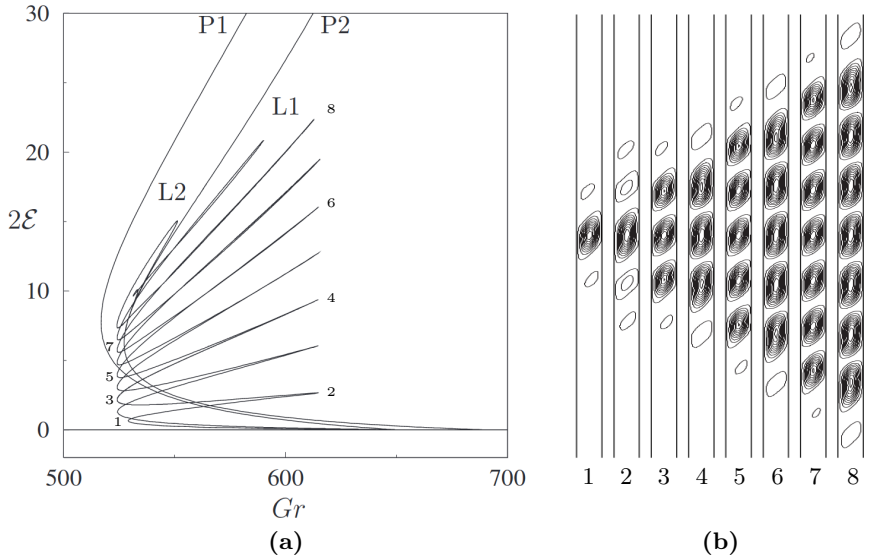

Figure 1.6: Convectons in a system of natural doubly diffusive convection in a two-dimensional periodic vertical domain with period 30. (a) Bifurcation diagram showing twice the kinetic energy $\mathcal{E}$ of the steady states as the Grashof number Gr varies. The Grashof number is equivalent to the Rayleigh number here since $Pr = 1$. (b) Stream-functions of convectons at successive saddle nodes on the branch of localised states L2. Owing to the symmetry of the system, we have reflected each profile about the vertical axis from [24] to illustrate the effects of the right sidewall having a higher temperature and solute concentration than the left. Adapted from [24].

state destabilises to a long-wave modulation [26]. These secondary branches extend towards lower Grashof (equivalently Rayleigh) numbers while the convection states become increasingly spatially modulated and fully localised by the first left saddle nodes, so that they either contain a single strong convection roll on L1 (panel 1 in figure 1.6(b)) or a pair of rolls on L2. The two branches proceed to intertwine as they oscillate upwards over a finite range of parameter values, which is associated with a pair of outer rolls strengthening between successive left or right saddle nodes (see alternate panels in figure 1.6(b)). This oscillatory behaviour continues until convection rolls fill the domain (panel 8 in figure 1.6(b)), at which point the rolls adjust their position and the branches either turn over to terminate at an Eckhaus instability near the saddle node of a potentially different primary branch (P2 in figure 1.6(a)) or extend towards larger parameter values [26]. This behaviour is typically referred to as homoclinic snaking and was first identified for the Swift–Hohenberg equation [190], but has since been observed across many other systems exhibiting localised states (see the review by Knobloch [99]).

Bergeon and Knobloch [24] further computed the stability of the localised convection states and found that those on branch segments between left and right saddle nodes as the branches are followed upwards (e.g., between points 3 and 4 in figure 1.6(a)) were stable. There is therefore a region of parameter values over which multiple stable localised convection states with different numbers of rolls coexist.

Later studies examined the nature of the snaking branches of convectons in different configurations of natural doubly diffusive convection. For example, Beaume et al. [12] showed these branches continued to undergo homoclinic snaking when no-slip boundary conditions were applied despite the absence of primary branches of periodic states. Similar behaviour has also been found in the Swift–Hohenberg equation with non-Neumann boundary conditions [80] and in binary fluid convection [128, 129] and might be expected since a localised state in a sufficiently large domain would be minimally affected by conditions at the ends of the domain.

Beaume et al. [12, 13, 14] also considered convectons in three-dimensional domains, where they showed that the third dimension enabled individual convection rolls to twist

about the vertical axis, as was previously found in small-aspect-ratio domains [22]. The authors showed that convectons with twisted rolls lie on secondary snaking branches that bifurcate from branches of convectons with untwisted rolls (see figure 7 of [12]), which they compared to behaviour observed in the two-dimensional Swift–Hohenberg [115]. They found that this twist instability destabilises all steady states and results in chaotic behaviour for supercritical Rayleigh numbers [12, 14] that originates from a crisis bifurcation near the primary bifurcation [9].

The snaking of the branches of localised states seen in figure 1.6 is highly dependent upon preserving symmetries within the system, which exist owing to the balance between thermal and solutal contributions to the fluid density obtained by fixing the buoyancy ratio to be $N = -1$ and by imposing identical fixed temperature and solutal concentration boundary conditions on the sidewalls. Despite this, the former constraint has yet to be relaxed for studies on convectons, while the latter has only recently been addressed by Lo Jacono et al. [120], who imposed Robin type boundary conditions on the solutal concentration. They showed how increasingly breaking this symmetry resulted in each of the steady states drifting vertically and a complex breakup of the snaking branches, where the branches first broke into a stack of disconnected figure-of-eight branch segments before later connecting with further branches of localised travelling pulses of convection.

These studies of natural doubly diffusive convection have only considered an isolated choice for parameter values, where $N = -1$, $Le = 11$ and $Pr = 1$ (see the point marked [5] in figure 1.4). In particular, this choice allows a motionless conduction state to exist and provides both subcriticality and bistability when periodic boundary conditions are applied in the vertical direction, as was seen in figure 1.6(a). These properties are frequently associated with the existence of localised states and, thus, there is an open question as to how the homoclinic snaking changes if the system ceases to exhibit each of these properties when each of the physical parameters are varied.

1.6 THESIS OVERVIEW

In this thesis, we aim to explore the effects that four physical parameters: the Prandtl number, Pr; the Lewis number, Le; the Rayleigh number Ra; and the buoyancy ratio, N, have on the system of natural doubly diffusive convection with opposing lateral thermal and solutal gradients. To do so, we focus on the parameter regime marked in green in figure 1.4, with the aim of extracting a general understanding as to how each of the physical parameters affects both states and the structure of the bifurcation diagram near the onset of convection. We are particularly interested in their impact on convectons since such an analysis might help us to develop further insight into whether localised states can exist in physical or experimental systems of natural doubly diffusive convection, similarly to how they do in other convective systems, e.g., [35, 101, 134]. With these goals in mind, the thesis is organised in the following way.

In Chapter 2, we summarise the numerical methods that were used to generate the results presented later in this thesis. This is followed, in Chapter 3, by reviewing a selection of theoretical and numerical results related to localised states. We focus on the one-dimensional Swift–Hohenberg equation as a prototypical model for spatial localisation, including convectons in natural doubly diffusive convection.

Motivated by understanding the parameter ranges where steady convection states exist, in Chapter 4, we present the linear stability analysis and a weakly nonlinear analysis for all Lewis and Prandtl numbers in the balanced system with $N = -1$, which enables us to divide (Le, Pr) parameter space according to whether the primary bifurcation was subcritical or supercritical (see figure 4.9). We numerically continue the resulting primary branches to larger amplitudes in order to determine their structure and stability, which allows us to obtain parameter regimes where the system exhibits coexistence between steady convection and stable conduction states.

In Chapter 5, we extend the analysis to vertically extended domains by determining how the structure of the snaking branches changes as the Prandtl number decreases and

the primary bifurcation changes from being subcritical to supercritical. We characterise this transition in five stages (see figure 5.3), which we interpret by considering how the steady states change form as a result of increasing inertial effects.

In Chapter 6, we explore what happens when we vary the buoyancy ratio away from $N = -1$, thereby breaking the restriction that the imposed thermal and solutal gradients balance. With this relaxation in a closed domain, the motionless conduction state at low Rayleigh numbers is replaced by a large-scale flow consisting of either clockwise ($N < -1$) or anticlockwise ($N > -1$) flow and the primary bifurcations unfold. We explore how the form of convectons, which have so far only been considered in the balanced case with $N = -1$, are affected by the absence of the conduction state by varying N into both thermally and solutally dominated regimes (see figure 6.11). We further investigate how the structure of branches on which convectons lie changes before we stop finding them in the thermally dominated regime with $N > -1$.

We end with conclusions and suggestions for future research in Chapter 7.

2 | NUMERICAL METHODS

In this chapter, we will outline the numerical schemes that were used to generate the results presented in this thesis, including spectral methods (section 2.1), time-stepping methods (section 2.2) and numerical continuation (section 2.3). Custom MATLAB codes were written to numerically continue the Swift–Hohenberg equations and perform the weakly nonlinear analysis of the system of doubly diffusive convection, while an adapted version of code developed by A. Bergeon and C. Beaume, which was detailed in [8], was used to numerically continue and time-step the coupled system for natural doubly diffusive convection.

2.1 SPECTRAL METHODS

We employed spectral methods, e.g., as described by Boyd [33] and Trefethen [174], to determine the spatial dependence of solutions to partial differential equations (PDEs). Typically these methods involve approximating the true solution by a linear combination of smooth global basis functions. The coefficients in this expansion are initially unknown, but can be found by substituting the approximate solution into the PDE and solving the resulting equations using either collocation or numerical quadrature. Spectral methods therefore reduce the infinite dimensional PDE to a finite number of coupled nonlinear equations for the coefficients, which may then be solved using linear algebra techniques. These methods additionally have exponential convergence, which means that results with the same level of accuracy can be achieved using fewer nodes than finite difference methods, for example.

2.1.1 FOURIER APPROXIMATIONS

The optimal choice of basis functions in the approximation depends upon the boundary conditions applied. In a periodic domain of length L, the functions are approximated using the finite Fourier series:

$$f(x) \approx a_0 + \sum_{n=1}^{N} \left(a_n e^{ik_n x} + \bar{a}_n e^{-ik_n x} \right), \text{ where } k_n = \frac{2\pi n}{L}, \tag{2.1}$$

where the overbar denotes complex conjugation and the coefficients a_n are defined:

$$a_0 = \frac{1}{L} \int_0^L f(x)\, dx, \tag{2.2}$$

$$a_n = \frac{1}{L} \int_0^L f(x) e^{-ik_n x}\, dx, \tag{2.3}$$

and approximated using the numerical quadrature schemes:

$$a_0 \approx \frac{1}{L} \sum_{m=0}^{N-1} f(x_m), \tag{2.4}$$

$$a_n \approx \frac{1}{L} \sum_{m=0}^{N-1} f(x_m) e^{-ik_n x_m}, \tag{2.5}$$

where $x_m = \frac{mx}{L}$ are regularly spaced nodes within the domain $[0, L]$. By substituting (2.4) and (2.5) back into the Fourier expansion (2.1), we see that an approximation for $f(x)$ may be constructed using the N values of the function evaluated at the nodes x_m.

2.1.2 POLYNOMIAL APPROXIMATIONS

If fixed boundary conditions are instead applied on a finite closed domain $[a, b]$, the function $f(x)$ may be more conveniently approximated using a linear combination of orthogonal polynomials, such as Legendre polynomials ($P_n(x)$) or Chebyshev polynomials ($T_n(x)$). Since both of these examples are defined over the closed interval $[-1, 1]$,

we first perform the linear transformation:

$$x \mapsto -1 + \frac{2}{b-a}(x-a). \tag{2.6}$$

to map the PDE defined over the closed interval $[a,b]$ onto the interval $[-1,1]$. This allows a unique polynomial of degree at most N to interpolate $f(x)$ at either:

- Chebyshev points ($x_n = -\cos\left(\frac{n\pi}{N}\right)$ for $n = 0,1,\ldots,N$) for Chebyshev polynomials, or
- Gauss–Lobatto–Legendre points ($x_0 = -1$, $x_N = 1$ and the x_i for $i = 1,...,N-1$ the $N-1$ roots of $\frac{dP_{N+1}}{dx}$) for Legendre polynomials.

We used the MATLAB package Chebfun [64] to compute the Chebyshev polynomial approximations.

In larger domains, it can be helpful to apply spectral element methods, where the domain is subdivided into a number of smaller parts, known as elements. Within each element, the functions are approximated by a single polynomial that are coupled to those in adjacent elements using continuity conditions at the interfacial points. These methods allow polynomials of lower degree to be used, which is beneficial as entries in the corresponding spectral differentiation matrices scale like N^2 and thus become less well-conditioned.

2.1.3 MATRIX-FREE METHODS

Approximating the functions using finite Fourier and/or polynomial approximations enables the PDEs to be approximated by a finite linear system of the form:

$$A\mathbf{x} = \mathbf{b}, \tag{2.7}$$

where $\mathbf{x}$ is a vector containing the function values evaluated at the collocation points. The matrix A incorporates the effects of the spatial derivatives on the functions and may

be dense owing to the global nature of spectral methods, which means that inverting the matrix A to solve (2.7) for $\mathbf{x}$ directly can be difficult. We instead choose to apply matrix-free methods, which are so-called because one only needs to know the action of the linear matrix A on vectors $\mathbf{v}$ rather than storing and inverting the full matrix A. Such methods are particularly useful when A represents a linear operator that cannot be inverted or whose matrix form is unknown.

Krylov subspace methods, including Generalized Minimum Residual Method (GMRES) [151], Biconjugate Gradient Stabilized Method (BiCGstab) [166] and Induced Dimension Reduction Method (IDRs) [167, 184], amongst others, are commonly used matrix-free methods. Their implementation, however, varies with Krylov subspace method applied and so we focus on a simple version of GMRES for simplicity and leave possible extensions of this algorithm and details of other Krylov subspace methods to the review by Saad [149].

Starting from an initial guess $\mathbf{x}_0$, where the residual vector is

$$\mathbf{r}_0 = \mathbf{b} - A\mathbf{x}_0, \tag{2.8}$$

approximate solutions $\mathbf{x}_m$ are iteratively found until the residual $\|\mathbf{b} - A\mathbf{x}_m\|$ lies below a specified threshold. This is achieved by first applying Arnoldi's method [2] to construct an orthonormal basis $\{\mathbf{v}_1, \mathbf{v}_2, \ldots, \mathbf{v}_m\}$ of the Krylov subspace $\mathcal{K}_m$ defined

$$\mathcal{K}_m(A, \mathbf{r}_0) = \text{span}\{\mathbf{r}_0, A\mathbf{r}_0, A^2\mathbf{r}_0, \ldots, A^{m-1}\mathbf{r}_0\}. \tag{2.9}$$

This is an orthogonalisation process that starts from

$$\mathbf{v}_1 = \frac{\mathbf{r}_0}{\|\mathbf{r}_0\|}, \tag{2.10}$$

and iteratively finds the next basis vector using the relation:

$$\mathbf{v}_{j+1} = \frac{A\mathbf{v}_j - \sum_{i=1}^{j} h_{ij}\mathbf{v}_i}{h_{j+1,j}}, \tag{2.11}$$

where the entries h_{ij} of the $(m+1) \times m$ upper Hessenberg matrix $\tilde{H}_m$ are defined

$$h_{ij} = \begin{cases} \langle A\mathbf{v}_j, \mathbf{v}_i \rangle & \text{for } i \leqslant j, \\ \|A\mathbf{v}_j - \sum_{i=1}^{j} h_{ij}\mathbf{v}_i\| & \text{for } i = j+1. \end{cases} \tag{2.12}$$

Rearranging (2.11), we find that the vector equations:

$$A\mathbf{v}_j = \sum_{i=1}^{j+1} h_{ij}\mathbf{v}_i, \tag{2.13}$$

are satisfied for $j = 1, \ldots, m$, which are equivalent to the matrix equation:

$$AV_m = V_{m+1}\tilde{H}_m, \tag{2.14}$$

where V_k is the matrix whose column vectors are $\mathbf{v}_1, \mathbf{v}_2, \ldots, \mathbf{v}_k$. We then constrain the approximate solution $\mathbf{x}_m$ to lie within the subspace:

$$\mathbf{x}_m \in \mathbf{x}_0 + \mathcal{K}_m, \tag{2.15}$$

which allows us to suppose that $\mathbf{x}_m = \mathbf{x}_0 + \mathbf{y}_m$, where $\mathbf{y}_m \in \mathcal{K}_m$.

This simplifies the minimisation of the residual $\|\mathbf{b} - A\mathbf{x}_m\|$ to one over the m-dimensional Krylov subspace $\mathcal{K}_m$, which may be seen by re-expressing the residual via the following steps. We can firstly note that

$$\|\mathbf{b} - A\mathbf{x}_m\| = \|\mathbf{b} - A\mathbf{x}_0 - A\mathbf{y}_m\|, \tag{2.16}$$

$$= \|\mathbf{r}_0 - A\mathbf{y}_m\|. \tag{2.17}$$

Since $\{\mathbf{v}_1, \mathbf{v}_2, \ldots, \mathbf{v}_m\}$ spans $\mathcal{K}_m$, we may write

$$\mathbf{y}_m = V_m\tilde{\mathbf{y}}_m, \tag{2.18}$$

where $\tilde{\mathbf{y}}_m \in \mathbb{R}^m$ and use this relation with (2.14) to simplify the right-hand side of (2.17)

to

$$\|\mathbf{b} - A\mathbf{x}_m\| = \|V_{m+1}\left(\|\mathbf{r}_0\|\mathbf{e}_1 - \tilde{H}_m\tilde{\mathbf{y}}_m\right)\|, \tag{2.19}$$

where we have also used that $\mathcal{K}_1 = \text{span}\{\mathbf{r}_0\}$ to write $\mathbf{r}_0 = \|\mathbf{r}_0\|\mathbf{e}_1$, where $\mathbf{e}_1$ is the first unit vector of $\mathbb{R}^m$. We finally use the orthonormality of the basis $\{\mathbf{v}_1, \ldots, \mathbf{v}_{m+1}\}$ to find that

$$\|\mathbf{b} - A\mathbf{x}_m\| = \|\|\mathbf{r}_0\|\mathbf{e}_1 - \tilde{H}_m\tilde{\mathbf{y}}_m\|. \tag{2.20}$$

Thus, finding the approximate solution $\mathbf{x}_m$ subject to (2.15) at each iteration is equivalent to solving the least-squares problem:

$$\tilde{H}_m\tilde{\mathbf{y}}_m = \|\mathbf{r}_0\|\mathbf{e}_1, \tag{2.21}$$

for $\tilde{\mathbf{y}}_m$, which is simple to solve via a QR factorisation of $\tilde{H}_m$.

If the residual $\|\mathbf{b} - A\mathbf{x}_m\|$ lies above some specified threshold then one must continue the algorithm to obtain the next approximation, $\mathbf{x}_{m+1}$. This process may not be computationally expensive, however, as the iterative nature of Krylov subspace methods means that each additional iteration builds upon the previous in the following way. A single iteration of Arnoldi's method first extends the orthonormal basis of $\mathcal{K}_m$ to one for $\mathcal{K}_{m+1}$ by the addition of a single vector $\mathbf{v}_{m+1}$. One then uses the upper Hessenberg matrix $\tilde{H}_{m+1}$, constructed via Arnoldi's method, to define a least-squares problem, analogous to (2.21), which is solved for $\tilde{\mathbf{y}}_{m+1}$ and hence $\mathbf{x}_{m+1}$. This process continues until the residual $\|\mathbf{b} - A\mathbf{x}_M\|$ is sufficiently small. We should note that the final solution $\mathbf{x}_M$ is an approximation to the true solution of (2.7) and will only be exact when $\mathbf{x} \in \mathbf{x}_0 + \mathcal{K}_M$. Nevertheless, one can often achieve good accuracy with $M \ll n$, where n is the (potentially large) dimension of our initial solution space.

2.2 TIME-STEPPING SCHEMES

Having detailed how spectral methods have been used to solve the spatial dependence of solutions to the PDEs, we will now introduce methods that can be used to solve the temporal dynamics. To achieve this, we consider a general first-order in time PDE for a variable u:

$$\frac{\partial u}{\partial t} = \mathcal{F}(u; x, t), \tag{2.22}$$

for which it is convenient to write the right-hand side as a sum of linear and nonlinear terms:

$$\frac{\partial u}{\partial t} = \mathcal{L}u + \mathcal{N}(u), \tag{2.23}$$

where $\mathcal{L}$ is a linear operator and $\mathcal{N}$ is a nonlinear operator.

2.2.1 SEMI-IMPLICIT EULER SCHEME

One of the simplest time-stepping schemes that we can apply is a first-order semi-implicit Euler scheme. In this method, we use a first-order approximation for the time-derivative and we treat the linear operator implicitly, while treating the nonlinear operator explicitly. Thus, at time $t + \Delta t$, we solve

$$\frac{u^{t+\Delta t} - u^t}{\Delta t} = \mathcal{L}u^{t+\Delta t} + \mathcal{N}(u^t). \tag{2.24}$$

Rearranging for $u^{t+\Delta t}$, this becomes

$$(I - \Delta t\mathcal{L})u^{t+\Delta t} = u^t + \Delta t\mathcal{N}(u^t), \tag{2.25}$$

$$\implies \quad u^{t+\Delta t} = (I - \Delta t\mathcal{L})^{-1}(u^t + \Delta t\mathcal{N}(u^t)). \tag{2.26}$$

When the operator $(I - \Delta tL)$ is easily invertible, equation (2.26) may be solved directly for $u^{t+\Delta t}$. Otherwise, it may be more convenient to solve (2.25) using matrix-free methods.

The order of the semi-implicit scheme can be improved, for example, by using an implicit Adams–Moulton method to integrate the linear terms and an explicit Adams–Bashforth method of the same order to integrate the nonlinear terms.

2.2.2 EXPONENTIAL TIME DIFFERENCING

Exponential time differencing (ETD) schemes are a family of higher order time-stepping methods developed by Beylkin et al. [29] and extended by Cox and Matthews [51]. These methods have been shown to be more stable and have better accuracy than the second-order semi-implicit scheme for several stiff systems [51] and are therefore a good candidate for time-stepping the Swift–Hohenberg equation, which contains a term with a fourth-order spatial derivative.

The schemes are derived by first multiplying (2.23) by an integrating factor $e^{-\Delta t\mathcal{L}}$ for the linear terms in (2.23) and then integrating the resultant equation over a single time-step from t to $t + \Delta t$. This enables us to derive the following expression for u at the later time:

$$u^{t+\Delta t} = e^{\Delta t\mathcal{L}}u^t + e^{\Delta t\mathcal{L}}\int_0^{\Delta t} e^{-\tau\mathcal{L}}\mathcal{N}(u^{t+\tau})\,d\tau, \tag{2.27}$$

Here, we see that the linear terms have been integrated exactly, while an integral representation has been used for the integration of the nonlinear terms. This integral may be approximated in various ways, including using Runge–Kutta schemes, with each approximation corresponding to a different member of the family of ETD schemes. We refer the reader to [51] for further details about how these schemes are formulated.

2.2.3 SPLITTING SCHEME FOR NATURAL DOUBLY DIFFUSIVE CONVECTION

More sophisticated numerical schemes need to be employed to time-step the coupled system for natural doubly diffusive convection:

$$\frac{1}{Pr}\left(\frac{\partial \mathbf{u}}{\partial t} + \mathbf{u}\cdot\nabla\mathbf{u}\right) = -\nabla p + \nabla^2\mathbf{u} + Ra\,(T + NC)\,\hat{\mathbf{z}}, \tag{2.28}$$

$$\nabla\cdot\mathbf{u} = 0, \tag{2.29}$$

$$\frac{\partial T}{\partial t} + \mathbf{u}\cdot\nabla T = \nabla^2 T, \tag{2.30}$$

$$\frac{\partial C}{\partial t} + \mathbf{u}\cdot\nabla C = \frac{1}{Le}\nabla^2 C, \tag{2.31}$$

primarily because the incompressibility condition (2.29) needs to be satisfied everywhere in space at each time-step. We proceed by following the derivation of the first-order scheme that advances (2.28–2.31) detailed by Beaume [8], but note that the formulation can be readily adapted to higher order schemes using different temporal discretisations (e.g., see coefficients listed in Table IV of [94]).

The thermal (2.30) and solutal (2.31) fields are advanced using a semi-implicit method, similar to that presented in section 2.2.1, where the diffusive terms and temporal derivatives are treated implicitly, while the advective terms are treated explicitly. This leads to the following first-order discretisation for the thermal evolution equation (2.30) between the $(n)^{\text{th}}$ and $(n+1)^{\text{th}}$ time steps:

$$\frac{T^{(n+1)} - T^{(n)}}{\Delta t} + \mathbf{u}\cdot\nabla T^{(n)} = \nabla^2 T^{(n+1)}, \tag{2.32}$$

which may be rearranged to

$$(\mathcal{I} - \Delta t\nabla^2)T^{(n+1)} = (T^{(n)} - \Delta t\,\mathbf{u}\cdot\nabla T^{(n)}), \tag{2.33}$$

$$T^{(n+1)} = (\mathcal{I} - \Delta t\nabla^2)^{-1}\left(T^{(n)} - \Delta t\,\mathbf{u}\cdot\nabla T^{(n)}\right). \tag{2.34}$$

In practice, we express $T^{(n+1)}$ as

$$T^{(n+1)} = -(\nabla^2 + \alpha_T \mathcal{I})^{-1} \left(\frac{1}{\Delta t} T^{(n)} - \mathbf{u} \cdot \nabla T^{(n)} \right), \tag{2.35}$$

where $\alpha_T = -(\Delta t)^{-1}$. This equation, along with subsequent Helmholtz and Poisson equations, is solved by inverting the Helmholtz operators using a Schur decomposition and imposing suitable boundary conditions on the domain walls. The solutal concentration at the $(n+1)^{th}$ time step is similarly found by solving

$$C^{(n+1)} = -(\nabla^2 + \alpha_C \mathcal{I})^{-1} \left(\frac{1}{\Delta t} C^{(n)} - \mathbf{u} \cdot \nabla C^{(n)} \right), \tag{2.36}$$

where $\alpha_C = -Le(\Delta t)^{-1}$.

The velocity field is time-stepped using the splitting scheme by Karniadakis et al. [94], which involves three substeps. An intermediate velocity $\hat{\mathbf{u}}$ is introduced in the first step by allowing the velocity field to evolve via inertia and buoyancy forcing:

$$\frac{\hat{\mathbf{u}} - \mathbf{u}^{(n)}}{Pr\Delta t} = -\frac{1}{Pr} \mathbf{u} \cdot \nabla \mathbf{u}^{(n)} + Ra(T^{(n)} + NC^{(n)})\hat{\mathbf{z}}, \tag{2.37}$$

$$\implies \hat{\mathbf{u}} = \mathbf{u}^{(n)} + \Delta t \left(-\mathbf{u} \cdot \nabla \mathbf{u}^{(n)} + RaPr(T^{(n)} + NC^{(n)})\hat{\mathbf{z}} \right). \tag{2.38}$$

The second step involves correcting this intermediate velocity via the introduction of a pressure term $\bar{p}^{(n+1)}$ to ensure that the corrected intermediate velocity field $\hat{\hat{\mathbf{u}}}$ is incompressible. The correction assumes the form:

$$\frac{\hat{\hat{\mathbf{u}}} - \hat{\mathbf{u}}}{Pr\Delta t} = -\nabla \bar{p}^{(n+1)}, \tag{2.39}$$

where $\bar{p}^{(n+1)}$ satisfies the Poisson equation:

$$\nabla^2 \bar{p}^{(n+1)} = -\nabla \cdot \left(\frac{\hat{\hat{\mathbf{u}}}}{Pr\Delta t} - \frac{\hat{\mathbf{u}}}{Pr\Delta t} \right) \tag{2.40}$$

$$= \nabla \cdot \left(\frac{\mathbf{u}^{(n)}}{Pr\Delta t} - \frac{1}{Pr} \mathbf{u} \cdot \nabla \mathbf{u}^{(n)} + Ra(T^{(n)} + NC^{(n)})\hat{\mathbf{z}} \right), \tag{2.41}$$

having assumed that both the velocity at the previous time step and $\hat{\mathbf{u}}$ are incompressible to within the order of the scheme. This Poisson equation is solved subject to the following Neumann boundary conditions that are derived from the momentum equation (2.28):

$$\frac{\partial p}{\partial n} = \hat{\mathbf{n}} \cdot \left(-\frac{1}{Pr}\mathbf{u} \cdot \nabla \mathbf{u} + Ra(T - C)\hat{\mathbf{z}} + \nabla(\nabla \cdot \mathbf{u}) - \nabla \times (\nabla \times \mathbf{u}) \right), \tag{2.42}$$

where $\hat{\mathbf{n}}$ is the outward normal and the viscous diffusion term has been decomposed into irrotational and solenoidal contributions. The Neumann boundary conditions on the pressure are applied numerically as

$$\frac{\partial \bar{p}^{(n+1)}}{\partial n} = \hat{\mathbf{n}} \cdot \left(-\frac{1}{Pr}\mathbf{u} \cdot \nabla \mathbf{u}^{(n)} + Ra(T^{(n)} - C^{(n)})\hat{\mathbf{z}} - \nabla \times \left(\nabla \times \mathbf{u}^{(n)} \right) \right). \tag{2.43}$$

where the irrotational contribution of the diffusive term, $\nabla(\nabla \cdot \mathbf{u})$, has been neglected as it can lead to instabilities [94]. The Poisson equation (2.41) is then solved subject to these boundary conditions (2.43) to first obtain $\bar{p}^{(n+1)}$ and subsequently $\hat{\mathbf{u}}$ via

$$\hat{\mathbf{u}} = \mathbf{u}^{(n)} + \Delta t \left(-\mathbf{u} \cdot \nabla \mathbf{u}^{(n)} + RaPr(T^{(n)} - C^{(n)})\hat{\mathbf{z}} \right) - Pr\Delta t \nabla \bar{p}^{(n+1)}. \tag{2.44}$$

The velocity field at the $(n+1)^{th}$ step is obtained after the third step of the splitting scheme, where the effects of viscous diffusion have been treated implicitly according to

$$\frac{\mathbf{u}^{(n+1)} - \hat{\mathbf{u}}}{Pr\Delta t} = \nabla^2 \mathbf{u}^{(n+1)}. \tag{2.45}$$

Using (2.44) and rearranging this expression, we find that $\mathbf{u}^{(n+1)}$ satisfies

$$\mathbf{u}^{(n+1)} = (\mathcal{I} - Pr\Delta t \nabla^2)^{-1} \hat{\mathbf{u}} \tag{2.46}$$

$$= \left(\nabla^2 + \alpha_u \mathcal{I}\right)^{-1} \left(-\frac{\mathbf{u}^{(n)}}{Pr\Delta t} + \frac{1}{Pr}\mathbf{u} \cdot \nabla \mathbf{u}^{(n)} - Ra(T^{(n)} - C^{(n)})\hat{\mathbf{z}} + \nabla \bar{p}^{(n+1)} \right) \tag{2.47}$$

where $\alpha_u = -(Pr\Delta t)^{-1}$. This equation is solved by inverting the Helmholtz operators using a Schur decomposition and thereby imposes Dirichlet boundary conditions on the

domain walls. We should note that while incompressibility of the velocity field is lost during this final stage, in favour of satisfying the boundary conditions, the resulting divergence of the velocity field was found to be negligible.

2.3 CONTINUATION METHOD

The majority of the results presented in the latter half of Chapter 4 and in Chapters 5 and 6 were obtained using numerical continuation. These methods have been widely applied over the past four decades as they enable both stable and unstable solutions to a system to be followed over parameter space and for bifurcations, where the nature of the system changes, to be detected. These methods have been the subject of a number of reviews that either explain the approach or detail some of its applications (e.g., [1, 62, 102, 103]).

We start the discussion of numerical continuation by focussing on one of the simplest implementations where we track steady states u as a bifurcation parameter r varies. These steady solutions satisfy

$$\mathcal{F}(u(x); r) = 0, \tag{2.48}$$

and are typically obtained via a two-stage process: a prediction stage, where an initial guess for the solution u is generated; and a correction stage, where a Newton–Krylov method is used to iteratively converge on a solution to (2.48) starting from this initial guess.

2.3.1 PREDICTION STAGE

To initiate the continuation process, one must obtain an appropriate initial guess of a solution to (2.48) for some parameter value r_0. This guess can be chosen in a number of ways: for example, using an analytical approximation, time-stepping towards a stable solution, or using homotopy methods starting from a known solution of a simpler system that is in some way close to the original system. The initial guess will then be corrected during the correction stage, as we will explain in the following section,

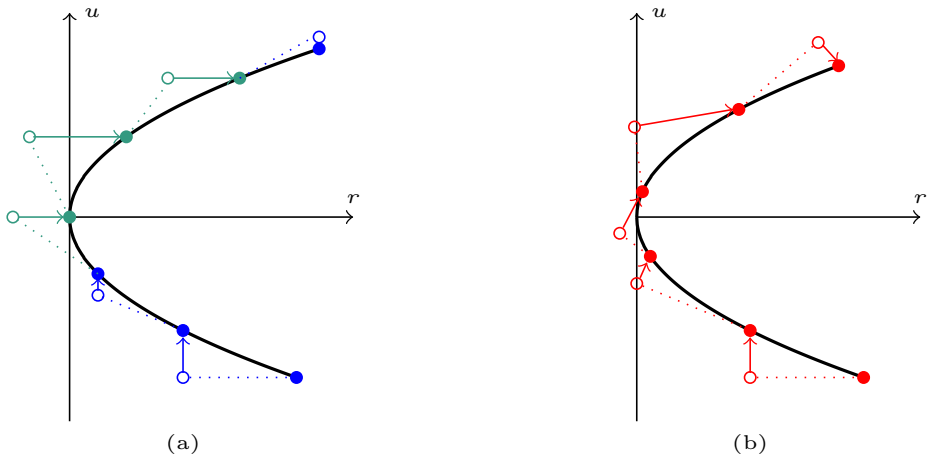

Figure 2.1: Sketches of (a) fixed parameter continuation and (b) pseudo-arclength continuation for the normal form of a saddle-node bifurcation: $\dot{u} = r - u^2$. The dotted lines indicate the linear extrapolation from previous iterations to reach the initial guess (open circle) during the prediction stage. The solid arrow represents the correction stage via Newton iterations to reach the converged solution (filled dot). Blue (green) dots and lines in (a) indicate when a parameter (component value) is fixed during the continuation step.

to compute the first numerical solution of (2.48). This computed solution will later be used as the initial guess for the next continuation step, where the solution of (2.48) at $r_1 = r_0 + \Delta r_0$ is obtained.

After the first two steps, there is a choice of continuation methods that can be applied, which affects both how the initial guesses at later continuation steps are computed and the system to solve during the correction stage. Figure 2.1 illustrates two common methods: fixed parameter continuation (figure 2.1(a)) and pseudo-arclength continuation (figure 2.1(b)).

FIXED PARAMETER CONTINUATION

In fixed parameter continuation, the bifurcation parameter r is fixed during each continuation step. This is achieved by introducing Δr_n as a small variation in the bifurcation

parameter and imposing that the bifurcation parameter at the $(n+1)^{th}$ step satisfies

$$r_{n+1} = r_n + \Delta r_n. \tag{2.49}$$

We further constrain the bifurcation parameter of the initial guess $\tilde{r}_{n+1}$ to satisfy $\tilde{r}_{n+1} = r_{n+1}$, which leads to us taking the initial guess at the $(n+1)^{th}$ step as

$$(\tilde{r}_{n+1}, \tilde{u}_{n+1}) = \left(r_{n+1}, u_n + \Delta r_n \frac{u_n - u_{n-1}}{r_n - r_{n-1}} \right), \tag{2.50}$$

since $\tilde{u}_{n+1}$ is obtained via linear extrapolation of the two previously computed solutions of (2.48): (r_{n-1}, u_{n-1}) and (r_n, u_n). This linear extrapolation and the resulting initial guess are depicted in figure 2.1(a) by the blue dotted lines and blue open circles, respectively. The correction stage then aims to solve the equation:

$$\mathcal{F}(u, r_{n+1}) = 0, \tag{2.51}$$

iteratively for u, starting from the initial guess (2.50) until the solution converges at (r_{n+1}, u_{n+1}). These corrections are depicted by the vertical blue arrows in figure 2.1(a) as the value of r is fixed throughout.

Fixing the bifurcation parameter will fail, however, when the branch of solutions undergoes a saddle-node bifurcation since one may impose a value of r for which there are no steady states in the vicinity of the initial guess, as is the case for two leftmost open green circles in figure 2.1(a). One approach for dealing with this potential failure is to switch to fixed value continuation when one of the components of the solution u changes sufficiently quickly with r. In doing so, we swap the roles of the bifurcation parameter r and the fastest growing component of u (u_k, say) so that we fix the value of u_k during each continuation step and allow r to be solved for during the correction stage. This process is illustrated in green in figure 2.1(a), where we note that the correction stages are depicted by the horizontal green arrows. We may later switch back to fixed parameter continuation when the component u_k changes sufficiently slowly with r.

PSEUDO-ARCLENGTH CONTINUATION

Pseudo-arclength continuation gives an alternative approach where we do not need to change method in order to follow a branch of solutions around a saddle-node bifurcation. The method was first introduced by Keller [95] and relies on introducing an approximate measure of the arc-length along the branch s, which is treated as a natural continuation parameter.

At each continuation step, one first approximates the derivatives of both r and u with respect to s using the solutions obtained during the previous steps. At the n^{th} step, this approximation is given by

$$(\dot{r}_n, \dot{u}_n) = \mathcal{N}\left(\frac{r_n - r_{n-1}}{\Delta s_{n-1}}, \frac{u_n - u_{n-1}}{\Delta s_{n-1}}\right), \tag{2.52}$$

where Δs_{n-1} is the step size in s used in the previous continuation step and $\mathcal{N}$ is a normalisation constant. Following [63], this normalisation constant is fixed by satisfying the relation:

$$\left\langle (\dot{r}_n, \dot{u}_n)\,,\, (\dot{r}_n, \dot{u}_n) \right\rangle = 1, \tag{2.53}$$

where the inner product is defined

$$\left\langle (r_1, u_1)\,,\, (r_2, u_2) \right\rangle = \theta_r^2 r_1 r_2 + \theta_u^2 u_1^T u_2, \tag{2.54}$$

for weights θ_r and θ_u that may either be fixed equal to $\theta_r = \theta_u = 1$ or chosen to treat the parameter r and each component of u comparably.

The derivatives with respect to arc-length (2.52) are used to derive the initial guess for the solution at the $(n+1)^{th}$ step:

$$(\tilde{r}_{n+1}, \tilde{u}_{n+1}) = (r_n, u_n) + \Delta s_n (\dot{r}_n, \dot{u}_n), \tag{2.55}$$

which are shown by the red open circles in figure 2.1(b). One then constrains iterates in the correction stage to lie on a hyperplane that is orthogonal to this tangent, as is

illustrated by the red arrows in figure 2.1(b). Numerically, this is achieved by solving the extended system:

$$0 = \mathcal{F}(u; r), \tag{2.56}$$

$$0 = \theta_u^2 \dot{u}_n^T (u - \tilde{u}_{n+1}) + \theta_r^2 \dot{r}_n (r - \tilde{r}_{n+1}), \tag{2.57}$$

for both r and u. We note that the extra condition (2.57), which we refer to as the orthogonality condition, is required as we need $N+1$ equations to solve for both the N components of u and the single component of r at each continuation step. Using the expressions for $\tilde{u}_{n+1}$ and $\tilde{r}_{n+1}$ in (2.55), the orthogonality condition can be reinterpreted as the distance from the previous solution in the continuation process:

$$0 = \theta_u^2 \dot{u}_n^T (u - u_n) + \theta_r^2 \dot{r}_n (r - r_n) - \Delta s_n. \tag{2.58}$$

Thus, we may interpret Δs_n as the increase in arc-length between the n^{th} and $(n+1)^{th}$ continuation steps.

STEP SIZE

Regardless of the continuation method used, one needs to appropriately choose the step size Δr_n or Δs_n at each prediction step. If the steps are too small, then one requires a large number of continuation steps in order to traverse each branch segment. In contrast, if the steps are too large, then the initial guess lies far from the previous solution, which may lead to the solution not converging at all during the correction stage, or to solutions jumping onto a different nearby branch. In practice, we fix a lower and upper limit for the step size and allow the step sizes to vary within this interval as each branch is followed. The step sizes are varied according to the total number of Newton iterations required during the correction stage: increasing when the number of iterations lies below a specified threshold, while decreasing when the number of iterations exceeds an upper limit.

2.3.2 CORRECTION STAGE

In the correction stage, we apply Newton–Krylov methods to generate a sequence of iterates that starts from the initial guess obtained during the prediction stage and converges on a steady state of the system. For notational simplicity, we will consider fixed parameter continuation and refer to the system to solve as

$$\mathcal{F}(u;r) = 0, \tag{2.59}$$

but note that this formulation can be easily amended to apply for pseudo-arclength continuation by introducing an extended variable $U = (u;r)$, expressing (2.56) and (2.57) in terms of U and replacing r in (2.59) with the arc-length s.

To motivate how the corrections are made, suppose that we have found an initial guess $(\tilde{u}_n, r_n)$ for the steady solution (u_n, r_n) at the n^{th} continuation step. Then, take the Taylor expansion of $\mathcal{F}(u_n; r_n)$ about this initial guess $(\tilde{u}_n, r_n)$:

$$\mathcal{F}(u_n;r_n) = \mathcal{F}(\tilde{u}_n;r_n) + \mathcal{F}_u(\tilde{u}_n;r_n)(u_n - \tilde{u}_n) + \mathcal{O}((u_n - \tilde{u}_n)^2). \tag{2.60}$$

The left-hand side vanishes since (u_n, r_n) solves (2.59) and we may neglect the nonlinear terms at leading order as $\tilde{u}_n(x)$ is assumed to be sufficiently close to the true solution u_n. If we additionally assume that $\mathcal{F}_u$ is invertible, then this expression can be rearranged to give the following approximation for u_n as

$$u_n \approx \tilde{u}_n - \underbrace{\mathcal{F}_u(\tilde{u}_n;r_n)^{-1}\mathcal{F}(\tilde{u}_n;r_n)}_{\Delta u_n}. \tag{2.61}$$

Thus, we would expect to obtain a better approximation to the steady state by making a correction Δu_n to $\tilde{u}_n$.

In practice, we need to make multiple corrections to find u_n, which we achieve iteratively

starting from $\tilde{u}_n^{(0)} = \tilde{u}_n$. We first find a correction $\Delta u_n^{(i)}$ by solving the linear system:

$$\mathcal{F}_u(\tilde{u}_n^{(i)}; r_n)\Delta u_n^{(i)} = \mathcal{F}(\tilde{u}_n^{(i)}; r_n), \tag{2.62}$$

using a Krylov subspace method, as described in section 2.1.3, because they can be used regardless of whether $\mathcal{F}_u$ is invertible. Once a correction $\Delta u_n^{(i)}$ has been obtained, it is then used to obtain the following iterate:

$$\tilde{u}_n^{(i+1)} = \tilde{u}_n^{(i)} - \Delta u_n^{(i)}. \tag{2.63}$$

We repeat this two-stage process ((2.62) and (2.63)) until we find an iterate where

$$\|\mathcal{F}(\tilde{u}_n^{(i)}; r_n)\| < \tau, \tag{2.64}$$

for a specified tolerance τ, and we say that the Newton–Krylov method has converged. While Newton's methods typically have quadratic convergence, here, the convergence is subquadratic as we only found approximate solutions to (2.62) using Krylov subspace methods [96].

CONTINUOUS SYMMETRIES

At this point it is helpful to comment on how we deal with a system that admits a continuous symmetry, e.g., a translation symmetry, where $\mathcal{F}_u$ is singular. A typical approach, but one that we do not take here, is to solve the non-singular extended system that consists of (2.59) together with a phase condition that fixes the phase of the solution. Instead, at each Newton iteration, we apply the Krylov subspace method to (2.63), which returns one of infinitely many potential corrections $\Delta u_n^{(i)}$ that are related by this continuous symmetry. While convergence to this solution is not guaranteed in singular systems [34], this was not found to be an issue here as we used appropriate preconditioning (see below). Applying this process at each continuation step may result in the phase of states changing along the branch, but this does not affect the bifurcation

diagrams, which show global properties such as kinetic energy or L_2 norms, as these properties are invariant under the continuous symmetry.

PRECONDITIONER

The linear system (2.62) may be difficult to solve in its current form and require a large number of Newton iterations in order to achieve convergence. We therefore introduce an invertible preconditioner $\mathcal{P}$ that pre-multiplies both sides of (2.62) to derive the linear system:

$$\mathcal{P}\mathcal{F}_u(\tilde{u}_n; r_n)\Delta u_n = \mathcal{P}\mathcal{F}(\tilde{u}_n; r_n), \tag{2.65}$$

after dropping superscripts, whose solutions are identical to those from (2.62), but typically require fewer iterations to obtain and are, therefore, easier to solve for. There are a wide range of potential preconditioners and the preferred choice often depends upon properties of the matrix representation of the linear operator (e.g., see reviews by Benzi [21], Pearson and Pestana [139], Wathen [188]). However, using spectral methods to solve (2.62) means that many of the traditional preconditioners will be unsuccessful and we need to apply other approaches.

We consider the preconditioner that was first introduced by Mamun and Tuckerman [123] in spherical Couette flow. This preconditioner can be derived from the first-order semi-implicit Euler scheme considered in section 2.2.1 and therefore one of its advantages is that it can be easily implemented from an existing time-stepping code [177]. Starting from the expression for $u^{t+\Delta t}$ in the Euler scheme (2.26) and subtracting u^t from both sides returns

$$u^{t+\Delta t} - u^t = (I - \Delta t\mathcal{L})^{-1}(u^t + \Delta t\mathcal{N}(u^t)) - u^t, \tag{2.66}$$

$$= \Delta t(I - \Delta t\mathcal{L})^{-1}(\mathcal{L}u^t + \mathcal{N}(u^t)). \tag{2.67}$$

Comparing this expression to the preconditioned linear system (2.65) with

$\mathcal{P} = \Delta t(I - \Delta t\mathcal{L})^{-1}$, we find that

$$\Delta t(I - \Delta t\mathcal{L})^{-1}(\mathcal{L} + \mathcal{N}_u(\tilde{u}_n; r))\Delta u_n = \Delta t(I - \Delta t\mathcal{L})^{-1}(\mathcal{L}\tilde{u}_n + \mathcal{N}(\tilde{u}_n; r_n)), \tag{2.68}$$

where the left- and right-hand sides respectively correspond to the changes in solution after integrating the linearised, $\mathcal{F}_u(\tilde{u}_n; r_n)$, and fully nonlinear, $\mathcal{F}(\tilde{u}_n; r_n)$, systems over a single time-step.

Despite this preconditioner being derived from a time-stepping scheme, the parameter Δt does not need to be small, but should rather be optimised for improved performance. In particular, we can consider the two limits, $\Delta t \ll 1$ and $\Delta t \gg 1$. In the former case, we have $P \approx \Delta t\mathcal{I}$ and (2.62) is solved without preconditioning. In contrast, taking the limit $\Delta t \gg 1$ means that the preconditioner takes the form $P \approx -\mathcal{L}^{-1}$, which was first considered in fluid systems by Carey et al. [43] who examined its effects in non-Newtonian flows and referred to it as Stokes preconditioning. In this case, we solve the preconditioned system:

$$(\mathcal{I} + \mathcal{L}^{-1}\mathcal{N}_u(\tilde{u}_n; r_n))\Delta u_n = \mathcal{L}^{-1}\mathcal{F}(\tilde{u}_n; r_n). \tag{2.69}$$

and thus it is particularly useful when contributions to the Jacobian from nonlinear terms are small and $\mathcal{L}^{-1}$ is approximately the inverse of the Jacobian $\mathcal{F}_u(\tilde{u}_n; r_n)$. In practice, there are intermediate values of Δt that provide optimal performance along different branch segments. Beaume [8] investigated the effect of Δt on the number of conjugate gradient iterations the BiCGstab method needed for convergence along test branch segments of the snaking in 3D natural doubly diffusive convection [12] and found a minimal number of iterations around $\Delta t \approx 0.1$. We therefore used $\Delta t = 0.1$ as the default value in the preconditioner for the continuation of natural doubly diffusive convection and only changed it within the range $0.1 \leqslant \Delta t \leqslant 0.5$ when convergence was found to be slow.

2.3.3 BIFURCATIONS

Applying the previously described prediction and correction steps allows us to track out a path of steady states within parameter space. However, these steps can be extended in order to determine the stability of the computed steady states and to detect bifurcations along the branch, which would allow us to ultimately obtain a more complete bifurcation diagram containing additional branches.

STABILITY ANALYSIS

The stability of a steady state $u_0(x)$ to the PDE:

$$\frac{\partial u}{\partial t} = \mathcal{F}(u; r), \tag{2.70}$$

may be determined by considering the evolution of the slightly perturbed state $u(x,t) = u_0(x) + \epsilon\tilde{u}(x,t)$, where $\epsilon \ll 1$. Applying a Taylor expansion of $\mathcal{F}(u;r)$ about $u_0(x)$, we find that the evolution of the small perturbation $\tilde{u}$ is governed by

$$\epsilon\frac{\partial \tilde{u}}{\partial t} = \mathcal{F}(u_0; r) + \epsilon\mathcal{F}_u(u_0; r)\tilde{u} + \mathcal{O}(\epsilon^2). \tag{2.71}$$

Introducing $\mathcal{J} = \mathcal{F}_u(u_0; r)$ as the Jacobian of the nonlinear operator $\mathcal{F}$, neglecting the $\mathcal{O}(\epsilon^2)$ terms and noting that $\mathcal{F}(u_0; r) = 0$ since $u_0(x)$ is a steady state, we find that the perturbation satisfies the linear equation:

$$\frac{\partial \tilde{u}}{\partial t} = \mathcal{J}\tilde{u}, \tag{2.72}$$

which has the exact solution:

$$\tilde{u}(x,t) = e^{\mathcal{J}t}\tilde{u}(x,0). \tag{2.73}$$

Supposing that $\tilde{u}$ is an eigenfunction of the Jacobian with eigenvalue λ, i.e., $\mathcal{J}\tilde{u} = \lambda\tilde{u}$, then $\tilde{u}(x,t) = e^{\lambda t}\tilde{u}(x,0)$ and the perturbation grows (decays) if $\lambda > 0$ ($\lambda < 0$). Thus, to determine the stability of the steady state $u_0(x)$, one needs to find the sign of the real

parts of the eigenvalues of the Jacobian evaluated at this state.

Since the dimension of the discretised system can be large, it may be impractical to compute the eigenvalues of the Jacobian directly and we instead choose to apply Arnoldi's method [2] to approximate the eigenvalues. The motivation behind such an approach comes from applying the power iteration method to approximate eigenvalues of an $n \times n$ matrix A. For simplicity in this discussion, we assume that A is diagonalisable, but note that this property is not necessary to apply the method. With this assumption, we may express an arbitrary state $\mathbf{x}_0$ as a linear combination of the eigenvectors of A:

$$\mathbf{x}_0 = \sum_{i=1}^{n} a_i \mathbf{w}_i, \tag{2.74}$$

where $\mathbf{w}_i$ is the normalised eigenvector with eigenvalue λ_i, which are ordered according to $|\lambda_1| \geqslant |\lambda_2| \geqslant \cdots \geqslant |\lambda_n|$. Repeatedly applying the matrix A on $\mathbf{x}_0$, for a total of k times, we find that

$$A^k \mathbf{x}_0 = a_1 \lambda_1^k \left(\mathbf{w}_1 + \sum_{i=2}^{n} \frac{a_i \lambda_i^k}{a_1 \lambda_1^k} \mathbf{w}_i \right). \tag{2.75}$$

Supposing that λ_1 is a dominant eigenvalue with $|\lambda_1| > |\lambda_2|$, then the summation term in this expression is subdominant for large k, which allows us to obtain the following approximation for the eigenvector:

$$\mathbf{w}_1 \approx \frac{A^k \mathbf{x}_0}{\|A^k \mathbf{x}_0\|}, \tag{2.76}$$

with leading eigenvalue:

$$\lambda_1 \approx \frac{\mathbf{w}_1^T A \mathbf{w}_1}{\mathbf{w}_1^T \mathbf{w}_1}. \tag{2.77}$$

Subdominant eigenvalues and the associated eigenvectors can be obtained by iteratively applying a similar approach on an initial state that is orthogonal to the subspace spanned by the eigenvectors previously approximated.

Computing eigenvalues with Arnoldi's method extends upon this approach by incorporating information from the previous iterates $A^i \mathbf{x}_0$ for $i = 0, \ldots, k-1$ as well as $A^k \mathbf{x}_0$, which enables multiple leading eigenvalues and their associated eigenvectors to be ob-

tained simultaneously. Letting $m = k + 1$, we first use Arnoldi's method, as described in section 2.1.3, to compute an orthonormal basis of the m-dimensional Krylov subspace:

$$\mathcal{K}_m(A, \mathbf{x}_0) = \text{span}\{\mathbf{x}_0, A\mathbf{x}_0, \ldots, A^{k-1}\mathbf{x}_0\}, \tag{2.78}$$

together with the upper Hessenberg matrix $\tilde{H}_m$ that satisfies (2.14). Post-multiplying (2.14) by an arbitrary vector $\mathbf{x} \in \mathbb{R}^m$ and rearranging, we find that

$$AV_m\mathbf{x} = V_m H_m \mathbf{x} + \mathbf{v}_{m+1} h_{m+1,m} \mathbf{e}_m^T \mathbf{x}, \tag{2.79}$$

where H_m is the $m \times m$ matrix obtained by taking the first m rows of the upper Hessenberg matrix $\tilde{H}_m$. We can then use this relation to show that if $\mathbf{x}$ is an eigenfunction of H_m with eigenvalue β, then $V_m\mathbf{x}$ is approximately an eigenfunction of A with eigenvalue β through the following sequence of equalities:

$$\begin{aligned} \|AV_m\mathbf{x} - \beta V_m\mathbf{x}\| &= \|AV_m\mathbf{x} - V_m H_m \mathbf{x}\|, && (2.80)\\ &= \|\mathbf{v}_{m+1} h_{m+1,m} \mathbf{e}_m^T \mathbf{x}\|, && (2.81)\\ &= |h_{m+1,m}||\mathbf{e}_m^T \mathbf{x}|, && (2.82) \end{aligned}$$

where we first used that $\mathbf{x}$ is an eigenvector of H_m, then applied the relation (2.79) and finally used the orthonormality of $\mathbf{v}_{m+1}$ to obtain (2.82). While the convergence of this scheme is not immediately clear from (2.82), and we refer to [150] for further details, our conclusion is that we can solve the simpler problem of finding eigenvalues of the upper Hessenberg matrix H_m to approximate leading eigenvalues of A. We implemented this method using the ARPACK package [110] in Fortran and the `eigs` subroutine in MATLAB.

In its current form, the Arnoldi method will pick out the eigenvalues of A with greatest magnitude, but different subsets of eigenvalues can be obtained by constructing suitable operators from A. For example, one can use A^{-1} to find eigenvalues with smallest magnitude or $(A - \sigma I)^{-1}$ to find eigenvalues close to σ. In our case, we wish to ex-

tract eigenvalues of the Jacobian with greatest real part, which is achieved by applying Arnoldi's method to find the leading eigenvalues and associated eigenfunctions of $e^{\mathcal{J}\Delta t}$. These may then be related back to those of $\mathcal{J}$ as an eigenfunction v of $e^{\mathcal{J}\Delta t}$ with eigenvalue μ is also an eigenfunction of $\mathcal{J}$ with eigenvalue λ, where λ and μ are related via

$$\lambda = \frac{1}{\Delta t} \log \mu. \tag{2.83}$$

Implementing Arnoldi's method on $e^{\mathcal{J}\Delta t}$ is not straightforward, however, because we do not have an explicit form of the operator $e^{\mathcal{J}\Delta t}$. Instead, we approximate the action of this operator on a general vector y by integrating

$$\frac{\partial y}{\partial t} = \mathcal{J} y, \tag{2.84}$$

over a single time-step since the exact solution is $e^{\mathcal{J}\Delta t} y$. For example, applying a first-order semi-implicit Euler scheme to integrate (2.84) leads to

$$y^{t+\Delta t} = (I - \Delta t \mathcal{L})^{-1}(I + \Delta t \mathcal{N}_u) y^t + \mathcal{O}((\Delta t)^2). \tag{2.85}$$

When $|\Delta t| \ll 1$, the operator on the right-hand side gives a first-order approximation to the exponential of the Jacobian, as

$$(I - \Delta t \mathcal{L})^{-1}(I + \Delta t \mathcal{N}_u) = e^{\mathcal{J}\Delta t} + \mathcal{O}((\Delta t)^2). \tag{2.86}$$

This implementation is convenient for doubly diffusive convection since it reuses the semi-implicit first-order Euler scheme used for time-stepping.

Higher order numerical schemes, including Exponential Time Differencing Runge–Kutta schemes [51], can be used in an equivalent way to derive higher-order approximations for the action of $e^{\mathcal{J}\Delta t}$. Such methods can prove advantageous in simpler PDEs, such as the Swift–Hohenberg equation, since they enable eigenvalues to be computed to the same level of accuracy with larger Δt. This is beneficial since power iteration methods

on $e^{\mathcal{J}\Delta t}$ converge with a rate

$$\frac{\mu_1}{\mu_2} = e^{\Delta t(\lambda_1 - \lambda_2)}, \tag{2.87}$$

where the eigenvalues λ_i and μ_i are related via (2.83) Thus, smaller Δt imply a slower rate of convergence and a Krylov subspace of higher dimension might be required to guarantee convergence.

BRANCH SWITCHING

We perform the above stability analysis to compute the leading eigenvalues of steady states at regular intervals along the branch, which allows us to detect bifurcation points when the real part of at least one of the eigenvalues of the Jacobian passes through zero. The corresponding eigenfunctions at the bifurcation points are important as their growth or decay is responsible for the gain or loss of stability of the steady solution.

Having detected when a branch undergoes a steady bifurcation between two states, we may wish to numerically continue the bifurcating branch away from the bifurcation point. To do so, we start by finding an initial guess for a state that lies on the new branch using a grid-based search similar to that depicted in figure 2.2. We first find the eigenfunction corresponding to the eigenvalue whose real part changes sign between two points (black circles in figure 2.2) on the original branch. We then add or subtract different positive multiples of this eigenfunction to each of the steady states, which generates a sequence of initial guesses (numbered blue open circles). These are considered in turn as the starting iterate for the Newton iterations until the solution converges at a steady state on the new branch, as indicated in figure 2.2 by the vertical blue arrow from the fifth initial guess. The process stops at this point and we return to applying the prediction and correction stages in order to follow this branch of solutions.

BIFURCATION TRACKING

We have so far focused on numerical continuation when a single parameter r is varied. However, it is also possible to extend this method to track stationary bifurcations in a

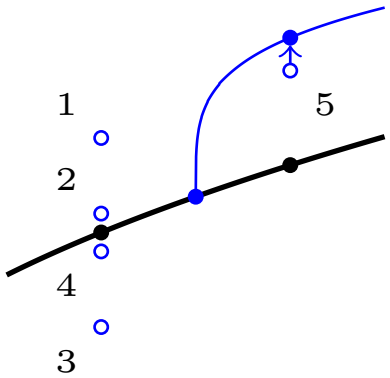

Figure 2.2: Grid-based search to find a steady state on a bifurcating branch. The original branch (black) undergoes a stationary bifurcation between the two points marked by the black dots. Blue open circles indicate initial guesses for the bifurcating branch (blue), with the adjacent number indicating the order in which they are attempted. The fifth initial guess is found to converge on the bifurcating branch during the correction stage, which is indicated by the blue arrow that terminates at the blue circle.

two-dimensional parameter space since the Jacobian evaluated at a bifurcation point has a non-trivial eigenvector with zero eigenvalue. We achieve this, by solving the extended system:

$$0 = \mathcal{F}(u; r, \nu), \tag{2.88}$$

$$0 = \mathcal{J}v, \tag{2.89}$$

$$0 = \|v\| - 1, \tag{2.90}$$

$$0 = \theta_u^2 \dot{u}_n^T (u - \tilde{u}_{n+1}) + \theta_v^2 \dot{v}_n^T (v - \tilde{v}_{n+1}) + \theta_r^2 \dot{r}_n (r - \tilde{r}_{n+1}) + \theta_\nu^2 \dot{\nu}_n (\nu - \tilde{\nu}_{n+1}), \tag{2.91}$$

for u, v, r and ν. The first three equations in this extended system respectively correspond to: u being a steady solution to the PDE with parameters r and ν (2.88) at a steady bifurcation point with marginal eigenvector v (2.89) whose norm is equal to one (2.90). The final equation (2.91) is an orthogonality condition required for pseudo-arclength continuation and is an extension of the simpler condition (2.57) discussed in

section 2.3.1. To be explicit, the terms in (2.91) are defined by

$$(\dot{r}_n, \dot{u}_n, \dot{v}_n, \dot{\nu}_n) = \mathcal{N}\left(\frac{r_n - r_{n-1}}{\Delta s_{n-1}}, \frac{u_n - u_{n-1}}{\Delta s_{n-1}}, \frac{v_n - v_{n-1}}{\Delta s_{n-1}}, \frac{\nu_n - \nu_{n-1}}{\Delta s_{n-1}}\right), \tag{2.92}$$

$$(\tilde{r}_{n+1}, \tilde{u}_{n+1}, \tilde{v}_{n+1}, \tilde{\nu}_{n+1}) = (r_n, u_n, v_n, \nu_n) + \Delta s_n(\dot{r}_n, \dot{u}_n, \dot{v}_n, \dot{\nu}_n), \tag{2.93}$$

where Δs_{i+1} is the step size at the i^{th} continuation step and the normalisation constant $\mathcal{N}$ now ensures that

$$\theta_u^2\|\dot{u}_n\|^2 + \theta_r^2\dot{r}_n^2 + \theta_v^2\|\dot{v}_n\|^2 + \theta_\nu^2\dot{\nu}_n^2 = 1. \tag{2.94}$$

While bifurcation tracking is straightforward to implement for 1D Swift–Hohenberg equations, it is significantly harder for the system of natural doubly diffusive convection primarily due to the increased system size owing to the coupled nature of the system. Nevertheless, we mention the possibility of this approach here as there are several instances where we have manually tracked bifurcations later in this thesis.

2.4 NUMERICAL VALIDATION

We end this chapter by briefly describing how we validated the numerical schemes applied to both the Swift–Hohenberg equation and the system of doubly diffusive convection. We first checked that our schemes generated results that are in qualitative agreement with those from previous studies, which we achieved by reproducing selected bifurcation diagrams using the same domains and parameter values as Burke and Knobloch [37], Knobloch et al. [100] and Bergeon and Knobloch [22, 24].

We then ran some resolution tests in order to find the number of Fourier modes or Gauss–Lobatto–Legendre points used in the computations. For the system of doubly diffusive convection, this involved computing the kinetic energy for a number of steady states using a range of resolutions. The value using the highest resolution was used to compute the relative error for each resolution and we found the point at which the error had stopped exponentially decreasing. This process was repeated over the range

of parameter values considered in this thesis to confirm a suitable resolution. For the Swift–Hohenberg equation, we generated wavenumber spectra for a number of steady states and confirm that the contributions from the highest frequency modes lie below a specified threshold.

We also ran some additional tests to confirm that there was quantitative agreement between results obtained using different numerical methods. Firstly, we validated the numerical computation of eigenvalues of the trivial states by comparing these with both the rate of decay of small-amplitude non-trivial states obtained via time-stepping and the eigenvalues obtained (semi-)analytically via a linear stability analysis. We also validated the kinetic energy of selected nonlinear steady stable states obtained via numerical continuation by comparing with those obtained after time-stepping a suitable initial condition to convergence.

3 | LOCALISED STATES

Doubly diffusive convection is one of a number of dissipative systems across a wide range of fields that admits spatially localised states as solutions, including: other systems of coupled convection [7, 11, 54, 117], shear flows [71, 161], cylindrical shell buckling [81, 82], nonlinear optics [32, 66], optical data storage [49], vegetation models [58, 195], mathematical biology [45] and phase-field crystals [145]. Despite the variety in the underlying physical mechanisms, localised states across these systems exhibit similarities both to those in other systems and to those in the much simpler Swift–Hohenberg equation, as has been described in the reviews by Dawes [56] and Knobloch [99]. In this chapter, we will review properties of localised states in the Swift–Hohenberg equation and introduce further background that will help in understanding later results on convectons in doubly diffusive convection.

3.1 SWIFT–HOHENBERG EQUATION

The Swift–Hohenberg equation, whose general form is

$$\frac{\partial u}{\partial t} = ru - (1 + \nabla^2)^2 u + f(u), \tag{3.1}$$

where $f(u)$ is a nonlinear term, is a canonical model that has often been used to illustrate theory behind localised states, both theoretically and numerically. Swift and Hohenberg [170] first derived this equation to model thermal fluctuations in Rayleigh–Bénard convection. Since then, many studies have considered the rich variety of patterns that the Swift–Hohenberg equation admits. These patterns include: rolls and hexagons [28],

travelling waves [153], standing waves [152, 155] and labyrinth patterns [169]. Early studies on localised states of (3.1), including those by Hilali et al. [79] and Sakaguchi and Brand [154], identified the coexistence of localised states with varying widths across a subcritical range of parameter values. Later studies have since identified further types of localised states and studied the associated bifurcation structure geometrically [16, 121], analytically [46, 59, 124] or numerically [3, 36–41, 100, 115].

3.1.1 BIFURCATION DIAGRAM

We start by reproducing selected results by Burke and Knobloch [37] who considered the one-dimensional Swift–Hohenberg equation with quadratic-cubic nonlinearity:

$$\frac{\partial u^*}{\partial t^*} = r^* u^* - (q_c^{*2} + \partial_{x^*}^2)^2 u^* + \nu^* u^{*2} - g^* u^{*3}, \tag{3.2}$$

with $q_c^* = 0.5$, $\nu^* = 0.41$ and $g^* = 1$. Rescaling (3.2) using:

$$x = q_c^* x^*, \qquad t = q_c^{*4} t^*, \qquad r = \frac{r^*}{q_c^{*4}}, \qquad u = \frac{\sqrt{g^*}}{q_c^{*2}} u^*, \qquad \nu = \frac{1}{\sqrt{g^*} q_c^{*2}} \nu^*, \tag{3.3}$$

here, we consider the equivalent system:

$$\frac{\partial u}{\partial t} = ru - (1 + \partial_x^2)^2 u + \nu u^2 - u^3, \tag{3.4}$$

with $\nu = 1.64$. We present the bifurcation diagram for a selection of steady states in a periodic domain with period 32π in figure 3.1.

The trivial state, $u = 0$, first undergoes a subcritical bifurcation at $r = 0$, where a branch of spatially periodic solutions, subsequently called P, bifurcates. This primary branch is shown in black in figure 3.1 and is initially once unstable as it heads into $r < 0$. States on P regain stability after the branch turns around at the left saddle-node bifurcation at $r \approx -0.27$ (figure 3.1(g)). Thus, as P extends into $r > 0$, there is a region of bistability between P and the trivial state when $-0.27 \lesssim r < 0$.

Two branches of localised states, L_0 (red) and L_π (blue), bifurcate subcritically from

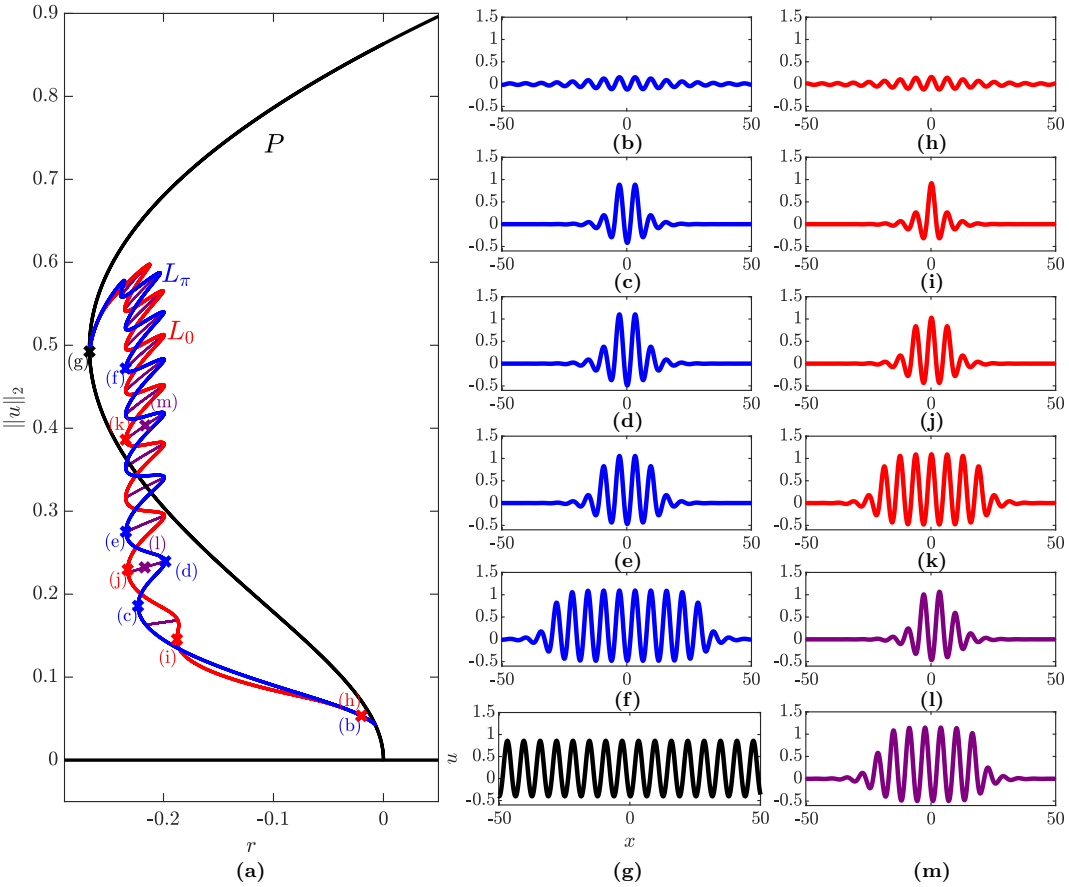

Figure 3.1: Steady solutions of the one-dimensional Swift–Hohenberg equation (3.4) with $\nu = 1.64$ in a periodic domain with period 32π. (a) Bifurcation diagram showing the L_2 norm of steady states on the branches of: periodic states P (black), symmetric localised solutions L_0 (red) and L_π (blue) and asymmetric localised rung states (purple). (b)–(m) Profiles of steady states on the different branches, with the colour indicating the branch on which the state lies.

P via an Eckhaus instability [26]. States on these secondary branches initially display small-amplitude oscillations that are weakly spatially modulated, with those on the two branches differing in the type of extrema they possess at $x = 0$; the state has a local minimum (L_π) or maximum (L_0) at $x = 0$, as seen in figures 3.1(b) and (h), respectively. The extent of spatial modulation and the maximum amplitude of the states both increase as each of L_0 and L_π is followed towards more negative values of r. Thus, by the first left saddle node on each branch, the states are fully localised and contain either one (figure 3.1(i)) or two (figure 3.1(c)) central oscillations with amplitudes that resemble those in states on the upper branch of P.

The two secondary branches, L_0 and L_π, enter what is referred to as a pinning region between $-0.234 \lesssim r \lesssim -0.199$ and proceed to intertwine as they pass between left and right saddle nodes in a process known as homoclinic snaking. The localised states increase in length by a pair of outer oscillations strengthening between successive left saddle nodes, as seen, for example, between figures 3.1(c) and (e). This process continues until around $\|u\|_2 \gtrsim 0.58$, where the localised states contain oscillations that nearly fill the domain. At this point, the states undergo a process of wavelength readjustment before reconnecting with P near the subcritical saddle node (figure 3.1(g)) in a second Eckhaus instability [26].

Figure 3.2(a) indicates the stability of localised states along L_0 (red in figure 3.1) by showing eigenvalues of selected eigenmodes as a function of the arc-length along the branch from the small-amplitude secondary bifurcation ($s = 0$) to where L_0 reconnects with P near the subcritical saddle node ($s \approx 14$). There are three eigenmodes of particular interest: a translation mode (black), a symmetric amplitude mode (green) and an antisymmetric phase mode (orange). All other eigenmodes remain stabilising over the entire extent of the branch. While the translation mode (e.g., figure 3.2(b)) arising from the periodic boundary conditions remains marginal ($\lambda = 0$) along L_0, the amplitude and phase eigenmodes repeatedly stabilise and destabilise over the branch.

The amplitude eigenmodes are responsible for the saddle-node bifurcations on the snaking branch as they gain (lose) stability at left (right) saddle nodes, which are respec-

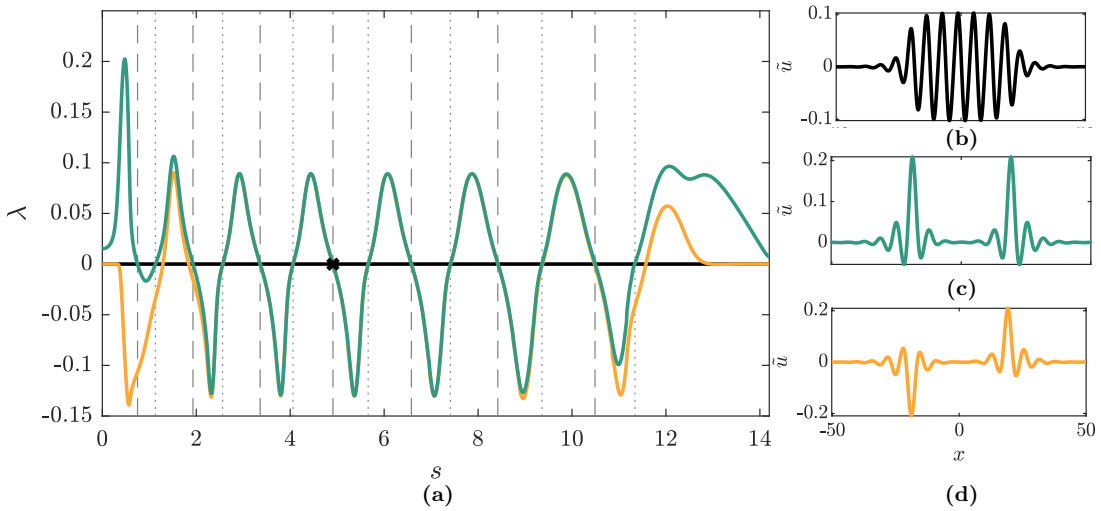

Figure 3.2: (a) Eigenvalues corresponding to the translation (black), amplitude (green) and phase (orange) modes for states on L_0 as a function of the arc-length s. Eigenvalues corresponding to the phase and amplitude modes are nearly indistinguishable on this scale between $s \approx 3$ and $s \approx 8.5$. Left (right) saddle nodes are indicated by the vertical dashed (dotted) black lines. (b)–(d) Profiles of the (b) marginal, (c) amplitude and (d) phase eigenmodes for the state at the left saddle node (figure 3.1(k)), which is indicated by the black cross at $s \approx 4.91$.

tively indicated by the vertical dashed (dotted) lines in figure 3.2. Figure 3.2(c) depicts the symmetric amplitude eigenmode associated with the left saddle node marked (k) in figure 3.1, from which we see that the non-trivial behaviour is focussed at the fronts of the localised state that connect the central oscillations to the trivial state. Such behaviour may be expected since we saw that the strengthening of these outer oscillations was the main change over a single snaking oscillation.

In contrast, the antisymmetric phase modes are responsible for the "rungs" (purple in figure 3.1(a)) that connect the L_0 and L_π branches when the modes gain (lose) stability shortly before (after) the left (right) saddle nodes. Similarly to the amplitude mode, the non-trivial behaviour of the phase mode is also localised at the fronts of the steady state, as seen in figure 3.2(d). However, we note that the eigenmode tends to strengthen oscillations at one front but weaken the oscillations at the second front. This may also be deduced by comparing states along a branch of asymmetric rung states; for example, we see that the oscillations at the left front weaken between figures 3.1(d), (l) and (j),

while the oscillations at the right front strengthen. This leads to a small translation of the localised states following the rung branches, which we have not shown in figure 3.1 as we have applied the translation symmetry to centre the states in figures 3.1(d) and (j) about $x = 0$.

The stability of states on L_π is largely similar to that shown in figure 3.2(a) for L_0. The main difference between the two branches is that the phase eigenmode is initially unstable but stabilises prior to the first left saddle node (figure 3.1(c)), when the first branch of rung states bifurcates from L_π [37]. We consequently find a multiplicity of coexisting stable localised states with different numbers of oscillations within the pinning region.

The Swift–Hohenberg equation also admits multipulse states, which, as the name suggests, contain multiple localised pulses that are separated over the domain. While Sakaguchi and Brand [154] identified this type of state in their early study on this equation, Burke and Knobloch [40] only later determined the structure of the branches on which they lie. They found that these multipulse states may lie on snaking branches or on figure-of-eight isolas within the pinning region, depending upon the separation between adjacent pulses. This type of state therefore also contributes to the multiplicity of states found that can be within the subcritical pinning region.

3.1.2 SPATIAL DYNAMICS

One approach that can be used to provide insight into why the Swift–Hohenberg equation admits localised states and when it does so involves considering the spatial dynamics of the system. Typically, dynamical systems consider the temporal dynamics of solutions by finding the spatial evolution of states in time. However, to understand localised states, it has proved more helpful to view the system in terms of the evolution of time-independent solutions through space.

For example, we can gain intuitive insight into why the Swift–Hohenberg equation admits localised states at small amplitude by considering the spatial dynamics of the linearised system. Consider taking a small-amplitude, time-independent disturbance to

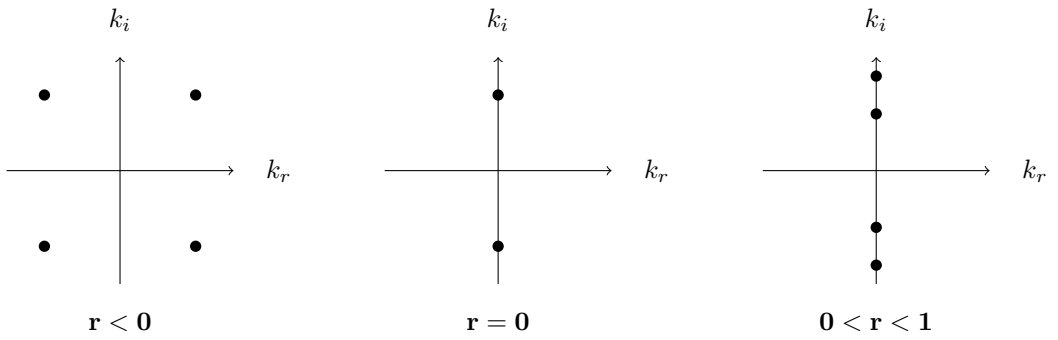

Figure 3.3: The Hamiltonian–Hopf bifurcation at $r = 0$ in the Swift–Hohenberg equation (3.4). As the bifurcation parameter r increases through $r = 0$, two pairs of complex-conjugate eigenvalues collide on the imaginary axis, before separating on the imaginary axis.

the trivial state of the form $u = \epsilon\, u_0\, e^{kx}$, where $\epsilon \ll 1$ and k is a spatial eigenvalue. Substituting this disturbance into (3.4) and neglecting nonlinear terms, we obtain the dispersion relation:

$$0 = r - (1 + k^2)^2, \tag{3.5}$$

which may be rearranged to find that the spatial eigenvalues satisfy

$$k = \pm\sqrt{-1 \pm \sqrt{r}}. \tag{3.6}$$

This form illustrates that the Swift–Hohenberg equation undergoes a Hamiltonian–Hopf bifurcation at $r = 0$, as depicted in figure 3.3. Here, the spatial eigenvalues occur in two complex conjugate pairs when $r < 0$, collide on the imaginary axis when $r = 0$ and separate to give four, purely imaginary eigenvalues when $r > 0$. Since $u = \epsilon u_0 e^{k_r x + i k_i x}$, spatial eigenmodes with $k_r > 0$ ($k_r < 0$) grow (decay) in space, while $k_i \neq 0$ corresponds to spatial oscillations. With this interpretation, one may view a localised state when $r < 0$ as a connection between a spatially growing eigenmode and a spatially decaying eigenmode. As these eigenmodes describe the dynamics along manifolds of the trivial state, localised states can arise provided that the corresponding stable and unstable manifolds of the trivial state intersect.

To clarify this idea of spatial dynamics, we consider the phase-space representations of

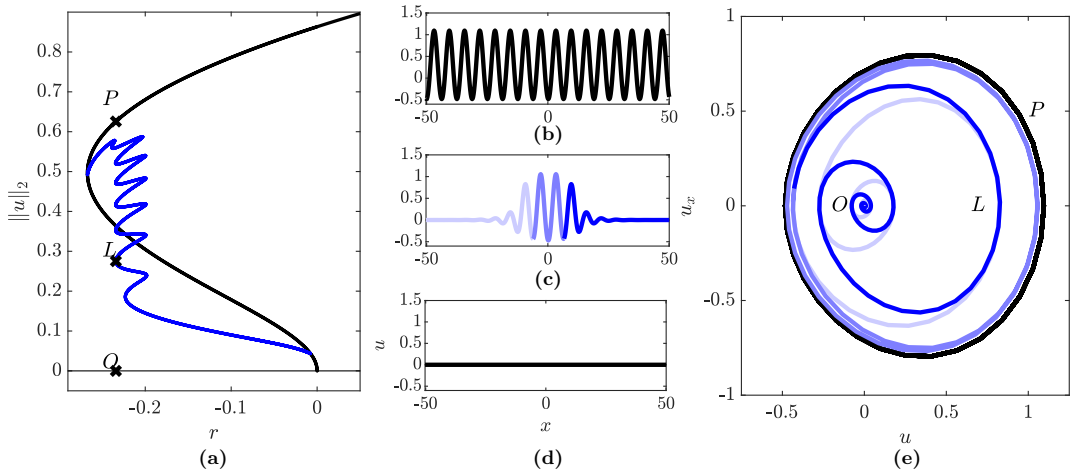

Figure 3.4: (a) Bifurcation diagram denoting the primary periodic branch (black) and L_π (blue) of the Swift–Hohenberg equation in a domain with $L_z = 32\pi$. (b)–(d) Profiles at $r \approx -0.234$ of the states marked (b) P, (c) L (d) O in (a). (e) Phase-space representation of the states O, L and P in (u, u_x) space. The different shades of blue in panels (c) and (e) denote corresponding sections of the localised state.

different steady states of (3.4) by plotting their amplitude u against their first spatial derivative u_x. With such a representation, fixed points correspond to spatially homogeneous solutions (see O in figure 3.4(e)), periodic orbits correspond to spatially periodic solutions (see P in figure 3.4(e)) and homoclinic orbits correspond to localised states (see L in figure 3.4(e)).

To highlight the connection between localised states and the associated homoclinic orbit, three sections of L in figure 3.4(c) and the associated segments of the phase-space trajectory in figure 3.4(e) are marked using different shades of blue. The homoclinic orbit starts near the homogeneous state O, while the localised state has small amplitude for large negative x, but spirals outwards as the amplitude of oscillations increases with increasing x, as seen in light blue. The orbit then approaches and follows the periodic orbit associated with a periodic state P (thick black orbit) around a number of times, while the localised states undergoes the same number of large-amplitude central oscillations, as seen in mid-blue. The homoclinic orbit finally spirals back inwards towards the fixed point corresponding to the trivial state O, while the amplitude of oscillations decreases back to zero, as seen in dark blue. Hence, determining when the spatial system admits

homoclinic orbits to the trivial state will help in understanding when localised states can exist.

3.1.3 UNFOLDING OF HAMILTONIAN–HOPF BIFURCATION

Normal-form theory has been used to prove the existence of small-amplitude homoclinic orbits to the origin in the unfolding of Hamiltonian–Hopf bifurcations [60, 89, 190]. Such results have relevance in both the Swift–Hohenberg equation, which we have shown undergoes a Hamiltonian–Hopf bifurcation (see figure 3.3), and natural doubly diffusive convection, which also undergoes this type of bifurcation at the onset of convection [24].

In the following, we summarise results obtained by Woods and Champneys [190], who presented a geometric argument as to why homoclinic orbits to the origin exist in the integrable limit of the bifurcation. They considered the normal form:

$$\frac{dA}{dt} = i\omega A + B + iAP\left(r; |A|^2, \frac{i}{2}\left(A\overline{B} - \overline{A}B\right)\right) + R_A, \tag{3.7}$$

$$\frac{dB}{dt} = i\omega B + iBP\left(r; |A|^2, \frac{i}{2}\left(A\overline{B} - \overline{A}B\right)\right) + AQ\left(r; |A|^2, \frac{i}{2}\left(A\overline{B} - \overline{A}B\right)\right) + R_B, \tag{3.8}$$

for state variables A and B, where the overbar denotes complex conjugation, r is the bifurcation parameter, $\pm i\omega$ are the eigenvalues of the bifurcation at $r = 0$, P and Q are the following polynomials with real coefficients:

$$P(r; x, y) = p_1 r + p_2 x + p_3 y, \quad Q(r; x, y) = -q_1 r + q_2 x + q_3 y + q_4 x^2, \tag{3.9}$$

and R_A and R_B are higher order terms. The sign of q_2 in (3.9) is of particular interest as it controls the criticality of the bifurcation, being subcritical when $q_2 < 0$ and supercritical when $q_2 > 0$. We further assume that this normal form is reversible, in that there is a reflection symmetry $\mathcal{R}$ that satisfies

$$\mathcal{R}(A, B) = \left(\overline{A}, -\overline{B}\right). \tag{3.10}$$

The normal form (3.7–3.9) is integrable when $R_A = R_B = 0$, where it admits the first integrals:

$$K = \frac{i}{2}\left(A\overline{B} - \overline{A}B\right), \tag{3.11}$$

$$H = |B|^2 - \int_0^{|A|^2} Q(r; s, K)\, ds. \tag{3.12}$$

Defining $x = |A|^2$ and after some algebraic manipulation using these first integrals, one can show that x satisfies

$$\left(\frac{dx}{dt}\right)^2 = 4f(x), \tag{3.13}$$

where $f(x)$ is the quartic polynomial:

$$f(x) = \frac{1}{3}q_4x^4 + \frac{1}{2}q_2x^3 + (q_3K - q_1\mu)x^2 + Hx - K^2. \tag{3.14}$$

We are particularly interested in using (3.13) and (3.14) to find homoclinic orbits to the origin, where $A = B = 0$ and the first integrals evaluate as $K = H = 0$. These conditions simplify the form of $f(x)$ in (3.14) to

$$f(x) = \frac{1}{3}q_4x^4 + \frac{1}{2}q_2x^3 - q_1\mu x^2. \tag{3.15}$$

Equation (3.13) is equivalent to

$$\frac{d^2x}{dt^2} = -\frac{d}{dx}\Big(-2f(x)\Big), \tag{3.16}$$

and hence the system may be interpreted as a nonlinear oscillator equation with potential $-2f(x)$. The equivalence between the normal form (3.7–3.9) and this oscillator equation means that we may interpret a homoclinic orbit to the origin as a particle trajectory where the particle starts from rest at $x = 0$, enters the region $x > 0$, since $x = |A|^2 \geqslant 0$, and reaches a maximum value x^*, before returning to $x = 0$. Using (3.13), we find that such a trajectory is only possible when $f(x) > 0$, or equivalently when the potential function $-2f(x)$ is negative. Further, we find that the maximum value

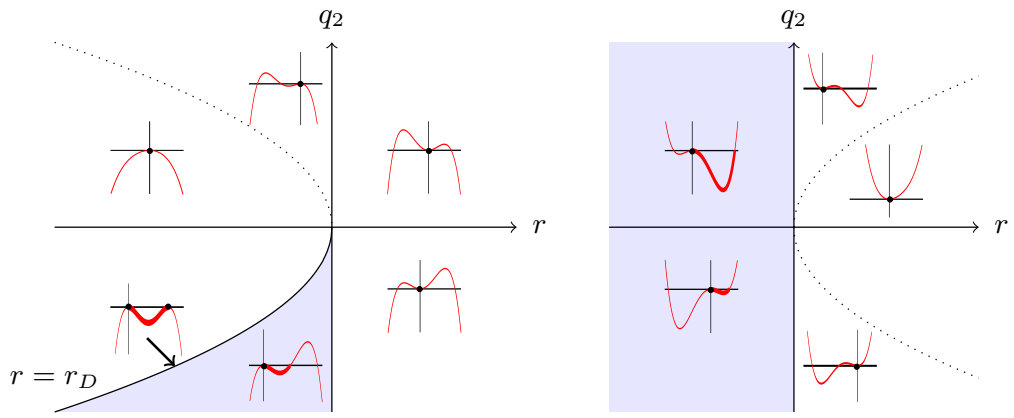

(a) $q_4 > 0$ **(b)** $q_4 < 0$

Figure 3.5: Regions of (r, q_2) parameter space where homoclinic orbits of the origin exist in the unfolding of the Hamiltonian–Hopf bifurcation are shaded in the two cases: (a) $q_4 > 0$ and (b) $q_4 < 0$. When $q_4 > 0$, this region is bounded between the negative q_2 axis and the line $r = r_D$ (3.17), whereas when $q_4 < 0$, this region is bounded only by the q_2 axis. Sketches of the potential function $-2f(x)$ for selected parameter values are also illustrated, with the black dots indicating equilibrium states of the normal form and thick red lines indicating the range of x related to homoclinic orbits. The number of roots of $f(x)$ changes across the dotted lines. Adapted from [190].

attained is governed by the constraint $f(x^*) = 0$ as this condition corresponds to zero particle velocity.

Woods and Champneys [190] analysed the properties of $f(x)$ for the two cases $q_4 > 0$ and $q_4 < 0$ to determine the parameter regimes in which the above conditions are satisfied, which allowed them to determine when homoclinic orbits in the unfolding of the Hamiltonian–Hopf bifurcation are admitted. We have presented their results in figure 3.5. When $q_4 < 0$ (figure 3.5(b)), they found that this region is the half-plane with negative r, whereas when $q_4 > 0$ (figure 3.5(a)), they found that this region is instead bounded on the right by the negative q_2 axis and on the left by the curve:

$$r_D = \frac{-3q_2^2}{16q_1q_4}. \tag{3.17}$$

As evidenced by the corresponding sketch of $-2f(x)$ on this curve, the maximum value that the particle trajectory would attain satisfies both $f(x^*) = 0$ and $f'(x^*) = 0$, where

the prime indicates differentiation with respect to x, and therefore corresponds to a non-trivial equilibrium of (3.13). The trajectory thus corresponds to the particle travelling between the two equilibria and can be related to a heteroclinic connection between the origin and a finite-amplitude periodic orbit of the normal form (3.7–3.9). As the normal form is invariant under the symmetry:

$$(A, B) \to \left(Ae^{i\phi}, Be^{i\phi}\right), \tag{3.18}$$

there is in fact a one-parameter family of heteroclinic connections that are parameterised by the phase ϕ.

The integrable nature of the normal form (3.7–3.9) may be lost upon including non-trivial higher-order terms R_A and R_B, which raises the question about whether the homoclinic orbits found in the integrable case (see figure 3.5) persist. Iooss and Pérouème [89] showed that the two homoclinic orbits associated with symmetric solutions with phases $\phi = 0$ and $\phi = \pi$ satisfying (3.10) persist for small r in both the subcritical ($q_2 < 0$) and supercritical ($q_2 > 0$) regimes.

3.1.4 HETEROCLINIC TANGLE

The persistence of the heteroclinic connection between the trivial and periodic states along the line $r = r_D$ displays more interesting behaviour, however, since the one-parameter family of heteroclinic connections is structurally unstable. Woods and Champneys [190] supposed that this family breaks up into a pair of heteroclinic tangencies, as depicted in the left panel of figure 3.6. Here, the unstable manifold of the origin, $W^u(0)$, lies tangent to the stable manifold of the periodic state $\gamma(\phi)$, instead of connecting as they would in the integrable system. The stable manifold of the origin, $W^s(0)$, similarly lies tangent to the unstable manifold of the periodic state, owing to the reversibility of the system.

For parameter values r between the cases of tangency, the unstable (stable) manifold of the origin intersects the stable (unstable) manifold of the periodic orbit transversely,

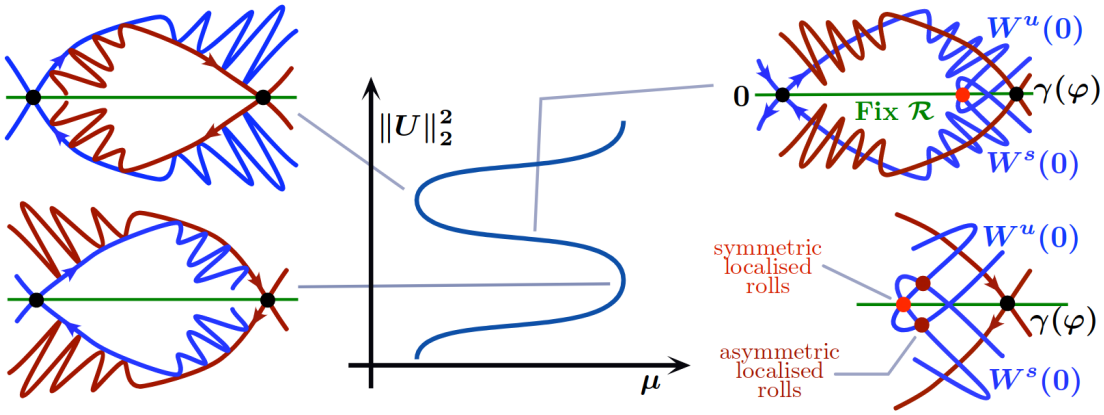

Figure 3.6: Relationship between localised states, the snaking branch and intersections between the stable and unstable manifolds of the trivial state $u = 0$ near the periodic state $\gamma(\varphi)$. From [16]. Copyright ©2009 Society for Industrial and Applied Mathematics. Reprinted with permission. All rights reserved.

as seen in the top right panel of figure 3.6, which is accompanied by infinitely many intersections between the stable and unstable manifolds of the origin (see [99] for an explanation for this behaviour). As we noted in section 3.1.2, such intersections may be related to homoclinic orbits to the origin and also localised states. The bottom right panel of figure 3.6 indicates that the intersections can occur either on Fix $\mathcal{R}$ (red dot), the set of all states that are invariant under the reflection symmetry (3.10), or away from this set (purple dots). While the former correspond to symmetric localised states, like those lying on the snaking branches L_0 and L_π in the Swift–Hohenberg equation (see figure 3.1), the latter correspond to asymmetric localised states, like those found on the rung branches in figure 3.1. The heteroclinic tangencies, therefore, correspond to the left and right folds in the snaking branch, between which one can find infinitely may localised states in an infinite domain. This behaviour is known as a heteroclinic tangle.

3.1.5 MAXWELL POINT

The variational nature of the Swift–Hohenberg equation provides a more physical understanding into when localised states can exist by considering when particular states

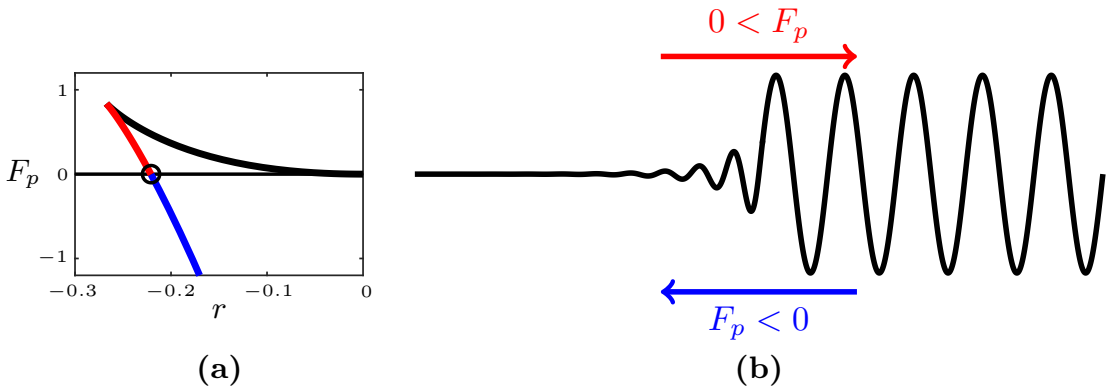

Figure 3.7: (a) Free energy of periodic states on P, F_p, using the following conventions for the colour: states on the lower branch segment (black), states on the upper branch segment with $F_p > 0$ (red) and states on the upper branch segment with $F_p < 0$ (blue). The circled point indicates the Maxwell point at $r_{MP} \approx -0.22$ when $F_p = 0$. (b) Sketch of an initial state where the trivial state is connected to a stable periodic state via a front. The arrows indicate the direction in which the front is expected to move depending upon the free energy of the periodic state, F_p.

are energetically favourable. We start by recasting (3.4) into variational form to find

$$\frac{\partial u}{\partial t} = -\frac{\delta F}{\delta u}, \tag{3.19}$$

where the free energy F is defined by

$$F = \int_0^L \left(-\frac{1}{2} r u^2 + \frac{1}{2} \left(\left(1 + \partial_x^2\right) u \right)^2 - \frac{1}{3} \nu u^3 + \frac{1}{4} u^4 \right) dx. \tag{3.20}$$

While the free energy of the trivial state clearly satisfies $F = 0$ for all values of the bifurcation parameter r, the free energy of periodic states, F_p, varies along the primary branch P. Figure 3.7(a) shows that F_p increases as P is followed from the primary bifurcation, where $F_p = 0$, to the subcritical saddle node at $r \approx -0.27$, where F_p attains its maximum value of $F_p \approx 0.84$, before decreasing as the upper primary branch is followed towards larger values of r. In particular, we find that F_p passes through zero at the Maxwell point, $r_{MP} \approx -0.22$, where the free energies of the trivial and periodic states are equal.

The variational formulation (3.19, 3.20) highlights that an arbitrary initial condition will reduce its free energy to a local minimum as the state evolves in time and converges

on a steady state. Thus, understanding the free energy of different steady states can help in determining the temporal dynamics of the system. For example, we consider the temporal evolution of a state where the stable trivial state is connected via a front to a stable periodic solution of (3.4), as illustrated in figure 3.7(b), which would be represented by a heteroclinic connection between the trivial and periodic states in phase space. The temporal evolution of this state depends on the free energy of the periodic state, F_p, in comparison to that of the trivial state: when $r < r_{MP}$ (red in figure 3.7(a)), the free energy of the trivial state is lower than that of the periodic state, i.e., $0 < F_p$, and we would expect the front connecting the states in figure 3.7(b) to move to the right as the trivial state invades the domain; when $r > r_{MP}$ (blue in figure 3.7(a)), the free energy of the periodic state is less than that of the trivial state, i.e., $F_p > 0$, and we would expect the front to move to the left as the periodic state invades the domain; and finally, when $r = r_{MP}$ (circle in figure 3.7(a)) and the free energies of the stable periodic and trivial states are equal, i.e., $F_p = 0$, we would expect the front to adjust slightly to provide a stable coexistence between the two states.

The above description does not, however, account for the structured nature of periodic states and their ability to adjust their wavelength in response to slight deviations away from the Maxwell point. Pomeau [141] suggested that these properties can lead to a "pinning" of the front onto the patterned structure that requires a finite disequilibrium of the free energies between the states before the front can move. Consequently, both steady fronts between the trivial and periodic states and localised states persist over a range of r that includes the Maxwell point. This concept of pinning also applies in non-conservative systems, such as natural doubly diffusive convection, where there is neither a free energy nor a Maxwell point, and we find patterned localised states over a range of parameter values, known as the pinning region.

3.1.6 WEAKLY NONLINEAR ANALYSIS

A complementary approach to understand parameter regimes in which small-amplitude localised solutions of the Swift–Hohenberg equation can exist is to perform a weakly

nonlinear analysis about the primary bifurcation of the trivial state at $r = 0$, which we detail below. We will apply a similar analysis for the system of natural doubly diffusive convection in Chapters 4 and 5.

We start by taking the small-amplitude solution u to be an asymptotic expansion in a small parameter $\epsilon \ll 1$:

$$u = \epsilon u_1 + \epsilon^2 u_2 + \epsilon^3 u_3 + \dots, \tag{3.21}$$

and rescale the bifurcation parameter r by setting $r = \epsilon^2 r_2$. The slow temporal and spatial scales are obtained by considering the linear stability analysis of the Swift–Hohenberg equation after supposing that the linear perturbation u_1 is proportional to $e^{\sigma t} e^{ikx}$, which leads to the dispersion relation:

$$\sigma = r - (1 + k^2)^2. \tag{3.22}$$

Balancing terms in this relation motivates a slow growth rate with $\sigma = \epsilon^2 \sigma_2$ and hence rescaling time as $t = T/\epsilon^2$. Rearranging (3.22) for the wavenumber k:

$$k = \pm 1 \pm \epsilon \sqrt{r_2 - \sigma_2}, \tag{3.23}$$

motivates the introduction of a slow spatial scale $X = \epsilon x$ to govern the modulation of steady states with wavenumber $k = \pm 1$ over larger periods. We initially treat this slow spatial scale X independently of the fast spatial scale x.

We use the above scalings to rescale the Swift–Hohenberg equation (3.4) and solve the resulting equation order-by-order in ϵ. The equation to solve at $\mathcal{O}(\epsilon)$ is

$$(1 + \partial_x^2)^2 u_1 = 0, \tag{3.24}$$

which we note has real solutions of the form:

$$u_1 = A_1(X, T) e^{ix} + \bar{A}_1(X, T) e^{-ix}. \tag{3.25}$$

At $\mathcal{O}(\epsilon^2)$, we find that

$$(1+\partial_x^2)^2 u_2 = -4\partial_{xX}(1+\partial_x^2)u_1 + \nu u_1^2, \tag{3.26}$$

$$= \nu(A_1^2 e^{2ix} + 2|A_1|^2 + \bar{A_1}^2 e^{-2ix}), \tag{3.27}$$

which has solution:

$$u_2 = A_2(X,T)e^{ix} + \bar{A_2}(X,T)e^{-ix} + \frac{\nu}{9}A_1^2 e^{2ix} + 2\nu|A_1|^2 + \frac{\nu}{9}\bar{A_1}^2 e^{-2ix}, \tag{3.28}$$

where A_2 is currently undetermined.

At $\mathcal{O}(\epsilon^3)$, both the time dependence of the system and the deviation away from the primary bifurcation are introduced, which leads to us solving

$$(1+\partial_x^2)^2 u_3 = -\frac{\partial u_1}{\partial T} + r_2 u_1 - 4\partial_{xX}(1+\partial_x^2)u_2 - (4\partial_x^2\partial_X^2 + 2(1+\partial_x^2)\partial_X^2)u_1 + 2\nu u_1 u_2 - u_1^3. \tag{3.29}$$

To avoid secular terms and ensure the existence of a solution, we must apply a solvability condition to (3.29), which we achieve by imposing that coefficients of terms proportional to e^{ix} and e^{-ix} in (3.29) vanish since the linear system is self-adjoint. This is achieved by substituting the previously determined forms for u_1 (3.25) and u_2 (3.28) into (3.29), multiplying each side by e^{-ix} and integrating over the interval $x \in [0, 2\pi]$. Doing so, we recover the Ginzburg–Landau equation:

$$\frac{\partial A_1}{\partial T} = r_2 A_1 + 4A_{1XX} + \left(\frac{38}{9}\nu^2 - 3\right)|A_1|^2 A_1, \tag{3.30}$$

that the linear amplitude $A_1(X,T)$ must satisfy.

The Ginzburg–Landau equation admits three steady solutions that we have a particular interest in. The first of these is the trivial solution:

$$A_1 = 0, \tag{3.31}$$

which is valid for all values of r_2 and corresponds to the trivial solution $u = 0$ of the

Swift–Hohenberg equation. The second is the spatially uniform solution:

$$A_1 = \left(\frac{9r_2}{27 - 38\nu^2}\right)^{1/2} e^{i\chi} \tag{3.32}$$

for some phase χ, which corresponds to small-amplitude spatially periodic states of (3.4). This solution is only valid provided that the fraction is positive, which restricts the sign of r_2 for given ν and demonstrates that the primary bifurcation of the trivial state in the Swift–Hohenberg equation is subcritical for $\nu > \sqrt{27/38}$ and supercritical for $\nu < \sqrt{27/38}$. The third type of steady solution of interest are small-amplitude spatially localised states with

$$A_1 = \left(\frac{-18r_2}{38\nu^2 - 27}\right)^{1/2} \operatorname{sech}\left(\frac{\sqrt{-r_2}X}{2}\right) e^{i\chi}, \tag{3.33}$$

where the phase χ is determined to be either $\chi = 0$ or $\chi = \pi$ by extending this analysis to include beyond-all-orders effects [46, 59]. These correspond to the following small-amplitude localised solutions of the Swift–Hohenberg equation:

$$u \approx 2\left(\frac{-9r}{38\nu^2 - 27}\right)^{1/2} \operatorname{sech}\left(\frac{\sqrt{-r}x}{2}\right) \cos(x + \chi), \tag{3.34}$$

which only exist for $r < 0$, corresponding to when the bifurcation is subcritical, and lie on one of a pair of branches that are characterised by the phase χ. These branches bifurcate directly from the origin in an infinite domain and thereafter exhibit similar small-amplitude behaviour to the branches L^+ and L^- in finite domains (see figure 3.1).

While the weakly nonlinear analysis is only formally valid in the limit $\epsilon \to 0$, previous studies have considered different approaches that extend this analysis away from the primary bifurcation. Burke and Knobloch [37], for example, reduced both the Swift–Hohenberg equation (3.2) and normal form (3.7–3.9) of the Hamiltonian–Hopf bifurcation with $R_A = R_B = 0$ to fifth-order Ginzburg–Landau equations and compared coefficients to determine which regime of the normal form theory in figure 3.5 applied. Alternatively, Chapman and Kozyreff [46] extended the multiple-scales analysis to in-

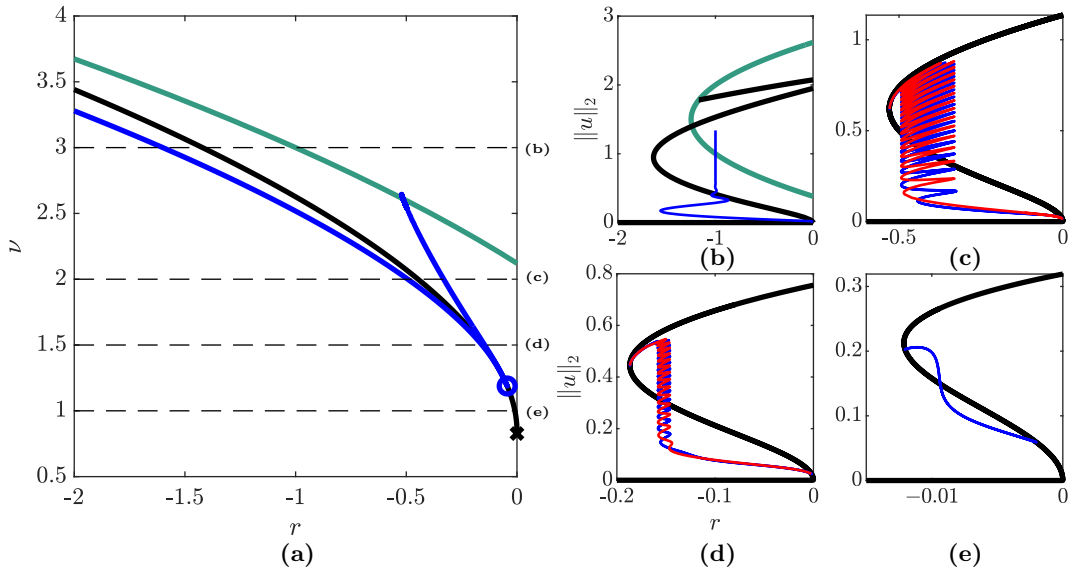

Figure 3.8: (a) Bifurcation tracking in (r, ν) parameter space using a domain with period 64π. The following lines are shown: (blue) the edges of the pinning region; (black) the Maxwell point corresponding to when the free energy (3.20) of the trivial state equals that for a state on the periodic branch P (see figure 3.7); and (green) the Maxwell point corresponding to when the free energy (3.20) of the trivial state equals that for a state on the spatially homogeneous branch. The blue open circle represents the end of snaking, while the black cross indicates the codimension-two point where the criticality of the primary bifurcation changes. (b)–(e) Bifurcation diagrams for (b) $\nu = 3$, (c) $\nu = 2$, (d) $\nu = 1.5$ and (e) $\nu = 1$ in a domain with period 32π that show: a branch of periodic states (black), the branch of homogeneous states (green) and branches of localised or modulated states (blue and red), only one of which is shown in panels (b) and (e). The branch of collapsed snaking in (b) was terminated to avoid connecting to a nearby isola.

corporate a beyond-all-orders analysis of front solutions near the Maxwell point, which allowed them to obtain analytical expressions for both the pair of snaking branches and the rungs connecting them.

3.1.7 BIFURCATION TRACKING

It is also of interest to consider how the structure of the bifurcation diagram changes as the parameter ν is varied towards the codimension-two point $(r, \nu) = (0, \sqrt{27/38})$, where the criticality of the primary bifurcation changes, since we will consider a similar question for the fluids system in Chapter 5. To do so, we replicate figure 18 of [37] in

figure 3.8(a) by considering a domain with period 64π and tracking both the eleventh right saddle node (of fifteen) on L_0 and the preceding left saddle node in (r, ν) parameter space to obtain a proxy for the extent of the pinning region. This pinning region is delimited by the blue lines in figure 3.8(a) and we further plot bifurcation diagrams for selected values of ν (figures 3.8(b)–(e)) to illustrate the main changes that arise.

The pinning region becomes smaller as the parameter ν decreases, which can be seen by comparing figures 3.8(c) and (d) for $\nu = 2$ and $\nu = 1.5$, respectively. However, we note that the region continues to contain the Maxwell point corresponding to when $F_P = 0$ (black line). Indeed, the snaking would continue to exist in an exponentially thin region around the Maxwell point if the codimension-two point was approached in an infinite domain [46]. In finite domains, however, the snaking does not persist all the way to the codimension-two point since pairs of left and right saddle nodes successively collide in cusp bifurcations and disappear [37]. The blue circle in figure 3.8(a), for example, indicates the parameter values where the tracked saddle nodes collide. Instead, we might find non-snaking branches of spatially modulated states, as in figure 3.8(e) for $\nu = 1$, provided that the domain is sufficiently large for the primary branch to undergo modulational instabilities given the proximity to the codimension-two point [55].

Burke and Knobloch [37] found that the typical homoclinic snaking breaks down around $\nu \approx 2.75$ because other Maxwell points enter the pinning region, including the one corresponding to when the free energies of the trivial state and states on the branch of spatially homogeneous states are equal (shown in green in figure 3.8(a)). They found a variety of different snaking behaviour beyond this boundary, including what is known as collapsed snaking, where the secondary branch extends vertically upwards as the localised states increase in width, as illustrated in figure 3.8(b) when $\nu = 3$. For further discussion about this breakup process and examples of the corresponding secondary branches, we refer the reader to [37].

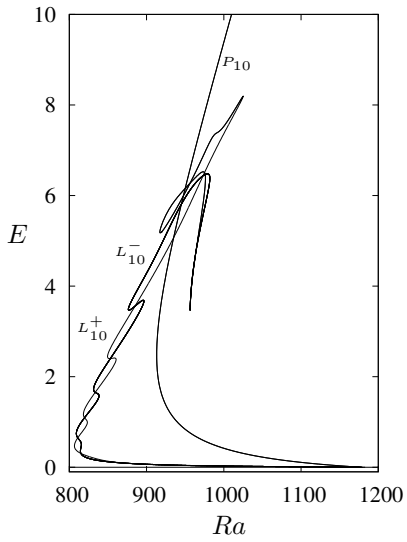

Figure 3.9: Bifurcation diagram illustrating the primary branch corresponding to states with ten rolls P_{10} and slanted snaking of secondary branches of localised states $L_{10}^{\pm}$ in rotating convection. Adapted from [11].

3.2 SNAKING WITHOUT BISTABILITY OR SUBCRITICALITY

Despite the previous subsections indicating that bistability and subcriticality are important for spatial localisation, neither property is essential. For example, as we mentioned in Chapter 1, localised states have been found in closed domains of binary fluid convection [129] and natural doubly diffusive convection [12], despite the absence of primary branches of periodic states and hence also the bistability found in these systems with periodic boundary conditions.

Alternatively, studies on systems involving a conserved quantity, including magneto-convection [54, 117, 118], rotating convection [11], vibrating granular or fluid layers [57, 142], optics [66] and phase-field crystal models [173], have shown that localised states can lie on slanted snaking branches that may extend outside of the bistable region. Figure 3.9 illustrates slanted snaking in a subcritical system of rotating convection described by Beaume et al. [11]. Here, we see that a pair of secondary branches $L_{10}^{\pm}$ bifurcate subcritically from the primary branch P_{10} and extend towards Rayleigh numbers

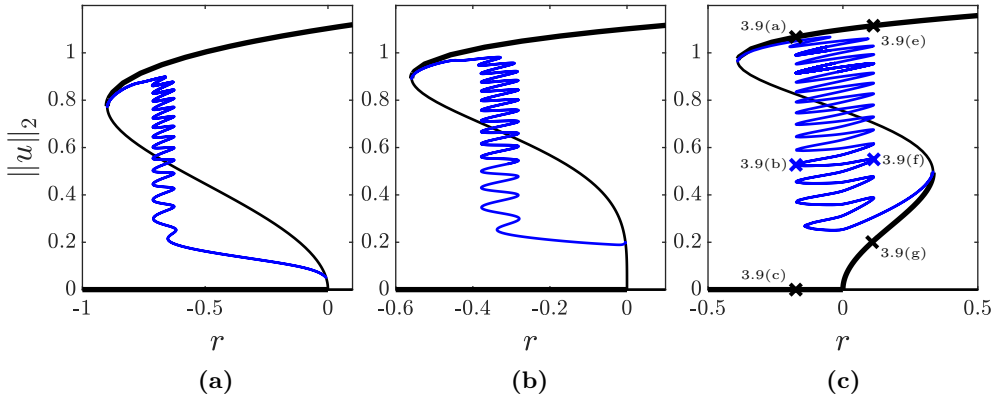

Figure 3.10: Bifurcation diagrams depicting the primary branch (black) and one of the secondary snaking branches (blue) for the cubic-quintic-septic Swift–Hohenberg equation (3.35) with parameter values (a, b, c) equalling: (a) $(-2, -1, 0)$, (b) $(0, 1.05, -0.5)$ and (c) $(2, 3.1, -1)$. Thick (thin) black lines indicate stable (unstable) states on the primary branch.

below the subcritical saddle node of P_{10}, where the trivial conduction state is the only stable state, before turning around at left saddle nodes and intertwining as they each snake towards larger Rayleigh numbers and additional rolls nucleate on the localised states. Consequently, the left saddle nodes are no longer vertically stacked as they were in the Swift–Hohenberg equation (figure 3.1(a)), but rather slant upwards towards larger Rayleigh numbers.

One of the explanations behind slanted snaking is that the conserved quantity provides non-local effects and generates a positive feedback mechanism that can maintain the localised states at lower parameter values than where domain-filling states can be found. Further, these non-local effects can lead to these secondary branches bifurcating from modulational instabilities of either subcritical or supercritical primary branches [11, 54].

The cubic-quintic-septic Swift–Hohenberg equation:

$$\frac{\partial u}{\partial t} = ru - (1 + \partial_x^2)^2 u + au^3 + bu^5 + cu^7, \tag{3.35}$$

can also exhibit homoclinic snaking when the primary bifurcation is supercritical [100]. Figure 3.10 illustrates how such snaking develops from the typical subcritical snaking

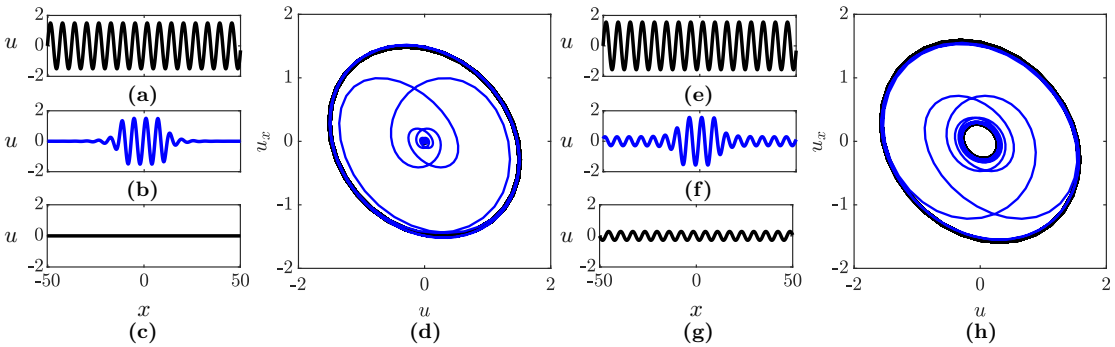

Figure 3.11: Solution profiles for states marked in figure 3.10(c) at (a)–(c) the left edge of the pinning region at $r \approx -0.17$ and (e)–(g) the right edge of the pinning region at $r \approx 0.11$. Phase-space representations of the depicted states at (d) $r \approx -0.17$ and (h) $r \approx 0.11$.

seen in the cubic-quintic Swift–Hohenberg equation (figure 3.10(a)) by linearly interpolating the parameters between $(a, b, c) = (-2, -1, 0)$ [39] and $(a, b, c) = (2, 3.1, -1)$ [100] (figure 3.10(c)).

As the parameter a increases, the primary bifurcation becomes less subcritical and changes criticality at $a = 0$ so that it is supercritical for $a > 0$. This impacts the location of the secondary bifurcation, which we find occurs at increasingly large amplitudes on the primary branch (figure 3.10(b)), before occurring near the first right saddle node when the primary bifurcation is supercritical (figure 3.10(c)). The secondary branches that bifurcate from these bifurcations continue to snake and terminate near the large-amplitude subcritical saddle node as the parameter a increases.

The pinning region moves towards larger values of r as the parameter values change and we find that it contains both positive and negative values of r when $(a, b, c) = (2, 3.1, -1)$ (figure 3.10(c)). This is notable since the spatial stability of the trivial state changes at $r = 0$, owing to the Hamiltonian–Hopf bifurcation at $r = 0$ (see figure 3.3) and we consequently find that the qualitative nature of the localised states changes over the snaking branch (compare figures 3.11(b) and (f)). At the left saddle nodes (e.g., figure 3.11(b)), the localised states resemble those found in the typical subcritical snaking seen in figure 3.1 as they contain a number of large-amplitude oscillations within a background

of the trivial state. At the right saddle nodes (e.g., figure 3.11(f)), however, the large-amplitude oscillations in the localised state now lie within a background of smaller oscillations associated with states on the stable small-amplitude segment of the primary branch (figure 3.11(g)). Thus, the spatial representation of localised states changes from being an orbit that is homoclinic to the origin at the left saddle nodes (figure 3.11(d)) to one that is homoclinic to the periodic orbit corresponding to the small-amplitude stable periodic state at right saddle nodes (figure 3.11(h)).

3.3 MULTISTABILITY

Knobloch et al. [100] showed that the cubic-quintic-septic Swift–Hohenberg equation (3.35) exhibits a rich variety of patterns, beyond those considered in figure 3.11. They attributed such behaviour to multiple (i.e., more than two) stable states coexisting at the same parameter values and the heteroclinic connections between them, which correspond to localised states containing two distinct patterns that could be connected directly (as in figure 3.11(f)) or via a third stable state. Some of these localised states were found to lie on branches that undergo more complicated snaking behaviour than the typical subcritical snaking seen in figure 3.1 (see figure 6 of their paper) when the qualitative nature of these localised states changes over a single snaking oscillation. Gandhi et al. [67] previously observed similar complex branch structures in a Gray–Scott model admitting tristability, which suggests that complicated snaking behaviour is a generic feature of systems admitting multistability.

The above studies considered bistability in systems with a supercritical primary bifurcation or the multistability of states on different primary branches. However, it is also of interest to consider how the typical snaking behaviour changes when a subcritical primary branch undergoes a cusp bifurcation and provides a region of tristability between the stable trivial state and two types of stable periodic states since this is a simplified scenario of behaviour found in the more complicated system of natural doubly diffusive convection, as we will see in Chapter 5. To this end, we extend upon (3.35) and consider

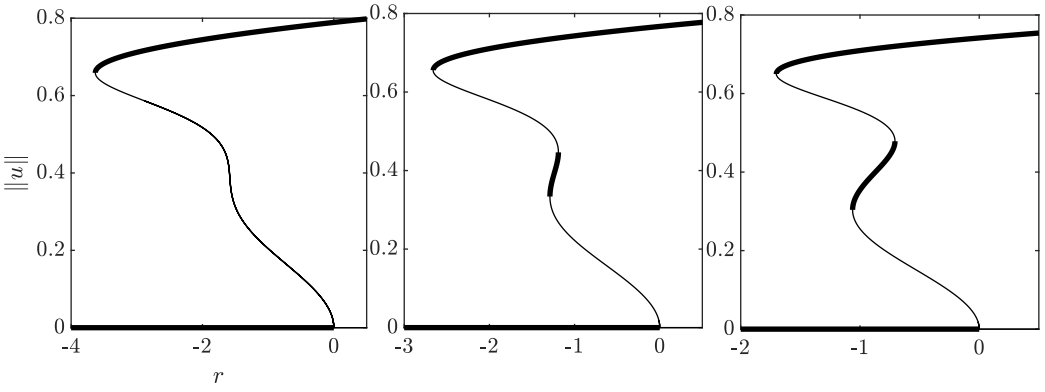

(a) $a = 22$ **(b)** $a = 20.5$ **(c)** $a = 19$

Figure 3.12: Primary branches of the Swift–Hohenberg equation (3.36) as it undergoes a cusp bifurcation at $a \approx 21.7$. Parameter values used: (a) $a = 22$, (b) $a = 20.5$ and (c) $a = 19$ and $b = -100$, $c = 180$ and $d = -100$ in a domain with period $L = 32\pi$. Bold (thin) lines indicate stable (unstable) branch segments.

the Swift–Hohenberg equation with ninth-order nonlinearity:

$$\frac{\partial u}{\partial t} = ru - (1 + \partial_x^2)^2 u + au^3 + bu^5 + cu^7 + du^9, \tag{3.36}$$

where a, b, c and d are real parameters. The choice of nonlinearity is somewhat arbitrary as we expect that using a fifth order polynomial with zero constant term for the nonlinearity could also provide the desired behaviour.

The model system (3.36) admits the trivial solution $u = 0$ for all parameter values. This state first destabilises at $r = 0$ to a primary branch P of spatially periodic states with wavenumber 1 that bifurcates either subcritically ($a > 0$) or supercritically ($a < 0$). The subsequent structure of the primary branch is sensitive to changes in parameter values. We are particularly interested in the changes in the snaking branches when the primary branch undergoes a cusp bifurcation and transitions from exhibiting a single subcritical saddle node to three subcritical saddle nodes. Thus, to obtain relevant parameter values, we first consider when the branch of non-trivial spatially homogeneous states has the desired structure by considering when the polynomial:

$$r - 1 + au^2 + bu^4 + cu^6 + du^8 = 0, \tag{3.37}$$

transitions from having two positive real solutions for u when $r < 0$ to having four. After further exploration around such regions, we fix $b = -100$, $c = 180$ and $d = -100$, while allowing a to vary between $a = 22$ (figure 3.12(a)) and $a = 19$ (figure 3.12(c)), which allows us to focus on the changes that arise near the cusp bifurcation at $a \approx 21.7$ and the widening of the stable segment between newly formed saddle nodes (figures 3.12(b) and (c)).

When $a = 22$, the branch of spatially homogeneous states that bifurcates from the trivial state at $r = 1$ extends towards low values of r, before turning around at a subcritical saddle node at $r \approx -3.835$. This leads to collapsed snaking [39] around $r \approx -1.673$. However, since our focus is on how the typical snaking changes, we consider our starting point shortly after the cusp bifurcation at $a = 20.5$, where collapsed snaking was not found.

Figure 3.13 depicts both the primary branch P (black) and one of the secondary branches that bifurcates from P at $r \approx -0.0078$ (blue) when $a = 20.5$. States on the secondary branch become increasingly modulated as the branch is followed to more negative values of r so that the state at $r \approx -0.847$ (figure 3.13(b)) is localised with a central peak at $x = 0$ and two smaller troughs on either side. The branch then undergoes a single small oscillation between $r \approx -1.08$ (figure 3.13(c) and $r \approx -1.06$ (figure 3.13(d)), where the central peaks and troughs increase in amplitude to become comparable with those in states on the stable middle segment on the primary branch (figure 3.13(l)).

The secondary branch proceeds towards more negative r before snaking upwards over the wider region $-2.28 \lesssim r \lesssim -1.13$ in the typical way. This snaking is primarily associated with the bistability between the trivial state and large-amplitude periodic states on the upper branch segment of P, which may be deduced by the central oscillations in localised states (figures 3.13(g)–(k)) having comparable amplitude to the periodic states on the upper primary branch (figure 3.13(m)). The influence of the stable middle branch segment is, however, observed near the right saddle nodes (figures 3.13(f), (h) and (j)) where the outer oscillations between the trivial state and central large-amplitude oscillations have comparable magnitude to states on this middle branch segment (fig-

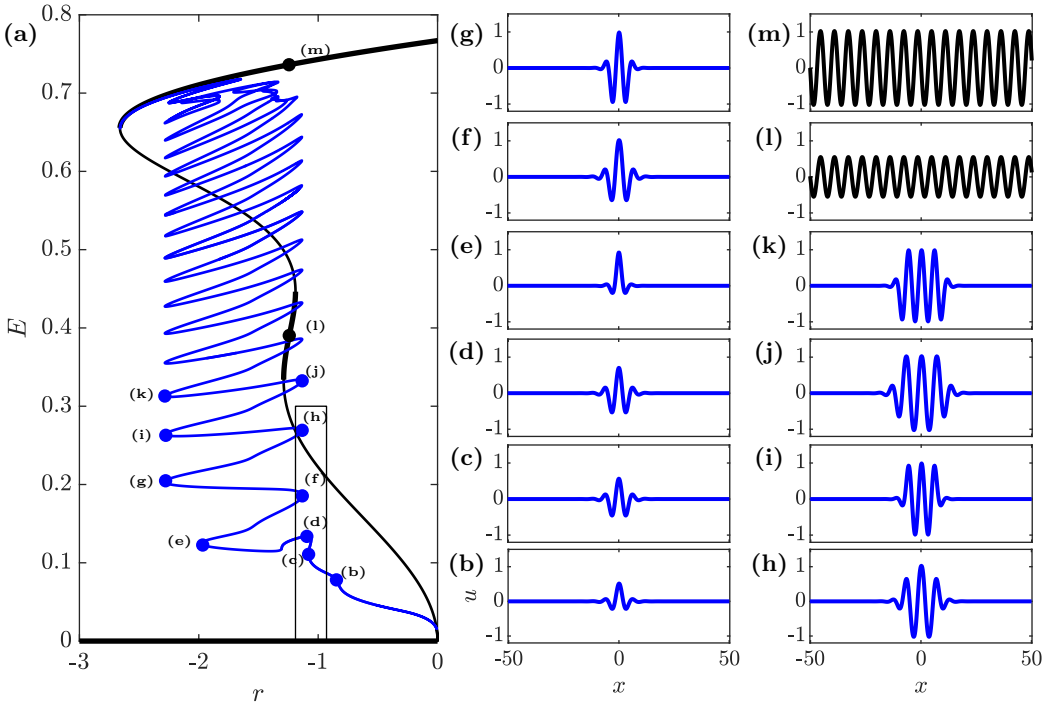

Figure 3.13: Bifurcation diagram and profiles for the Swift–Hohenberg equation (3.36) with $a = 20.5$, $b = -100$, $c = 180$ and $d = -100$ in a domain with period $L = 32\pi$. (a) The branches shown are: the trivial state at $u = 0$, the primary branch with wavenumber one, P, (black) and the snaking secondary branch that terminates near the large-amplitude saddle node of P (blue). Stable (unstable) states on the primary branch are indicated by thick (thin) black lines. The small bounded region indicates the section of the bifurcation diagram considered in figure 3.14(a). (b)–(k) Profiles of the localised states marked on the snaking secondary branch. (l) and (m) Profiles of the domain-filling periodic states on the stable segments of P.

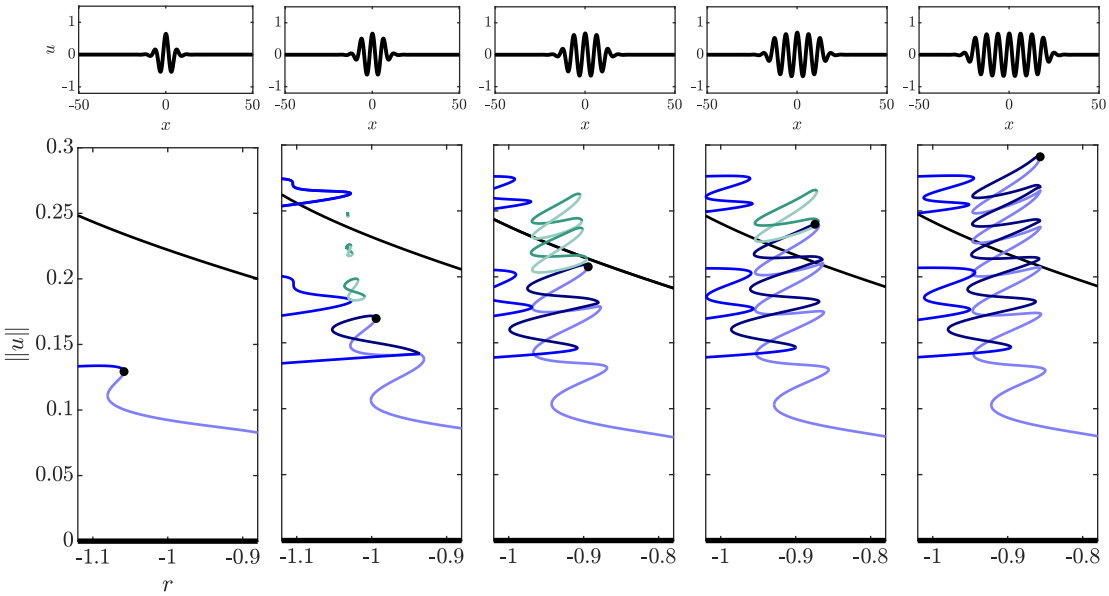

Figure 3.14: Bifurcation diagrams depicting the manner in which isolas (green) successively connect to one of the snaking branches (blue) between (a) $a = 20.5$ and (e) $a = 19.45$. To improve the visualisation of the stack of now-connected isolas, the branch segment from the secondary bifurcation of P and traversing up the stack is shown in light blue, the segment traversing down the stack is shown in dark blue and the segment snaking towards large amplitude is shown in blue. A similar convention is used for the isolas so that when they connect to the top of the stack dark (light) green segments connect to dark (light) blue segments. The points at which the secondary branch changes from traversing up to traversing down the stack of connected isolas are marked by the black dots and the corresponding profiles are shown in the top row.

ure 3.13(l)). The localised state extends by a pair of central peaks over each snaking oscillation until the pattern nearly fills the domain. At which point, the snaking stops and the secondary branch terminates at an Eckhaus instability near the large-amplitude saddle node of P at $r \approx -2.66$.

As a decreases and the region of bistability between the two stable segments of the primary branch increases, the small-amplitude behaviour of the snaking branch changes from that described for $a = 20.5$. This occurs by figure-of-eight isolas successively connecting first to the lower part of each snaking branch and later stacking upwards between $a \approx 20.5$ and $a \approx 19.4$, as evidenced in figure 3.14. The first isola connects between

$a = 20.5$ (figure 3.14(a)) and $a = 20$ (figure 3.14(b)) near the right saddle node of the first small oscillation of the secondary branch (marked in figure 3.14(a)). Afterwards, the secondary branch follows half of the isola (shown in light blue) upwards to the next right saddle node as the amplitudes of the two outer peaks increase and become comparable to that of the central peak (top panel in figure 3.14(b)). These outer oscillations reduce in amplitude as the secondary branch follows the second half of the isola (shown in dark blue) back down towards the right saddle node close to the point of initial connection. After following this isola around, the secondary branch (now shown in blue) returns to snaking upwards over the region $-1.99 \lesssim r \lesssim -1.03$.

Figure 3.14 shows the next three isolas to connect. These isolas originate after the onset of bistability between the trivial state and middle primary branch segment and become larger as a decreases prior to them connecting to the secondary branch near the right saddle node at the top of the stack. With each isola that joins, the stack extends upwards and the number of oscillations in the uppermost localised state increases, as seen in the top row of figure 3.14. This process continues until the localised state contains oscillations that almost fill the domain.

The up (light blue) and down (dark blue) segments of each stack later separate to give two distinct pairs of snaking branches. Figures 3.15(a) and (h) show two of these branches at $a = 19$, shortly after the separation at $a \approx 19.4$. The first of these, which is associated with the up segment of the stack, bifurcates from a secondary bifurcation of P at small-amplitude, as seen in figure 3.14(a). This branch proceeds to snake over the narrow region $-0.885 < r < -0.802$ where, over a single snaking oscillation, the outer pair of peaks or troughs increase in amplitude, as seen in figures 3.14(b)–(f). This continues until oscillations fill the domain and the branch turns over to terminate at the first left saddle node of P (figure 3.14(g)).

The down segment of the stack connects to the large-amplitude snaking branch seen when $a = 20.5$ (figure 3.13) and exhibits the more complicated structure shown in figure 3.15(h). This branch bifurcates from P at the right saddle node (figure 3.15(n)) and initially follows the stable middle primary branch segment towards more negative

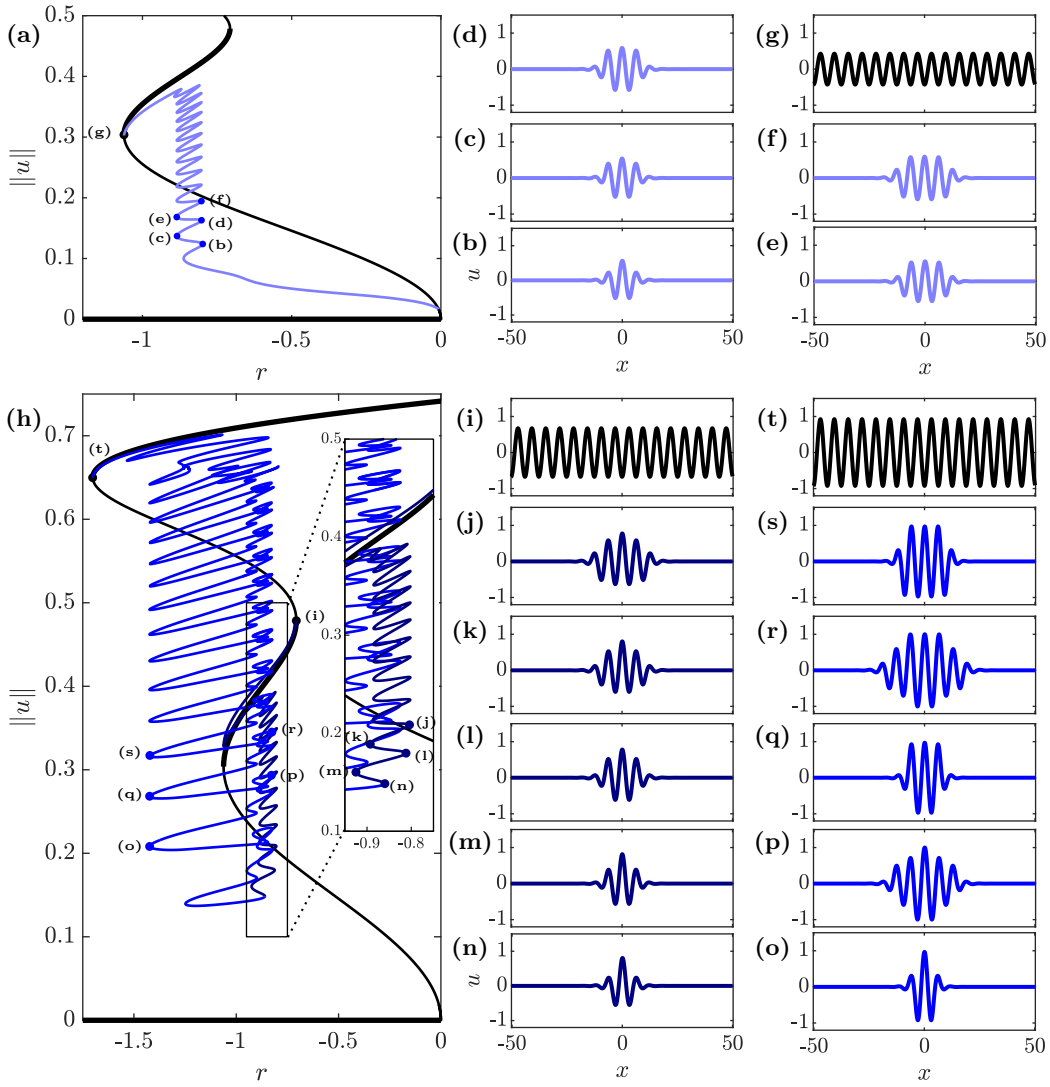

Figure 3.15: Bifurcation diagram and profiles for the Swift–Hohenberg equation (3.36) with $a = 19$, $b = -100$, $c = 180$ and $d = -100$ in a domain with period $L = 32\pi$. (a), (h) Bifurcation diagram showing the primary branch P (black) together with (a) the secondary branch that originated from the upward segments of the stack in figure 3.14 (light blue) or (h) the secondary branch that originated from the downward segments of the stack (dark blue) and the large-amplitude snaking (blue). Stable (unstable) states on the primary branch are indicated by thick (thin) black lines. (b)–(g) and (i)–(t) Profiles of the steady states marked in (a) and (h). The colour of these plots indicates the branch on which they lie.

values of r, before turning around near the first left saddle node of P and entering the pinning region associated with the small-amplitude snaking described above. The branch proceeds to snake downwards, with the localised states losing a pair of outer peaks or troughs over a single snaking oscillation as was observed when the secondary branch in figure 3.15(a) is followed downwards. By comparing the localised states in figures 3.15(n)–(j) to those in figures 3.15(b)–(f), we notice that the main difference between the two branches is that the central peak of localised states on this second branch (dark blue) has slightly larger amplitude than those on the first branch (light blue).

The downwards snaking continues until the localised state contains a main central peak and two smaller troughs, as seen in figure 3.15(n). The branch subsequently heads towards more negative values of r and snakes upwards (as shown in blue), in a similar, but more complicated, way to the original large-amplitude snaking branch when $a = 20..5$ (figure 3.13). This complexity is evidenced by the small figure-of-eight branch segments near the right saddle nodes (figures 3.15(p) and (r)), where a pair of oscillations in each of the fronts that connect the large-amplitude oscillations at the centre of the localised state to the trivial state strengthen in a spatially modulated manner, before later weakening. The net effect over a single of these larger snaking oscillations is that the localised state has increased by a pair of peaks or troughs whose amplitude is comparable to states on the stable upper primary branch. These snaking oscillations continue until states on the secondary branch are domain-filling and the branch terminates at the large-amplitude left saddle node of P (figure 3.15(t)).

Thus, we have shown how a secondary branch that exhibits typical homoclinic snaking can vary as the primary branch starts to exhibit a region of tristability within the existing pinning region. In particular, we found that this snaking branch broke into two separate snaking branches after a number of smaller isolas successively connect onto the original snaking branch at small amplitudes. This process therefore separates localised states associated with the bistability between the trivial state and large-amplitude periodic states, which remain on the snaking branch that extends towards large amplitude, and those associated with the bistability between the trivial state and the smaller amplitude

periodic state, which lie on the snaking branches at smaller amplitudes.

4 | NEAR-ONSET DYNAMICS

We now return our attention to natural doubly diffusive convection, where, in spite of the availability of a comprehensive linear stability analysis when the thermal and solutal gradients exactly balance for more than two decades [70], little is known about the nonlinear dynamics near the onset of convection in the balanced case. This makes it difficult to extrapolate the system's dynamics away from the parameter values used in previous studies of natural doubly diffusive convection [12, 22–24, 70, 191].

In this chapter, we address the above problem by performing a comprehensive nonlinear analysis of the system over a range of Prandtl and Lewis numbers. We present the mathematical framework associated with our case of natural doubly diffusive convection in section 4.1, before reviewing and extending the linear stability analysis of the system in section 4.2.1. Motivated by finding when natural doubly diffusive can admit spatially localised states, we then perform a weakly nonlinear analysis to determine when the system is subcritical in section 4.2.2, as we did for the Swift–Hohenberg equation in Chapter 3. In section 4.3, we augment this analysis by numerically continuing the resulting branches of spatially periodic states in a small-aspect-ratio domain into the nonlinear regime and determine their stability to find regions of bistability and other stable attracting states. We conclude with a short discussion in section 4.4.

4.1 MATHEMATICAL FORMULATION

We first consider the natural doubly diffusive convection of an incompressible binary fluid in a two-dimensional domain with periodic boundary conditions in the vertical

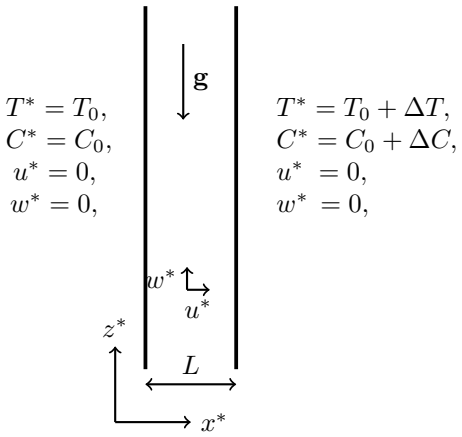

Figure 4.1: Sketch of the two-dimensional domain of natural doubly diffusive convection, together with the dimensional form of the boundary conditions.

direction. The sidewalls are rigid, impermeable and maintained at fixed temperatures and solutal concentrations. The right wall is held at a higher temperature ($T_0 + \Delta T$) and solutal concentration ($C_0 + \Delta C$) than the left wall, where the temperature is T_0 and the solutal concentration is C_0. This configuration is depicted in figure 4.1.

The governing equations are non-dimensionalised as described in Chapter 1, which results in the following set of equations:

$$\frac{1}{Pr}\left(\frac{\partial \mathbf{u}}{\partial t} + \mathbf{u}\cdot\nabla\mathbf{u}\right) = -\nabla p + \nabla^2\mathbf{u} + Ra\,(T + NC)\,\hat{\mathbf{z}}, \tag{4.1}$$

$$\nabla\cdot\mathbf{u} = 0, \tag{4.2}$$

$$\frac{\partial T}{\partial t} + \mathbf{u}\cdot\nabla T = \nabla^2 T, \tag{4.3}$$

$$\frac{\partial C}{\partial t} + \mathbf{u}\cdot\nabla C = \frac{1}{Le}\nabla^2 C. \tag{4.4}$$

The associated boundary conditions read:

$$u = 0, \quad w = 0, \quad -\frac{\partial p}{\partial x} + \frac{\partial^2 u}{\partial x^2} = 0, \quad T = 0, \quad C = 0 \quad \text{on} \quad x = 0, \tag{4.5}$$

$$u = 0, \quad w = 0, \quad -\frac{\partial p}{\partial x} + \frac{\partial^2 u}{\partial x^2} = 0, \quad T = 1, \quad C = 1 \quad \text{on} \quad x = 1, \tag{4.6}$$

where the pressure boundary condition is the projection of the Navier–Stokes equation

on the boundary. Each variable is periodic in the vertical direction.

In this chapter, we will restrict our attention to the case $N = -1$, where the full system (4.1–4.4, 4.5, 4.6) admits the steady conduction state with linear temperature and concentration profiles between the sidewalls:

$$\mathbf{u} = \mathbf{0}, \quad T = x, \quad C = x, \tag{4.7}$$

as a solution. We further introduce convective variables as the departures of the temperature and concentration from the conduction state:

$$\Theta = T - x, \tag{4.8}$$

$$\Phi = C - x. \tag{4.9}$$

Using these new variables, the conduction state takes the form:

$$\mathbf{u} = \mathbf{0}, \quad \Theta = 0, \quad \Phi = 0, \tag{4.10}$$

and the system (4.1–4.4) can be written as:

$$\frac{1}{Pr}\left(\frac{\partial \mathbf{u}}{\partial t} + \mathbf{u}\cdot\nabla\mathbf{u}\right) = -\nabla p + \nabla^2\mathbf{u} + Ra\,(\Theta - \Phi)\,\hat{\mathbf{z}}, \tag{4.11}$$

$$\nabla\cdot\mathbf{u} = 0, \tag{4.12}$$

$$\frac{\partial\Theta}{\partial t} + \mathbf{u}\cdot\nabla\Theta = -u + \nabla^2\Theta, \tag{4.13}$$

$$\frac{\partial\Phi}{\partial t} + \mathbf{u}\cdot\nabla\Phi = -u + \frac{1}{Le}\nabla^2\Phi, \tag{4.14}$$

with homogeneous boundary conditions:

$$u = 0, \quad w = 0, \quad -\frac{\partial p}{\partial x} + \frac{\partial^2 u}{\partial x^2} = 0, \quad \Theta = 0, \quad \Phi = 0 \quad \text{on} \quad x = 0, 1. \tag{4.15}$$

The formulation involving the convective variables allows two symmetries of the system

to be identified. These are the reflection symmetry:

$$S_\Delta : \quad (x,z) \mapsto (1-x,-z), \quad (u,w,\Theta,\Phi) \mapsto -(u,w,\Theta,\Phi), \tag{4.16}$$

and the continuous translation symmetry:

$$T_\delta : \quad (x,z) \mapsto (x,z+\delta), \qquad (u,w,\Theta,\Phi) \mapsto (u,w,\Theta,\Phi). \tag{4.17}$$

These generate the symmetry group $\mathcal{O}(2)$ and restrict the types of bifurcation that can occur from the conduction state, as detailed by Crawford and Knobloch [52].

In many of the numerical computations that we performed both for this chapter and for later ones, it proved helpful to manually impose the reflection symmetry S_Δ on selected states. This was achieved by first taking a single time-step of the governing equations over the full domain (see details in Chapter 2). The solution with $z \geqslant L_z/2$, where L_z is the vertical extent of the domain, was kept and used to generate the solution within $z < L_z/2$ by applying the symmetry S_Δ. The resulting symmetric state was then used as the starting point for the next time-step or Newton iteration, where the same process occurs and we consequently end up with states that are invariant under S_Δ.

The geometry of the system (as depicted in figure 4.1) admits a further symmetry where the roles of temperature and solutal concentration are exchanged owing to the formal equivalence of associated equations and boundary conditions, which allows us to assume that $Le > 1$ without loss of generality. To understand this, consider a solution (u,w,p,Θ,Φ) to (4.11–4.15) when the physical parameters are (Ra, Le, Pr) and construct the related solution:

$$(t',x',z') = \left(\frac{t}{Le}, 1-x, z\right), \tag{4.18}$$

$$(u',w',p',\Theta',\Phi') = (-Le\,u, Le\,w, Le\,p, -\Phi, -\Theta), \tag{4.19}$$

$$(Ra',Le',Pr') = \left(Ra\,Le, \frac{1}{Le}, Pr\,Le\right). \tag{4.20}$$

This solution satisfies

$$\frac{1}{Pr'}\left(\frac{\partial \mathbf{u}'}{\partial t'} + \mathbf{u}' \cdot \nabla' \mathbf{u}'\right) = -\nabla' p' + \nabla'^2 \mathbf{u}' + Ra'(\Theta' - \Phi')\hat{\mathbf{z}}, \tag{4.21}$$

$$\nabla' \cdot \mathbf{u}' = 0, \tag{4.22}$$

$$\frac{\partial \Theta'}{\partial t'} + \mathbf{u}' \cdot \nabla' \Theta' = -u' + \nabla'^2 \Theta', \tag{4.23}$$

$$\frac{\partial \Phi'}{\partial t'} + \mathbf{u}' \cdot \nabla' \Phi' = -u' + \frac{1}{Le'} \nabla'^2 \Phi', \tag{4.24}$$

together with boundary conditions:

$$u' = 0, \quad w' = 0, \quad -\frac{\partial p'}{\partial x'} + \frac{\partial^2 u'}{\partial x'^2} = 0, \quad \Theta' = 0, \quad \Phi' = 0 \quad \text{on} \quad x' = 0, 1. \tag{4.25}$$

This is the same system that would have been derived if the rate of solutal diffusivity, D, had been used in initially non-dimensionalising (1.2–1.5), instead of thermal diffusivity, κ. This transformation can also be generalised to hold for arbitrary $N < 0$, which means that any solution of the full system (4.1–4.4) with $Le < 1$ is related to a second with $Le > 1$.

4.2 WEAKLY NONLINEAR PREDICTIONS

To predict the pattern formation present in our system, we start by performing the linear stability analysis of the conduction state $(u, w, p, \Theta, \Phi) = (0, 0, 0, 0, 0)$, which was previously computed by Ghorayeb and Mojtabi [70] and Xin et al. [191]. We briefly rederive their results in the following subsection so that they can be applied in the later weakly nonlinear analysis, where we derive Ginzburg–Landau equations to model the small-amplitude behaviour close to the primary bifurcation for all Lewis and Prandtl numbers.

4.2.1 LINEAR STABILITY ANALYSIS

We first consider small-amplitude stationary normal mode perturbations to the conduction state:

$$(u, w, p, \Theta, \Phi)^T = \epsilon \left((U_1(x), W_1(x), P_1(x), \Theta_1(x), \Phi_1(x))^T e^{ikz} + c.c. \right) + O(\epsilon^2), \quad (4.26)$$

where *c.c.* denotes the complex conjugate of the preceding term, $\epsilon \ll 1$ and k is the vertical wavenumber of the perturbation. Inserting the expansion (4.26) into the system (4.11–4.14) and linearising the resulting equations yields the eigenvalue problem:

$$\mathcal{L}(Ra)\mathbf{\Psi}_1 = \mathbf{0}, \quad (4.27)$$

for Ra and $\mathbf{\Psi}_1$ where

$$\mathbf{\Psi}_1 = (U_1, W_1, P_1, \Theta_1, \Phi_1)^T e^{ikz} + c.c., \quad (4.28)$$

and

$$\mathcal{L}(Ra) = \begin{pmatrix} \nabla^2 & 0 & -\partial_x & 0 & 0 \\ 0 & \nabla^2 & -\partial_z & Ra & -Ra \\ \partial_x & \partial_z & 0 & 0 & 0 \\ -1 & 0 & 0 & \nabla^2 & 0 \\ -1 & 0 & 0 & 0 & \frac{1}{Le}\nabla^2 \end{pmatrix}. \quad (4.29)$$

The complex functions U_1, W_1, Θ_1 and Φ_1 satisfy Dirichlet boundary conditions on the sidewalls:

$$U_1(x) = W_1(x) = \Theta_1(x) = \Phi_1(x) = 0 \quad \text{on } x = 0, 1, \quad (4.30)$$

while the complex function for the pressure perturbation, P_1, satisfies a projection of the Navier–Stokes equation onto the boundary:

$$0 = -\frac{\partial P_1}{\partial x} + \frac{\partial^2 U_1}{\partial^2 x} \quad \text{on } x = 0, 1. \quad (4.31)$$

Solutions to (4.27–4.31) are independent of Pr and satisfy $\Phi_1 = Le\,\Theta_1$. They are obtained numerically using a Chebyshev–Legendre collocation method after posing the system as the generalised eigenvalue problem:

$$\begin{pmatrix} D^2 - k^2 I & 0 & -D & 0 \\ 0 & D^2 - k^2 I & -ikI & 0 \\ D & ikI & 0 & 0 \\ -I & 0 & 0 & D^2 - k^2 I \end{pmatrix} \begin{pmatrix} U_1 \\ W_1 \\ P_1 \\ \Theta_1 \end{pmatrix} = Ra(Le-1) \begin{pmatrix} 0 & 0 & 0 & 0 \\ 0 & 0 & 0 & I \\ 0 & 0 & 0 & 0 \\ 0 & 0 & 0 & 0 \end{pmatrix} \begin{pmatrix} U_1 \\ W_1 \\ P_1 \\ \Theta_1 \end{pmatrix}, \tag{4.32}$$

where D is the Chebyshev differentiation matrix obtained using the package Chebfun [64] and U_1, W_1, P_1 and Θ_1 here denote vectors containing values of the corresponding function at the Chebyshev collocation points. The Dirichlet boundary conditions for U_1, W_1 and Θ_1 (4.30) are applied directly to (4.32), using an approach suggested by Trefethen [174], where the columns and rows that correspond to the boundaries $x = 0$ and $x = 1$ in these functions are removed.

The generalised eigenvalue problem (4.32) returns multiple eigenvalues for fixed wavenumber that are associated with different horizontal dependencies. Since we are interested in the primary bifurcation of the conduction state, we only consider the smallest positive eigenvalue $Ra_c(Le-1)$ of (4.32) for a range of wavenumbers k. These are subsequently used to form the marginal stability curve in figure 4.2. The minimum of this curve at $k_c \approx 2.5318$ and $Ra_c|Le-1| \approx 6509$, which is consistent with the earlier work by Ghorayeb and Mojtabi [70] and Xin et al. [191] on the primary instability of the conduction state. The linear stability analysis highlights two notable points. Firstly, the absolute value in the eigenvalue arises from the invariance of the system associated with heating from the left sidewall compared to the right sidewall and secondly, there is no net buoyancy forcing on the linear system when the rates of thermal and solutal diffusion D are equal ($Le = 1$), which results in the conduction state being linearly stable for all Rayleigh numbers.

Twenty Chebyshev nodes were used in these computations, which was motivated by the convergence of both the eigenvalue Ra_c and wavenumber k_c with N. In the absence

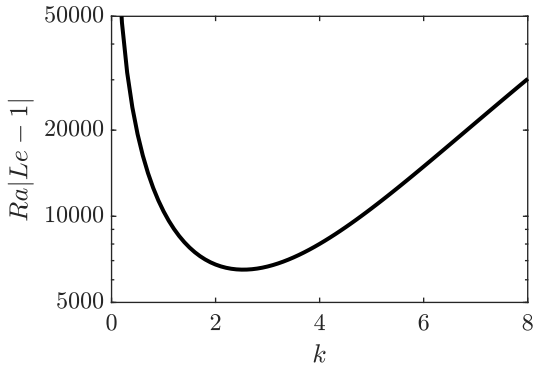

Figure 4.2: Marginal stability curve for the onset of doubly diffusive convection. The conduction state is stable to modes with wavenumber k below the curve, and unstable to them above the curve. The minimum of this curve is $Ra_c|Le-1| \approx 6509$ with wavenumber $k_c \approx 2.5318$ and corresponds to the location of the primary bifurcation.

of exact values for these quantities, their computed value when $N = 50$ was used as a proxy in determining the relative error for varying N. These convergence results are presented in figure 4.3, where we see the exponential convergence in both quantities as N increases to $N \approx 16$, as expected owing to the use of a spectral method. The error in the eigenvalue plateaus around 7×10^{-12} for $N \geqslant 20$, while the error in wavenumber fluctuates around 10^{-7} with a slight upward trend as N increases.

The eigenfunction associated with the critical Rayleigh number and wavenumber corresponds to the marginal eigenmode at the primary bifurcation. Contour plots presenting the profiles for the velocity components, streamfunction, temperature and concentration of this eigenmode for $Le = 11$ are shown in figure 4.4. When $Le > 1$, the conduction state is thus first unstable to a spatially periodic state constituted of counter-rotating convection rolls that slant downwards from the hotter wall, filling the domain and extending to the cold wall. This form of the eigenvector may be understood using the following fluid parcel argument by Xin et al. [191]. Initially suppose that a hotter, high-solute fluid parcel near the right sidewall is displaced leftwards into colder, low-solute fluid. This fluid parcel equilibrates its temperature faster than its solutal concentration so becomes denser than the surrounding fluid and sinks. An analogous argument holds when a cold, low-solute fluid parcel is displaced to the right into hotter, high-solute fluid as the parcel equilibrates its temperature but remains less dense than the

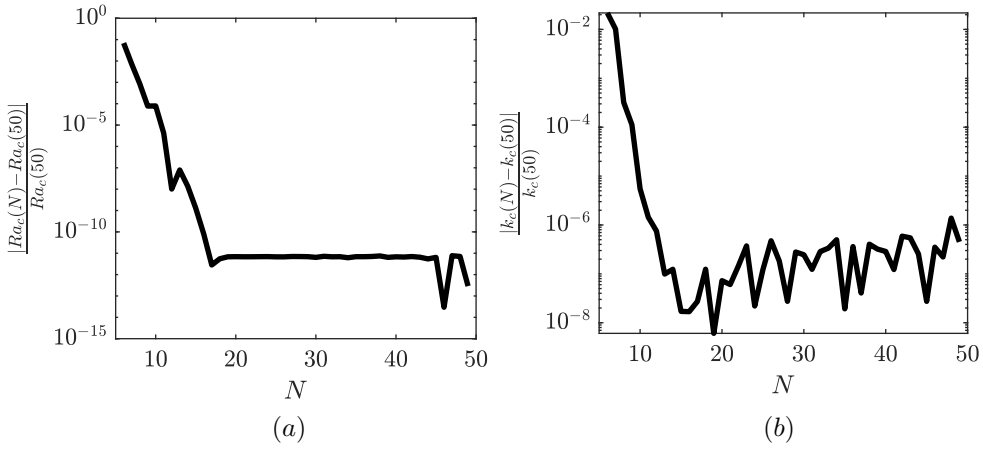

Figure 4.3: Relative error between the numerically computed quantities with N Chebyshev nodes and with $N = 50$ nodes for (a) the eigenvalue $Ra_c|Le - 1|$ and (b) the critical wavenumber k_c.

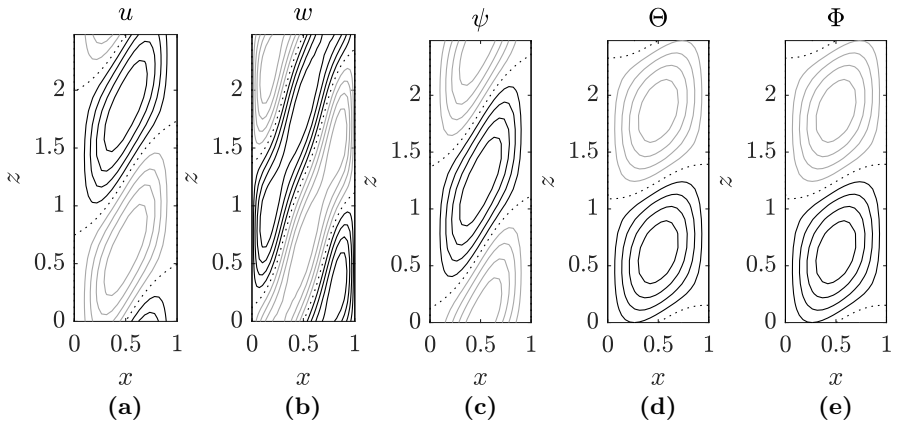

Figure 4.4: Contour plots of a single wavelength of the real critical eigenvector $\mathbf{\Psi}_1$ for $Le = 11$ ($k_c \approx 2.53$). The profiles show the perturbations in (a) horizontal velocity, (b) vertical velocity, (c) velocity streamfunction where $u = -\psi_z$ and $w = \psi_x$, (d) temperature and (e) concentration. Black (grey, dotted) lines indicate positive (negative, zero) values and are separated by 20% of the maximum absolute value.

surrounding fluid and therefore rises. These motions together explain the inclination of the streamlines seen in figure 4.4.

While it is not critical for the following weakly nonlinear analysis, we should also note that the conduction state can also undergo Hopf bifurcations when the growth rate of the normal mode perturbations is purely imaginary. To illustrate this, we consider oscillatory normal mode perturbations of the form

$$\begin{aligned}(u, w, p, \Theta, \Phi)^T = \epsilon \Big(a \Big((U_1(x), W_1(x), P_1(x), \Theta_1(x), \Phi_1(x))^T e^{i(kz+\omega t)} + c.c. \Big) \\ + \Big(b \, (U_2(x), W_2(x), P_2(x), \Theta_2(x), \Phi_2(x))^T e^{i(-kz+\omega t)} + c.c. \Big) \Big) + O(\epsilon^2),\end{aligned} \tag{4.33}$$

where $\omega \in \mathbb{R}$, a and b are real constants and the two normal modes are related via

$$\begin{aligned}(U_1(x), W_1(x), &P_1(x), \Theta_1(x), \Phi_1(x)) = \\ &(U_2(1-x), W_2(1-x), -P_2(1-x), \Theta_2(1-x), \Phi_2(1-x)).\end{aligned} \tag{4.34}$$

This form of perturbation admits two special cases: firstly, the perturbation is an upward or downward travelling wave when exactly one of a and b is non-zero, and, secondly, the perturbation is a standing wave when a and b are equal.

Inserting this perturbation into the full system (4.11–4.14) and linearising the resulting equations yields the eigenvalue problem:

$$\frac{i\omega}{Pr} U_1 = -DP_1 + (D^2 - k^2)U_1, \tag{4.35}$$

$$\frac{i\omega}{Pr} W_1 = -ikP_1 + (D^2 - k^2)W_1 + Ra(\Theta_1 - \Phi_1), \tag{4.36}$$

$$0 = DU_1 + ikW_1, \tag{4.37}$$

$$i\omega\Theta_1 = -U_1 + (D^2 - k^2)\Theta_1, \tag{4.38}$$

$$i\omega\Phi_1 = -U_1 + \frac{1}{Le}(D^2 - k^2)\Phi_1, \tag{4.39}$$

where $D = d/dx$ and, for given k, Pr and Le, both the Rayleigh number and the fre-

quency are unknowns to be solved for. The parameter dependence of the solutions to this eigenvalue problem is more complicated than that for stationary perturbations, where the obtained eigenvalue incorporates both the Lewis and Rayleigh numbers after applying the transformation $\Phi_1 = Le\Theta_1$ and the solutions have no Prandtl number dependence. Thus, the system (4.35–4.39) must be solved separately for different values of these parameters.

Fixing values for the parameters Le, Pr, k and ω, the system (4.35–4.39) is solved as a generalised eigenvalue problem to find consistent Rayleigh numbers using a Chebyshev–Legendre collocation method with 20 nodes. These eigenvalues typically assume complex values as seen in figure 4.5(a), which are not physically significant. There are, however, isolated values of the frequency ω where one of the obtained Rayleigh numbers is purely real: those with $\omega = 0$, which correspond to a stationary bifurcation of the conduction state, and others with non-trivial frequencies, which correspond to Hopf bifurcations of the conduction state. These two cases are illustrated in figure 4.5(a) by the blue and red dots, which respectively correspond to the conduction state with $Le = 11$ and $Pr = 1$ first destabilising to a stationary mode with wavenumber $k = 2$ at $Ra \approx 678$ and later to an oscillatory mode with wavenumber $k = 2$ and frequency $\omega \approx 64.68$ at $Ra \approx 57\,060$.

Locations of these Hopf bifurcations can then be determined in a similar manner for a range of wavenumbers k, while still fixing the values of Pr and Le. This allows us to obtain marginal stability curves and identify the critical Rayleigh number when the conduction state first destabilises to an oscillatory mode and the critical wavenumber associated with this marginal mode. Figure 4.5(b) illustrates the marginal stability curve for $Pr = 1$ and $Le = 11$, from which we conclude that the conduction state first destabilises to an oscillatory mode with wavenumber $k_H \approx 3.16$ and frequency $\omega_H \approx 70.6$ at $Ra_H \approx 48\,118$ for these parameter values.

There are two states associated with this Hopf bifurcation that are of particular interest. The first of these are travelling waves when one of $a = 0$ or $b = 0$ in (4.33). Figure 4.6 depicts the marginal mode associated with downward travelling waves ($b = 0$), with their

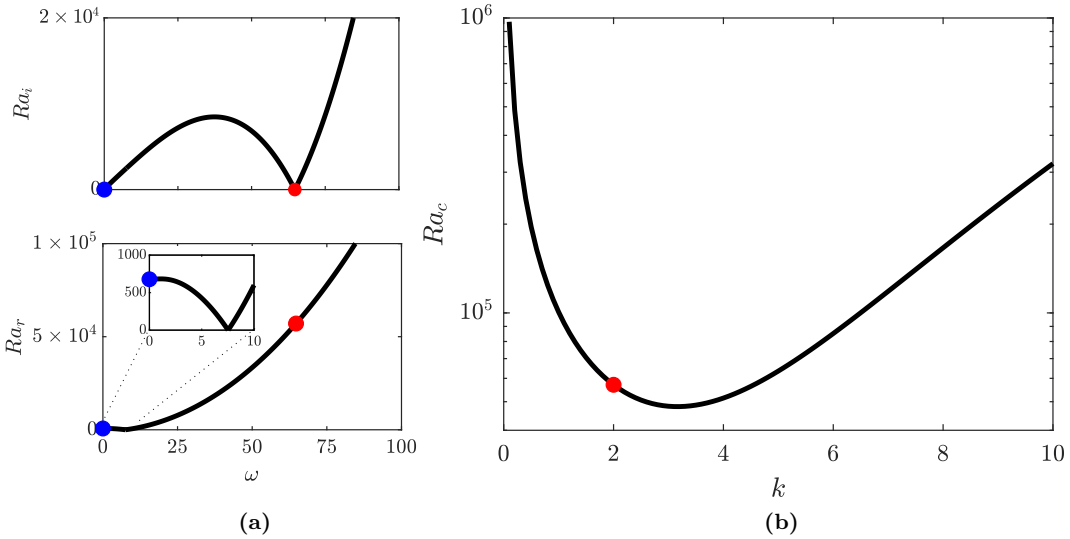

Figure 4.5: (a) Imaginary (top) and real (bottom) parts of the Rayleigh number $Ra = Ra_r \pm iRa_i$ with smallest real part for different frequencies when $k = 2$, $Pr = 1$ and $Le = 11$. The stationary and Hopf bifurcation are marked with the blue and red dots respectively. (b) Marginal stability curve for the first Hopf bifurcation of the conduction state when $Pr = 1$ and $Le = 11$. The minimum of this curve is located at $Ra_H \approx 48\,118$ and $k_H \approx 3.16$. The Hopf bifurcation shown in (a) when $k = 2$ is again marked by the red dot.

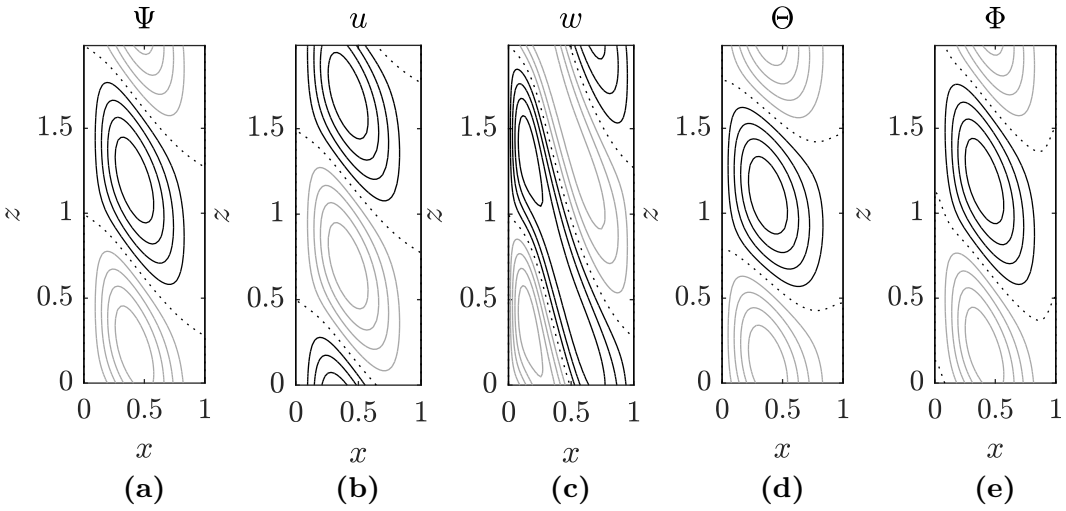

Figure 4.6: Contour plots of the critical eigenvector associated with the downward travelling wave when $Le = 11$ and $Pr = 1$ ($k_H \approx 3.16$). The profiles show the perturbations in (a) horizontal velocity, (b) vertical velocity, (c) velocity streamfunction where $u = -\psi_z$ and $w = \psi_x$, (d) temperature and (e) concentration. Black (grey, dotted) lines indicate positive (negative, zero) values and are separated by 20% of the maximum absolute value.

upward travelling counterparts ($a = 0$) being related to these via a centre-point rotation of 180°. The downward travelling state shown consists of counterrotating rolls that do not extend across the full horizontal extent of the domain, but are instead centred closer towards the colder left sidewall and slant downwards from this wall towards the hotter right sidewall. While this differs from the eigenmode associated with the stationary bifurcation, we should note that the fluid parcel argument previously considered should not be applied in this time-dependent case as streaklines, detailing trajectories of fluid parcels, differ from the streamlines shown in panel (a). We also observe differences between the shape of contours and the phase of the perturbations to the thermal (d) and solutal (e) fields, which is expected with the absence of a simple transformation relating the two fields for oscillatory modes.

The second state of interest are the standing waves that occur when $a = b$ in (4.33). Figure 4.7 depicts streamfunctions over half a period of one such standing wave oscillation. The state at $t = 0$ consists of counterrotating rolls that incline downwards from the

colder wall towards the hotter wall, similarly to the upward and downward travelling states except that the rolls in this state are centred on the horizontal midline $x = 0.5$. These rolls proceed to slowly turn in an anticlockwise direction, thereby reducing the angle at which each roll inclines over the first quarter period of the oscillation until $t \approx \pi/2\omega$, where we find that the centre of individual rolls inclines upward towards the hotter wall. During the next stage of the oscillation ($\pi/2\omega < t < 2\pi/3\omega$), two local extrema of the streamfunction appear within each roll, which affects the outer streamlines of each roll and leads to each clockwise and anticlockwise roll splitting into two smaller rolls, with one lying within $x > 0.5$ and the second within $x < 0.5$. These smaller rolls do not persist for long as, shortly after forming, they merge with a second smaller roll with the same sense of circulation on the other side of the domain. This leads to the elongated negatively inclined rolls seen when $t = 2\pi/3\omega$, which initially strengthen before once again slowly rotating in the anticlockwise direction and reducing their angle of inclination.

While the above details for marginal stability and the form of travelling and standing waves were specific to $Le = 11$ and $Pr = 1$, the conduction state was found to undergo Hopf bifurcations for a range of Prandtl and Lewis numbers. However, for all the parameter values tested, these bifurcations occurred at Rayleigh numbers that were orders of magnitude larger than the primary stationary bifurcation. The dynamics associated with these oscillatory modes are therefore unlikely to affect the dynamics near the onset of stationary convection and so we do not go into further details here.

4.2.2 WEAKLY NONLINEAR ANALYSIS

To investigate the weakly nonlinear regime around the primary stationary bifurcation, we set $Ra = Ra_c + \epsilon^2 r$ with $r = \mathcal{O}(1)$ and $\epsilon \ll 1$ and assume that the system evolves on a slow temporal scale $T_1 = \epsilon^2 t$. We also introduce a long spatial scale, $Z = \epsilon z$, to allow small-amplitude states with long spatial modulations. We emphasise that each of the state variables of our system—u, w, p, Θ and Φ—depends upon the independent variables: x, z, Z and T_1. Using this multiple-scale approach, the partial derivatives

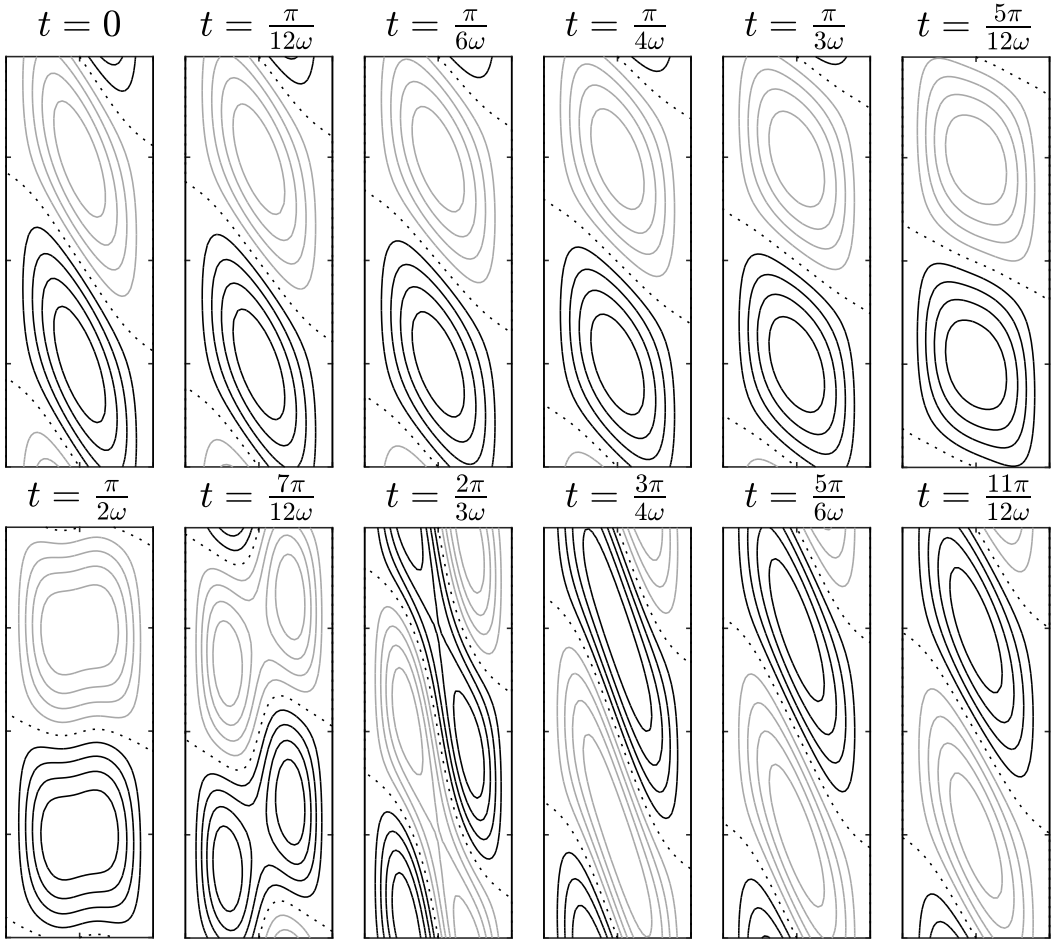

Figure 4.7: Contour plots of the streamfunction over half a period of the marginal standing wave oscillation when $Le = 11$ and $Pr = 1$ ($k_H \approx 3.16$, $\omega_H \approx 70.6$). Profiles are shown at time intervals $t = \pi/12\omega$. Black (grey, dotted) lines indicate positive (negative, zero) values and are separated by 20% of the maximum absolute value.

become

$$\frac{\partial}{\partial t} \mapsto \epsilon^2 \frac{\partial}{\partial T_1} \qquad \text{and} \qquad \frac{\partial}{\partial z} \mapsto \frac{\partial}{\partial z} + \epsilon \frac{\partial}{\partial Z}. \tag{4.40}$$

Introducing the notation $\mathbf{\Psi} = (u, w, p, \Theta, \Phi)^T$, we can express each of the variables as a perturbation expansion in ϵ about the conduction state $\mathbf{\Psi}_0 = (0, 0, 0, 0, 0)^T$, which is the leading order solution:

$$\mathbf{\Psi} = \mathbf{\Psi}_0 + \epsilon \mathbf{\Psi}_1 + \epsilon^2 \mathbf{\Psi}_2 + \dots, \tag{4.41}$$

where $\mathbf{\Psi}_j = (u_j, w_j, p_j, \theta_j, \phi_j)^T$ for $j = 1, 2, \dots$ is the correction at $\mathcal{O}(\epsilon^j)$ for $j = 1, 2, \dots$. The corrections to the conduction state are periodic in z and satisfy the homogeneous boundary conditions:

$$u_j = w_j = \theta_j = \phi_j = 0 \qquad \text{on } x = 0, 1, \quad j = 1, 2, \dots, \tag{4.42}$$

and the pressure boundary condition:

$$-\frac{\partial p_j}{\partial x} + \frac{\partial^2 u_j}{\partial x^2} = 0 \qquad \text{on } x = 0, 1, \quad j = 1, 2, \dots \tag{4.43}$$

at each order in ϵ.

The expansion (4.41) is substituted into the full system (4.11–4.14) and the perturbations are solved numerically order-by-order in ϵ using an extension of the aforementioned collocation method. By further extracting the parameter dependence of the perturbations at each order, we obtain a Ginzburg–Landau equation that can be applied for all parameter values and will indicate the criticality of the primary bifurcation. We proceed by detailing this formulation, which should be applied to the cases $Le > 1$ and $Le < 1$ separately, owing to the parameter combination $Ra(1 - Le)$ changing sign between the two regimes. Since each system with $Le < 1$ can be related to a second with $Le > 1$ via the transformation (4.18–4.20), the difference in the end result between the two cases is minimal, as we shall see.

ORDER ϵ

At $\mathcal{O}(\epsilon)$, the correction is given by the solution to linear system (4.27):

$$\mathbf{\Psi}_1 = A_1(Z, T_1)\Big(U_1(x), W_1(x), P_1(x), \Theta_1(x), Le\Theta_1(x)\Big)^T e^{ik_c z} + c.c., \tag{4.44}$$

where k_c is the critical wavenumber. The phase of the linear eigenfunction is not constrained at this point, but its amplitude is fixed using

$$\langle U_1\,,\, U_1\rangle + \langle W_1\,,\, W_1\rangle + \langle P_1\,,\, P_1\rangle + \langle \Theta_1\,,\, \Theta_1\rangle = 1, \tag{4.45}$$

with the inner product defined

$$\langle f\,,\, g\rangle = \frac{1}{\lambda_c}\int_0^{\lambda_c}\int_0^1 \overline{f}^T g\, dx\, dz, \tag{4.46}$$

where $\lambda_c = 2\pi/k_c$ is the wavelength of the critical eigenvector, the overbar denotes complex conjugation and the superscript T denotes the transposition operation when f is a vector. Since explicit expressions for the solutions to this perturbation problem are not available, each inner product needs to be computed numerically, which we achieved using a Clenshaw–Curtis quadrature on the collocation nodes used in section 4.2.1. The amplitude of the linear correction, A_1, evolves over both long spatial and temporal scales according to an amplitude equation that will be determined at higher order.

ORDER ϵ^2 AND THE ADJOINT SYSTEM

At $\mathcal{O}(\epsilon^2)$, the linear operator $\mathcal{L}$ acts on the second-order terms and is forced by both the nonlinear terms between the $\mathcal{O}(\epsilon)$ corrections and terms proportional to the slow

f_{ij}		j 0	1	2
	1	$\overline{U}_1\frac{dU_1}{dx} + ik_c\overline{W}_1U_1 + c.c.$	$-2ik_cU_1$	$U_1\frac{dU_1}{dx} + ik_cW_1U_1$
	2	$\overline{U}_1\frac{dW_1}{dx} + ik_c\overline{W}_1W_1 + c.c.$	$-2ik_cW_1 + P_1$	$U_1\frac{dW_1}{dx} + ik_cW_1^2$
i	3	0	$-W_1$	0
	4	$\overline{U}_1\frac{d\Theta_1}{dx} + ik_c\overline{W}_1\Theta_1 + c.c.$	$-2ik_c\Theta_1$	$U_1\frac{d\Theta_1}{dx} + ik_cW_1\Theta_1$

Table 4.1: Functions f_{ij} ($i = 1,2,3,4$, $j = 0,1,2$) in the nonlinear term $\mathcal{N}_2$ at $\mathcal{O}(\epsilon^2)$ in (4.47). The overbar denotes complex conjugation.

spatial derivative of the $O(\epsilon)$ correction A_{1Z}:

$$\mathcal{L}(Ra_c)\mathbf{\Psi}_2 = \underbrace{\begin{pmatrix} \frac{1}{Pr}f_{10}|A_1|^2 + \left(A_{1Z}f_{11}e^{ik_cz} + c.c.\right) + \frac{1}{Pr}\left(f_{12}A_1^2e^{2ik_cz} + c.c.\right) \\ \frac{1}{Pr}f_{20}|A_1|^2 + \left(A_{1Z}f_{21}e^{ik_cz} + c.c.\right) + \frac{1}{Pr}\left(f_{22}A_1^2e^{2ik_cz} + c.c.\right) \\ \left(A_{1Z}f_{31}e^{ik_cz} + c.c.\right) \\ f_{40}|A_1|^2 + \left(A_{1Z}f_{41}e^{ik_cz} + c.c.\right) + \left(f_{42}A_1^2e^{2ik_cz} + c.c.\right) \\ Lef_{40}|A_1|^2 + \left(A_{1Z}f_{41}e^{ik_cz} + c.c.\right) + Le\left(f_{42}A_1^2e^{2ik_cz} + c.c.\right) \end{pmatrix}}_{\mathcal{N}_2}, \tag{4.47}$$

where the functions $f_{ij}(x)$ for $i = 1,2,3,4$ and $j = 0,1,2$ are independent of Pr and Le and are given in table 4.1.

To ensure the existence of a unique solution at this order, we derive a solvability condition using the Fredholm alternative theorem. This involves the adjoint operator to $\mathcal{L}$, $\mathcal{L}^\dagger$, defined through the relationship:

$$\langle f\,,\,\mathcal{L}g\rangle = \langle \mathcal{L}^\dagger f\,,\,g\rangle, \tag{4.48}$$

which holds for all vector functions f and g. Integrating the left-hand side by parts, we

find that the adjoint operator takes the form:

$$\mathcal{L}^\dagger = \begin{pmatrix} \nabla^2 & 0 & -\partial_x & -1 & -1 \\ 0 & \nabla^2 & -\partial_z & 0 & 0 \\ \partial_x & \partial_z & 0 & 0 & 0 \\ 0 & Ra_c & 0 & \nabla^2 & 0 \\ 0 & -Ra_c & 0 & 0 & \frac{1}{Le}\nabla^2 \end{pmatrix}, \tag{4.49}$$

together with the adjoint boundary conditions:

$$u^\dagger = 0,\, w^\dagger = 0,\, \theta^\dagger = 0,\, \phi^\dagger = 0 \quad \text{on } x = 0, 1, \tag{4.50}$$

$$-\frac{\partial p^\dagger}{\partial x} + \frac{\partial^2 u^\dagger}{\partial x^2} = 0 \quad \text{on } x = 0, 1, \tag{4.51}$$

and periodicity in the vertical direction.

The Fredholm alternative allows us to pose the adjoint problem:

$$\mathcal{L}^\dagger \mathbf{\Psi}^\dagger = \mathbf{0}, \tag{4.52}$$

whose solution is unique up to a vertical translation and a multiplicative constant. This solution may be written in the form:

$$\mathbf{\Psi}^\dagger = \left(U^\dagger(x), W^\dagger(x), P^\dagger(x), \frac{1}{1-Le}\Theta^\dagger(x), -\frac{Le}{1-Le}\Theta^\dagger(x) \right)^T e^{ik_c z} + c.c., \tag{4.53}$$

where the parameter dependence of the components has been extracted. The amplitude and phase are fixed by imposing the conditions:

$$\langle U^\dagger\,,\, U^\dagger \rangle + \langle W^\dagger\,,\, W^\dagger \rangle + \langle P^\dagger\,,\, P^\dagger \rangle + \langle \Theta^\dagger\,,\, \Theta^\dagger \rangle = 1, \tag{4.54}$$

and

$$Im\left(\langle U^\dagger\,,\, U_1 \rangle \right) = 0, \tag{4.55}$$

where Im represents the imaginary part, respectively.

Using this adjoint solution, we then apply the $\mathcal{O}(\epsilon^2)$ solvability condition:

$$\langle \Psi^\dagger , \mathcal{N}_2 \rangle = 0. \tag{4.56}$$

Owing to the vertical wavenumber dependence of terms in $\mathcal{N}_2$, the only non-trivial contributions come from those proportional to A_{1Z} and their complex conjugates and (4.56) reduces to

$$-2ik_c\langle U^\dagger, U_1\rangle - 2ik_c\langle W^\dagger, W_1\rangle + \langle W^\dagger, P_1\rangle - \langle P^\dagger, W_1\rangle - 2ik_c\langle \Theta^\dagger, \Theta_1\rangle = 0, \tag{4.57}$$

which may be further simplified to

$$\left\langle \mathbf{\Psi}^\dagger , \frac{\partial \mathcal{L}\mathbf{\Psi}_1}{\partial k_c} \right\rangle = 0. \tag{4.58}$$

This solvability condition is automatically satisfied as the primary bifurcation occurs at a quadratic minimum of the marginal stability curve (see figure 4.2).

The $\mathcal{O}(\epsilon^2)$ system (4.47) can be solved to find that the second-order correction to the conduction state is

$$\mathbf{\Psi}_2 = |A_1|^2\mathbf{\Psi}_2^0 + ((A_2\mathbf{\Psi}_1^1 + A_{1Z}\mathbf{\Psi}_2^1)e^{ik_cz} + c.c.) + (A_1^2\mathbf{\Psi}_2^2 e^{2ik_cz} + c.c.), \tag{4.59}$$

where $\mathbf{\Psi}_2 = (u_2, w_2, p_2, \theta_2, \phi_2)^T$ and the functions $\mathbf{\Psi}_2^i$ for $i = 0, 1, 2$ have the following parameter dependence:

$$\mathbf{\Psi}_2^0 = \left(0, \frac{1}{Pr}\tilde{w}_2 + (1+Le)\tilde{w}_3, \frac{1}{Pr}\tilde{p}_2, \tilde{\theta}_3, Le^2\tilde{\theta}_3\right)^T, \tag{4.60}$$

$$\mathbf{\Psi}_2^1 = \left(\tilde{u}_7, \tilde{w}_7, \tilde{p}_7, \tilde{\theta}_7, Le\,\tilde{\theta}_7\right)^T, \tag{4.61}$$

$$\begin{aligned}\mathbf{\Psi}_2^2 = \Bigg(&\frac{1}{Pr}\left(\tilde{u}_4, \tilde{w}_4, \tilde{p}_4, \tilde{\theta}_4, Le\tilde{\theta}_4\right) + (1+Le)(\tilde{u}_5, \tilde{w}_5, \tilde{p}_5, 0, 0) \\ &+ (0, 0, 0, \tilde{\theta}_5, Le^2\tilde{\theta}_5) + Le(0, 0, 0, \tilde{\theta}_6, \tilde{\theta}_6)\Bigg)^T.\end{aligned} \tag{4.62}$$

The newly introduced functions $\tilde{u}_i$, $\tilde{w}_i$, $\tilde{p}_i$ and $\tilde{\theta}_i$ for $i = 2, ..., 7$ are independent of Le and Pr and satisfy the forced linear systems:

$$\begin{pmatrix} -D & 0 & 0 & 0 \\ 0 & D^2 & 0 & 0 \\ 0 & 0 & D^2 & Ra_c(1-Le) \\ 0 & 0 & 0 & D^2 \end{pmatrix} \begin{pmatrix} \tilde{p}_2 \\ \tilde{w}_2 \\ \tilde{w}_3 \\ \tilde{\theta}_3 \end{pmatrix} = \begin{pmatrix} f_{10} \\ f_{20} \\ 0 \\ f_{40} \end{pmatrix}, \tag{4.63}$$

$$\begin{pmatrix} D^2-4k_c^2 & 0 & -D & 0 \\ 0 & D^2-4k_c^2 & -2ik_c & Ra_c(1-Le) \\ D & 2ik_c & 0 & 0 \\ -1 & 0 & 0 & D^2-4k_c^2 \end{pmatrix} \begin{pmatrix} \tilde{u}_4 \\ \tilde{w}_4 \\ \tilde{p}_4 \\ \tilde{\theta}_4 \end{pmatrix} = \begin{pmatrix} f_{12} \\ f_{22} \\ 0 \\ 0 \end{pmatrix}, \tag{4.64}$$

$$\begin{pmatrix} D^2-4k_c^2 & 0 & -D & 0 & 0 \\ 0 & D^2-4k_c^2 & -2ik_c & Ra_c(1-Le) & 0 \\ D & 2ik_c & 0 & 0 & 0 \\ -1 & 0 & 0 & D^2-4k_c^2 & 0 \\ -1 & 0 & 0 & 0 & D^2-4k_c^2 \end{pmatrix} \begin{pmatrix} \tilde{u}_5 \\ \tilde{w}_5 \\ \tilde{p}_5 \\ \tilde{\theta}_5 \\ \tilde{\theta}_6 \end{pmatrix} = \begin{pmatrix} 0 \\ 0 \\ 0 \\ f_{42} \\ 0 \end{pmatrix}, \tag{4.65}$$

$$\begin{pmatrix} D^2-k_c^2 & 0 & -D & 0 \\ 0 & D^2-k_c^2 & -ik_c & Ra_c(1-Le) \\ D & ik_c & 0 & 0 \\ -1 & 0 & 0 & D^2-k_c^2 \end{pmatrix} \begin{pmatrix} \tilde{u}_7 \\ \tilde{w}_7 \\ \tilde{p}_7 \\ \tilde{\theta}_7 \end{pmatrix} = \begin{pmatrix} f_{11} \\ f_{21} \\ f_{31} \\ f_{41} \end{pmatrix}, \tag{4.66}$$

where $D = \dfrac{d}{dx}$, and $\tilde{u}_i$, $\tilde{w}_i$ and $\tilde{\theta}_i$ satisfy homogeneous boundary conditions and the pressure boundary conditions come from a projection of the Navier–Stokes equation onto the sidewalls:

$$\tilde{u}_i = 0, \quad \tilde{w}_i = 0, \quad -\frac{\partial \tilde{p}_i}{\partial x} + \frac{\partial^2 \tilde{u}_i}{\partial x^2} = 0 \quad \tilde{\theta}_i = 0 \quad \text{on} \quad x = 0, 1 \tag{4.67}$$

ORDER ϵ^3

Continuing to $\mathcal{O}(\epsilon^3)$, both the deviation away from the critical Rayleigh number and the slow time dependence of the solution appear in the right-hand side of the resulting system, in addition to nonlinear terms between first and second-order corrections and terms with slow spatial derivatives. The system to solve at third order is

$$\mathcal{L}(Ra_c)\mathbf{\Psi}_3 = \underbrace{\begin{pmatrix} \frac{1}{Pr}\left(\frac{\partial u_1}{\partial_{T_1}} + J(\mathbf{u},u)\right) - 2\frac{\partial^2 u_2}{\partial z \partial Z} - \frac{\partial^2 u_1}{\partial Z^2} \\ \frac{1}{Pr}\left(\frac{\partial w_1}{\partial_{T_1}} + J(\mathbf{u},w)\right) - r\left(\theta_1 - \phi_1\right) - 2\frac{\partial^2 w_2}{\partial z \partial Z} - \frac{\partial^2 w_1}{\partial Z^2} + \frac{\partial p_2}{\partial Z} \\ -\frac{\partial w_2}{\partial Z} \\ \left(\frac{\partial \theta_1}{\partial_{T_1}} + J(\mathbf{u},\theta)\right) - 2\frac{\partial^2 \theta_2}{\partial z \partial Z} - \frac{\partial^2 \theta_1}{\partial Z^2} \\ \left(\frac{\partial \phi_1}{\partial_{T_1}} + J(\mathbf{u},\phi)\right) - \frac{2}{Le}\frac{\partial^2 \phi_2}{\partial z \partial Z} - \frac{1}{Le}\frac{\partial^2 \phi_1}{\partial Z^2} \end{pmatrix}}_{\mathcal{N}_3}, \tag{4.68}$$

where the advective terms are

$$J(\mathbf{u},f) = \mathbf{u}_1 \cdot \nabla f_2 + \mathbf{u}_2 \cdot \nabla f_1 + w_1 \partial_Z f_1, \tag{4.69}$$

and f_1 and f_2, respectively, refer to the first- and second-order corrections of the variables $f = u, w, \theta$ and ϕ.

The solvability condition at this order:

$$\langle \mathbf{\Psi}^\dagger \, , \, \mathcal{N}_3 \rangle = 0, \tag{4.70}$$

is no longer trivially satisfied because some nonlinear terms contained in $\mathcal{N}_3$ have $e^{ik_c z}$ dependence arising from terms proportional to A_1, $|A_1|^2 A_1$, A_{1ZZ}, A_{2Z} and their complex conjugates. However, the contributions to (4.70) from terms proportional to A_{2Z}, cancel for the same reason that the solvability condition at $O(\epsilon^2)$ was satisfied. Consequently, A_2 remains arbitrary at this order. Collecting the remaining terms in (4.70) and

dropping subscripts from A_1 and T_1, we obtain the Ginzburg–Landau equation holding for both $Le > 1$ and $Le < 1$:

$$\alpha A_T = \gamma r A + \beta |A|^2 A + \delta A_{ZZ}, \tag{4.71}$$

where table 4.2 indicates which terms of $\mathcal{N}_3$ contribute to each term above. This equation is equivariant under the $O(2)$ symmetry so we choose the phase of the $\mathcal{O}(\epsilon)$ correction so that these coefficients are real. The coefficient δ is independent of the physical parameters Pr and Le, while α, β and γ satisfy the relations:

$$\begin{aligned}
\alpha &= \frac{1}{Pr}\left(\langle U^\dagger, U_1\rangle + \langle W^\dagger, W_1\rangle\right) + \frac{1}{1-Le}\langle \Theta^\dagger, \Theta_1\rangle - \frac{Le^2}{1-Le}\langle \Theta^\dagger, \Theta_1\rangle, && (4.72)\\
&= \frac{1}{Pr}\alpha_1 + (1+Le)\alpha_2, && (4.73)\\
\gamma &= \langle W^\dagger, \Theta_1 - Le\Theta_1\rangle, && (4.74)\\
&= (1-Le)\gamma_1, && (4.75)\\
\beta &= -\left(\frac{1}{Pr}\langle U^\dagger, \mathcal{N}_3^U\rangle + \frac{1}{Pr}\langle W^\dagger, \mathcal{N}_3^W\rangle + \frac{1}{1-Le}\langle \Theta^\dagger, \mathcal{N}_3^\Theta - Le\mathcal{N}_3^\Phi\rangle\right), && (4.76)\\
&= \frac{1}{Pr^2}\beta_1 + \frac{1+Le}{Pr}\beta_2 + (1+Le^2)\beta_3 + Le\beta_4, && (4.77)\\
\delta &= \langle U^\dagger, U_1\rangle + \langle W^\dagger, W_1\rangle + \langle \Theta^\dagger, \Theta_1\rangle \\
&\qquad + 2ik_c\left(\langle U^\dagger, \tilde{u}_7\rangle + \langle W^\dagger, \tilde{W}_7\rangle + \langle \Theta^\dagger, \tilde{\theta}_7\rangle\right) + \langle P^\dagger, \tilde{w}_7\rangle - \langle W^\dagger, \tilde{p}_7\rangle, && (4.78)
\end{aligned}$$

where the nonlinear functions $\mathcal{N}_3^F$ for $F = U, W, \Theta, \Phi$ in the expression for β are

$$\mathcal{N}_3^F = U_1\frac{dF_2^0}{dx} + \bar{U}_1\frac{dF_2^2}{dx} + U_2^2\frac{d\bar{f}_1}{dx} + 2ik_c\bar{W}_1F_2^2 + ik_cW_2^0F_1 - ik_cW_2^2\bar{F}_1. \tag{4.79}$$

The full expressions used to compute α_i, β_i, γ_1 and δ are tabulated and numerically evaluated in table 4.3. Finally, by dividing (4.71) through by α, the Ginzburg–Landau equation is more conveniently written as

$$A_T = a_1 r A + a_2|A|^2A + a_3A_{ZZ}, \tag{4.80}$$

	Term in Ginzburg–Landau equation (4.71)			
	αA_{T_1}	$\gamma r A$	$\beta \lvert A \rvert^2 A$	δA_{ZZ}
Term in $\mathcal{N}_3$ proportional to	$\dfrac{\partial f_1}{\partial T_1}$	$r(\theta_1 - \phi_1)$	$\mathbf{u}_1 \cdot \nabla f_2$, $\mathbf{u}_2 \cdot \nabla f_1$	$\dfrac{\partial^2 f_2}{\partial z \partial Z}$, $\dfrac{\partial p_2}{\partial Z}$, $\dfrac{\partial^2 f_1}{\partial Z^2}$, $\dfrac{\partial w_2}{\partial Z}$

Table 4.2: Terms from $\mathcal{N}_3$ (see (4.68)) contributing to each term in the Ginzburg–Landau equation (4.71). The column in which these terms are placed informs on the term to which they contribute. Here, f_1 and f_2, respectively refer to first- and second-order corrections of the variables $f = u, w, \theta$ and ϕ.

where $a_1 = \gamma/\alpha$, $a_2 = \beta/\alpha$ and $a_3 = \delta/\alpha$.

SOLUTIONS OF THE GINZBURG–LANDAU EQUATION

The solutions to the Ginzburg–Landau equation (4.80) are good approximations of the small-amplitude solutions of the full doubly diffusive system (4.11–4.14). Of particular interest in this chapter are the two steady solutions that are invariant with respect to the long spatial scale Z. The first of these solutions is the trivial solution:

$$A = 0. \tag{4.81}$$

This solution is valid for all r and corresponds to the conduction state (4.10). The second important solution is

$$A = \left(-\frac{a_1 r}{a_2} \right)^{1/2} e^{i\chi}, \tag{4.82}$$

where χ is an arbitrary phase. This solution relates to states of small-amplitude spatially periodic convection that can be found near the primary bifurcation. These fluid states can then be approximated by

$$(u, w, p, \Theta, \Phi)^T \approx \sqrt{-\frac{a_1(Ra - Ra_c)}{a_2}} \left(U_1(x), W_1(x), P_1(x), \Theta_1(x), Le\Theta_1(x) \right)^T e^{ik_c z} + c.c., \tag{4.83}$$

	Numerical value	Expression
α_1	1.11×10^{-4}	$\langle U^\dagger\,,\, U_1\rangle + \langle W^\dagger\,,\, W_1\rangle$
α_2	2.27×10^{-4}	$\langle \Theta^\dagger\,,\, \Theta_1\rangle$
β_1	-4.43×10^{-9}	$-\left\langle U^\dagger, \overline{U}_1 \frac{d\tilde{u}_4}{dx} + \tilde{u}_4 \frac{d\overline{U}_1}{dx} + 2ik_c\tilde{u}_4\overline{W}_1 + ik_c\tilde{w}_2 U_1 - ik_c\tilde{w}_4\overline{U}_1 \right\rangle$ $-\left\langle W^\dagger, U_1 \frac{d\tilde{w}_2}{dx} + \overline{U}_1 \frac{d\tilde{w}_4}{dx} + \tilde{u}_4 \frac{d\overline{W}_1}{dx} + ik_c\overline{W}_1\tilde{w}_4 + ik_c W_1\tilde{w}_2 \right\rangle$
β_2	-1.63×10^{-8}	$-\left\langle U^\dagger, \overline{U}_1 \frac{d\tilde{u}_5}{dx} + \tilde{u}_5 \frac{d\overline{U}_1}{dx} + 2ik_c\tilde{u}_5\overline{W}_1 + ik_c\tilde{w}_3 U_1 - ik_c\tilde{w}_5\overline{U}_1 \right\rangle$ $-\left\langle W^\dagger, U_1 \frac{d\tilde{w}_3}{dx} + \overline{U}_1 \frac{d\tilde{w}_5}{dx} + \tilde{u}_5 \frac{d\overline{W}_1}{dx} + ik_c\overline{W}_1\tilde{w}_5 + ik_c W_1\tilde{w}_3 \right\rangle$ $-\left\langle \Theta^\dagger, \overline{U}_1 \frac{d\tilde{\theta}_4}{dx} + \tilde{u}_4 \frac{d\overline{\Theta}_1}{dx} + 2ik_c\overline{W}_1\tilde{\theta}_4 + ik_c\tilde{w}_2\Theta_1 - ik_c\tilde{w}_4\overline{\Theta}_1 \right\rangle$
β_3	7.47×10^{-8}	$-\left\langle \Theta^\dagger, U_1 \frac{d\tilde{\theta}_3}{dx} + \overline{U}_1 \frac{d\tilde{\theta}_5}{dx} + \tilde{u}_5 \frac{d\overline{\Theta}_1}{dx} + 2ik_c\overline{W}_1\tilde{\theta}_5 + ik_c\tilde{w}_3\Theta_1 - ik_c\tilde{w}_5\overline{\Theta}_1 \right\rangle$
β_4	1.58×10^{-7}	$-\left\langle \Theta^\dagger, U_1 \frac{d\tilde{\theta}_3}{dx} + \overline{U}_1 \left(\frac{d\tilde{\theta}_5}{dx} + \frac{d\tilde{\theta}_6}{dx}\right) + 2\tilde{u}_5 \frac{d\overline{\Theta}_1}{dx} + 2ik_c\left(\overline{W}_1\left(\tilde{\theta}_5 + \tilde{\theta}_6\right) + \tilde{w}_3\Theta_1 - \tilde{w}_5\overline{\Theta}_1\right) \right\rangle$
γ_1 $(Le > 1)$	-8.85×10^{-7}	$\langle W^\dagger, \Theta_1\rangle$
γ_1 $(Le < 1)$	8.85×10^{-7}	
δ	7.38×10^{-4}	$\langle U^\dagger\,,\, U_1\rangle + \langle W^\dagger\,,\, W_1\rangle + \langle \Theta^\dagger\,,\, \Theta_1\rangle$ $+2ik_c\left(\langle U^\dagger\,,\, \tilde{u}_7\rangle + \langle W^\dagger\,,\, \tilde{w}_7\rangle + \langle \Theta^\dagger\,,\, \tilde{\theta}_7\rangle\right)$ $+\langle P^\dagger\,,\, \tilde{w}_7\rangle - \langle W^\dagger\,,\, \tilde{p}_7\rangle$

Table 4.3: Numerical values and expressions for the coefficients α_1, α_2, β_1, β_2, β_3, β_4, γ_1 and δ in (4.71). The sign of γ_1 depends upon whether $Le > 1$ or $Le < 1$ as $\gamma > 0$ for all Le, while all other coefficients are independent of the parameters Le and Pr.

where the phase χ has been absorbed into z via a vertical translation. These states only exist at small amplitude for Rayleigh numbers that satisfy

$$\frac{a_1}{a_2}\left(Ra_c - Ra\right) > 0. \tag{4.84}$$

Consequently, the sign of the ratio a_1/a_2 determines the criticality of the primary bifurcation and the initial direction of branching.

The numerical values in table 4.3 allow the coefficients a_i to be computed for all parameter values. The coefficients a_1 and a_3 are positive for all Pr provided $Le \neq 1$, whereas the sign of a_2 changes as these parameters are varied. This occurs when $\beta = 0$, which we may find explicitly by taking the positive root of equation (4.77), to find

$$Pr_c = \frac{-(1+Le)\beta_2 + \sqrt{(1+Le)^2\beta_2^2 - 4\beta_1\left[(1+Le^2)\beta_3 + Le\beta_4\right]}}{2[(1+Le^2)\beta_3 + Le\beta_4]}. \tag{4.85}$$

As a result, there exists a boundary in parameter space that separates regions where the primary bifurcation is subcritical ($a_2 > 0$) from those where it is supercritical ($a_2 < 0$). This boundary is shown in figure 4.8 and implies that, for any value of the Lewis number, there exists a critical value of the Prandtl number, $Pr_c(Le)$, expressed in (4.85), above which the bifurcation is subcritical. This critical value tends to 0.376 for small Lewis numbers while it approaches the asymptotic relation $Pr_c \sim 0.376/Le$ as the Lewis number tends to infinity. We further note that the parameter values for physical doubly diffusive systems from Schmitt [157] all lie within the region where the primary bifurcation is subcritical. While we are unaware of further fluid systems lying within the supercritical region of parameter space, we expect that they exist since some of the physical systems identified in figure 4.8, including humidity/heat and stellar interiors (marked (6) and (8), respectively), have parameter values that are within an order of magnitude of the sub/supercritical boundary.

The numerical values of the ratio a_1/a_2 were validated by comparing the small-amplitude behaviour of the linear approximation (4.83) against solutions obtained via

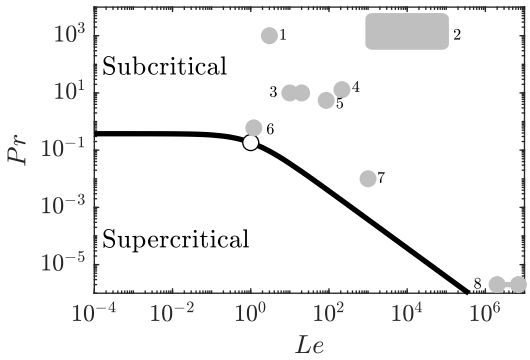

Figure 4.8: Boundary $a_2 = 0$ in (Le, Pr) parameter space separating the region where the primary bifurcation from the conduction state is subcritical (above) from that where it is supercritical (below). The conduction state is linearly stable for all Ra at $Le = 11$ and this point is indicated by the open circle. The grey regions indicate parameter values from [157] for the physical doubly diffusive systems: (1) salt/sugar, (2) magmas, (3) oxide semiconductors, (4) heat/salt 0°C, (5) heat/salt 30°C, (6) humidity/heat, (7) liquid metals and (8) stellar interiors.

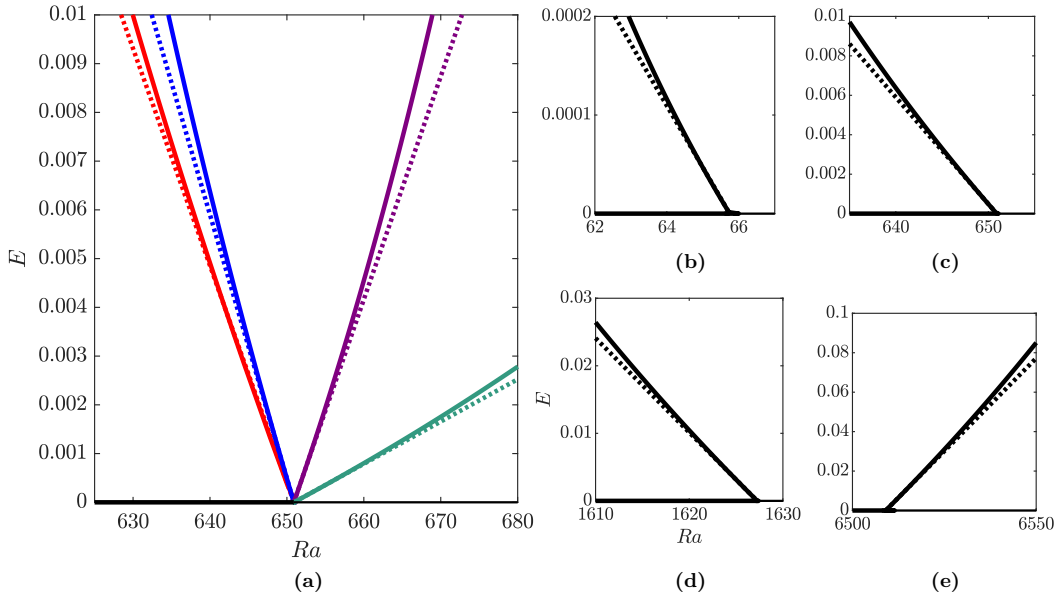

Figure 4.9: Bifurcation diagrams comparing solutions obtained via numerical continuation (solid line) with the linear approximation (4.83) derived from the weakly nonlinear analysis (dotted line) using the parameter values: (a) $Le = 11$ with $Pr = 1$ (red), $Pr = 0.1$ (blue), $Pr = 0.02$ (purple) and $Pr = 0.01$ (green); (b) $Pr = 0.1$ and $Le = 100$, (c) $Pr = 0.1$ and $Le = 11$, (d) $Pr = 0.1$ and $Le = 5$ and (e) $Pr = 0.1$ and $Le = 2$.

numerical continuation in a domain with $L_z = \lambda_c$. Figure 4.9 presents comparisons for a selection of parameter values, including both instances when the primary bifurcation is sub- and supercritical, by showing the kinetic energy:

$$E = \frac{1}{2} \int_0^{\lambda_c} \int_0^1 \left(u^2 + w^2 \right) \, dx \, dz, \tag{4.86}$$

against Rayleigh number for both solutions. In each case, we see how the numerical solution (solid lines) is initially tangent to the approximation (dotted lines) at the primary bifurcation but deviates from it at larger amplitudes, where higher order terms in the approximation should be included. The numerical values of the ratio a_3/a_1 were similarly validated against the numerical solutions. However, since the associated term in the Ginzburg–Landau equation, A_{ZZ}, corresponds to long spatial modulations of the amplitude, this validation required vertically extended domains and will be presented in Chapter 5.

We can gain physical insight into the criticality of the primary bifurcation by examining the contributions that each of the nonlinear terms from equations (4.1–4.4) make to a_2, using a similar approach to the one that Requilé et al. [144] applied to plane Poiseuille and plane Couette flows with viscous dissipation. The expression of the coefficient β (4.77) and the corresponding numerical values provided in table 4.3, show that the inertial term $\mathbf{u} \cdot \nabla \mathbf{u}$ (contributing to β_1 and β_2) provides a negative contribution to a_2, whereas thermal $\mathbf{u} \cdot \nabla T$ and solutal $\mathbf{u} \cdot \nabla C$ advective terms (mostly contributing to β_3 and β_4) provide a positive contribution to a_2. This is further seen by introducing the factors ζ_1 and ζ_2 that multiply the thermal and solutal advective terms, respectively, and numerically perform the weakly nonlinear analysis for the modified system:

$$\frac{1}{Pr} \left(\frac{\partial \mathbf{u}}{\partial t} + \mathbf{u} \cdot \nabla \mathbf{u} \right) = -\nabla p + \nabla^2 \mathbf{u} + Ra(T - C)\hat{\mathbf{z}}, \tag{4.87}$$

$$\nabla \cdot \mathbf{u} = 0, \tag{4.88}$$

$$\frac{\partial T}{\partial t} + \zeta_1 \mathbf{u} \cdot \nabla T = \nabla^2 T, \tag{4.89}$$

$$\frac{\partial C}{\partial t} + \zeta_2 \mathbf{u} \cdot \nabla C = \frac{1}{Le} \nabla^2 C, \tag{4.90}$$

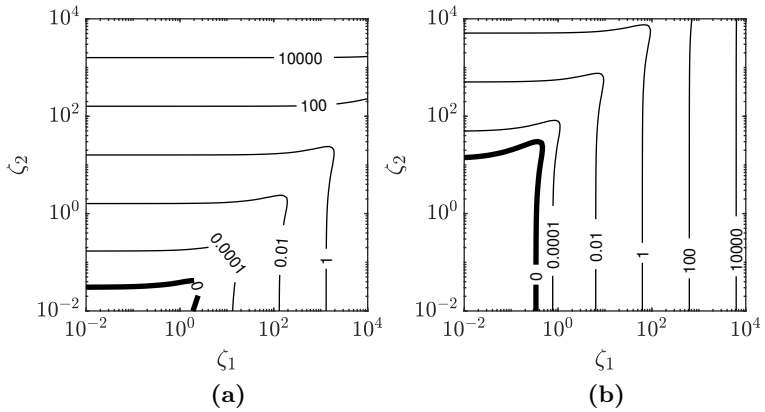

Figure 4.10: Contours of the coefficient a_2 as a function of ζ_1 and ζ_2, which respectively multiply thermal and solutal advective nonlinearities in (4.87–4.90), for (a) $Le = 11$, $Pr = 1$ and (b) $Le = 1/11$, $Pr = 1$. The contour $a_2 = 0$, which marks the boundary between subcriticality and supercriticality, is shown in bold.

with ζ_1, $\zeta_2 \in [10^{-2}, 10^4]$ and selected values of the Prandtl and Lewis numbers. The coefficient a_2 tends to increase when one of ζ_1 or ζ_2 increases, while keeping the other fixed, as indicated by the contours in figure 4.10. Thus, both the advection of heat and of solute enhance the subcriticality of the primary bifurcation, while inertial effects drive the supercriticality. This means that reducing the Prandtl number reduces the subcriticality of the bifurcation since the effects of inertia are strengthened.

The final term in the Ginzburg–Landau equation (4.80), $a_3 A_{ZZ}$, allows small-amplitude solutions of the doubly diffusive system in vertically extended domains to exhibit long-scale amplitude modulation. These solutions include phase-winding states that describe patterns whose wavenumbers are close to the critical wavenumber k_c [53], and spatially modulated states that can develop into localised states away from the primary bifurcation [23]. While the former are out of the scope of this thesis, we will consider the effect of the term $a_3 A_{ZZ}$ on the origin of spatially localised states in the next chapter.

4.3 FULLY NONLINEAR BEHAVIOUR

Having established the region of (Le, Pr) parameter space in which the bifurcation is subcritical, we can now investigate the nonlinear behaviour of the system near the onset of convection. In particular, we focus on the structure and stability of the primary branch of spatially periodic convection states with wavenumber k_c as it extends towards larger amplitudes. For this, we consider a single-wavelength domain with $L_z = \lambda_c = 2\pi/k_c$, which precludes modulational instabilities arising in large domains that are captured by our weakly nonlinear analysis through the A_{ZZ} term in (4.80).

We numerically continue the primary branch against the Rayleigh number across a range of Lewis ($Le \in [5, 100]$) and Prandtl ($Pr \in [2 \times 10^{-3}, 10]$) numbers. The solution branches will be identified on bifurcation diagrams showing either the total kinetic energy of steady states:

$$E = \frac{1}{2} \int_0^{\lambda_c} \int_0^1 \left(u^2 + w^2 \right) \, dx \, dz, \tag{4.91}$$

or the average velocity $\|\mathbf{u}\|_2 = \sqrt{2E/\lambda_c}$, against the Rayleigh number Ra.

Computations were carried out using a spectral element numerical method based on a Gauss–Lobatto–Legendre discretisation and supplemented by Stokes preconditioning with $\Delta t = 0.1$, as detailed by Beaume [8]. Numerical results were validated against a discretisation of up to 4 spectral elements with 29 nodes in both the x and z directions. The stability of the steady states was computed using an Arnoldi method based on a time-stepping scheme [123]. Further direct numerical simulations used a stiffly stable second-order splitting scheme based on [94] with time-step $\Delta t = 10^{-3}$.

4.3.1 BIFURCATION STRUCTURE

The results can be summarised by dividing parameter space according to the qualitative nature of the bifurcation diagram. Figure 4.11(a) indicates the four main regimes found. Region (1) describes the moderate and large Pr behaviour for all Le. In this region, the primary bifurcation is strongly subcritical and the primary branch has a single saddle

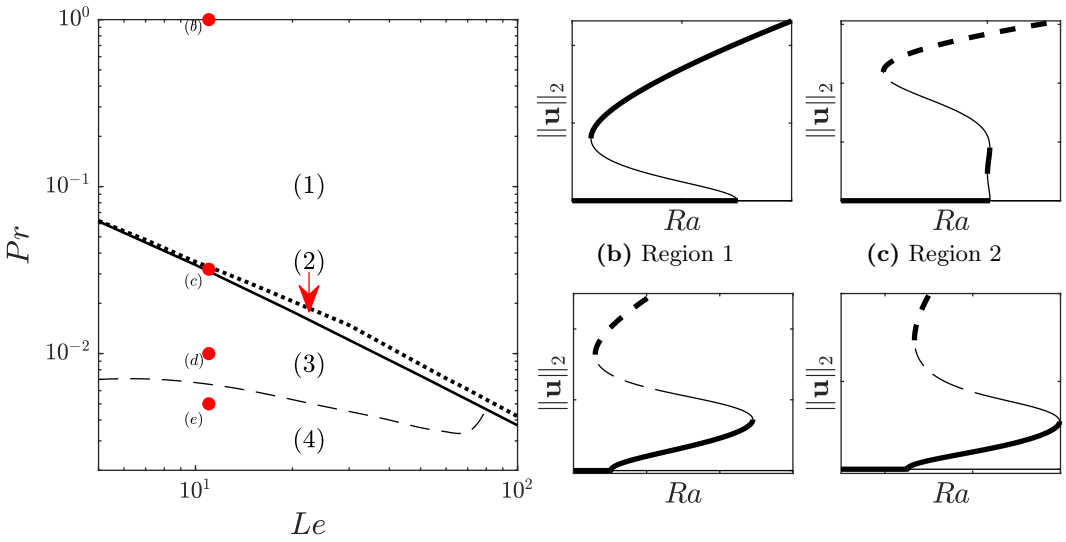

(a) **(b)** Region 1 **(c)** Region 2 **(d)** Region 3 **(e)** Region 4

Figure 4.11: (a) Enlargement of a subset of the parameter space shown in figure 4.8 showing four regions where the bifurcation diagrams exhibit qualitatively different behaviour. The thick line separates subcritical from supercritical branching, while the additional region boundaries are identified with either dotted or dashed lines. (b–e) Representative bifurcation diagrams for parameter values within each of the four regions. The stability of the branch segments is also indicated using thick solid lines for stable solutions, thin lines for solutions unstable to amplitude perturbations and dashed lines for solutions unstable to drift. The location of bifurcations depend upon the specific parameter values used, so those used for each sketch have been marked in panel (a).

node, as shown in figure 4.11(b). Parameter values within this region have received the most attention in previous studies focusing on subcritical pattern formation (e.g., see [24, 191]). Region (2) occupies a small region of parameter space above the boundary $Pr = Pr_c$, where the primary bifurcation is weakly subcritical, and separates the typical subcritical behaviour in region (1) from the supercritical behaviour in regions (3) or (4). The steady convection state branches typically have three saddle nodes in region (2), as exemplified in figure 4.11(c). Regions (3) and (4) identify the two qualitatively different types of bifurcation diagrams observable when the primary bifurcation is supercritical. In both cases, the primary branch has two saddle nodes, with the first lying in the supercritical region $Ra > Ra_c$. The difference between the regions is the location of the second saddle node: in region (3), it is found for $Ra < Ra_c$ (see figure 4.11(d)), whereas, in region (4), it is found in $Ra > Ra_c$ (see figure 4.11(e)). Consequently, a large-amplitude convection state may coexist with the stable conduction state when the primary bifurcation is supercritical, but, for sufficiently small Pr, steady convection states are found entirely within the supercritical region, where the conduction state is unstable. There may exist a fifth region, where the primary branch increases monotonically in both Rayleigh number and in amplitude but we have not identified it in this study.

We now determine the structure of the primary branch as Pr decreases for a fixed value of Le. To achieve this, we follow the locations of its three saddle nodes with respect to Ra and Pr. In doing so, we observed two different scenarios according to whether the pair of saddle nodes is created on the lower or upper part of the primary branch. These are exemplified in figure 4.12 for $Le = 11$ (representative of $5 \leqslant Le \lesssim 15$) and $Le = 20$ (representative of $19 \lesssim Le < 100$). Since the transition between the two scenarios occupies a small region of parameter space within region (2) for $15 \lesssim Le \lesssim 19$, we did not investigate it any further.

To help interpret the plots in figure 4.12, figure 4.13 demonstrates the evolution of the bifurcation diagrams as Pr decreases for $Le = 11$ (panels (a–f)) and $Le = 20$ (panels (g–l)). The structure of the bifurcation diagrams in region (1), for high Pr, remain similar, as shown in figures 4.13(a) and 4.13(g). From the primary bifurcation, the primary branch

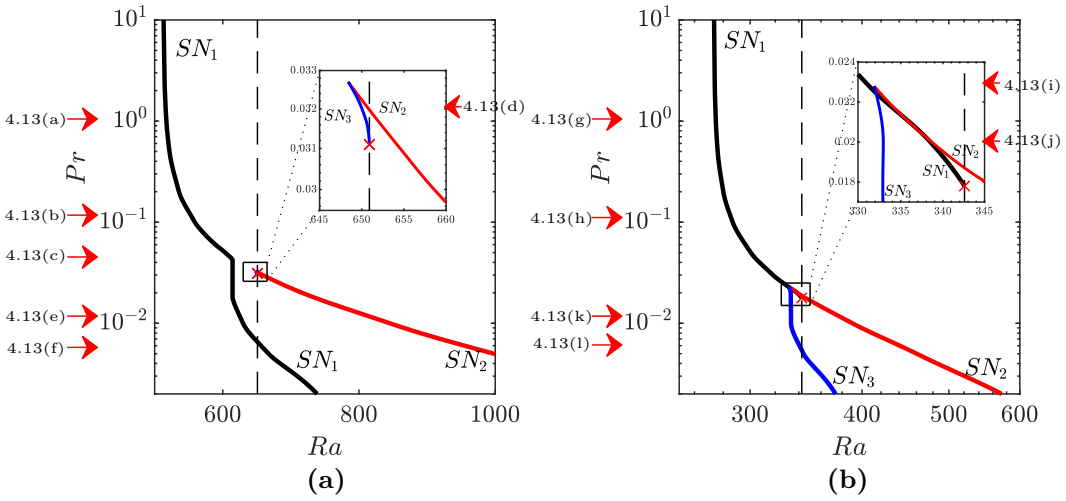

Figure 4.12: Location of the three saddle-node bifurcations of the primary branch in (Ra, Pr) parameter space for (a) $Le = 11$ and (b) $Le = 20$. The dashed line marks the critical Rayleigh number at which the primary bifurcation is found, Ra_c, and the cross marks the codimension-two point (Ra_c, Pr_c) explained in the text. The insets provide enlargements of the area around Ra_c in each case. Arrows mark the bifurcation diagrams shown in figure 4.13.

extends towards lower Rayleigh numbers and proceeds to turn around at a saddle node, hereafter referred to as SN_1, before heading towards large-amplitude convection states at large Ra. Figure 4.12 suggests that, as $Pr \to \infty$, the location of SN_1 tends to a constant Rayleigh number, dependent upon Le. This figure also shows that SN_1 occurs at larger Ra as the Prandtl number is decreased and the primary bifurcation becomes less subcritical.

Upon decreasing the Prandtl number, the primary branch undergoes a cusp bifurcation at $Pr \approx Pr_{cusp}(Le) > Pr_c(Le)$, while still subcritical, denoting the beginning of region (2). The cusp produces two additional saddle nodes along the primary branch: SN_2 and SN_3. The exact process by which this is achieved depends on the Lewis number. For $Le \lesssim 15$, the cusp bifurcation occurs at smaller amplitude than SN_1 and the saddle nodes are labelled SN_3, SN_2, SN_1 as the branch is followed in the direction of increasing energy (see, for example, figure 4.13(d) for $Le = 11$ and $Pr = 0.032$, near the cusp parameter value: $Pr_{cusp} \approx 0.033$). In contrast, for $Le \gtrsim 19$, the cusp bifurcation occurs at higher amplitude

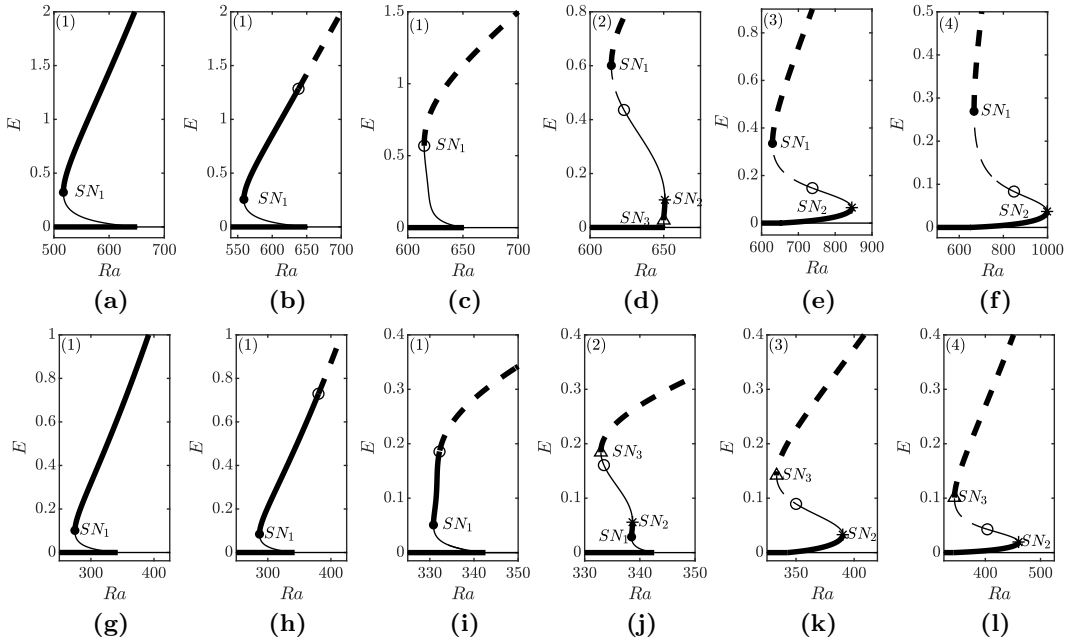

Figure 4.13: Bifurcation diagram showing the primary branch of steady convection and the stability of the related states across the four regions, indicated in the top left corner. Thick solid lines indicate stable solutions, thin lines indicate solutions unstable to amplitude perturbations and dashed lines indicate solutions unstable to drift. Saddle nodes are marked by symbols: SN_1 (filled circle), SN_2 (asterisk) and SN_3 (triangle). The open circle corresponds to the destabilising drift bifurcation. The parameter values, also indicated by the arrows in figure 4.12, are: $Le = 11$, and (a) $Pr = 1$, (b) $Pr = 0.1$, (c) $Pr = 0.042$, (d) $Pr = 0.032$, (e) $Pr = 0.01$, (f) $Pr = 0.005$, as well as $Le = 20$, and (g) $Pr = 1$, (h) $Pr = 0.1$, (i) $Pr = 0.023$, (j) $Pr = 0.02$, (k) $Pr = 0.01$ and (l) $Pr = 0.005$. For $Le = 11$ (resp. $Le = 20$), $Pr_c \approx 0.031$, $Pr_{cusp} \approx 0.033$ (resp. $Pr_c \approx 0.018$, $Pr_{cusp} \approx 0.023$).

than SN_1 and saddle nodes are labelled SN_1, SN_2, SN_3, as shown in figure 4.13(i) for $Le = 20$, $Pr = 0.023 \approx Pr_{cusp}$.

Continuing to reduce Pr across region (2) (from Pr_{cusp} to Pr_c), the Rayleigh number associated with SN_2 increases so that it reaches the supercritical region before $Pr = Pr_c$. During this transition, the saddle node with smallest amplitude (SN_3 for $Le \lesssim 15$; SN_1 for $Le \gtrsim 19$) moves to larger Rayleigh numbers but with decreasing amplitude until it collides with the primary bifurcation at $Pr = Pr_c$ and $Ra = Ra_c$, where the primary bifurcation changes from subcritical to supercritical. This process is highlighted in the insets of figure 4.12 and results in the primary branch possessing only two saddle nodes in the supercritical regime ($Pr < Pr_c$).

The locations of the remaining two saddle nodes go toward larger Ra as Pr decreases and are found in the supercritical region ($Ra > Ra_c$) in region (4), as shown in figure 4.11. It is therefore clear that multiple steady convection states can exist for the same parameter values near the onset of convection, regardless of the criticality of the primary bifurcation. This result extends earlier observations on the number of saddle-node bifurcations occurring along the primary branch in related systems [176].

More insight into these results can be obtained by representing, as in figure 4.14, the location of the saddle nodes for various Lewis numbers as a function of the reduced Prandtl number Pr/Pr_c and combined parameter $Ra|Le - 1|$. These transformed parameters allow us to identify the location where the criticality of the primary bifurcation changes as the single coordinate point: $Pr/Pr_c = 1$, $Ra|Le - 1| \approx 6509$. Figure 4.14 shows that, for $Pr < Pr_c$ and the chosen values of the Lewis number, the location of the first supercritical saddle node SN_2 can be approximated by:

$$Ra_{SN_2} \approx \frac{6460}{|Le - 1|} \left(\frac{Pr}{Pr_c} \right)^{-0.24}. \tag{4.92}$$

For $Pr < 10^{-2}$ (not shown), the location of saddle node SN_2 deviates from the relation above, indicating a potentially different asymptotic regime. These results also illustrate the large Pr behaviour of the subcritical saddle node SN_1: $Ra_{SN_1}|Le - 1|$ tends to a

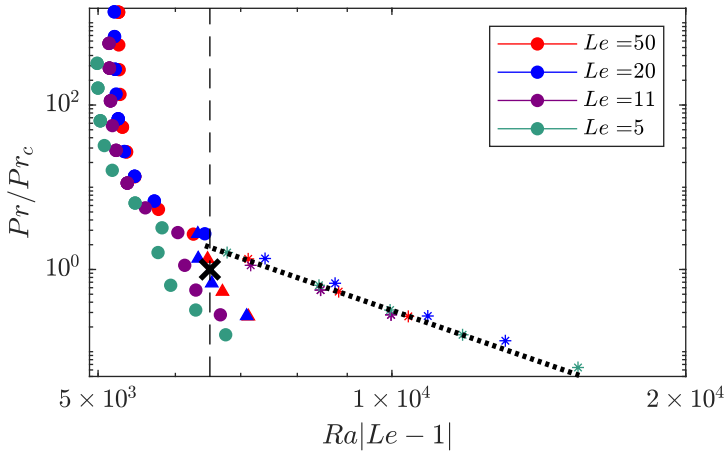

Figure 4.14: Locations of the saddle-node bifurcations in $(Ra|Le-1|, Pr/Pr_c)$ parameter space for $Le = 5$ (green), $Le = 11$ (purple), $Le = 20$ (blue) and $Le = 50$ (red). The black dashed line marks the location of the primary bifurcation and the red cross marks the codimension-two point where the criticality of the primary bifurcation changes, at $Pr = Pr_c$. The black dotted line represents relationship (4.92). The saddle nodes are marked by circles for SN_1, asterisks for SN_2 and triangles for SN_3.

constant as the Prandtl number tends to infinity. This constant increases with Le and saturates for large values of the Lewis number. These results echo those obtained in doubly diffusive convection in a 2D vertical porous enclosure, where Mamou et al. [122] used a parallel flow approximation to demonstrate that the Rayleigh number at which the subcritical saddle node occurs is proportional to $1/(1-Le)$ for large enough Lewis numbers.

4.3.2 SOLUTION PROFILES

Despite the different scenarios obtained at different values of the Prandtl number (see figure 4.11), the steady convection states undergo similar structural changes along their branch, as evidenced in figure 4.15 for $Le = 11$ and $Pr = 1, 0.032, 0.01$ and 0.005. The streamfunction profiles are similar near the primary bifurcation regardless of the value of the Prandtl number (see second column of figure 4.15), which is in agreement with the linear stability results from figure 4.4(c). Moving along the branches in the direction of increasing energy, the first change that we observe is the strengthening of

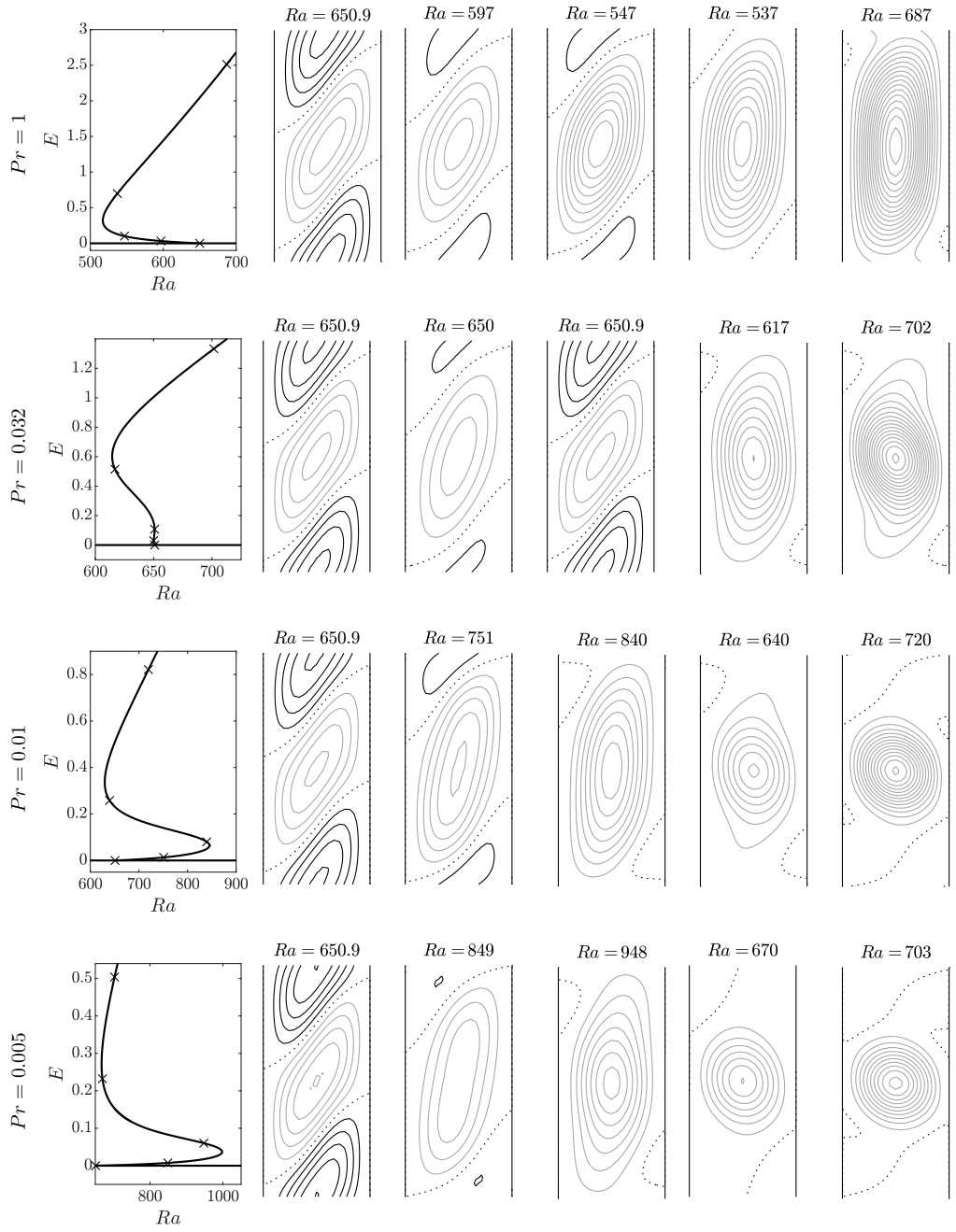

Figure 4.15: Streamfunctions of the steady states on the primary branch when $Le = 11$ for different values of the Prandtl number: top row $Pr = 1$, second row $Pr = 0.032$, third row $Pr = 0.01$ and bottom row $Pr = 0.005$. The left column shows the respective bifurcation diagrams and indicates with a cross which solutions have been represented in the subsequent panels. Black (grey, dotted) contours indicate positive (negative, zero) values of the streamfunction. The following contour intervals are used: 10^{-4} (first column, top two rows); 10^{-5} (first column, third row); 2×10^{-5} (first column, bottom row); 0.02 (second column, top two rows); 0.01 (second column, bottom two rows); 0.02 (third column); 0.05 (fourth and fifth columns).

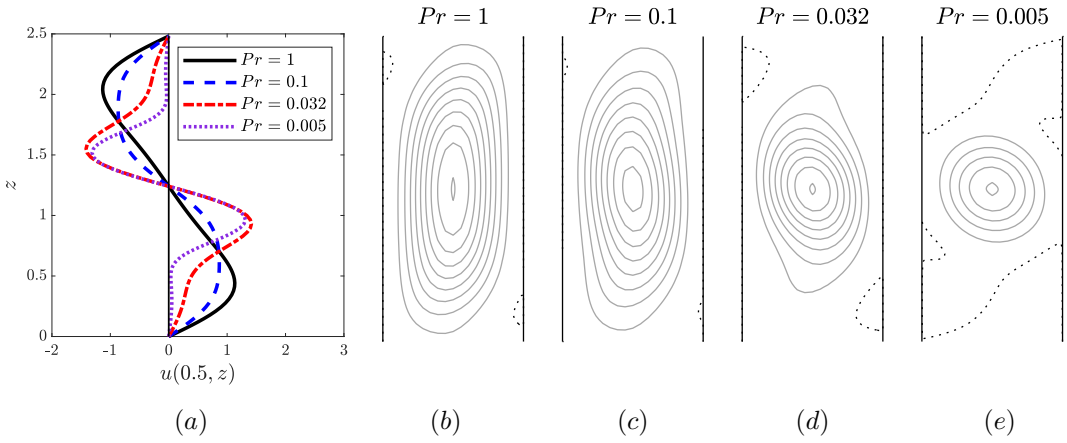

Figure 4.16: Horizontal velocity and streamfunction of solutions from the upper segment of the primary branch at $Ra = 700$ for $Pr = 1, 0.1, 0.032, 0.005$ and $Le = 11$ represented via (a) the midline horizontal velocity ($u(x = 0.5, z)$) and streamfunction contours plots for (b) $Pr = 1$, (c) $Pr = 0.1$, (d) $Pr = 0.032$ and (e) $Pr = 0.005$ with contour intervals 0.1.

the anticlockwise roll, where fluid near the hotter wall moves upwards. This occurs in both the subcritical and the supercritical regimes, as can be seen in the third column of figure 4.15. Continuing the branches to the large-amplitude saddle node and beyond, the amplitude of the weaker roll decreases, leaving room for the stronger roll to straighten. At large enough amplitude, an anticlockwise roll occupies the domain, irrespective of the value of Pr. Its amplitude grows as the upper branch is followed to larger values of Ra, where the Prandtl number starts to impact the flow: the roll occupies a smaller area at lower values of the Prandtl number, as seen within the final column of figure 4.15. This resembles the fly-wheel convection, with nearly circular streamlines, seen in low-Prandtl Rayleigh–Bénard convection as studied by Clever and Busse [47].

To characterise these observations in more detail, figure 4.16 reports the horizontal velocity profiles observed on the upper branch for $Pr = 1$, 0.1, 0.032 and 0.005. The decrease in roll size is apparent when Pr is decreased. This is particularly evident for $Pr = 0.005$, where the horizontal velocity remains small except within the range $0.6 \lesssim z \lesssim 1.9$, in such a way that the roll only occupies about half of the extent of the domain. Figure 4.16(a) additionally shows the transition to these states from the large rolls observed

at $O(1)$ Prandtl numbers. For $Pr = 1$, the maximum horizontal velocity is achieved far from the centre of the roll, at $z \approx 0.44$ and $z \approx 2.04$, producing a region of strong shear between the rolls and gentle quasi-linear velocity variations inside the rolls. As Pr is lowered, these maxima move towards the centre of the roll by initially becoming less pronounced and creating flatter extrema (see figure 4.16(c)), followed by the emergence of peaks around $z \approx 1$ and $z \approx 1.5$. The maximum horizontal velocity does not change significantly within this range of Prandtl number values in such a way that the low Pr rolls represent narrow regions of strong shear surrounded by low amplitude flow.

4.3.3 PHYSICAL INTERPRETATION OF CHANGING ROLL PROFILES

To interpret the changes in roll structure seen in figures 4.15 and 4.16 when the Prandtl number decreases, we consider the vorticity equation:

$$\frac{1}{Pr}\left(\frac{\partial \omega}{\partial t} + \mathbf{u}\cdot\nabla\omega\right) = \nabla^2\omega - Ra\left(\frac{\partial \Theta}{\partial x} - \frac{\partial \Phi}{\partial x}\right), \tag{4.93}$$

where $\omega = \hat{\mathbf{y}}\cdot(\nabla\times\mathbf{u})$ is the only non-zero component of the vorticity. Since our focus here is on the steady states of the system, we may set the first term of (4.93) equal to zero, which results in a three-way balance between inertia, I, viscous diffusion, D and horizontal variations in the buoyancy force, B:

$$\underbrace{\frac{1}{Pr}\left(\mathbf{u}\cdot\nabla\omega\right)}_{I} - \underbrace{\nabla^2\omega}_{D} + \underbrace{Ra\left(\frac{\partial \Theta}{\partial x} - \frac{\partial \Phi}{\partial x}\right)}_{B} = 0. \tag{4.94}$$

The contributions to (4.94) from each of these terms vary both spatially over the domain and with the physical parameters.

Figure 4.17 presents the relative importance of the three terms across the domain for four different Prandtl numbers using the steady states shown in figure 4.16. At $Pr = 1$ (top row), the balance in the vorticity equation (4.94) is primarily between viscous dissipation and buoyancy. Inertia plays a subdominant role across the domain, except within a pair of thin, white 'S'-shaped strips that follow the vertical sides of the roll and bend

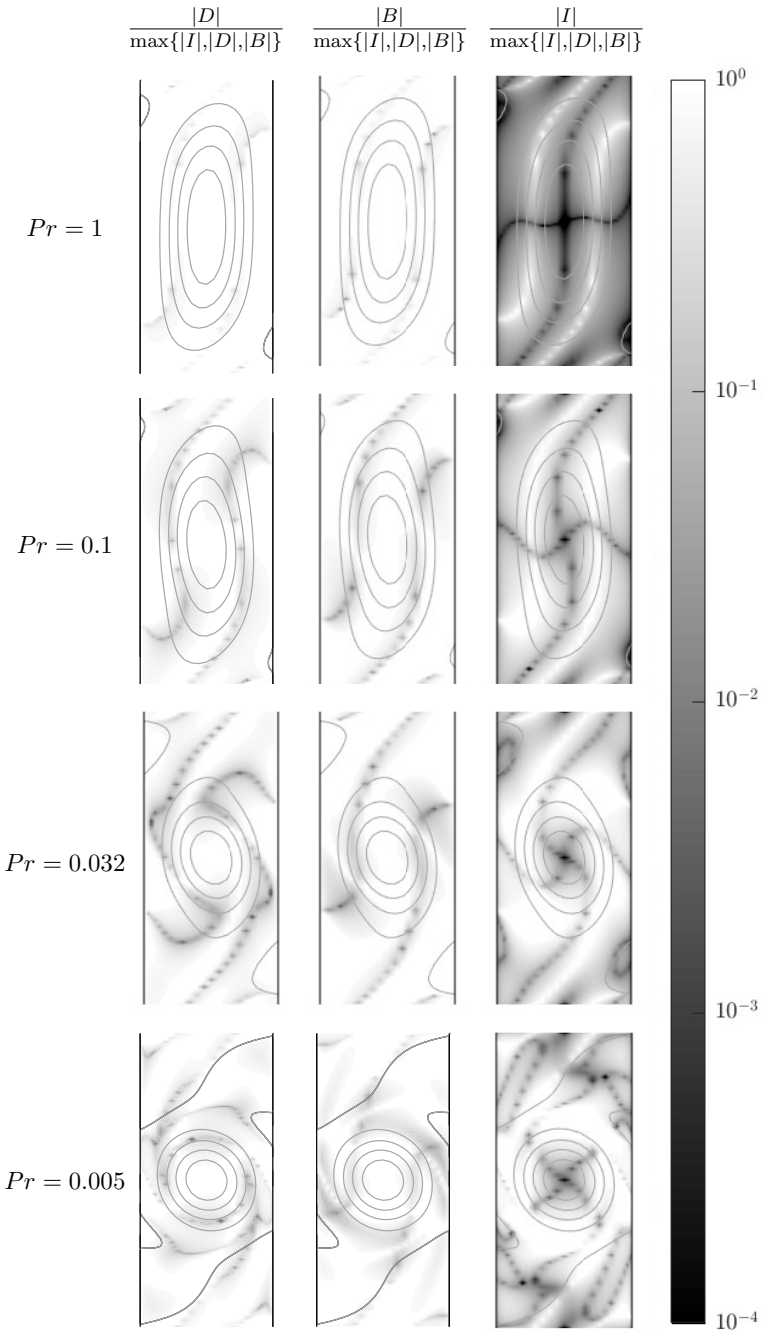

Figure 4.17: Fraction of the dominant term ($\max\{|I|, |D|, |B|\}$) that the viscous dissipation term $|D|$ (first column), buoyancy term $|B|$ (second column), and inertial term $|I|$ (third column) contribute to the vorticity equation (4.94) for the steady states shown in figure 4.16 at $Ra = 700$ for $Pr = 1$ (top row), $Pr = 0.1$ (second row), $Pr = 0.032$ (third row) and $Pr = 0.005$ (bottom row). The colour bar on the right indicates the logarithmic scale used where white indicates a dominant term, while grey and black indicates a subdominant term. Streamlines of the steady flow are superposed onto each subplot. The dotted nature of these subplots comes from approximating the derivatives using a finite discretisation.

down (up) towards the colder (hotter) wall. However, the contribution of inertia to the balance increases throughout the domain as the Prandtl number decreases. This change is particularly seen by the white 'S'-shaped strips widening by $Pr = 0.1$ (second row), then curving and moving towards the centre of the domain as they continue to follow the outer edges of the roll that becomes smaller with decreasing Prandtl number (e.g., $Pr = 0.032$ (third row)).

By $Pr = 0.005$ (bottom row), we find that the domain can be divided into three regions according to both the balance within the vorticity equation and the magnitude of individual terms: at the centre of the roll, inertia is subdominant, while there is a balance between the dominant diffusive and buoyancy terms; towards the edges of the roll, the main balance is between inertia and buoyancy with viscous dissipation providing a non-negligible contribution; outside the roll, where each of the terms are small in (4.94), the primary balance is again between buoyancy and viscous dissipation. The inertial term being small at the centre of the roll and outside the roll is consistent with fly-wheel convection where the lines of constant vorticity become coincident with the streamlines [47]. Thus, the roll structure changes with decreasing Prandtl number since inertia changes from being subdominant at high Prandtl numbers to being dominant at low Prandtl numbers.

4.3.4 STABILITY OF THE NONLINEAR STATES

The stability of states on the primary branch is controlled by two eigenmodes: an amplitude mode that preserves the S_Δ symmetry of the system and a drift mode that breaks the S_Δ symmetry. The translation mode (also known as the Goldstone mode) that is associated with vertical translations due to the periodic boundary conditions, remains marginal along the branch and none of the other eigenmodes become destabilising over the range of parameters considered.

Close to the onset of convection, the amplitude mode is initially destabilising when the bifurcation is subcritical ($Pr > Pr_c$), whereas it is stabilising when the bifurcation is

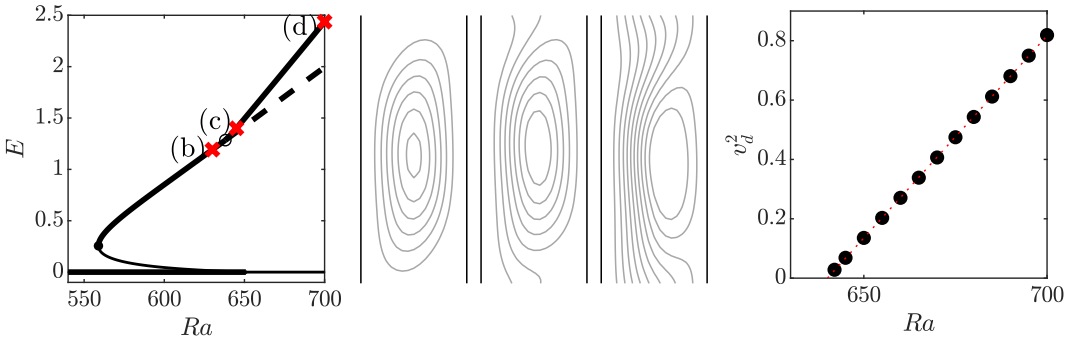

Figure 4.18: Drift bifurcation and downward-travelling waves for $Pr = 0.1$, $Le = 11$, for which $Ra_d \approx 638$. (a) Bifurcation diagram showing the kinetic energy E as a function of the Rayleigh number Ra for steady states and travelling waves. Thick lines indicate stable solutions, thin lines indicate solutions unstable to amplitude perturbations and dashed thick lines indicate solutions unstable to drift. The drift bifurcation is shown by the open circle. (b) Stable convection state at $Ra = 630$ shown by contours of its streamfunction with intervals 0.1 (first red cross on panel (a)). Further panels show similar representations of stable travelling waves at: (c) $Ra = 645$ and (d) $Ra = 700$. (e) Squared drift speed along the stable branch as a function of the Rayleigh number. The dotted line shows the fitting law: $v_d \approx 0.12\sqrt{Ra - 640}$.

supercritical ($Pr < Pr_c$). This mode subsequently changes stability at successive saddle nodes. In particular, it becomes stabilising at saddle nodes SN_1 and SN_3, where the branch turns towards higher Ra, but becomes destabilising at SN_2, where the branch turns towards lower Ra. As a result, the upper branches of steady convection states are always stable to amplitude perturbations for all Le and Pr.

The drift mode is stabilising near the primary bifurcation at $Ra = Ra_c$ for all Pr, but becomes destabilising at a drift-pitchfork bifurcation further along the branch at $Ra = Ra_d$, whose location depends upon both Le and Pr, as can be seen in figure 4.13. The marginal mode is identical to the translation mode at this bifurcation and its destabilisation leads to a pair of branches of travelling wave solutions, as shown in figure 4.18(a) for $Pr = 0.1$ and $Le = 11$. Close to their onset, these states take the form of a single large-amplitude convection roll (see figure 4.18(c)) that slowly drifts either upwards or downwards. As these branches are followed beyond the drift bifurcation, an asymmetric streaming flow strengthens while the convection roll weakens and moves towards the wall where the

streaming flow is the weakest. This transition is shown from figure 4.18(b) at $Ra = 630$ to figure 4.18(d) at $Ra = 700$. At the same time, the drift speed increases at a rate approximately proportional to $\sqrt{Ra - Ra_d}$, as shown in figure 4.18(e). This result extends the findings obtained for $Le = 1.2$, $Pr = 1$ by Xin et al. [191] to a wider range of parameter values.

The stability of the travelling waves is determined by the location of the drift bifurcation: these states are initially stable when the bifurcation occurs on the upper branch of steady convection states, whereas they are unstable when the bifurcation occurs along the lower branch. Both cases can be achieved for a given Le when Pr is varied, as figure 4.13 illustrates for selected values of the Prandtl number with $Le = 11$ and $Le = 20$. For large values of the Prandtl number, the drift bifurcation occurs on the upper branch at large Rayleigh numbers. This location moves closer to the saddle node with decreasing Prandtl numbers so that the two coincide at $Pr = Pr^*$ and $Ra = Ra^*$. For $Le = 11$, we found that $Pr^* \approx 0.042$ and $Ra^* \approx 614.9$ (see figure 4.13(c) for a bifurcation diagram at similar values of the parameters). For smaller values of the Prandtl number, the drift bifurcation occurs along the lower branch of convection states and at a value of the Rayleigh number that increases as Pr is decreased. For all the parameter values tested, this bifurcation was found to occur at larger amplitude than saddle node SN_2 and, consequently, the small-amplitude steady convection states remain stable to drift.

4.3.5 DYNAMICAL ATTRACTORS

The temporal dynamics of the system change as the drift-pitchfork bifurcation passes below the subcritical saddle node since the travelling wave states and the steady convection states on the upper branch are destabilised in the process. While many initial conditions will consequently decay towards the conduction state at low Pr and Ra, this decay is not possible when the conduction state is unstable for $Ra > Ra_c$ and we instead find that the dynamics converge on time-dependent states. To gain insight into the origin of these time-dependent states, we first consider the unfolding of a saddle node-pitchfork bifurcation, which we expect to represent the dynamics of the full system in

the vicinity of the codimension-two point (Ra^*, Pr^*) where the drift and saddle-node bifurcations coincide. This unfolding is a two-dimensional system of ordinary differential equations for x, which represents the drift speed of the state, and z, which represents the amplitude of the convection states, and involves the two unfolding parameters μ_1 and μ_2, which respectively represent the deviations $Pr - Pr^*$ and $Ra - Ra^*$ from the codimension-two point. The governing equations for the variables x and z are deduced by comparing the aforementioned results for the doubly diffusive system with those from the possible unfoldings of the saddle node-pitchfork bifurcation detailed by Guckenheimer and Holmes [73] and are found to be

$$\dot{x} = -\mu_1 x + b_1 xz, \tag{4.95}$$

$$\dot{z} = \mu_2 - x^2 - z^2 + b_2 z^3, \tag{4.96}$$

where $b_1 > 0$ and $b_2 < 0$.

To validate the use of the unfolding (4.95, 4.96), particularly with regards to the signs of b_1 and b_2, we proceed by following the analysis of Guckenheimer and Holmes [73] to chart regions of (μ_1, μ_2) parameter space around this codimension-two point. The normal form (4.95, 4.96) admits four fixed points in the vicinity of the bifurcation, which are approximated as

$$(x, z) \approx \begin{cases} X_1^{\pm} = \left(0, \pm\sqrt{\mu_2}\right) & \text{for} \quad \mu_2 \geqslant 0, \\ X_2^{\pm} = \left(\pm\sqrt{\mu_2 - \left(\dfrac{\mu_1}{b_1}\right)^2}, \dfrac{\mu_1}{b_1}\right) & \text{for} \quad \mu_2 \geqslant \left(\dfrac{\mu_1}{b_1}\right)^2. \end{cases} \tag{4.97}$$

The first of these pairs relate to the steady convection states in the doubly diffusive system, while the second pair relate to the travelling wave states. We further see that $X_2^{\pm}$ bifurcate from X_1^{+} when $\mu_1 = b_1\sqrt{\mu_2}$ and X_1^{-} when $\mu_1 = -b_1\sqrt{\mu_2}$.

The stability of the fixed points are then obtained by evaluating the eigenvalues of the

	$\mu_1 < -b_1\sqrt{\mu_2}$	$-b_1\sqrt{\mu_2} < \mu_1 < 0$	$0 < \mu_1 < b_1\sqrt{\mu_2}$	$b_1\sqrt{\mu_2} < \mu_1$
X_1^+	$(+,-)$	$(+,-)$	$(+,-)$	$(-,-)$
X_1^-	$(+,+)$	$(-,+)$	$(-,+)$	$(-,+)$
$X_2^\pm$	—	$(+,+)$	$(-,-)$	—

Table 4.4: Stability of fixed points $X_1^\pm$ and $X_2^\pm$ in four regions of (μ_1, μ_2) parameter space with $\mu_2 > 0$. Stability (instability) of the fixed point in the (x, z) directions are indicated using $-$ $(+)$ symbols. Stability entries are not defined for $X_2^\pm$ and $\mu_2 < \mu_1^2/b_1^2$, when these states do not exist.

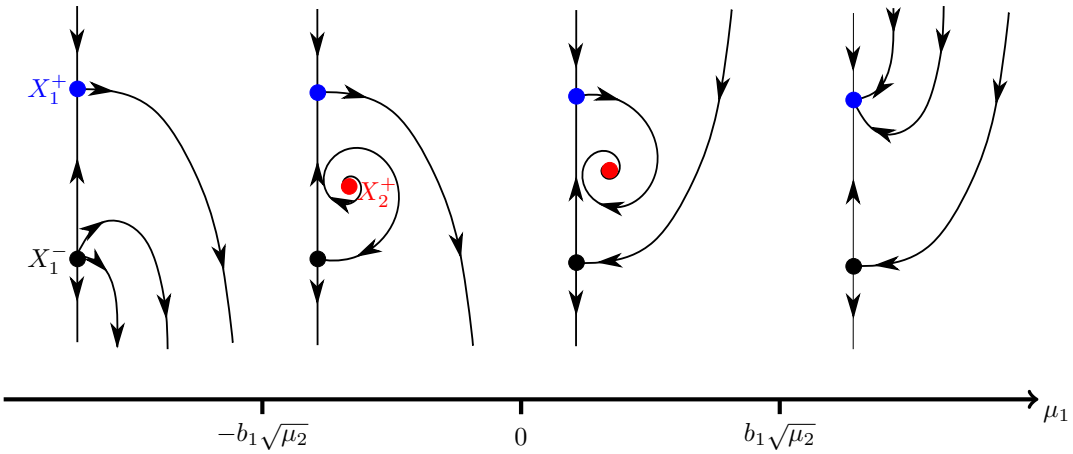

Figure 4.19: Sketches of trajectories in four stability regimes of the normal form for the saddle node-pitchfork bifurcation (4.95,4.96) in (x, z) parameter space with $x > 0$. In each of these sketches, the fixed points on the vertical line (blue and black dots) represent steady convection states $X_1^\pm$, while the fixed point away from the vertical line (red dot) represents the travelling wave state X_2^+.

Jacobian:

$$J(x,z) = \begin{pmatrix} -\mu_1 + b_1 z & b_1 x \\ -2x & -2z + 3b_2 z^2 \end{pmatrix} \tag{4.98}$$

at each point. This leads to the four stability regimes when $\mu_2 > 0$, which are indicated in table 4.4. The corresponding temporal dynamics are depicted visually in figure 4.19 and we can see that these results are analogous to the stability of the steady convection states and travelling waves found in the previous subsection.

This stability analysis further shows that $X_2^\pm$ changes stability and undergoes a Hopf bifurcation when $\mu_1 = 0$, which implies the existence of a limit cycle. However, it pro-

vides neither the stability of the resulting periodic orbit, nor the region of parameter space in which it may be found. To obtain these details, we determine when a heteroclinic connection with $x > 0$ between the two fixed points $X_1^{\pm}$ is possible, since this is the limiting case for the existence of these periodic orbits. This is achieved by first rescaling the variables in (4.95) and (4.96) via

$$t' = \epsilon t, \quad x' = \epsilon^{-1} x, \quad z' = \epsilon^{-1} z, \quad \mu_1' = \epsilon^{-2}\mu_1, \quad \mu_2' = \epsilon^{-2}\mu_2, \tag{4.99}$$

in order to make the leading order system integrable. After dropping the introduced primed notation, the original ODEs (4.95) and (4.96) become

$$\dot{x} = b_1 xz - \epsilon\mu_1 x, \tag{4.100}$$

$$\dot{z} = \mu_2 - x^2 - z^2 + \epsilon b_2 z^3. \tag{4.101}$$

The leading order system with $\epsilon = 0$ is

$$\dot{x} = b_1 xz, \tag{4.102}$$

$$\dot{z} = \mu_2 - x^2 - z^2, \tag{4.103}$$

which admits the first integral:

$$H(x,z) = \frac{b_1}{2} x^{\frac{2}{b_1}} \left(\mu_2 - z^2 - \frac{x^2}{1+b_1} \right). \tag{4.104}$$

where H satisfies

$$\frac{dH}{dt} = \frac{\partial H}{\partial x}\dot{x} + \frac{\partial H}{\partial z}\dot{z} = 0. \tag{4.105}$$

Thus, trajectories in the leading order system correspond to the integral curves $H(x,z) = c$, where c is a constant, that are shown in figure 4.20. Of particular interest is the curve $H = 0$ (shown in bold) that is comprised of the vertical axis $x = 0$ and the curve $x = \pm\sqrt{(1+b_1)(\mu_2 - z^2)}$, which connects the two fixed points $(x,z) = (0, \pm\sqrt{\mu_2})$.

The heteroclinic connection between the two fixed points in general breaks once the

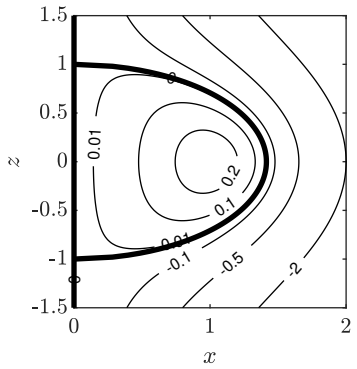

Figure 4.20: Integral curves for the leading order solution of the rescaled normal form (4.100, 4.101) with parameter values $\mu_2 = 1$ and $b_1 = 1$. The contours of H are labelled and curves with $H = 0$ are shown in bold. Only the right half-plane $x \geqslant 0$ is shown, owing to the symmetry $x \mapsto -x$ of the system.

higher order terms in ϵ of (4.100, 4.101) are considered. Consequently, we aim to derive a condition on μ_1 and μ_2 such that this heteroclinic connection persists. Including the $\mathcal{O}(\epsilon)$ terms in the full system, the function (4.104) is no longer a first integral, but instead evolves according to

$$\frac{dH}{dt} = \epsilon x^{\frac{2}{b_1}} \left(-\mu_1(\mu_2 - z^2 - x^2) - b_1 b_2 z^4 \right). \tag{4.106}$$

If we suppose that a heteroclinic connection H_0 exists between $(0, \sqrt{\mu_2})$ and $(0, -\sqrt{\mu_2})$, then (4.106) may be integrated along this curve to find

$$\begin{aligned} \int_{H_0} \frac{dH}{dt}\, dt &= \epsilon \int_{H_0} x^{\frac{2}{b_1}} \left(-\mu_1(\mu_2 - z^2 - x^2) - b_1 b_2 z^4 \right) dt \\ &= 0, \end{aligned} \tag{4.107}$$

since $H = 0$ at both fixed points. This integral may be transformed into one over space using $dt = dz/\dot{z}$ and the leading order approximation of x along H_0: $x \approx \sqrt{(1 + b_1)(\mu_2 - z^2)}$. With these substitutions, (4.107) is approximately equivalent

to

$$\begin{aligned} 0 &= \epsilon \int_{\sqrt{\mu_2}}^{-\sqrt{\mu_2}} \left((1+b_1)(\mu_2 - z^2)\right)^{1/b_1} \left(-\mu_1 + \frac{b_2 z^4}{\mu_2 - z^2}\right) dz + \mathcal{O}(\epsilon^2) \\ &= \epsilon(1+b_1)^{1/b_1} \mu_2^{1/b_1+1/2} \int_{-1}^{1} \left((1-\xi^2)^{1/b_1}\mu_1 - b_2\mu_2\xi^4(1-\xi^2)^{1/b_1-1}\right) d\xi + \mathcal{O}(\epsilon^2), \end{aligned} \tag{4.108}$$

which may be rearranged to find the relation:

$$\mu_1 \approx b_2\mu_2 \frac{\int_{-1}^{1} \xi^4(1-\xi^2)^{1/b_1-1}\, d\xi}{\int_{-1}^{1}(1-\xi^2)^{1/b_1}\, d\xi}, \tag{4.109}$$

which controls whether such a heteroclinic connection exists. Thus, when $b_2 < 0$, limit cycles arise for μ_1 within the interval

$$b_2\mu_2 \frac{\int_{-1}^{1} \xi^4(1-\xi^2)^{1/b_1-1}\, d\xi}{\int_{-1}^{1}(1-\xi^2)^{1/b_1}\, d\xi} < \mu_1 < 0. \tag{4.110}$$

Since $X_2^{\pm}$ are unstable for these parameter values (see table 4.4), the Hopf bifurcation at $\mu_1 = 0$ is supercritical and the limit cycles are stable.

The above analysis of the unfolding of (4.95, 4.96) in the vicinity of the codimension-two point is summarised in figure 4.21(a), using five observable phase portraits. Relating the unfolding back to the system of natural doubly diffusive convection, the stable limit cycles found in region III correspond to relative periodic orbits consisting of drifting states that originate either from a travelling wave undergoing a Hopf bifurcation or from a global bifurcation where two steady convection states connect heteroclinically.

Although the normal form (4.95, 4.96) only formally represents the dynamics of the full system close to the codimension-two point, each of the regions shown in figure 4.21 continues to be observed an appreciable distance away from this point. Figures 4.21(b) and (c) illustrate the extent of the corresponding regions in the doubly diffusive system when $Le = 11$ and we anticipate that similar results will hold for other values of the Lewis number. In this figure, the regions have been subdivided according to the

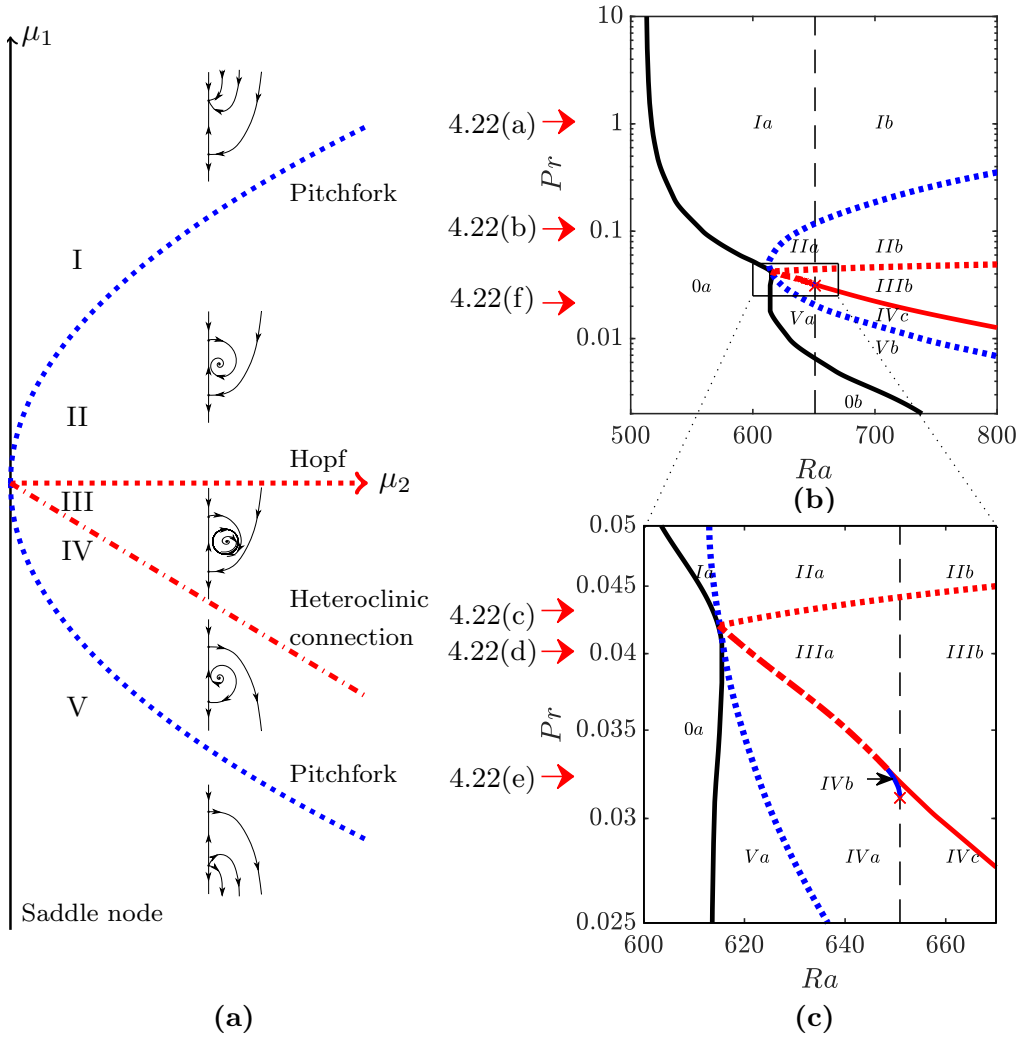

Figure 4.21: (a) Unfolding near the codimension-two saddle node-pitchfork bifurcation at $\mu_1 = \mu_2 = 0$ given by system (4.95, 4.96), after [73]. The different phase portraits are classified in five different regions labelled using Roman numerals and accompanied with a sketch of the corresponding phase space. In each of these sketches, the fixed points on the vertical line represent steady convection states. The vertical (resp. horizontal) direction is the eigendirection related to the amplitude (resp. drift) mode. (b) Analogy with the doubly diffusive convection problem is made by replacing μ_1 by $Pr - Pr^*$ and μ_2 by $Ra - Ra^*$ and regions of the (Ra, Pr) parameter space are shown as a function of the observed temporal behaviour for $Le = 11$. Arrows indicate the values of Pr used to produce the bifurcation diagrams in figure 4.22. (c) Magnification of panel (b) near (Ra^*, Pr^*). The bifurcations are represented by the vertical dashed lines (primary stationary bifurcation of the conduction state), black, blue and red solid lines (saddle nodes), blue dotted lines (drift bifurcation), red dotted lines (Hopf bifurcation) and red dot-dashed lines (heteroclinic connection).

State	Stable in region?												
	Oa	Ob	Ia	Ib	IIa	IIb	IIIa	IIIb	IVa	IVb	IVc	Va	Vb
O	x	—	x	—	x	—	x	—	x	x	—	x	—
SOC_s	—	x	—	—	—	—	—	—	—	x	x	—	x
SOC_l	—	—	x	x	—	—	—	—	—	—	—	—	—
TW	—	—	—	—	x	x	—	—	—	—	—	—	—
PO	—	—	—	—	—	—	x	x	—	—	—	—	—

Table 4.5: Stability of the states found in the system of natural doubly diffusive convection within each region of the parameter space from figure 4.21. The naming convention used is as follows: O, conduction state; SOC_s, small-amplitude stationary overturning convection; SOC_l, large-amplitude stationary overturning convection; TW, travelling wave; and PO, relative periodic orbit. The regions Oa, ..., Vb refer to the regions introduced in figure 4.21.

types of stable attracting states that they display. The subdivisions occur owing to the instability of the conduction state at Ra_c and the creation of a pair of saddle nodes at (Ra_{cusp}, Pr_{cusp}), which enrich the previous unfolding. The resulting subregions, together with their associated attracting states, are summarised in table 4.5 and on the bifurcation diagrams in figure 4.22. As Pr varies, the system admits one of seven qualitatively distinct bifurcation diagrams. Six of these are presented in figure 4.22, which also indicate the range of kinetic energies achieved over each relative periodic orbit, which we obtained via time-stepping. The seventh type of bifurcation diagram, where the primary branch lies entirely within the supercritical regime, is not shown but possesses similar features to that seen for $Pr = 0.02$ in figure 4.22(f), including stable small-amplitude steady convection states and relative periodic orbits.

The three most relevant stable attracting states close to the primary bifurcation at high Pr ($Pr > Pr^*$ here) are: the conduction state (O), the large-amplitude steady convection states (SOC_l) and the travelling wave states (TW). Below the onset of convection (region Oa), all initial conditions decay towards the first of these. In region Ia, above subcritical onset but before the drift instability, initial conditions converge towards SOC_l, as evidenced by the energy-time and drift speed-time plot in figure 4.23(a). Increasing Ra beyond the drift instability into region IIa, SOC_l is now unstable and the flow converges towards TW. Figure 4.23(b) shows that the former state may still be observed in the

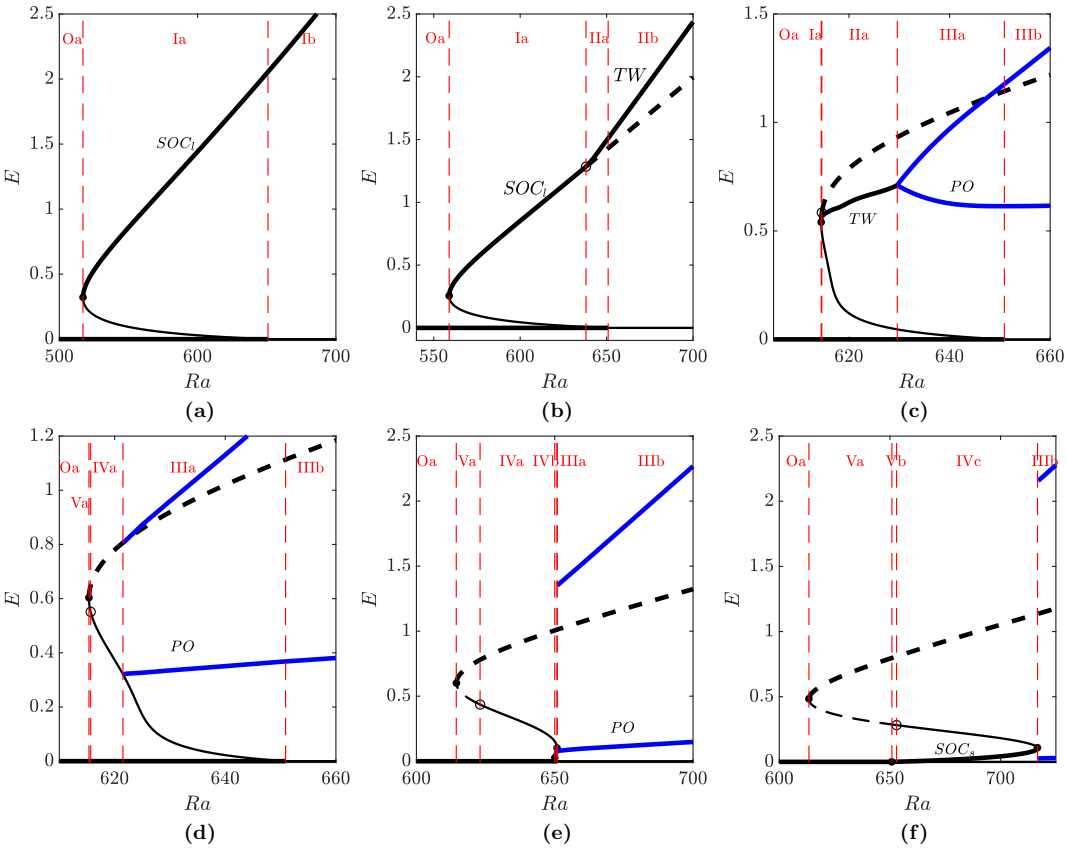

Figure 4.22: Bifurcation diagrams showing the primary branch and other stable attracting states for $Le = 11$, and (a) $Pr = 1$, (b) $Pr = 0.1$, (c) $Pr = 0.043$, (d) $Pr = 0.04$, (e) $Pr = 0.032$ and (f) $Pr = 0.02$. The solid circles mark the saddle nodes and open circles indicate where the drift bifurcation occurs. Thick (thin) lines represent states stable (unstable) to the amplitude mode, whilst solid (dashed) lines show those stable (unstable) to the drift mode. Thick blue lines indicate the minimal and maximal energies achieved in the stable limit cycle, which starts in a Hopf bifurcation in (c) and in a heteroclinic bifurcation in (d,e,f). The unstable branches of travelling waves are not shown.

temporal dynamics, however, as the initial condition first rapidly changes amplitude to approach SOC_l before it builds vertical drift and converges to TW.

The stable branch of travelling waves destabilises in a supercritical Hopf bifurcation that leads to a stable relative periodic orbit, as shown in figure 4.22 for $Pr = 0.043$. Figures 4.24(a)–(e) depict such an orbit shortly after the bifurcation at $Ra = 650$ and $Pr = 0.043$, where we see that the states exhibit small oscillations about a drifting state. The Hopf bifurcation moves towards lower Rayleigh numbers as Pr approaches Pr^* from above, which reduces the extent over which stable TW are found. This continues until $Pr = Pr^*$, when stable TW cease to exist and the relative periodic orbit bifurcates directly from codimension-two bifurcation at the saddle node.

Upon further decrease of the Prandtl number, so that the drift bifurcation occurs on the lower branch of steady convection, the system admits neither stable SOC_l nor stable TW. Instead, the bifurcation diagrams are similar to that shown for $Pr = 0.04$ in figure 4.22(d), where a branch of unstable TW extends from the drift bifurcation towards higher Rayleigh numbers and stable relative periodic orbits exist after a global bifurcation, where the stable manifold of SOC_l connects heteroclinically with the unstable manifold of the convection state on the lower branch and vice versa.

The lack of stability of the nonlinear states before the heteroclinic connection lead all initial conditions to decay down to the conduction state in regions IVa and Va. Figures 4.23(d) and (f) illustrate this tendency for $Pr = 0.032$ when $Ra = 630$ and $Ra = 620$, respectively. In both cases, the amplitude of the initially imposed roll rapidly decreases to approach that of SOC_l rolls. Afterwards, the drift speed of the state increases, as SOC_l is unstable to drift, and reaches a maximum around $t \approx 50$. The drift speed subsequently decays down to zero, due to the instability of TW, and the time-dependent state converges on the conduction state, which is the only stable attractor in these regions.

Beyond the heteroclinic connection, initial conditions tend to converge towards the relative periodic orbit, as they invariably do in region IIIb, where the conduction state is unstable. Figure 4.23(c) illustrates this convergence starting from a large-amplitude roll

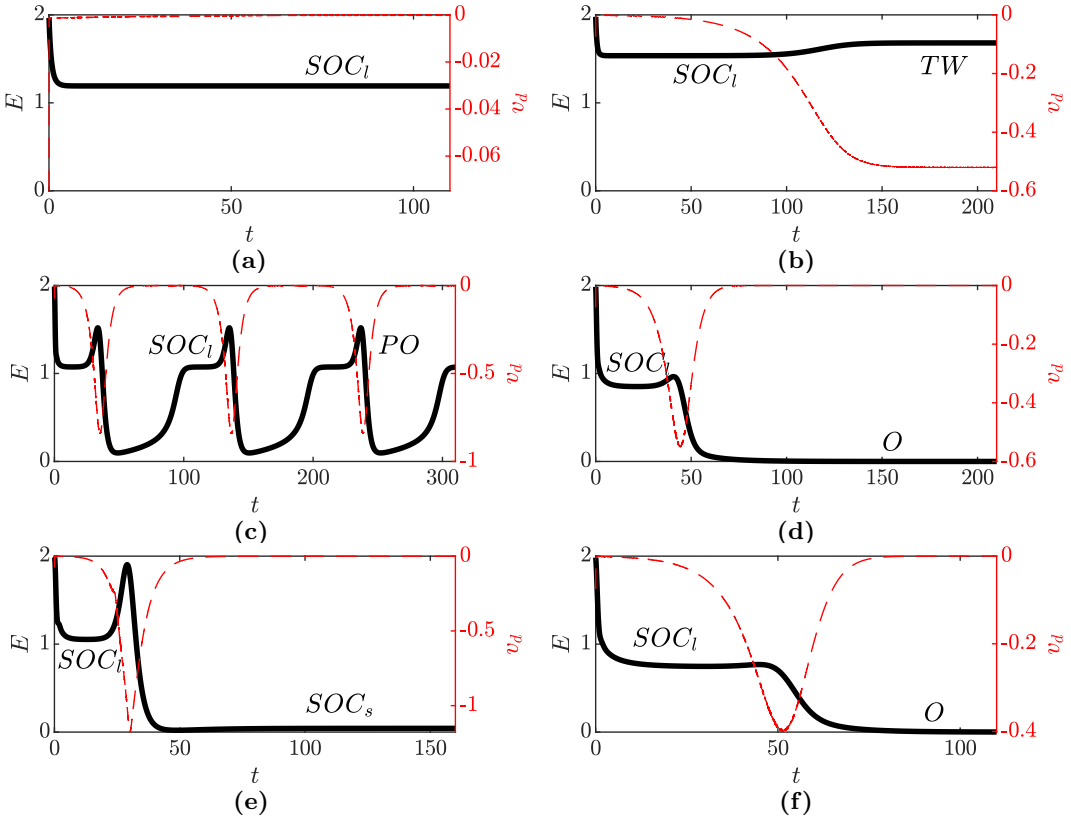

Figure 4.23: Energy-time (black) and drift speed-time (red) plots illustrating regions I–V in figure 4.21 with $Le = 11$. In each case, the initial state was the large-amplitude convection state at $Ra = 700$ for $Pr = 0.1$ that was perturbed in the direction of its unstable drift eigenmode. States approached during the trajectory are labelled as follows: (a) region Ia, convergence to SOC_l when $Pr = 0.1$ and $Ra = 630$; (b) region IIb, convergence to TW when $Pr = 0.1$ and $Ra = 660$; (c) region IIIb, convergence to PO when $Pr = 0.032$ and $Ra = 660$, (d) region IVa, convergence to O when $Pr = 0.032$ and $Ra = 630$; (e) region IVc, convergence to SOC_s when $Pr = 0.02$ and $Ra = 700$; and (f) region Va, convergence to O when $Pr = 0.032$ and $Ra = 620$.

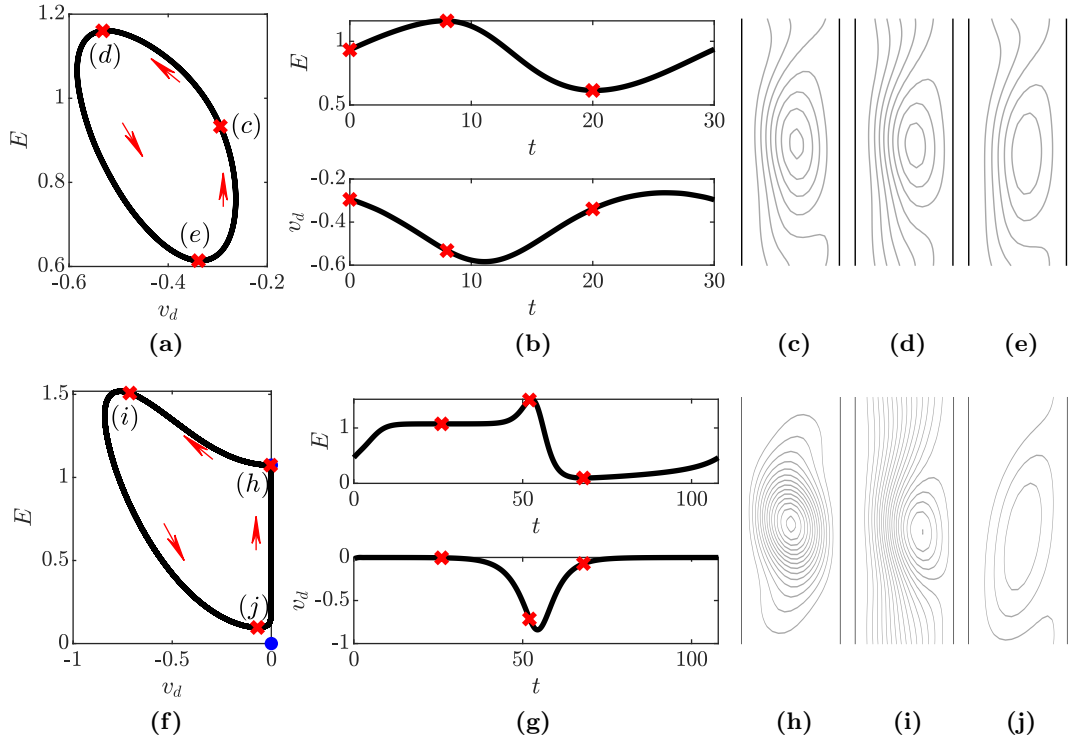

Figure 4.24: Temporal evolution of downward-travelling states across one cycle of two relative periodic orbits at: (a)–(e) $Ra = 650$ with $Pr = 0.043$ and $Le = 11$ and (f)–(j) $Ra = 660$ with $Pr = 0.032$ and $Le = 11$ (as in figure 4.23(c)). (a) and (f) Anticlockwise trajectory of the periodic orbit in drift speed-energy phase space. Blue dots in (f) mark the conduction and steady convection states. (b) and (g) Energy-time (top) and drift speed-time (bottom) plots. (c)–(e) Streamfunctions of states along the orbit in (a) at (d) $t = 0$, (d) $t = 8$ and (e) $t = 20$ with contour intervals 0.1. (h)–(j) Streamfunctions of states along the orbit in (f) at (h) $t = 26$, (i) $t = 52$ and (j) $t = 68$, with contour intervals 0.05. The streamfunctions have been translated vertically for better visual representation.

with $Pr = 0.032$ and $Ra = 660$ perturbed in the direction of its unstable drift eigenmode. A single cycle of this orbit is shown in further detail in figures 4.24(f)–(j). This relative periodic orbit cycles between the three states: SOC_l, TW and a steady small-amplitude convection state, in the following manner. The first stage of the orbit, from $15 \lesssim t \lesssim 40$, resembles the temporal behaviour seen in region IIa (figure 4.23(b)), where the solution remains close to SOC_l in profile (figure 4.24(c)) while the drift speed slowly increases in magnitude. Following this, between $t \approx 40$ and $t \approx 54$, the drift speed and kinetic energy rapidly increase as the profile of the state exhibits properties of the travelling wave

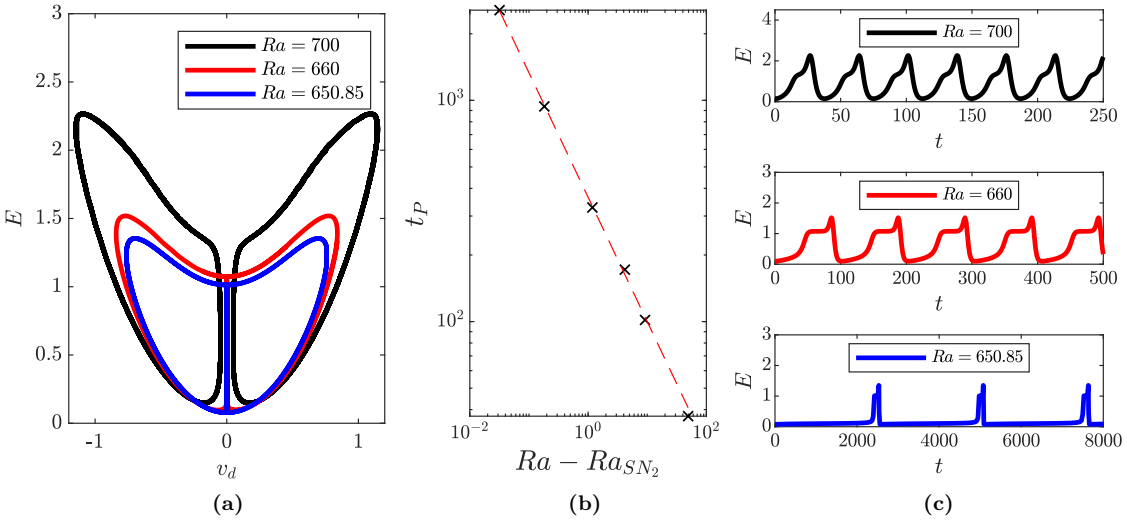

Figure 4.25: Relative periodic orbits for $Le = 11$, $Pr = 0.032$ where $Ra_{SN_2} \approx 650.82$ (a) Trajectories in (v_d, E) phase space for $Ra = 650.85$ (blue), $Ra = 660$ (red) and $Ra = 700$ (black). For $Ra = 700$ and $Ra = 660$, a pair of relative periodic orbits associated with either negative or positive drift velocity are shown, while for $Ra = 650.85$, a single periodic orbit with alternating negative and positive drift velocities is shown. (b) Period t_P of orbits for selected $Ra > Ra_{SN_2}$. The red dashed line shows that approximately $t_P \propto (Ra - Ra_{SN_2})^{0.56}$. (c) Energy-time plots for $Ra = 700$ (top), $Ra = 660$ (middle) and $Ra = 650.85$ (bottom).

(TW) solution (figure 4.24(d)). Between $t \approx 54$ and $t \approx 68$, both the drift speed and kinetic energy decrease as the state approaches a small-amplitude, non-drifting convection state with inclined rolls (figure 4.24(e)). The final stage of this orbit is the transition from the small-amplitude back to large-amplitude steady convection, which is indicated by the monotonic increase in kinetic energy while maintaining $v_d \approx 0$ for $t \gtrsim 70$ and $t \lesssim 15$ in figure 4.24(b).

The heteroclinic connection leading to these orbits moves towards higher Rayleigh numbers as Pr decreases and coincides with SN_2 for $Pr \lesssim 0.032$ (see figures 4.22(e) and (f)). This suggests that a saddle node infinite period (SNIPER) bifurcation explains the origin of the relative periodic orbits at low Prandtl and high Rayleigh numbers. However, by considering various properties of the relative periodic orbits for $Pr = 0.032$ and $Le = 11$ as Ra approaches Ra_{SN_2} from above (figure 4.25), we additionally find that a gluing bifurcation occurs in the vicinity of the SNIPER bifurcation.

At large Rayleigh numbers, a pair of relative periodic orbits with states drifting either upwards or downwards are related by the reflection symmetry. The maximal energy and drift speed attained along these orbits decrease with decreasing Rayleigh number and the trajectories approach the stable and unstable manifolds of SOC_l, as seen in figure 4.25(a). This leads to the two relative periodic orbits connecting in a gluing bifurcation around $Ra \approx 652$ so that the trajectories become a single periodic orbit where states alternately drift in opposite directions. This is reminiscent of the pulsating waves seen in nonlinear magnetoconvection [125].

The resulting single periodic orbit persists until Ra_{SN_2}, where it terminates in the SNIPER bifurcation. This is evidenced by the period of a single loop of the orbit scaling like $t_P \propto (Ra - Ra_{SN_2})^{-0.56}$ as SN_2 is approached, which is close to the expected $t_P \approx |Ra - Ra_{SN_2}|^{-0.5}$ scaling. The energy-time plots in figure 4.25(c) illustrate that the predominant increase in duration occurs near the small-amplitude steady convection state as the orbit approaches the steady state at SN_2 in phase space. We also find that the time spent near SOC_l increases, whilst the time where the state has large drift speed remains small, implying that the global bifurcation is due to the collision of the periodic orbit with the stable manifold of SOC_l.

The final attracting state that the flow may converge to is SOC_s, as figure 4.23(e) illustrates for $Pr = 0.02$ and $Ra = 700$. This is possible for $Pr < Pr_{cusp}$ in the supercritical regions Ob, IVc and Vb, where it is the only stable attracting state, and in the subcritical region IVb, where convergence towards the stable conduction state is also possible.

4.4 DISCUSSION

This chapter deals with natural doubly diffusive convection driven by horizontal gradients of temperature and concentration. We have extended the linear stability analysis of Ghorayeb and Mojtabi [70] by performing a thorough weakly nonlinear analysis of the system. This was complemented by a numerical exploration of the nonlinear regime, thereby also extending the analysis of Xin et al. [191], who focussed on $Pr = 1$ and

$Le = 1.2$. From this analysis, we unravelled the relationships between saddle nodes, drift and global bifurcations.

We have identified regions where the resulting primary branch exhibits qualitatively different behaviour. For large values of the Prandtl number, the bifurcation is subcritical and hysteresis takes place between the conduction state and large-amplitude convection. Whereas, for Prandtl numbers below a critical value, the primary bifurcation is supercritical but this is preceded by the creation of two saddle nodes without affecting the existence of large-amplitude convection. Despite this, we did not find any hysteresis in the supercritical regime owing to the presence of a destabilising drift bifurcation along the primary branch.

By determining the stability of steady convection states along the primary branch, we identified a codimension-two point between a large-amplitude saddle node and a drift bifurcation. We analysed the dynamics around this codimension-two point using its normal form and numerical simulations by investigating new Hopf and heteroclinic bifurcations that give rise to periodic orbits. Such time-dependent states are common features of low Prandtl number doubly diffusive convection (see also Umbría and Net [182]). Finally, we provided a classification of the various regions in (Ra, Pr) parameter space according to the nature of their dynamical attractors for a representative value of the Lewis number.

Lastly, the coexistence of steady overturning convection with the stable conduction state when the primary bifurcation is supercritical has important dynamical implications. In particular, it makes this system a candidate for spatially localised pattern formation in a supercritical fluid system, owing to the similarity of the primary branch structure with the Swift–Hohenberg equation considered by Knobloch et al. [100]. Exploration of this phenomena forms the subject of the following chapter.

5 | TOWARDS SUPERCRITICAL CONVECTONS

In the previous chapter, we performed a weakly nonlinear analysis of the natural doubly diffusive system to identify the criticality of the primary bifurcation of the conduction state and used numerical continuation to determine the nonlinear behaviour of the bifurcating primary branch in small-aspect-ratio domains. We now wish to extend the results to large-aspect-ratio domains, where spatially localised states, known as convectons, have previously been found for the specific parameter values $Pr = 1$ and $Le = 11$ [12, 23, 24]. In this specific case, the primary bifurcation is subcritical and there is bistability between the stable conduction state and states of spatially periodic convection, which results in convectons being found on a pair of branches that undergo homoclinic snaking, as was also found in the quadratic-cubic Swift–Hohenberg equation [37]. The question that we wish to consider in this chapter is: what happens to this snaking as the Prandtl number decreases and the primary bifurcation changes from being subcritical to supercritical, whilst maintaining coexistence between different steady states? This is of interest since our current knowledge of localised states when the primary bifurcation is supercritical is limited to model systems, including the variational cubic-quintic-septic Swift–Hohenberg equation [100], and to systems that additionally exhibit large-scale modes, such as rotating convection [11] or magnetoconvection [54].

This chapter is organised as follows. In section 5.1, we detail the vertically extended system under consideration. In section 5.2, we perform a linear stability analysis of the spatially periodic states found via the weakly nonlinear theory in the previous chapter, which allows us to identify secondary bifurcations of the primary branch, from which branches of convectons bifurcate. In section 5.3, we detail the transition from typical

snaking in the subcritical regime to the, previously unknown, structure of convecton branches in the supercritical regime. This chapter is concluded in section 5.4 with a discussion.

5.1 MATHEMATICAL FORMULATION

In this chapter, we again consider natural doubly diffusive convection within a vertical slot with periodic boundary conditions imposed in the vertical direction. This time, however, we consider vertically extended domains so that the system can admit spatially localised states. We continue to consider the case $N = -1$, where the thermal and solutal gradients imposed by the vertical sidewalls exactly balance so that a motionless conduction state exists.

The non-dimensional governing equations remain unchanged from those described 4.1 in Chapter 4 and are repeated here for convenience. They read

$$\frac{1}{Pr}\left(\frac{\partial \mathbf{u}}{\partial t} + \mathbf{u}\cdot\nabla\mathbf{u}\right) = -\nabla p + \nabla^2\mathbf{u} + Ra\,(T-C)\,\hat{\mathbf{z}}, \tag{5.1}$$

$$\nabla\cdot\mathbf{u} = 0, \tag{5.2}$$

$$\frac{\partial T}{\partial t} + \mathbf{u}\cdot\nabla T = \nabla^2 T, \tag{5.3}$$

$$\frac{\partial C}{\partial t} + \mathbf{u}\cdot\nabla C = \frac{1}{Le}\nabla^2 C, \tag{5.4}$$

and are solved together with non-dimensional boundary conditions:

$$u = 0, \quad w = 0, \quad -\frac{\partial p}{\partial x} + \frac{\partial^2 u}{\partial x^2} = 0, \quad T = 0, \quad C = 0 \quad \text{on} \quad x = 0, \tag{5.5}$$

$$u = 0, \quad w = 0, \quad -\frac{\partial p}{\partial x} + \frac{\partial^2 u}{\partial x^2} = 0, \quad T = 1, \quad C = 1 \quad \text{on} \quad x = 1, \tag{5.6}$$

where the pressure boundary condition is the projection of the Navier–Stokes equation on the boundary and each variable is periodic in the z direction.

Numerical continuation of branches in the doubly diffusive system was carried out us-

ing a spectral element numerical method based on a Gauss–Lobatto–Legendre discretisation and supplemented by Stokes preconditioning, as detailed by [8, 22]. The domain was discretised using 24 spectral elements with 25 nodes in both the x and z directions. The results are presented using bifurcation diagrams showing the kinetic energy:

$$E = \int_0^1 \int_0^{L_z} \left(\frac{1}{2} \left(u^2 + w^2 \right) \right) dx\, dz, \tag{5.7}$$

of steady states as a function of the Rayleigh number, which is treated as the bifurcation parameter. Profiles of these steady states are depicted primarily using the streamfunction ψ, where $(u, w) = (-\psi_z, \psi_x)$. Relations between different steady states at the same parameter values are shown using a phase-space representation that depicts the vertical velocity of the states against their horizontal velocity along the vertical line $x \approx 0.746$. This value for x was chosen primarily so that the trajectories resemble those for localised states in the Swift–Hohenberg equation, as seen in figure 3.4 in Chapter 3.

5.2 FINDING SECONDARY BIFURCATIONS OF THE PRIMARY BRANCH

Previous studies of convectons in doubly diffusive convection with periodic boundary conditions and $Le = 11$, $Pr = 1$ [23, 24] found that a pair of secondary branches of convectons bifurcate from a secondary bifurcation of the subcritical primary branch. We start by deriving a general expression for the location of these small-amplitude secondary bifurcations, when they exist.

Our starting point for this analysis is the Ginzburg–Landau equation (4.80) that we derived in Chapter 4 by performing a weakly nonlinear analysis of the full nonlinear system (5.1–5.6) around the primary bifurcation of the conduction state. Introducing a small parameter $\epsilon \ll 1$ that was used to define the slow temporal scale, $T = \epsilon^2 t$, the long spatial scale, $Z = \epsilon z$, and to quantify the deviation away from the primary bifurcation at Ra_c via $Ra = Ra_c + \epsilon^2 r$, we obtained the equation:

$$A_T = a_1 r A + a_2 |A|^2 A + a_3 A_{ZZ}, \tag{5.8}$$

for the long spatial and slow temporal evolutions of the amplitude A of the linear correction to the conduction state with wavenumber k_c, where a_1, a_2 and a_3 are the real coefficients obtained in section 4.2.2.

In addition to the steady solutions of (5.8) that were previously found in Chapter 4, namely:

$$A = 0, \tag{5.9}$$

which is valid for all r and corresponds to the conduction state; and

$$A = \left(-\frac{a_1 r}{a_2}\right)^{1/2} e^{i\chi}, \tag{5.10}$$

which is valid provided that $a_1 r/a_2 < 0$ and corresponds to states of small-amplitude spatially periodic convection; in infinite domains, the Ginzburg–Landau equation further admits the solution:

$$A = \left(-\frac{2a_1 r}{a_2}\right)^{1/2} \operatorname{sech}\left(\left(\frac{-a_1 r}{a_3}\right)^{1/2} Z\right) e^{i\chi}, \tag{5.11}$$

which is valid provided that both $a_1 r/a_2 < 0$ and $a_1 r/a_3 < 0$. This solution corresponds to small-amplitude convection states with long spatial modulation. While the phase χ appears to be arbitrary in (5.11), including beyond-all-orders effects results in spatial locking between the two spatial scales z and Z and fixes the phase to either $\chi = 0$ or $\chi = \pi$ in the Swift–Hohenberg equation [46], with the same likely being true in natural doubly diffusive convection [23]. Similarly to the Swift–Hohenberg equation [37], the two types of modulated states extend towards lower r and develop into fully localised states.

In finite domains, however, the latter states do not exist and the two branches of localised states are instead found to originate from an Eckhaus instability of the primary branch [26]. By performing a linear stability analysis on the non-trivial, uniform solutions to the Ginzburg–Landau equation (5.10), we can determine when this secondary bifurcation occurs. We first move into the frame of reference of the non-trivial periodic state with

$\chi = 0$ and make a small, real perturbation b that is even in Z:

$$A(Z,T) = \left(-\frac{a_1 r}{a_2}\right)^{1/2} + b(Z,T). \tag{5.12}$$

for both simplicity and connection with the form of (5.11). In this frame of reference, the Ginzburg–Landau equation becomes

$$b_T = -2a_1 r b + 3\left(-a_1 a_2 r\right)^{1/2} b^2 + a_2 b^3 + a_3 b_{ZZ}. \tag{5.13}$$

Linearising this equation about a potential secondary bifurcation at r_0, we find that the leading-order deviation from the constant amplitude state satisfies

$$b_T = -2a_1 r_0 b + a_3 b_{ZZ} + \mathcal{O}(\epsilon^2), \tag{5.14}$$

which has solution:

$$b = \epsilon B_1 e^{\lambda T}\cos(lZ) + \mathcal{O}(\epsilon^2), \tag{5.15}$$

where B_1 is the amplitude of the perturbation and where the wavenumber l, growth rate λ and the location of a secondary bifurcation are related via

$$r_0 \approx -\frac{\lambda + l^2 a_3}{2a_1}. \tag{5.16}$$

Since l is real, the relation (5.16) at a stationary bifurcation with $\lambda = 0$ requires that $a_1 r_0/a_3 < 0$. When this condition is combined with $a_1 r_0/a_2 < 0$, which is necessary for the existence of a uniform, steady, finite-amplitude solution A, we find that such a small-amplitude secondary bifurcation can only occur when a_2 and a_3 take the same sign, as depicted in figure 5.1. Thus, since $a_3 > 0$ for all values of the Prandtl and Lewis numbers, this linear stability theory predicts that the primary branch only undergoes a small-amplitude secondary bifurcation when this branch is subcritical.

To determine the location of the first of the secondary bifurcations, we note that the periodic boundary conditions in the vertical direction discretises the possible wavenumbers

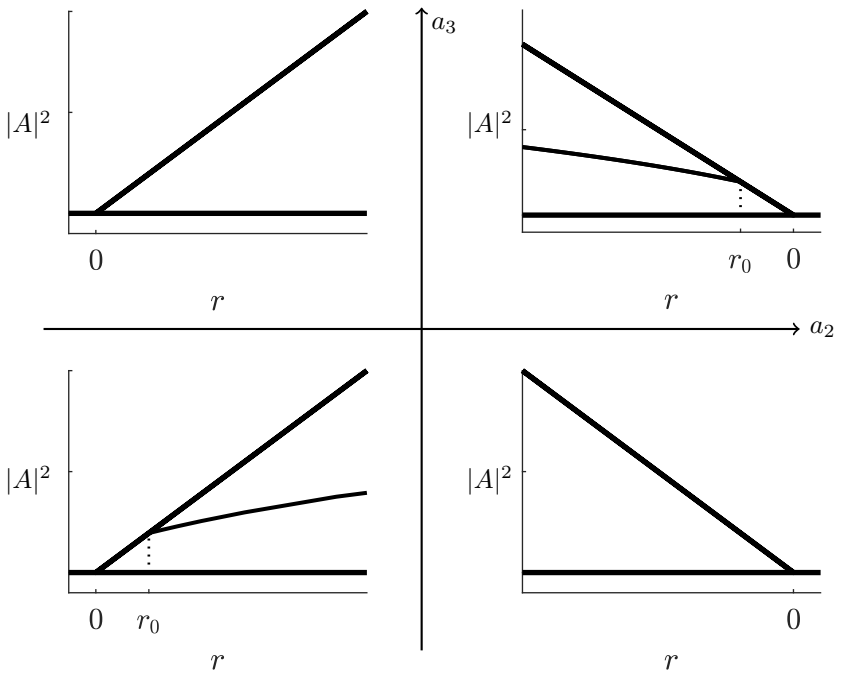

Figure 5.1: Sketches of the nature of the primary and secondary bifurcations of the Ginzburg–Landau equation (5.8) in different regimes of (a_2, a_3) parameter space when $a_1 > 0$. The secondary bifurcation occurs at $r = r_0$ and the direction of branching is obtained numerically.

to $l = 2\pi n/(\epsilon L_z)$ for $n = 1, 2, ...$, which means that the first of these secondary bifurcations occurs when $l = 2\pi/(\epsilon L_z)$. From (5.16), this wavenumber gives the expected location of the first secondary bifurcation as

$$Ra \approx Ra_c - \frac{2\pi^2}{L_z^2}\frac{a_3}{a_1}. \tag{5.17}$$

Using the parameter dependence of the coefficients a_1 and a_3 from Chapter 4, this location may be expressed more generally as

$$Ra \approx \frac{1}{|1 - Le|}\left(6509 - \frac{2\pi^2}{L_z^2}\frac{\delta}{|\gamma_1|}\right), \tag{5.18}$$

which we see is independent of the Prandtl number.

The above analysis holds for sufficiently large domains away from the codimension-two point (Ra_c, Pr_c), where the primary bifurcation changes criticality. Figure 5.2 confirms this by comparing the theoretical location of the first secondary bifurcation (5.18) with that obtained numerically for a range of domain sizes and Prandtl numbers. In the domains with $L_z = 12\lambda_c$ and $L_z = 20\lambda_c$, where $\lambda_c = 2\pi/k_c$ is the critical wavelength, the stationary bifurcations approach the theoretical limit (dotted) as the Prandtl number increases, which validates the numerical value of a_3 obtained in Chapter 4. However, decreasing the Prandtl number towards Pr_c in each domain, the stationary secondary bifurcations move away from this theoretical limit and towards lower Rayleigh numbers. This bifurcation proceeds to collide with a second stationary bifurcation and becomes an oscillatory bifurcation before moving towards the primary bifurcation as the codimension-two point is approached.

To capture the additional details in finite domains near the codimension-two point seen in figure 5.2, an alternative rescaling that leads to a higher order Ginzburg–Landau equation should be used, similarly to the analyses by Dawes [55] and Kao and Knobloch [93]. However, we have not considered such analysis here, because the focus of the subsequent results will be on the large-amplitude snaking behaviour. Nevertheless, the results obtained via numerical continuation indicate that a supercritical primary branch

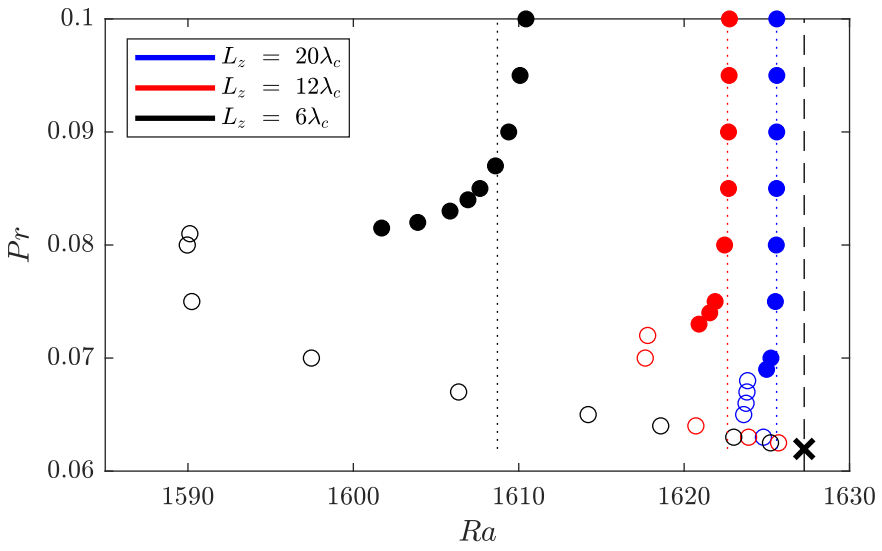

Figure 5.2: Location of the first secondary bifurcation of the primary branch for different values of the Prandtl number when $Le = 5$ in domains with $L_z = 20\lambda_c$ (blue), $L_z = 12\lambda_c$ (red) and $L_z = 6\lambda_c$ (black). Stationary (Hopf) bifurcations are depicted using filled (open) circles. The vertical dotted lines indicate the theoretical location of the secondary bifurcation (5.18) obtained via linear stability analysis. The vertical dashed line at $Ra \approx 1627.26$ denotes the location of the primary bifurcation and the black cross on this line at $Pr = Pr_c \approx 0.062$ indicates the Prandtl number for the codimension-two point, below which the primary bifurcation is supercritical.

does not undergo a small-amplitude secondary bifurcation.

5.3 TRANSITION FROM SUBCRITICAL TO SUPERCRITICAL

One of the main results that we obtained in Chapter 4 was the existence of parameter regimes where the primary bifurcation is supercritical and the stable conduction state coexists with states of spatially periodic convection. This coexistence arises as the by-product of the evolution of the primary branch as it transitions from being subcritical at high Prandtl numbers to supercritical at low Prandtl numbers and undergoes a cusp bifurcation, where two new saddle nodes emerge. One of the three saddle nodes terminates at the codimension-two point (Ra_c, Pr_c), resulting in the primary branch taking an 'S'-shape structure below the critical Prandtl number. In this regime, the primary branch initially heads towards supercritical Rayleigh numbers, turns around at a saddle node and heads back towards lower Rayleigh numbers, before turning around at a second saddle node and proceeding to large Rayleigh numbers and amplitude. This second saddle node lies in the subcritical region $Ra < Ra_c$ for certain parameter values, which provides the coexistence between the stable conduction state and states of spatially periodic convection.

Despite the primary branch not undergoing a small-amplitude secondary bifurcation in the supercritical regime, we find that supercritical systems of natural doubly diffusive can admit convectons that are supported by this coexistence. In the remainder of the chapter, we are not only interested in details of these convectons in the supercritical regime, but also in understanding their origin in relation to how the typical snaking branches that exist in the subcritical regime develop as the Prandtl number decreases and the primary bifurcation becomes supercritical.

The following numerical results consider a domain that is periodic in the vertical direction with a period $L_z \approx 12\lambda_c$, where $\lambda_c \approx 2.48$ is the wavelength of the critical eigenmode from the primary bifurcation of the conduction state for all values of the Prandtl and Lewis numbers [70, 191]. We further fix the Lewis number to be $Le = 5$,

where the primary bifurcation at $Ra_c \approx 1627.26$ changes criticality at a critical Prandtl number, $Pr_c \approx 0.062$. These parameters are chosen so that the system can admit convectons and that both the sub- and supercritical regimes are numerically accessible. This allows us to explore how the structure of the snaking branches of convectons changes as the Prandtl number varies between $Pr = 1$ and $Pr = 0.06$ and the primary bifurcation changes from being subcritical to supercritical. This transition is characterised in five stages, which are depicted using representative bifurcation diagrams in figure 5.3 and briefly summarised in the following paragraph. Some of the branches shown either in this figure or in others throughout this chapter have been manually terminated at points represented by the marked dots. While the branches continue beyond these points, they tend to exhibit complicated behaviour that is typically associated with states influenced by the finite size of the domain (e.g., domain-filling states). As our focus is on localised states that are unaffected by the period of the domain used, we have terminated these branches to improve the readability of the figures.

The first of these stages is the subcritical regime for large Prandtl numbers ($Pr \gtrsim 0.15$), subsequently referred to as Stage 1, where we find that the convectons lie on a pair of branches that undergo homoclinic snaking, similar to that found by Bergeon and Knobloch [24]. The structure of the snaking branches becomes increasingly complex during Stage 2 ($0.11 \lesssim Pr \lesssim 0.15$) as rolls in convectons change between buoyancy-driven rolls, hereafter referred to as R1, like those in Stage 1, and rolls driven by a balance between buoyancy and inertia, hereafter referred to as R2. Within Stage 3 ($0.102 \lesssim Pr \lesssim 0.11$), each snaking branch breaks up into a main branch containing convectons with R2 rolls and a collection of isolas containing convectons with R1 rolls. During Stage 4 ($Pr_c \lesssim Pr \lesssim 0.102$), the main branch further breaks up into a set of disconnected branch segments, while the set of isolas connect together to give small-amplitude snaking between primary branches. When the primary bifurcation is supercritical in Stage 5 ($Pr \lesssim Pr_c$), this small-amplitude snaking no longer exists. However, the disconnected branch segments from the previous stage persist and maintain their organised structure, which results in finding convectons containing only R2 rolls in the

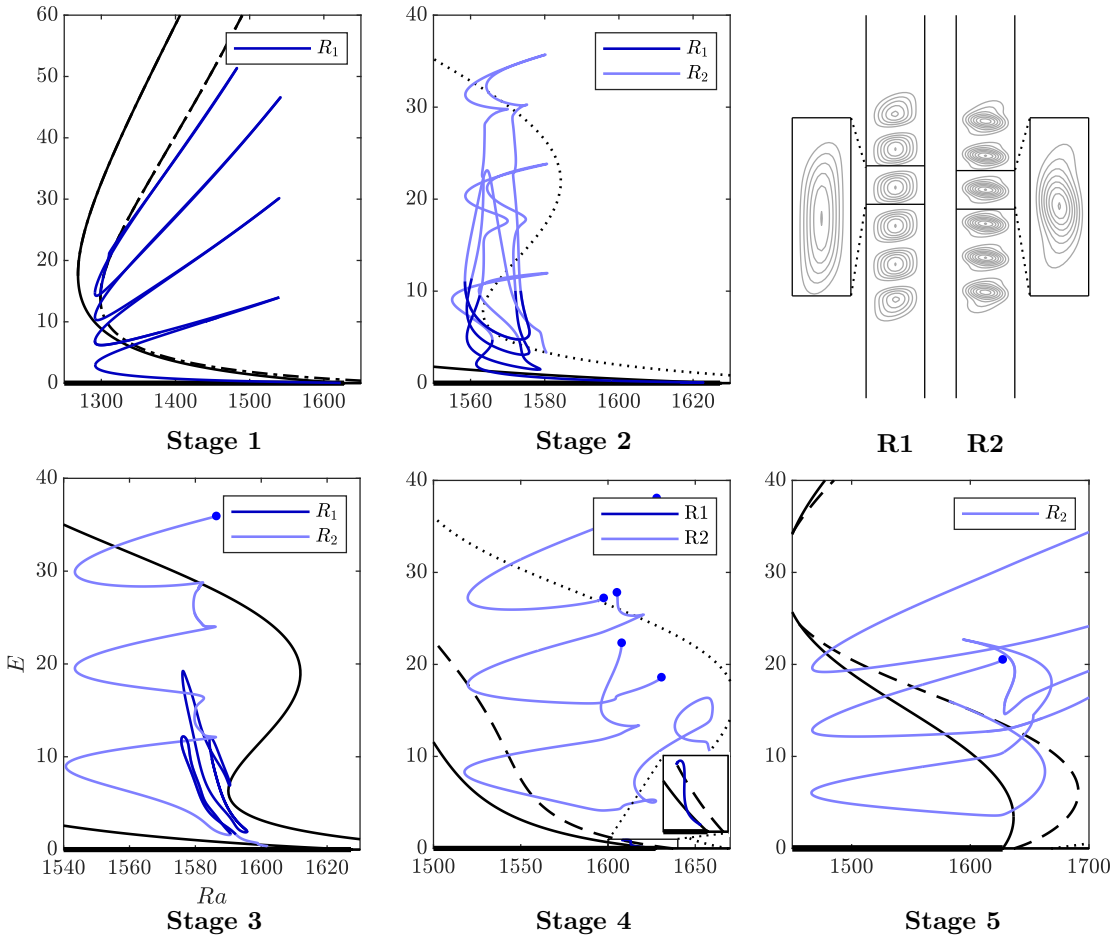

Figure 5.3: Summary of the five different stages that are seen in the transition from the primary bifurcation being subcritical to supercritical. Illustrative bifurcation diagrams for the five stages: Stage 1 ($Pr = 1$); Stage 2 ($Pr = 0.11$); Stage 3 ($Pr = 0.102$); Stage 4 ($Pr = 0.09$); and Stage 5 ($Pr = 0.06$). Branches of convectons with an even number of rolls are shown in blue and the branch segments predominantly corresponding to the two types of rolls are separated by showing convectons with R1 rolls in dark blue and R2 rolls in light blue. Blue dots indicate points at which the branches have been terminated (see text for details). The primary branches PN, consisting of steady spatially periodic states with N rolls, are shown in black with the following line styles: P12 (solid), P11 (dashed), P10 (dotted) and P9 (dash-dotted). Streamfunctions of convectons distinguishing the two types of roll (R1 and R2) are shown in the top right. The smaller panels show streamfunctions for a single convection roll of each type and have been magnified so that the rolls are to-scale.

supercritical regime.

5.3.1 STAGE 1: TYPICAL HOMOCLINIC SNAKING

We start by describing the large Prandtl number behaviour found within Stage 1 ($Pr > 0.15$), which is illustrated in figures 5.4 and 5.5. Here, we recover the homoclinic snaking similar to that found in the Swift–Hohenberg equation (cf. Chapter 3), which was first identified in this system by Bergeon and Knobloch [24]. For these large Prandtl numbers, the stable conduction state first destabilises subcritically at $Ra_c \approx 1627$ to an eigenmode with twelve pairs of counterrotating rolls. The resulting primary branch, named P12, extends towards lower Rayleigh numbers before regaining stability at a subcritical saddle node ($Ra \approx 1269$ for $Pr = 1$ in figure 5.4(a) or $Ra \approx 1364$ for $Pr = 0.2$ in figure 5.5(a)). The stable upper branch (shown in bold in figures 5.4(a) and 5.5(a)) heads towards large Rayleigh numbers, but may later destabilise in a drift-pitchfork bifurcation, like that seen at $Ra \approx 1491$ for $Pr = 0.2$ (figure 5.5(a)).

The conduction state later destabilises to eigenmodes with $N \neq 12$ pairs of counterrotating rolls, where the primary branches PN bifurcate. These bifurcations may be either sub- or supercritical, depending upon the number of rolls and the Prandtl number. The subsequent structure and stability of these branches are highly variable and will not be considered in detail here. However, we should note that following each of the primary branches towards larger amplitude, the anticlockwise rolls within the steady states strengthen at the expense of the clockwise rolls. This results in states on PN that are sufficiently far from the primary bifurcation consisting of N corotating anticlockwise rolls (see figures 5.4(b), (e) and 5.5(b), (e) for $N = 12$, figures 5.4(c), (f) for $N = 9$ and figures 5.5(c), (f) for $N = 10$).

Shortly after the primary bifurcation at Ra_c, two secondary branches, L^- and L^+, bifurcate subcritically from a modulational instability of P12 at $Ra \approx 1622.8$, which is in agreement with the theoretical result (5.18). As these secondary branches head towards lower Rayleigh numbers, the steady states that lie on them become increasingly spatially

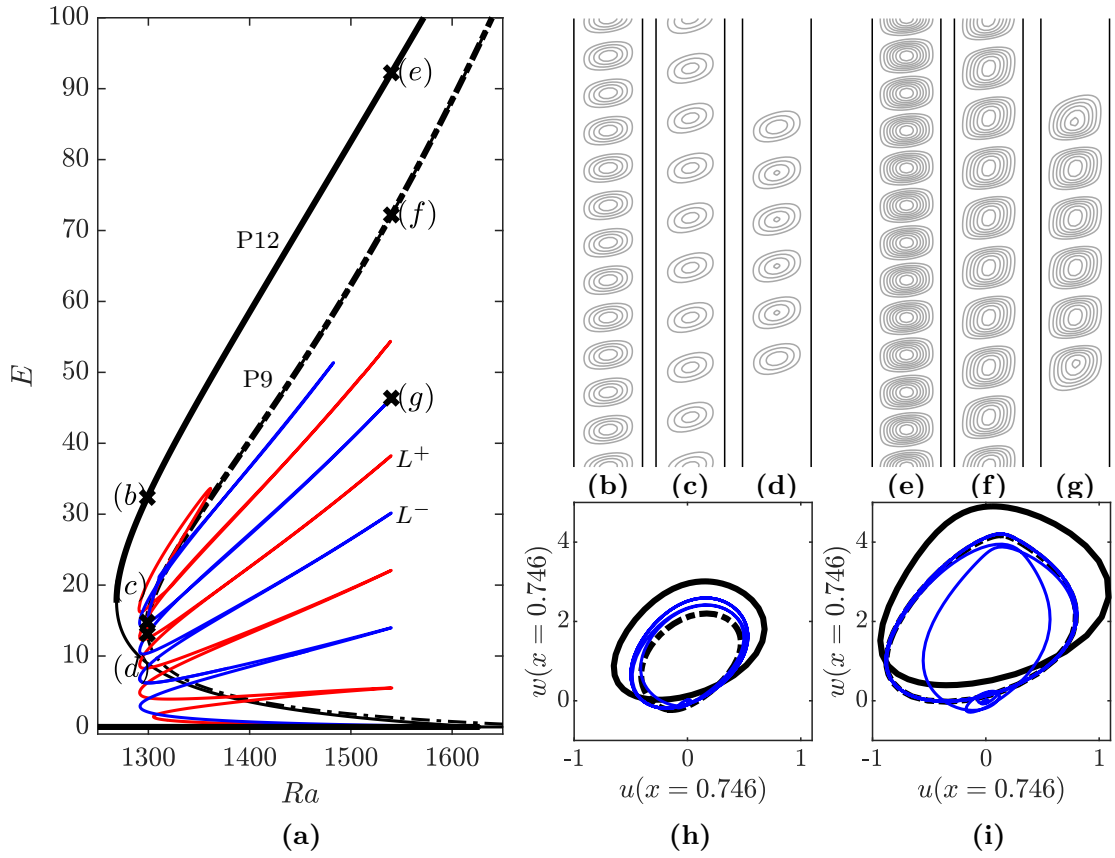

Figure 5.4: Typical homoclinic snaking and steady states for $Pr = 1$. (a) Bifurcation diagram showing P12 (black solid), P9 (black dash-dotted), L^+ (red solid) and L^- (blue solid). Thick (thin) black lines indicate stable (unstable) spatially periodic states on the primary branches, while the stability of the secondary branches is not indicated. (b)–(d) Streamfunctions of states at $Ra = 1299$ on (b) P12, (c) P9, (d) L^- and (e)–(g) states at $Ra = 1540$ on (e) P12, (f) P9 and (g) L^-. Phase-space representation of the marked states at (h) $Ra = 1299$ and (i) $Ra = 1540$, where (b) and (e) are shown via the black solid lines, (c) and (f) are shown via the black dash-dotted lines and (d) and (g) are shown via the blue solid lines.

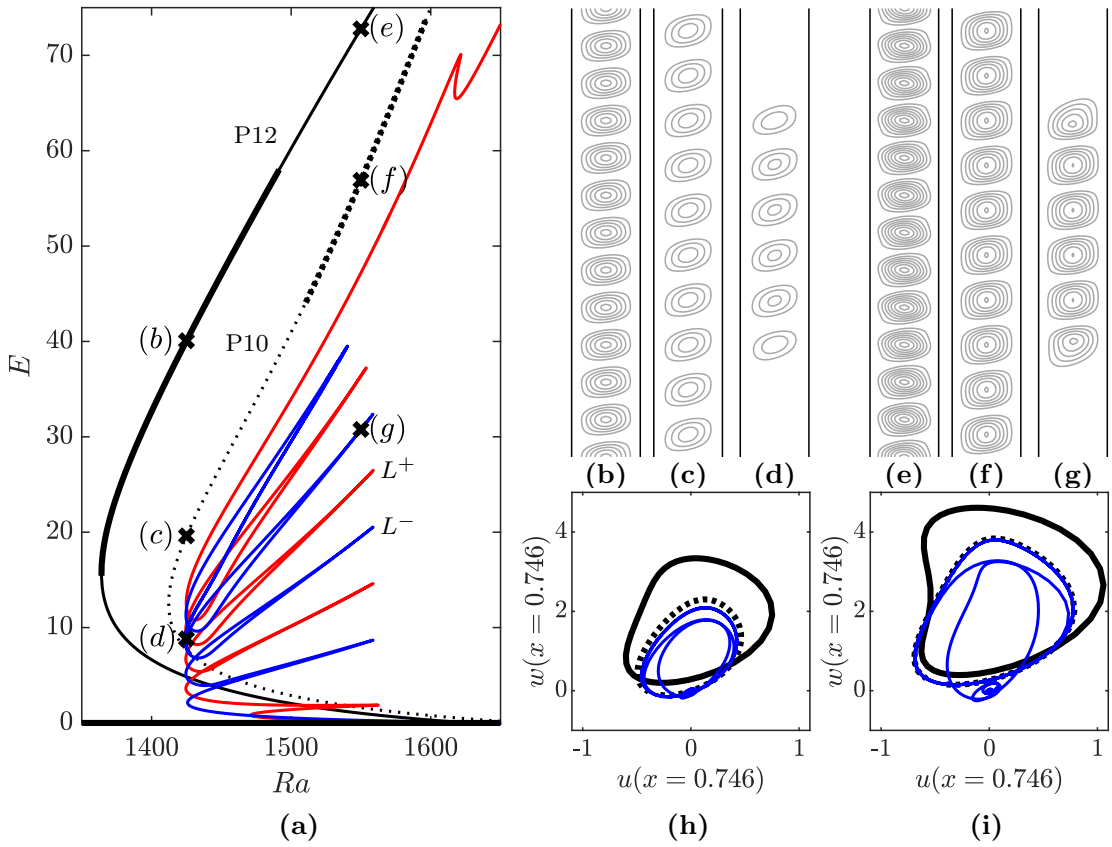

Figure 5.5: Typical homoclinic snaking and steady states for $Pr = 0.2$. (a) Bifurcation diagram showing P12 (black solid), P10 (black dotted), L^+ (red solid) and L^- (blue solid). Thick (thin) black lines indicate stable (unstable) spatially periodic states on the primary branches, while the stability of the secondary branches is not indicated. (b)–(d) Streamfunctions of states at $Ra = 1425$ on (b) P12, (c) P10, (d) L^- and (e)–(g) states at $Ra = 1550$ on (e) P12, (f) P10 and (g) L^-. Phase-space representation of the marked states at (h) $Ra = 1425$ and (i) $Ra = 1550$, where (b) and (e) are shown via the black solid lines, (c) and (f) are shown via the black dotted lines and (d) and (g) are shown via the blue solid lines.

modulated and exhibit the same strengthening of anticlockwise rolls and weakening of clockwise rolls as states on the primary branches. This leads to states on L^+ consisting of a single anticlockwise roll and those on L^- consisting of two anticlockwise rolls by their respective first left saddle node. Both secondary branches proceed by undergoing the following oscillatory behaviour, known as homoclinic snaking, over a finite range of Rayleigh numbers: the interior rolls first strengthen as the branches go from left-to-right saddle nodes; a roll nucleates on either side of the existing convecton rolls at the right saddle nodes; and finally the outer rolls strengthen while the interior rolls weaken as the branches go from right-to-left saddle nodes. The number of rolls in convectons therefore increases as the branches are followed towards larger amplitude until rolls nearly fill the domain. When this point is reached, the secondary branches L^+ and L^- either turn over and connect a primary branch of periodic states (e.g., P9 when $Pr = 1$ and P10 when $Pr = 0.2$), or extend towards higher Rayleigh numbers, depending upon the preferred wavelength of the localised state [26]. This preferred wavelength varies with both the Rayleigh number and Prandtl number, which may be inferred from comparing roll separation within the convectons shown in figures 5.4(d), (g) and 5.5(d), (g).

The central convecton rolls closely resemble those of individual rolls in a state at the same Rayleigh number on the upper branch segment of one of the primary branches, especially near the right saddle nodes (e.g., compare figures 5.4(f) and (g) and figures 5.5(f) and (g)). The flow near the centre of these rolls is approximately a vertical shear flow that is nearly parallel to the sidewalls, whereas the flow is inclined upwards (resp. downwards) towards the hotter (resp. colder) wall at the bottom (resp. top) of the roll. These rolls are subsequently referred to as R1 and may be characterised by the inertial term playing a subdominant role in the steady-state balance of the vorticity equation:

$$\underbrace{\frac{1}{Pr}\left(\mathbf{u}\cdot\nabla\omega\right)}_{I} - \underbrace{\nabla^2\omega}_{D} + \underbrace{Ra\left(\frac{\partial T}{\partial x} - \frac{\partial C}{\partial x}\right)}_{B} = 0, \tag{5.19}$$

where $\omega = \hat{\mathbf{y}}\cdot\nabla\times\mathbf{u}$. This is evidenced in figure 5.6, which shows the spatial dependence of the fraction that each term of the vorticity equation contributes compared to

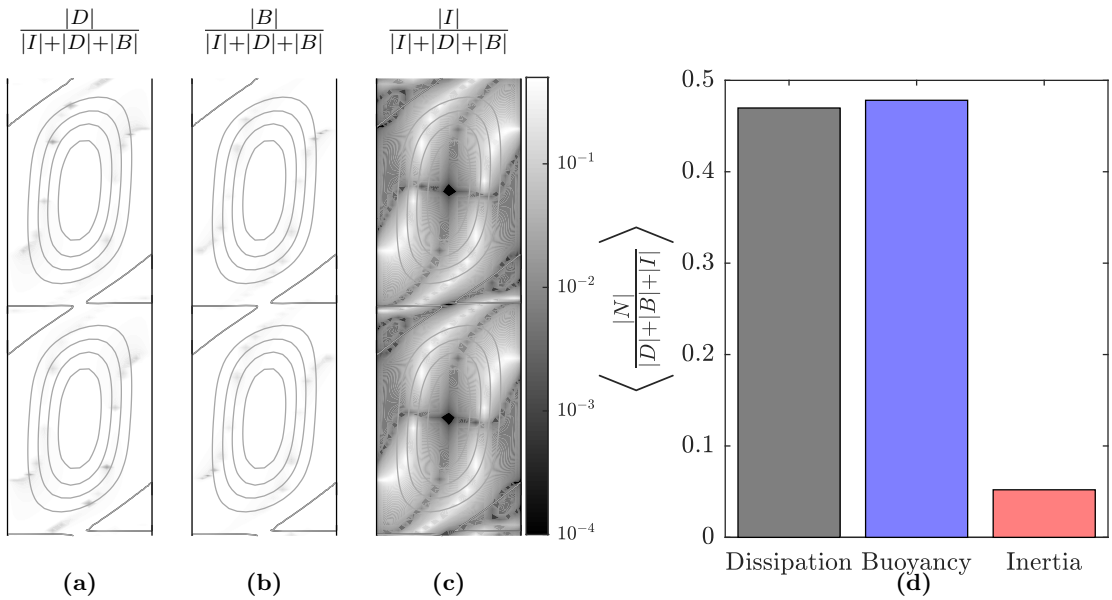

Figure 5.6: Vorticity balance (5.19) for the two central rolls of the six-roll convecton with $Pr = 1$ and $Ra = 1540$ (figure 5.4(g)). Spatial dependence of the fraction that (a) the viscous dissipation term $|D|$, (b) the buoyancy term $|B|$ and (c) the inertial term $|I|$ contribute to the sum of terms $|I| + |D| + |B|$ at each point. The colour bar on the right indicates the logarithmic scale used: white indicates a dominant term, while grey and black indicate a subdominant term. Streamlines of the steady flow are superposed onto each plot. (d) Average fraction of each term in (a)–(c) over the domain shown.

the sum of the absolute values of all terms at the same point, for the central two rolls of the six-roll convecton at $Ra = 1540$ and $Pr = 1$, shown in figure 5.4(g). Panels (a) and (b) illustrate that viscous dissipation, D, and buoyancy, B, provide the balance in (5.19), while inertia, I, is subdominant, except in a pair of thin 'S' shaped white strips on both sides of each roll. This is further observed in panel (d), where the domain-averaged fractions for both viscous dissipation and buoyancy are 0.47 and 0.478, respectively, while that for inertia is 0.05. Thus, at large Prandtl numbers, the anticlockwise convection rolls arise primarily via a balance between viscous dissipation and the buoyancy forcing.

The similarity between rolls in convectons and periodic states can also be illustrated by plotting different steady states at the same parameter values together in the phase space defined by the velocity components of the state along the vertical line $x \approx 0.746$. In this phase-space representation, the conduction state becomes a single point located at the origin, whereas the spatially periodic states on primary branches become closed periodic orbits. Selected states on the upper primary branches are shown by the black curves in figures 5.4(h), (i) and 5.5(h), (i), where the line-style corresponds to the associated primary branch, i.e., black solid, dotted and dash-dotted orbits represent states on P12, P10 and P9, respectively.

The spatial trajectories of the six-roll convectons (figures 5.4(d), (g), 5.5(d), (g)) are represented by the blue curves in these phase-space plots (figures 5.4(h), (i), 5.5(h), (i)). Each of these trajectories starts near the origin, as the flow is almost motionless away from the convecton rolls, and proceeds to spiral outwards as the weak rolls that constitute the front connecting the conduction state to convection rolls are traversed. The trajectory then approaches a periodic orbit corresponding to a state on the upper branch of P9 (black dash-dotted) when $Pr = 1$ in figures 5.4(h), (i) or P10 (black dotted) when $Pr = 0.2$ in figures 5.5(h), (i) and follows this periodic orbit around four times as the four interior convecton rolls are traversed. The trajectory finally spirals back towards the origin as the front connecting the convection rolls to the conduction state is traversed.

Convecton rolls continue to have the form of R1 rolls and appear in phase space as trajectories that follow the periodic orbit for a state on the upper branch of P10 as

the Prandtl number decreases through the remainder of Stage 1 ($0.15 \lesssim Pr < 0.2$). The structure of the snaking branches prior to termination or large-amplitude behaviour also remains qualitatively unchanged over this interval.

5.3.2 STAGE 2: CHANGING SNAKING

The structure of the snaking branches changes across Stage 2 ($Pr \approx 0.15$ to $Pr \approx 0.11$), as P10 undergoes a cusp bifurcation on its upper branch segment at $Pr \approx 0.14$ and $Ra \approx 1547$ (second column of figure 5.7). This bifurcation introduces a pair of additional saddle nodes and branch segments on the P10 branch, as can be seen in the final three columns of figure 5.7. Of particular interest are the two branch segments with positive gradient, which, in order of increasing kinetic energy, will hereafter be referred to as the second and upper branch segments of P10. We shall see that the change in snaking structure arises because the form of the convecton rolls changes from R1 to a second form, referred to as R2, and that the homoclinic orbits associated with convectons change from approaching periodic orbits corresponding to states on the second branch segment at low Rayleigh numbers to those on the upper branch segment at large Rayleigh numbers. This change occurs despite both the second and upper branch segments being unstable to modulational and drift instabilities, respectively.

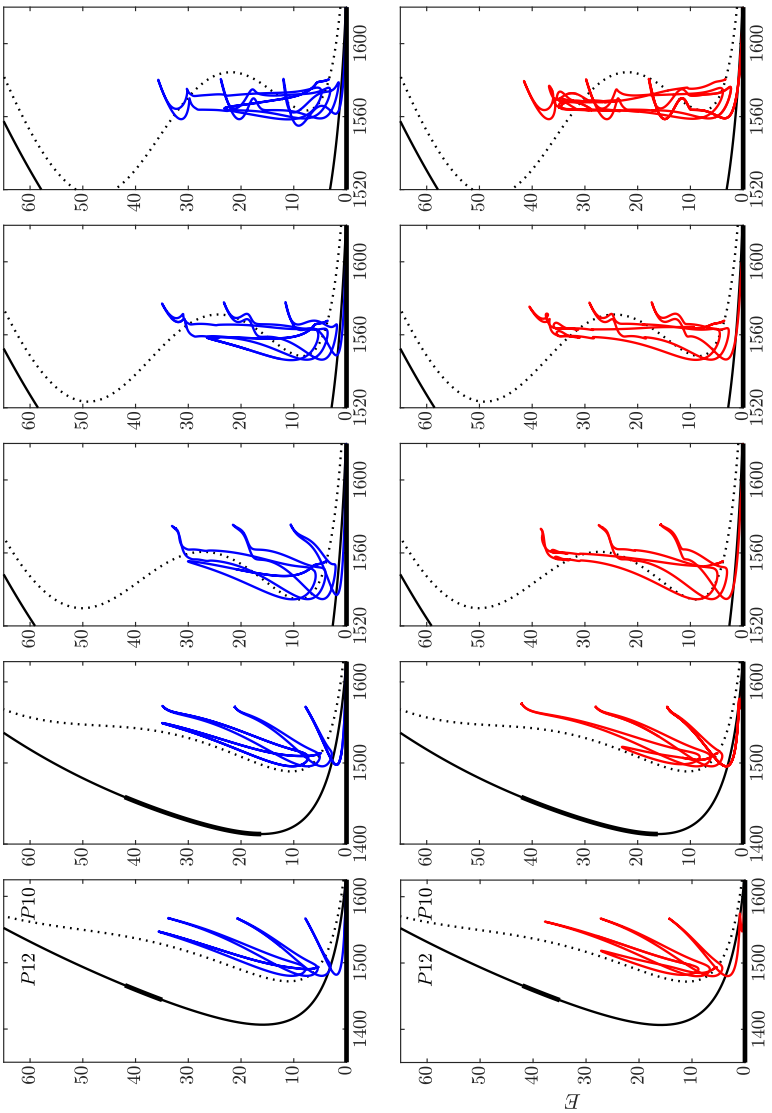

(a) $Pr = 0.15$ (b) $Pr = 0.14$ (c) $Pr = 0.12$ (d) $Pr = 0.115$ (e) $Pr = 0.11$

Figure 5.7: Bifurcation diagrams for (a) $Pr = 0.15$, (b) $Pr = 0.14$, (c) $Pr = 0.12$. (d) $Pr = 0.115$ and (e) $Pr = 0.11$, which show how the structure of the secondary branches changes over Stage 2. The marked branches include: the primary branches P12 (black solid) and P10 (black dotted) and secondary branches L^- (blue branches in top row) and L^+ (red branches in bottom row). Stable (unstable) segments of the primary branches are indicated using bold (thin) black lines, while the stability of the secondary branches is not indicated.

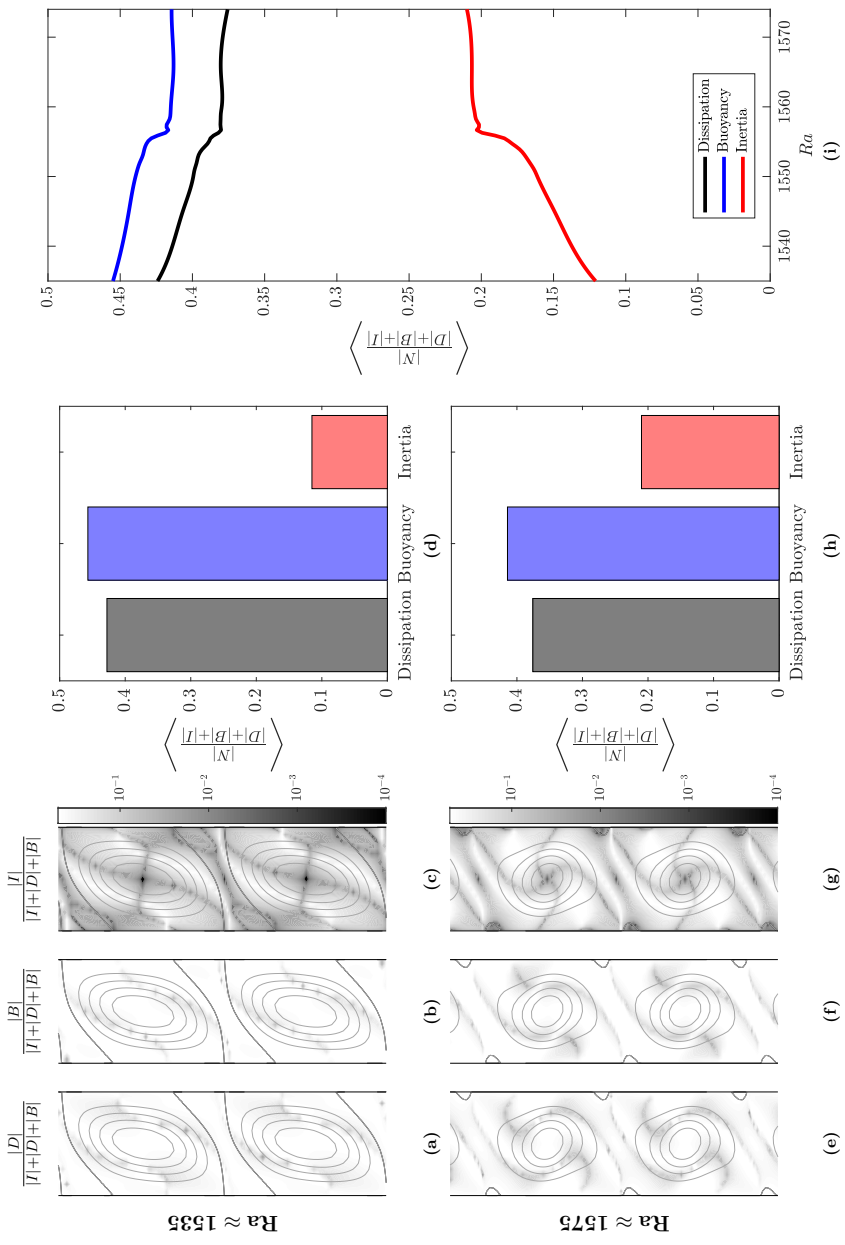

Figure 5.8: (a)–(h) Similar to figure 5.6, the states are the six-roll convectons for $Pr = 0.12$ at: (a)–(d) the left saddle node at $Ra \approx 1535$ (figure 5.9(g)) and (e)–(h)) the right saddle node at $Ra \approx 1575$ (figure 5.9(j)). (i) Domain-averaged fraction of maximum term in the vorticity equation for each of viscous dissipation (black), buoyancy (blue) and inertial (red) terms over the branch segment between these left and right saddle nodes.

The differences between the two types of rolls can be understood by considering how terms in the vorticity balance (5.19) of steady convectons change both spatially and in magnitude when the Rayleigh and Prandtl numbers are varied. Figure 5.8 presents such a comparison when the central two rolls of a six-roll convecton with $Pr = 0.12$ are considered between the left saddle node at $Ra \approx 1535$ (panels (a)–(d)), where rolls are R1, and the right saddle node at $Ra \approx 1575$ (panels (e)–(h)), where rolls are R2.

At the left saddle node, the spatial dependence of terms in the vorticity equation (figures 5.8(a)–(c)) resemble those seen in figure 5.6. Dissipation and buoyancy are dominant and respectively contribute approximately 42% and 46% of the domain-averaged values (figure 5.8(d)), while the inertial term is subdominant and contributes approximately 12% of the balance. The slight increase in inertial contributions between figures 5.6(c) and 5.8(c) is seen through the widening of the white strips in the top left and bottom right regions of each roll and the overall decrease in intensity of the greyscale.

The inertial contribution increases further with increasing Rayleigh number along the branch segment corresponding to six-roll convectons when $Pr = 0.12$, as can be seen in figure 5.8(i). This increase has a near uniform rate until $Ra \approx 1555$, as rolls strengthen whilst maintaining the form of R1 rolls, and is accompanied by the contributions from both buoyancy and dissipation decreasing at a lower rate. At $Ra \approx 1556$, the fraction that inertia (buoyancy, viscous dissipation) contributes to the balance rapidly increases (decreases) to 0.20 (0.42, 0.38) and remains approximately at this level towards the right saddle node at $Ra \approx 1575$. The rapid change, which we will explore further in the following paragraph, is associated with the central rolls in the convecton changing from R1 to a second form R2, where inertia is not negligible.

Aside from the different proportions in the vorticity balance, the two types of rolls also have qualitatively different structures, which are evidenced in the streamfunctions in figure 5.8. Firstly, we find that R2 rolls (figures 5.8(e)–(g)) are smaller yet stronger than R1 rolls (figures 5.8(a)–(c)) and secondly, we find that the long axis of the near elliptical streamlines at the centre of the roll have different orientations. In R1 rolls, this axis inclines upwards towards the hotter right sidewall, while the long axis at the centre of

R2 rolls inclines upwards towards the colder left sidewall. The latter observation can be clarified using the grey lines that originate from the centre of each roll in panels (c) and (g), which correspond to $|I| \approx 0$, where streamlines are parallel to lines of constant vorticity. While these lines are approximately straight throughout the R1 roll, they have bent in an anticlockwise direction in the centre of the R2 roll, owing to the increased effects of inertia, which affects the orientation of this roll. We will subsequently use these qualitative differences to classify the type of rolls that a convecton has by eye, rather than compute the vorticity balance for individual states.

Having observed that the form of the convecton rolls changes along the snaking branches when $Pr = 0.12$, we now want to understand how and why these changes occur by relating the convectons to the periodic convection states on the primary branches. To do so, we present streamfunctions and phase-space representations of convectons over a single snaking oscillation for $Pr = 0.12$ in figure 5.9. The form of individual rolls varies across each convecton and we have therefore used different colours in the phase-space plots to indicate their form separately.

As claimed above, the behaviour at the left saddle nodes (e.g., figures 5.9(e) and (e')) resembles that observed in Stage 1, where convectons consist of weak R1 rolls. These rolls (indicated by the red and indistinguishable blue and purple trajectories in the phase-space plot (e')) most closely resemble those in states on the second branch segment of P10 at the same Rayleigh number (thin black dotted trajectory). Rolls continue to have this form as the branches are followed towards higher Rayleigh numbers. This changes, however, around $Ra \approx 1555$ where we see a near vertical increase in both the kinetic energy of the states (figure 5.9(a)) and contribution from inertia in the vorticity equation (figure 5.8(i)). This corresponds to a rapid strengthening of the central rolls, which also change in form from R1 rolls close to those on the second primary branch segment, to R2 rolls on the upper primary branch segments. This is seen in figures 5.9(c') and (f'), where the innermost rolls, represented by the blue trajectories, are similar to rolls in states on one of the upper primary branches, represented by either the thick black dotted or solid trajectories. Continuing to follow the branch segments to the right saddle

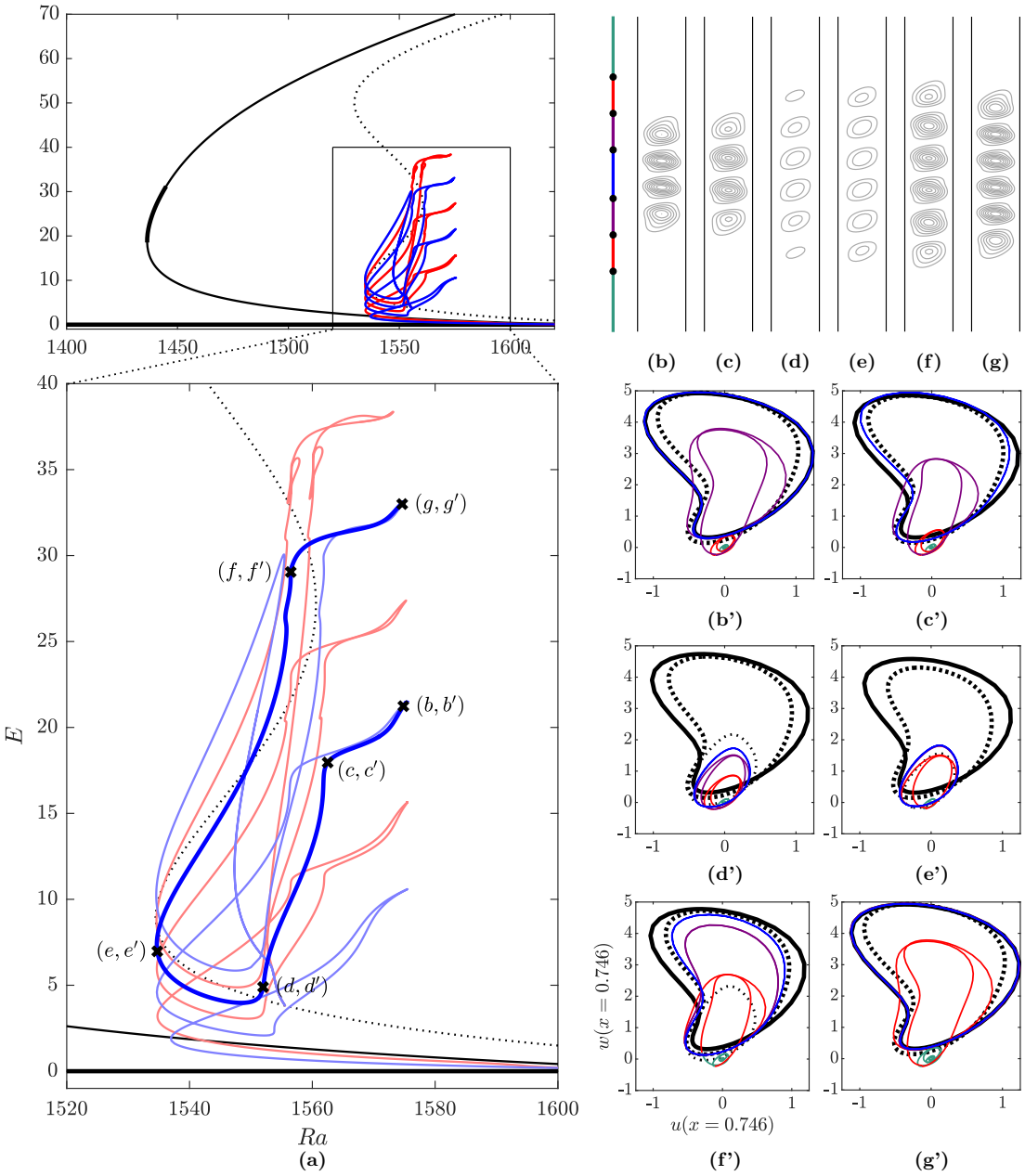

Figure 5.9: (a) Bifurcation diagrams when $Pr = 0.12$ showing: the conduction state (thick black solid), P12 (thin black solid), P10 (black dotted), L^+ (red solid) and L^- (blue solid). Stable (unstable) segments of the primary branches are indicated using bold (thin) black lines, while the stability of the secondary branches is not indicated. (b)–(g) Streamfunction profiles and (b′)–(g′) corresponding phase-space representations of selected marked states on L^-. Different types of rolls are represented using different colours in the phase-space plots: strong interior rolls (blue), outer rolls that strengthen to match interior rolls (purple), weak outermost rolls that strengthen over the oscillation (red) and weak-amplitude background rolls (green). The bar to the left of panel (b) relates these to the streamfunction profiles. Also shown in the phase-space plots are states on the upper branch of P12 (thick black solid) and P10 (thick black dotted) and, where applicable, on the second P10 branch segment (thin black dotted) at the same value of the Rayleigh number.

nodes (b,b′) and (g,g′), we find that the central rolls adjust their wavelength to become closer together so that the trajectories, shown in blue, are nearly identical to those on the upper branch of P12 (thick black line). Thus, towards the right edge of the pinning region, when the second branch segment of P10 does not exist, the central rolls in the convectons are R2 rolls. We further see that the homoclinic orbits of the stable conduction state associated with these localised states being homoclinic orbits between now approach the periodic orbit of a state on an upper primary branch.

The near figure-of-eight loops seen along the L^+ branch at large-amplitude correspond to amplitude modulated convectons. However, the origin of these states on this branch is currently unclear. They could have arisen when fronts on either side of the nearly domain-filling convectons interact owing to the finite period of the domain, which could have led to amplitude modulation of the rolls. Alternatively, they may have arisen as an artefact of the numerical code switching between L^+ and a neighbouring branch containing these modulated states if too large a step size is used. Further numerical tests using smaller step sizes, different discretisation or larger domains should be considered in order to distinguish whether this is the true branch structure of L^+ or one of the above effects arose.

The steep branch segments near the right saddle nodes (e.g., near (b) and (g) in figure 5.9(a)) continue to steepen as the Prandtl number decreases until each segment undergoes a cusp bifurcation just below $Pr = 0.12$. This leads to the additional saddle nodes that provide the hook-like structure of the branches when $Pr = 0.115$ (fourth column of figure 5.7). The newly formed left saddle node from each pair moves towards lower Rayleigh numbers as the Prandtl number decreases, which increases the multiplicity of convectons within the pinning region. This multiplicity is exhibited in figure 5.10 for $Pr = 0.11$, where we see convectons consisting of weak R1 rolls and those with stronger R2 rolls coexisting at the same Rayleigh number.

Transitioning between the two types of convectons contributes to the more complex structure of a single snaking oscillation, like the one shown in bold in figure 5.10(a). To interpret the structure of this snaking oscillation, one may consider the oscillation as a

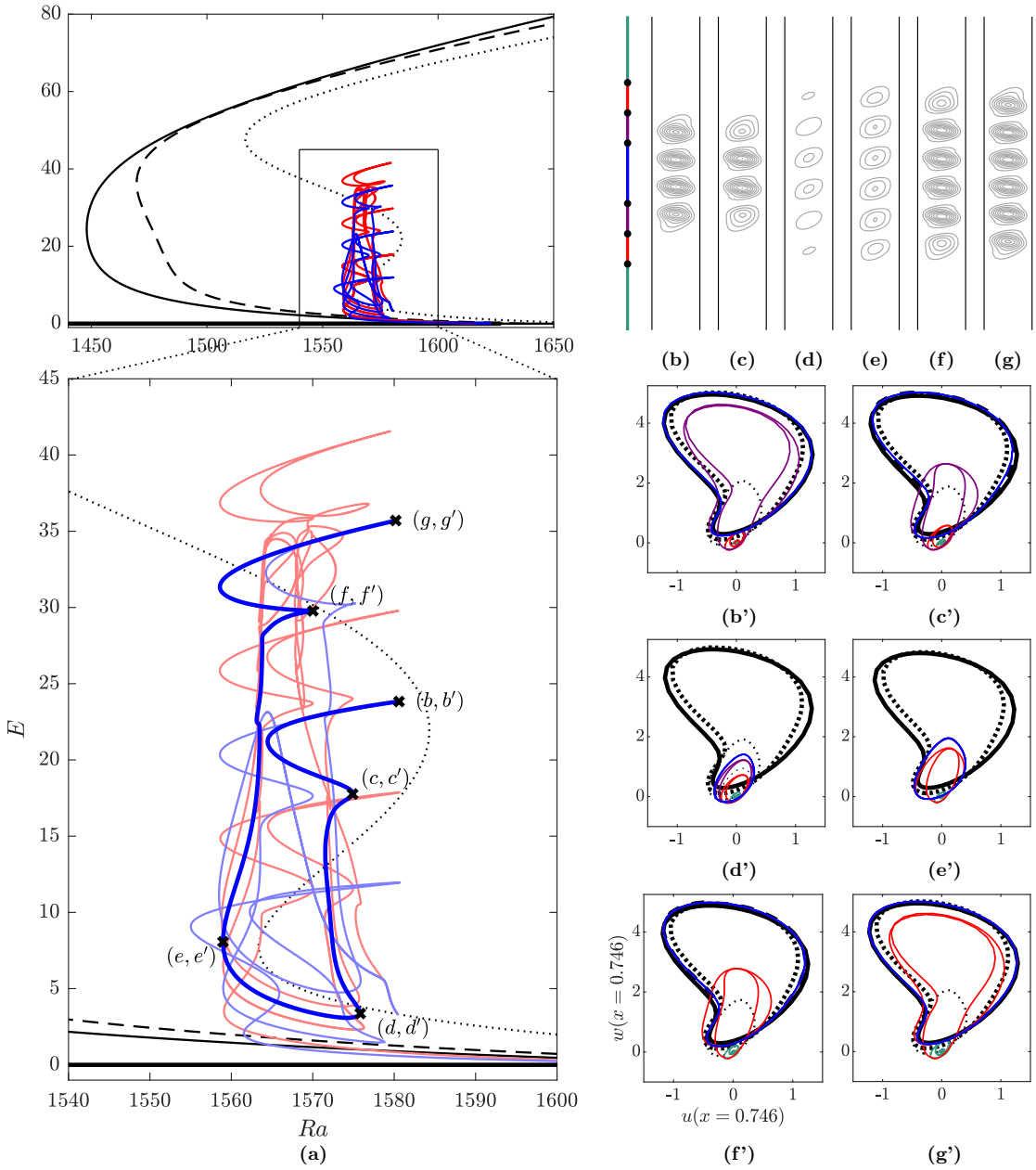

Figure 5.10: (a) Bifurcation diagrams when $Pr = 0.11$, showing: the conduction state (thick black solid), P12 (thin black solid), P11 (black dashed), P10 (black dotted), L^+ (red solid) and L^- (blue solid). (b)–(g) Streamfunction profiles and (b')–(g') corresponding phase-space representations of selected marked states on L^-. Different types of rolls are represented using different colours in the phase-space plots: strong interior rolls (blue), outer rolls that strengthen to match interior rolls (purple), weak outermost rolls that strengthen over the oscillation (red) and weak-amplitude background rolls (green). The bar to the left of panel (b) relates these to the streamfunction profiles. Also shown in the phase-space plots are states at the same value of the Rayleigh number on the upper branch of P12 (thick black solid) and P10 (thick black dotted) and, where applicable, on the upper branch of P11 (thick black dashed) and on the first and second P10 branch segments (thin black dotted).

combination of three sets of branch segments according to the form of convectons that lie on them. The first set of branch segments, (b,b′)–(c,c′) and (f,f′)–(g,g′), originate from the cusp bifurcations near the right edge of the pinning region and consequently contain convectons with strong R2 central rolls. The form of these central rolls most closely resembles rolls in states on the upper branch of P12, which is seen in the phase-space representations at the right saddle nodes (b′) and (g′) by the blue trajectories (central rolls) following the thick black solid trajectories (upper branch of P12). The preferred wavelength of the central rolls increases as each branch segment is followed to either (c) or (f). This is seen through the blue trajectories in phase space most closely resembling trajectories that correspond to states on the upper branch of P11 (thick black dashed lines in (c′) and (f′)). The branch segment (d,d′)–(e,e′) contains convectons with weak R1 central rolls, which are most similar in form to rolls in states on the lower branch segments of P10. This is evidenced in figures 5.10(d′) and (g′), by the small, nearly elliptical trajectories associated with convectons that approach the thin black dotted lines, which are associated with states on the second P10 branch segment. We should note, however, that convectons containing these weak R1 rolls can be found at lower Rayleigh numbers than the first left saddle node of P10 and thus coexistence between states is not strictly necessary for the existence of homoclinic orbits associated with localised states. The remaining pair of branch segments, (c,c′)–(d,d′) and (e,e′)–(f,f′), correspond to convectons transitioning between the two regimes with convecton rolls weakening and changing form from R2 to R1, or strengthening and changing form from R1 to R2, respectively.

5.3.3 STAGE 3: SNAKING BREAKING INTO MAIN BRANCHES AND ISOLAS

The first two saddle nodes of P10 continue to move towards larger values of the Rayleigh number as Pr decreases, as may be seen in figure 5.11. Indeed, by $Pr = 0.102$, the first of these saddle nodes has moved past the right edge of the pinning region. This leads to each of the snaking secondary branches breaking into a main branch and a number of isolas. The two types of convectons—those with R1 rolls (e.g., figures 5.10(f) and (g)) and

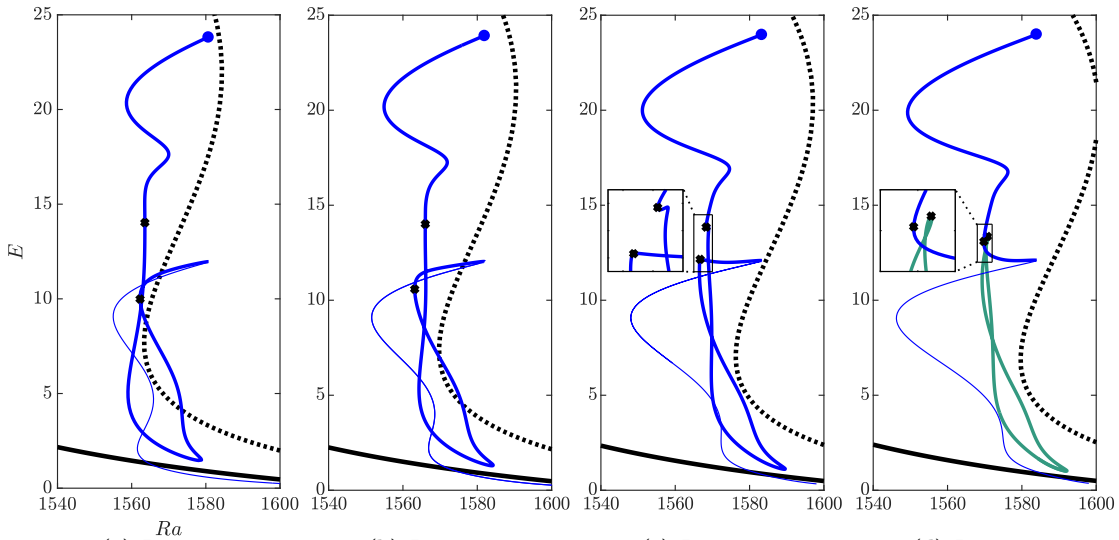

(a) $Pr = 0.11$ (b) $Pr = 0.108$ (c) $Pr = 0.106$ (d) $Pr = 0.105$

Figure 5.11: Bifurcation diagrams illustrating part of the breakup of the snaking L^- branch (blue) into a main branch (blue) and isolas (green) for (a) $Pr = 0.11$, (b) $Pr = 0.108$, (c) $Pr = 0.106$ and (d) $Pr = 0.105$. The primary P12 (black solid) and P10 (black dotted) branches are also shown. The connected branch segment between the right saddle nodes corresponding to two- or four-roll convectons and the segments that it breaks into are marked in bold for clarity.

those with R2 rolls (e.g., figures 5.10(b) and (j))—now lie on distinct branch segments as a result of this disconnection. We characterise this transition between $Pr \approx 0.11$ and $Pr \approx 0.102$ as Stage 3.

The panels in figure 5.11 detail this process by showing how L^- breaks up between the right saddle nodes corresponding to the two- and four-roll convectons. To aid the reader in following the process, we have marked two points that approach each other, connect and later separate as the Prandtl number decreases. Between $Pr = 0.11$ (figure 5.11(a)) and $Pr \approx 0.106$ (figure 5.11(c)), the state at the marked left saddle node increases in amplitude, while the second state approaches this saddle node as the near-vertical return branch segment pinches away towards lower Rayleigh numbers (see inset of figure 5.11(c)). These states proceed to connect at some point between $Pr = 0.106$ and $Pr = 0.105$ in a transcritical bifurcation, before later separating as Pr decreases. This imperfect bifurcation results in an isola (shown in green in figure 5.11(d)) disconnecting from the main branch.

The forms of both the convectons that lie on this isola and those that remain on the main branch may be deduced by first relating the isola and main branch when $Pr = 0.105$ (figure 5.11(d)) back to the corresponding segments of the following snaking oscillation when $Pr = 0.11$ (figure 5.11(a)). In doing so, we find that convectons on the isola originated from states on the branch segment between the marked points, which corresponds to convectons with R1 rolls and the transition between R1 and R2 rolls, as was seen between points (c,c′) and (f,f′) in figure 5.10. In contrast, convectons remaining on the main branch originated from other sections of the $Pr = 0.11$ snaking oscillation, where the central rolls resembled those on the upper primary branch segments. This breakup process therefore separates convectons with R1 rolls, which now lie on the isola, from convectons with smaller and stronger R2 rolls, which remain on the main branch.

The following snaking oscillations of L^- and those on L^+ undergo similar, albeit more complicated, breakup processes. For each oscillation, analogous points to those marked in figure 5.11 connect. However, this occurs in multiple stages and results in several isolas disconnecting from the main branch instead of the single one shown in figure 5.11(e),

which we will not discuss here.

This breakup process ultimately leads to convectons lying on one of the two main branches that display different snaking behaviour (e.g., see figure 5.12(a) for $Pr = 0.102$) to that seen at higher Prandtl numbers or one of a number of isolas that are not shown in figure 5.12(a), owing to their complexity. In describing the initial snaking behaviour of these main branches, we first note that the isola seen in figure 5.11(e) when $Pr = 0.105$ reconnects to L^- at small amplitude and is responsible for the initial excursion to $E \approx 12$ that this branch exhibits before returning to small amplitudes.

The branch proceeds to snake upwards, with each snaking oscillation between the right saddle nodes associated with convectons containing n and $n + 2$ rolls being composed of two shorter parts: a smaller section between right saddle nodes like (b,b′) and (c,c′), and a larger section between right saddle nodes like (c,c′) and (e,e′). The first part of the oscillation (between (b,b′) and (c,c′)) is associated with the nucleation and strengthening of a pair of outer R1 rolls, which are shown by the red trajectories in (b′) and (c′). Meanwhile, the outer central rolls (purple trajectories) strengthen to match the inner central rolls (blue trajectories), so that the blue and purple trajectories are indistinguishable by the right saddle node (c′). These central R2 rolls additionally change wavelength over this small segment to go from resembling rolls in states on the upper branch of P11 (thick black dashed trajectory in (b′)) to resembling those on the upper branch of P10 (thick black dotted trajectory in (c′)). The second part of the oscillation (between (c,c′) and (e,e′)) is predominantly associated with the outermost R1 rolls that nucleated in the first part of the oscillation strengthening and transitioning to R2 rolls. The four central rolls additionally adjust their wavelength and change from resembling P10 rolls at (c,c′) to P12 rolls at the following left saddle node (d,d′) before returning to P11 rolls at the right saddle node (e,e′). Consequently, the net effect of a complete snaking oscillation, composed of these two parts, is for the convecton to extend in length by two central R2 rolls.

This kind of snaking stops when L^+ reaches a five-roll state and L^- reaches a six-roll state, marked by the dots in figure 5.12(a). The branches instead exhibit different be-

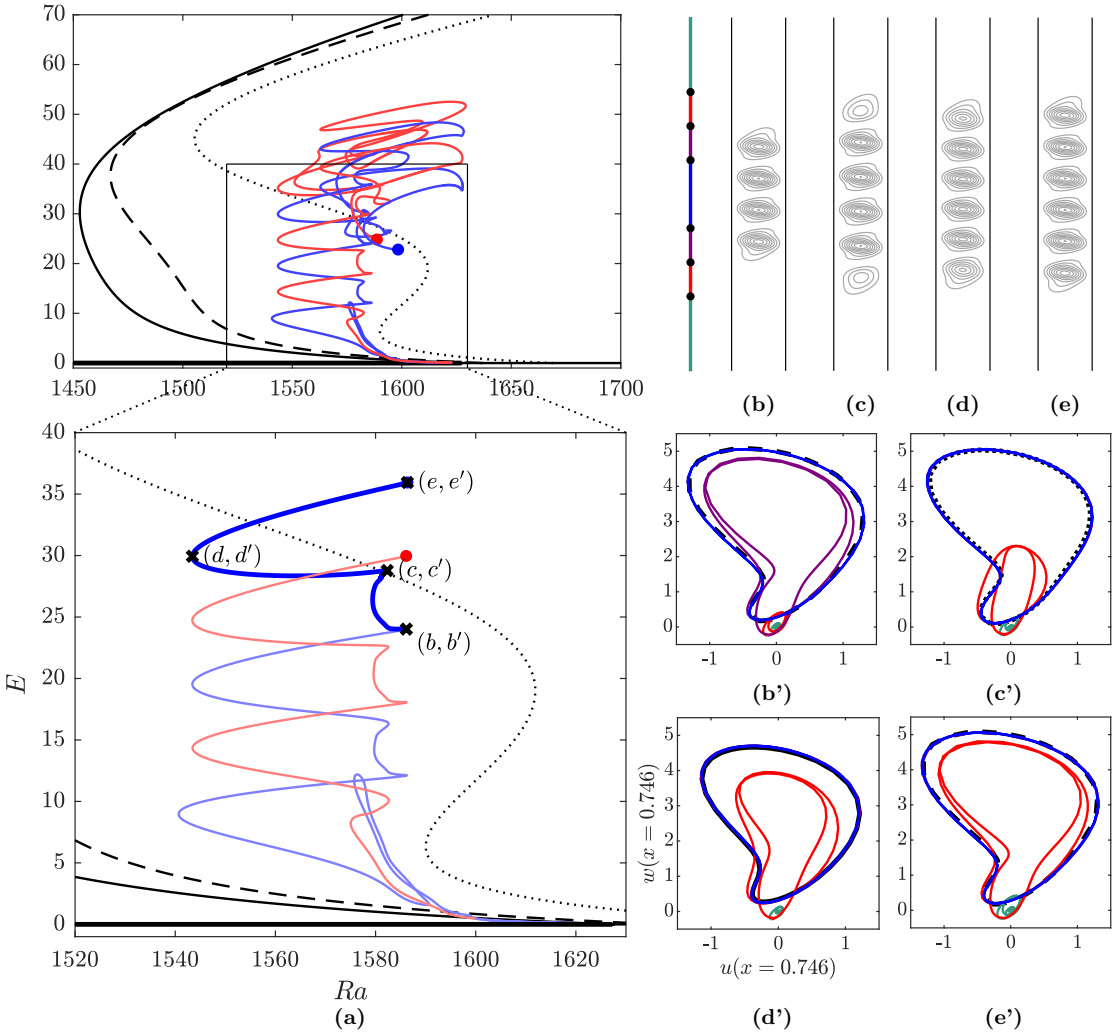

Figure 5.12: (a) Bifurcation diagrams when $Pr = 0.102$ showing: the conduction state (thick black solid), P12 (thin black solid), P11 (black dashed), P10 (black dotted), L^+ (red solid) and L^- (blue solid). In the upper panel, L^- and L^+ are terminated at the blue and red points, whereas they are terminated at $E = 40$ in the lower panel for clarity. (b)–(g) Streamfunction profiles and (b')–(g') corresponding phase-space representations of selected marked states on L^-. In (b')–(g'), different types of rolls are represented using different colours in the phase-space plots: strong interior rolls (blue), outer rolls that strengthen to match interior rolls (purple), weak outermost rolls that strengthen over the oscillation (red) and weak-amplitude background rolls (green). The bar to the left of panel (b) relates these to the streamfunction profiles. Also shown in the phase-space plots are states on the upper segment of the primary branch whose rolls at the same value of the Rayleigh number are most similar to the interior convecton rolls, again using the convention: P12 (thick black solid), P11(thick black dashed) and P10 (thick black dotted).

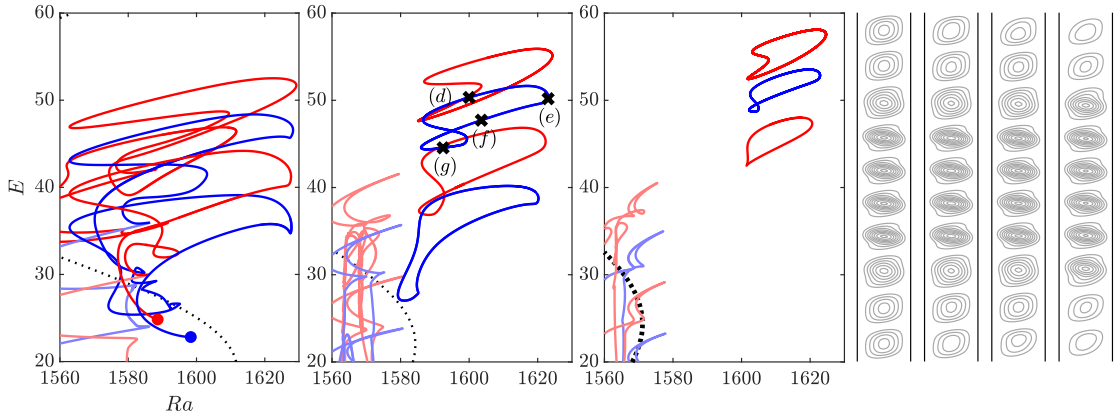

(a) $Pr = 0.102$ (b) $Pr = 0.11$ (c) $Pr = 0.115$ (d) (e) (f) (g)

Figure 5.13: Branch segments and profiles of non-uniform, domain-filling patterned states. (a) Extension of the bifurcation diagram shown in figure 5.12(a) for $Pr = 0.102$, again with branches terminated at the marked points for clarity. (b) Snaking L^+ and L^- branches for $Pr = 0.11$ with four isolas, which correspond to states with two (lower blue), three (lower red), four (upper blue) or five (upper red) stronger interior rolls in a background of weaker rolls. (c) Similarly to (b), except for $Pr = 0.115$, where only the isolas with three or four stronger central rolls are found. (d)–(g) Streamfunction profiles for the marked states on the four strong roll isola when $Pr = 0.11$.

haviour, magnified in figure 5.13(a), that is bounded between $Ra \approx 1563$ and $Ra \approx 1629$, which we note is close to the critical Rayleigh number $Ra_c \approx 1627$. These oscillations correspond to domain-filling patterned states with ten rolls, similar to those in figures 5.13(d)–(g), where central R2 rolls are embedded in a background of weaker R1 rolls. Tracking these states into higher Prandtl numbers, we find that they lie on isolas that are disconnected from both each other and the main snaking branches (see figure 5.13(b)). Along an individual isola, the number of stronger central rolls remains the same, while the background rolls change from having a near-uniform amplitude (e.g., figure 5.13(d)) to displaying a larger variation in amplitude (e.g., figure 5.13(g)). The isolas become smaller as the Prandtl number increases, but at different rates, so that by $Pr = 0.115$ (figure 5.13(c)), the isola containing the patterned states with two strong central rolls no longer exists, while the one containing states with four central rolls persists until about $Pr \approx 0.1191$.

Figure 5.14 depicts how the isola with four stronger central rolls that was marked in

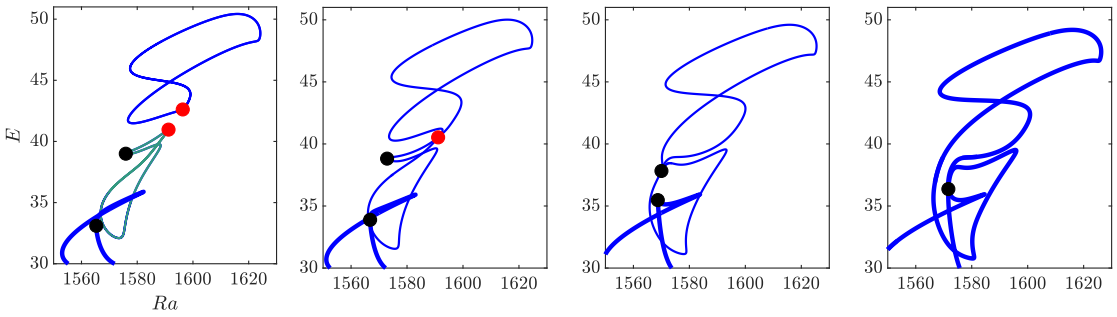

(a) $a = 0.107$ (b) $a = 0.106$ (c) $a = 0.105$ (d) $Pr = 0.104$

Figure 5.14: Bifurcation diagrams showing how the isolas of domain-filling patterned states with stronger central rolls connect to L^- for (a) $Pr = 0.107$, (b) $Pr = 0.106$, (c) $Pr = 0.105$ and (d) $Pr = 0.104$. The main branch L^- is shown by the thick blue line. The isolas originating from that marked in figure 5.13(b) are shown by the thin blue lines. A second isola that connects to this isola at $Pr \approx 0.106$ is shown in green. The red and black dots mark points that successively connect as the Prandtl number decreases.

figure 5.13(b) connects to L^- as the Prandtl number decreases from $Pr = 0.107$ (figure 5.14(a)) to $Pr = 0.104$ (figure 5.14(d)). We first find that this isola connects to the top right section of a second isola (green in figure 5.14(a)) of lower energy states, whose outer rolls are amplitude-modulated in a similar way to those shown in figure 5.13(g). This connection is illustrated in figures 5.14(a) and (b) by the two red dots at $Pr = 0.107$ meeting by $Pr = 0.106$. The isola resulting from this merger proceeds to connect to L^- between $Pr = 0.105$ (figure 5.14(c)) and $Pr = 0.104$ (figure 5.14(d)). This is shown by the black dots in figure 5.14, as the point that was originally a left saddle node of the lower isola at $Pr = 0.107$ moves to lower energy and towards the pinch-off point of L^- seen at $Pr = 0.105$ (figure 5.14(c)). The two points connect by $Pr = 0.104$, so, after reaching the six-roll convectons, the L^- branch heads towards larger energy and follows the path of the isola, before heading towards lower energy as it does at higher Prandtl numbers. At the lower-Pr limit of Stage 3, L^+ and L^- therefore contain both convectons and domain-filling patterned states.

The subsequent behaviour of the branches L^+ and L^- after these oscillations, i.e., beyond the blue and red dots in figure 5.14(a), is unclear. We found that they connected to some of the later isolas that disconnected from the main branch between $Pr = 0.11$ and

$Pr = 0.105$. However, the branches displayed no organised structure, nor could they be followed to a point of termination.

5.3.4 STAGE 4: SNAKING BREAKING INTO DISCONNECTED SEGMENTS AND ORIGIN OF SMALL-AMPLITUDE SNAKING

In the previous stage, we saw how the pair of rolls that nucleate at the right saddle nodes (e.g., (b) in figure 5.12) take similar form to R1 rolls in states on the lower branch segments of P10. However, as the Prandtl number continues to decrease, the primary bifurcation of the conduction state becomes increasingly supercritical and the first two saddle nodes of the P10 branch continue to move towards higher Rayleigh numbers, further away from the right edge of the pinning region. This impacts the snaking in two main ways. Firstly, each snaking branch breaks up into two snaking branches: one with small-amplitude convectons and one with large-amplitude convectons. Secondly, the branch segments between convectons with n and $n+2$ rolls disconnect, with convectons on these branches instead continuously transitioning into domain-filling states similar to those discussed at the end of the previous section. We will consider these two changes in this section and refer to them as Stage 4.

BIFURCATION DIAGRAM FOR $Pr = 0.09$

Figure 5.15 presents the bifurcation diagram for $Pr = 0.09$, which demonstrates the behaviour after the changes within this stage have occurred. In particular, we note that there is a pair of small-amplitude snaking branches that bifurcate from P12 and terminate on P11 and five disconnected branch segments of large-amplitude convectons. We introduce the notation L_i to label the branch of convectons with i rolls when $Ra < Ra_c$. While these branches are now disconnected from each other, the organised nature of the convecton branches for subcritical Rayleigh numbers persists and the left saddle nodes vertically align around $Ra \approx 1520$.

Changes along the organised branch segments can be understood by following each

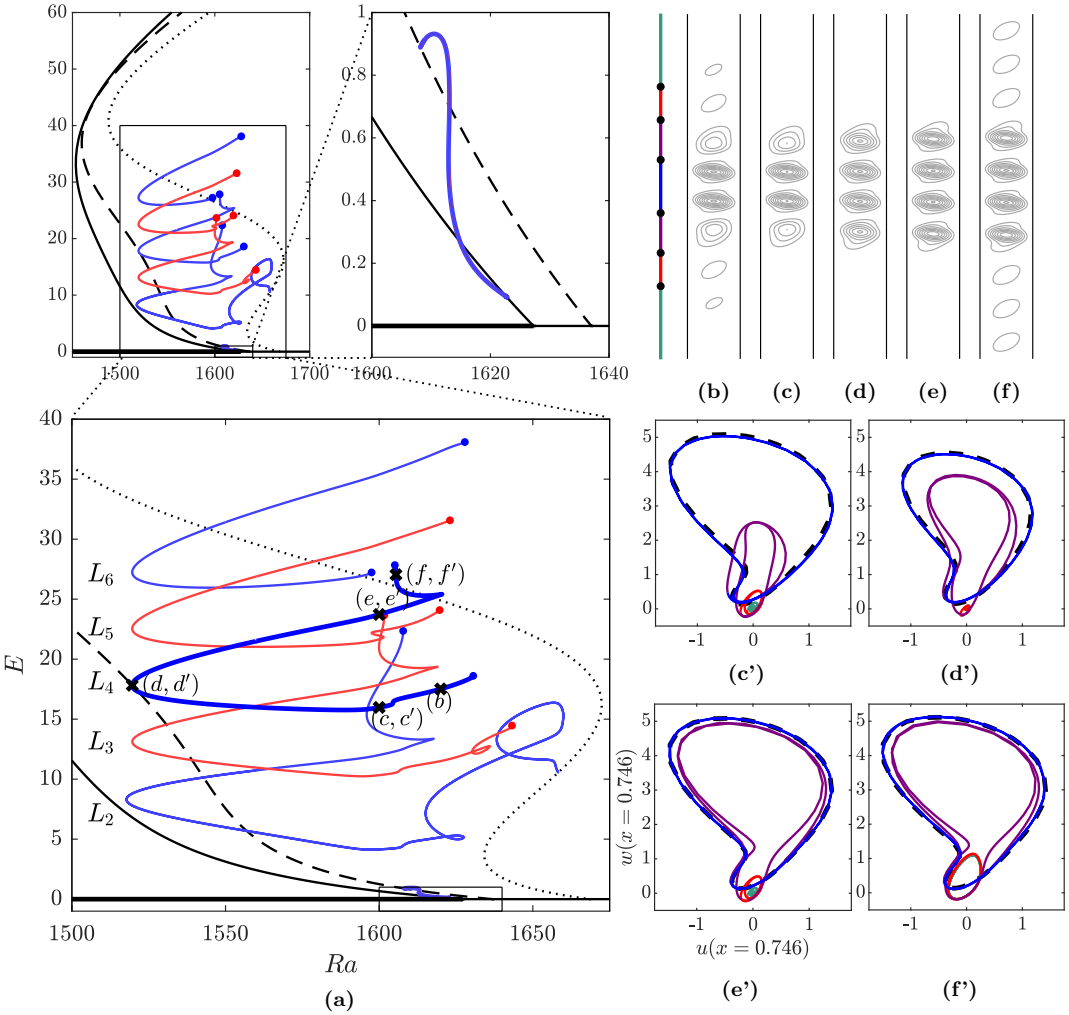

Figure 5.15: (a) Bifurcation diagrams when $Pr = 0.09$. Top left: zoomed out bifurcation diagram. Top right: magnification around the secondary bifurcation of P12. The branches shown in (a) are: conduction state and P12 (black solid), P11 (black dashed), P10 (black dotted) and L_i, branch of convectons with i rolls (blue (red) when i is even (odd)). The branches L_i have been terminated at the marked cusp bifurcations and right saddle nodes where they subsequently head back towards lower Rayleigh numbers, for clarity. (b)–(f) Streamfunctions of the labelled states of L_4 and (c′), (d′), (e′) and (f′) corresponding phase-space representations for four of these states. The phase-space plots show the convectons on L_4 (blue) and the state on the upper branch of P11 (black dashed) at the same value of the Rayleigh number.

branch segment L_i in the direction of increasing energy between $Ra \approx 1600$ on the lower and upper branch segments. Considering the branch of four-roll convectons L_4, for example, we find that the convecton at $Ra \approx 1600$ on the lower branch segment (figure 5.15(c,c′)) contains two inner R2 rolls (blue trajectories in (c′)) whose form closely follows those in states on the upper branch of P11 (thick black dashed trajectory in (c′)) and two outer R1 rolls (purple trajectories in (c′)). The inner convecton rolls continue to follow those on the upper branch of P11 at the same Rayleigh number as L_4 is followed firstly towards the left saddle node at $Ra \approx 1520$ (d,d′) and later towards higher Rayleigh numbers (e,e′). We should note that differs from the results when $Pr = 0.102$, where the inner rolls changed from resembling rolls on the upper branch segments of P10 (figure 5.12(c′)) to P12 (figure 5.12(d′)) and P11 (figure 5.12(e′)) over the corresponding oscillation. Meanwhile, the two outer rolls undergo a similar increase in amplitude and change in structure to that seen when $Pr = 0.102$, in that they change from R1 rolls on the lower branch segment (figure 5.15(c′)) to R2 rolls at the left saddle node (figure 5.15(d′)), before increasing in amplitude as the branch is followed towards higher Rayleigh numbers (figure 5.15(e′)).

Continuing each upper branch segment of L_i from $Ra \approx 1600$ towards larger kinetic energy (e.g., figure 5.15(e,e′) to (f) and beyond), we find that the background conduction state fills with weak rolls that are uniform in amplitude, instead of nucleating a pair of rolls outside of the existing convecton that was seen at higher Prandtl numbers. The subsequent steady states are thus domain-filling states with i strong interior rolls within a background of weaker rolls, as illustrated in figure 5.15(f). Following this background nucleation, the branches exhibit a number of complex, non-structured oscillations that appeared to be bounded between $Ra \approx 1520$ and $Ra \approx 1650$ for the duration over which we extended them. These oscillations are not indicated in figure 5.15(a) as we truncated each branch segment at a right saddle node, marked by the blue and red dots to improve the readability of this figure.

Contrasting behaviour arises as each lower branch segment of L_i is continued towards higher Rayleigh numbers (e.g., figure 5.15(c,c′) to (b) and beyond), as we find that weak

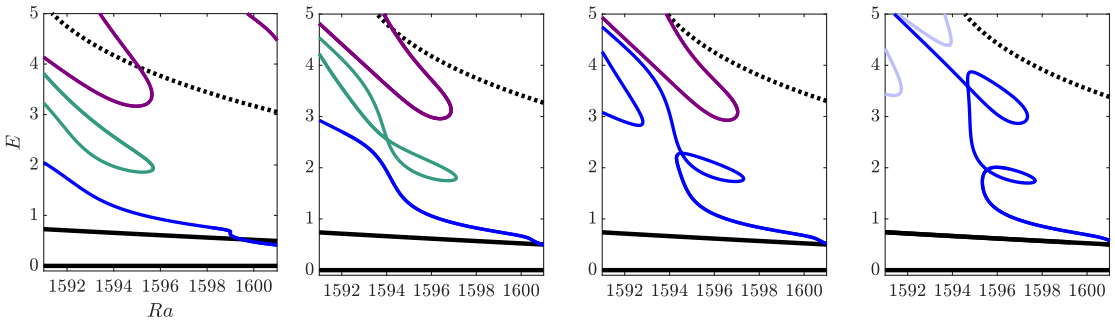

(a) $Pr = 0.102$ (b) $Pr = 0.1013$ (c) $Pr = 0.1012$ (d) $Pr = 0.101$

Figure 5.16: Magnification of bifurcation diagrams for (a) $Pr = 0.102$, (b) $Pr = 0.1013$, (c) $Pr = 0.1012$ and (d) $Pr = 0.101$ showing how the isolas reconnect to the secondary branch during Stage 4. The branches shown are: conduction state (black solid), P12 (black solid), P10 (black dotted), secondary branch L^- that bifurcates from P12 (blue), isolas that break from the snaking L^- branch during Stage 3 (green), a secondary branch containing states with an even number of rolls that bifurcates from a secondary bifurcation of P10 and extends towards large-amplitude (purple) and the branch segment that disconnects from L^- and snakes at large-amplitude (light blue).

R1 rolls successively nucleate and strengthen outside of the stronger central R2 rolls. This strengthening is non-uniform and rather occurs in a spatially modulated manner so that the amplitude of these background rolls decreases outwards from the central rolls, as seen in figure 5.15(b). Along L_2, the branch of two-roll convectons (lowest blue branch in figure 5.15(a)), this modulation is accompanied by the inner rolls changing to resemble rolls on the second branch segment of P10 and the branch is seen to bifurcate from a modulational instability of P10 around $Ra \approx 1658$. We were unable to determine the origin of the other branches of convectons seen in figure 5.15(a). However, we found that they did not bifurcate from the first secondary bifurcation of P12, as was the case when $Pr = 0.102$, since the pair of secondary branches that instead bifurcate from that point undergo small-amplitude snaking over a narrow range of Rayleigh numbers and terminate on P11.

SMALL-AMPLITUDE SNAKING

We now turn our attention to both the origin and properties of the small-amplitude snaking that was seen in the top right panel of figure 5.15(a). Parts of the branch seg-

ments involved in this snaking come from the lower part of the isolas that disconnected from the main snaking branches in Stage 3. This is shown in figure 5.16, where the isola containing states with six weak R1 rolls (marked in green) undergoes multiple twists (figure 5.16(b)) before joining to the lower part of the secondary branch (marked in blue) near the first of these crossing points. This leads to the small loop seen at $Pr = 0.1012$ (figure 5.16(c)) and a subsequent excursion (not shown), where the branch first follows the remaining section of the isola before heading to lower Rayleigh numbers by continuing its original path and snaking at large-amplitude.

Between $Pr = 0.1012$ and $Pr = 0.101$ (figure 5.16(d)), the lower part of the secondary branch that bifurcates from a modulational instability of P10 (marked in purple in figure 5.16(c)) connects with L^-. This likely occurs by the former branch first twisting over itself to form a second small loop between $1595 < Ra < 1597$ with $E \approx 3$. The lower part of this twisted branch proceeds to merge with the secondary branch bifurcating from P12 (shown in blue) to form the second small loop seen when $Pr = 0.101$ (figure 5.16(d)). This separates the secondary branch L^- when $Pr = 0.102$ (shown in blue) into two: a small-amplitude snaking branch that bifurcates from P12 and terminates on P10 (blue in figure 5.16(d)); and a branch segment that continues to large amplitude and contains fully localised states similar to those seen in figure 5.12 (shown in light blue in figure 5.16(d)). In larger domains, we anticipate that the additional isolas formed during Stage 3 undergo similar twists and connections to the secondary branch, which would increase the number of small loops before the final separation occurs.

States evolve along the resulting narrow snaking branches (shown in figures 5.17(a) and (b) for $Pr = 0.101$ and $Pr = 0.1$, respectively) in the typical way. After an initial spatial modulation, states enter the small pinning region with either three or four weak R1 rolls, depending upon the secondary branch. Additional pairs of rolls nucleate outside the existing state and proceed to grow in amplitude as the two secondary branches intertwine whilst oscillating over a narrow range of Rayleigh numbers. The form of rolls in these small-amplitude convectons appears to be controlled by the lower P10 branch, since the orbits for the two inner rolls (outer blue curves) in an established

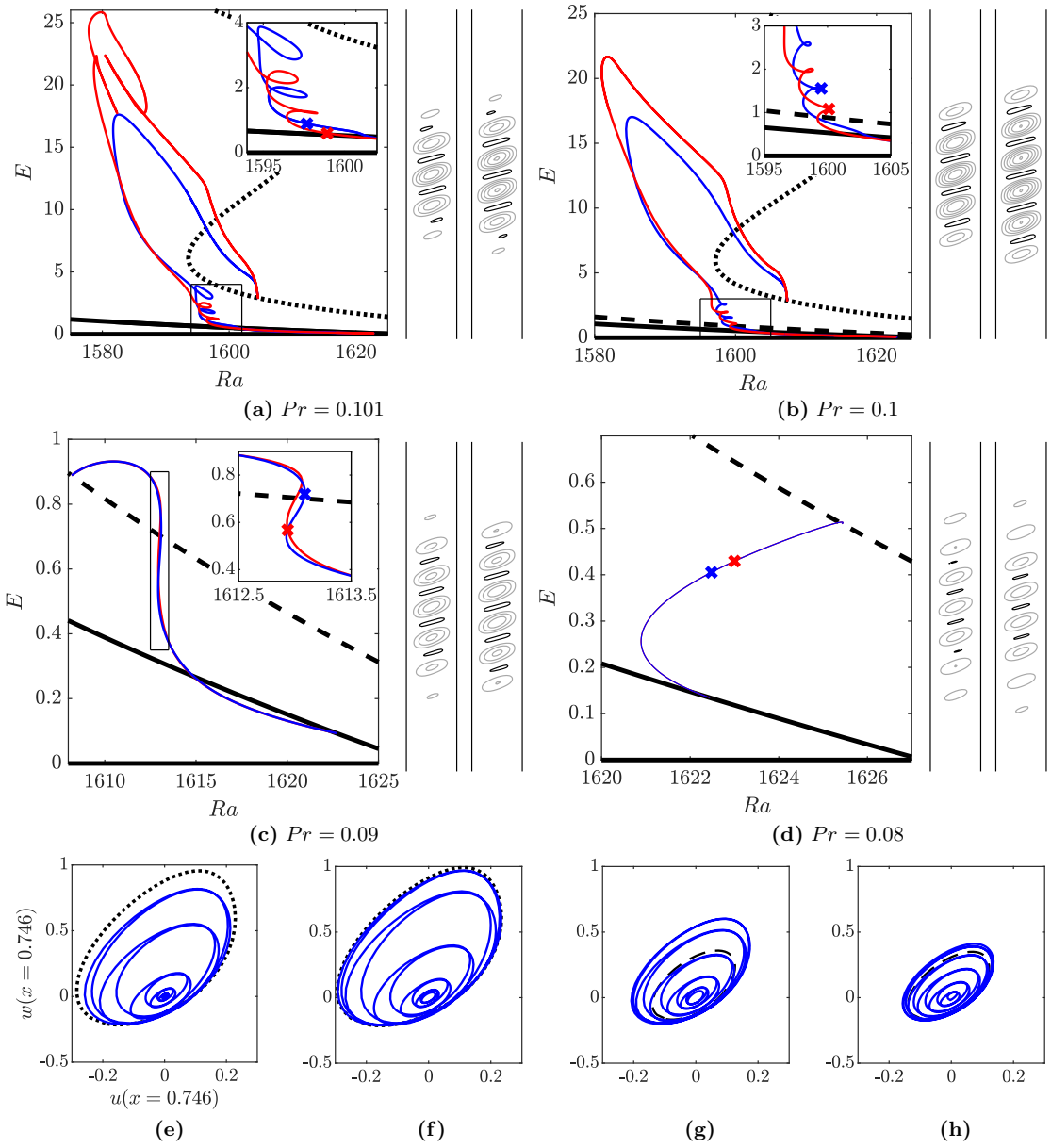

Figure 5.17: Small-amplitude snaking secondary branches for (a) $Pr = 0.101$, (b) $Pr = 0.1$, (c) $Pr = 0.09$ and (d) $Pr = 0.08$. The branches shown in the bifurcation diagrams are: conduction state (thick black solid), P12 (thin black solid), P11 (black dashed), P10 (black dotted), L^+ (red solid) and L^- (blue solid). The pair of streamfunction profiles indicate the steady states marked on both of the secondary branches (left: L^+, right: L^-). Contour intervals of 0.05 were used and grey (black) contours represent anticlockwise (clockwise) flow. (e)–(h) Phase-space plots of the marked small-amplitude states on L^- for (e) $Pr = 0.101$, (f) $Pr = 0.1$, (g) $Pr = 0.09$ and (h) $Pr = 0.08$. These plots show the trajectories for the convecton on L^- (blue), together with either states on the lower P10 (black dotted in (e,f)) or P11 (black dashed in (g,h)) branch at the same value of the Rayleigh number.

convecton for $Pr = 0.1$ closely follow the orbit for weakest P10 rolls (black dotted curve) in figure 5.17(f). When $Pr \geqslant 0.1$, this snaking is followed by an excursion to larger roll amplitudes, before both secondary branches terminate at a modulational instability of P10 prior to the first left saddle node.

Since the P10 branch becomes increasingly supercritical as the Prandtl number decreases, its first saddle node moves towards larger Rayleigh numbers. We find that the thin snaking branches cease to terminate on P10 by $Pr = 0.09$ and they instead terminate on P11 (see figures 5.17(c) and (d)). Continuing to decrease the Prandtl number towards Pr_c, where the primary bifurcation transitions from being subcritical to supercritical, we observe similar trends to those seen in other approaches to supercriticality in finite domains (e.g., [37, 93]). These include the width of the snaking decreasing until the branches become nearly indistinguishable by $Pr = 0.08$ (figure 5.17(d)), and saddle nodes colliding in cusp bifurcations from the bottom of the snaking to increase the number of rolls in the convectons. In an infinite domain, we might thus anticipate that the pinning region for this small-amplitude snaking becomes exponentially thin as Pr_c is approached and that these localised states persist up to this limit. However, in the 12-wavelength domain considered here, finite-size effects result in the first secondary bifurcation of P12 changing from being stationary at $Pr = 0.073$ to oscillatory at $Pr = 0.072$, as was seen by the red points in figure 5.2. This means that the amplitude-modulated small-amplitude states seen in figure 5.17 become time-dependent and we were unable to numerically continue the corresponding branches.

It is of interest to compare the origin of this small-amplitude snaking to the behaviour observed in the Swift–Hohenberg equation with ninth-order nonlinearity (3.36) considered in Chapter 3:

$$\frac{\partial u}{\partial t} = ru - (1 + \partial_x^2)^2 u + au^3 + bu^5 + cu^7 + du^9, \tag{5.20}$$

with $b = -100$, $c = 180$, $d = -100$ and a varying between $a = 20.5$ and $a = 19$. In this model system, we found that a single snaking branch when $a = 20.5$ (cf. figure 3.13)

broke up into two separate snaking branches by $a = 19$ (cf. figure 3.15) after the subcritical primary branch underwent a cusp bifurcation and provided a region of tristability between the trivial state and two periodic states of different amplitude within the pinning region. We found that this breakup occurred after a number of smaller isolas, containing localised states associated with the new type of bistability, successively connect to the original snaking branch at small amplitudes, much like in the doubly diffusive system (cf. figure 5.16). This process separated localised states associated with the bistability between the trivial state and large-amplitude periodic states (equivalent to R2 rolls), which remain on the snaking branch that extends towards large amplitude, and those associated with the bistability between the trivial state and the smaller amplitude periodic state (equivalent to R1 rolls), which were found to lie on the snaking branches at smaller amplitudes.

The Swift–Hohenberg model further motivates why the branch of large-amplitude two-roll convectons (L_2) when $Pr = 0.09$ and the branch of small-amplitude snaking of R1 convectons when $Pr = 0.101$ bifurcate at modulational instabilities prior to the first right (figure 5.15(a)) and left (figure 5.17(a)) saddle nodes of P10, respectively, owing to where the corresponding large- and small-amplitude snaking branches of the model system bifurcate and accounting for the preferred wavelength of convectons. The model system does not, however, explain why the main snaking branch breaks into disconnected branch segments between $Pr = 0.102$ and $Pr = 0.09$, which suggests that additional behaviour should be incorporated. The parameter values used in (5.20) could also be optimised in order to better model the changes in the doubly diffusive system between stages 2 and 4. For example, we might aim to find those that enable the primary branch to undergo a cusp bifurcation on its upper branch, as was found for P10 when $Pr \approx 0.14$, and for the first two saddle nodes to move through the pinning region and into supercritical parameter values. However, we should note that this optimisation may be difficult, since we wish to avoid the branch of homogeneous states leading to collapsed snaking in the regions of interest.

5.3.5 STAGE 5: SUPERCRITICAL CONVECTONS

We now return to the system of natural doubly diffusive convection and consider Prandtl numbers with $Pr < Pr_c \approx 0.062$, where the primary bifurcation is supercritical. Within this supercritical regime, the primary branch no longer undergoes an Eckhaus instability shortly after onset, as we showed in section 5.2 via the linear stability analysis, and we cease finding the small-amplitude snaking seen in figure 5.17 that was associated with convectons containing R1 rolls. However, the large-amplitude convectons that developed in Stage 2 persist into this regime and continue to lie on an organised set of disconnected branches (L_i for $i = 1, ..., 6$) within subcritical Rayleigh numbers, as evidenced when $Pr = 0.06$ in figure 5.18(a).

Figures 5.18(b,b')–(g,g') indicate the changes that the steady states on L_2 undergo as the branch is followed away from where it bifurcates at a modulational instability of P11 at $Ra \approx 1577$, along with L_1. States on L_2 initially contain eleven rolls, whose form resemble rolls on states on the middle segment of P11. As the branch is followed away from the secondary bifurcation towards larger Rayleigh numbers, the two central rolls strengthen, whilst the nine background rolls weaken in line with the middle P11 state to give states like the one shown in (b) and (b'). The background rolls continue to weaken as the branch turns around to lower Rayleigh numbers at $Ra \approx 1663$, so that when L_2 re-enters the subcritical region $Ra < Ra_c$, around the point marked (c), convectons contain two stronger rolls within a nearly quiescent background. These stronger rolls (blue trajectories in the phase-space plots) resemble those on the middle portion of P11 (thin black dashed trajectory), albeit with larger amplitude, as seen in (c'). These central rolls strengthen and adjust their profile to resemble rolls in states on the upper P11 branch (thick black dashed trajectory) as L_2 is followed towards the left saddle node at $Ra \approx 1467$ (d,d') and back to $Ra \approx Ra_c$ on the following upper branch segment (e,e').

As the branch re-enters supercritical Rayleigh numbers and heads towards the saddle node marked (f), nine weak rolls strengthen uniformly outside the two central rolls, thereby replacing the now-unstable conduction state, which resembles behaviour found

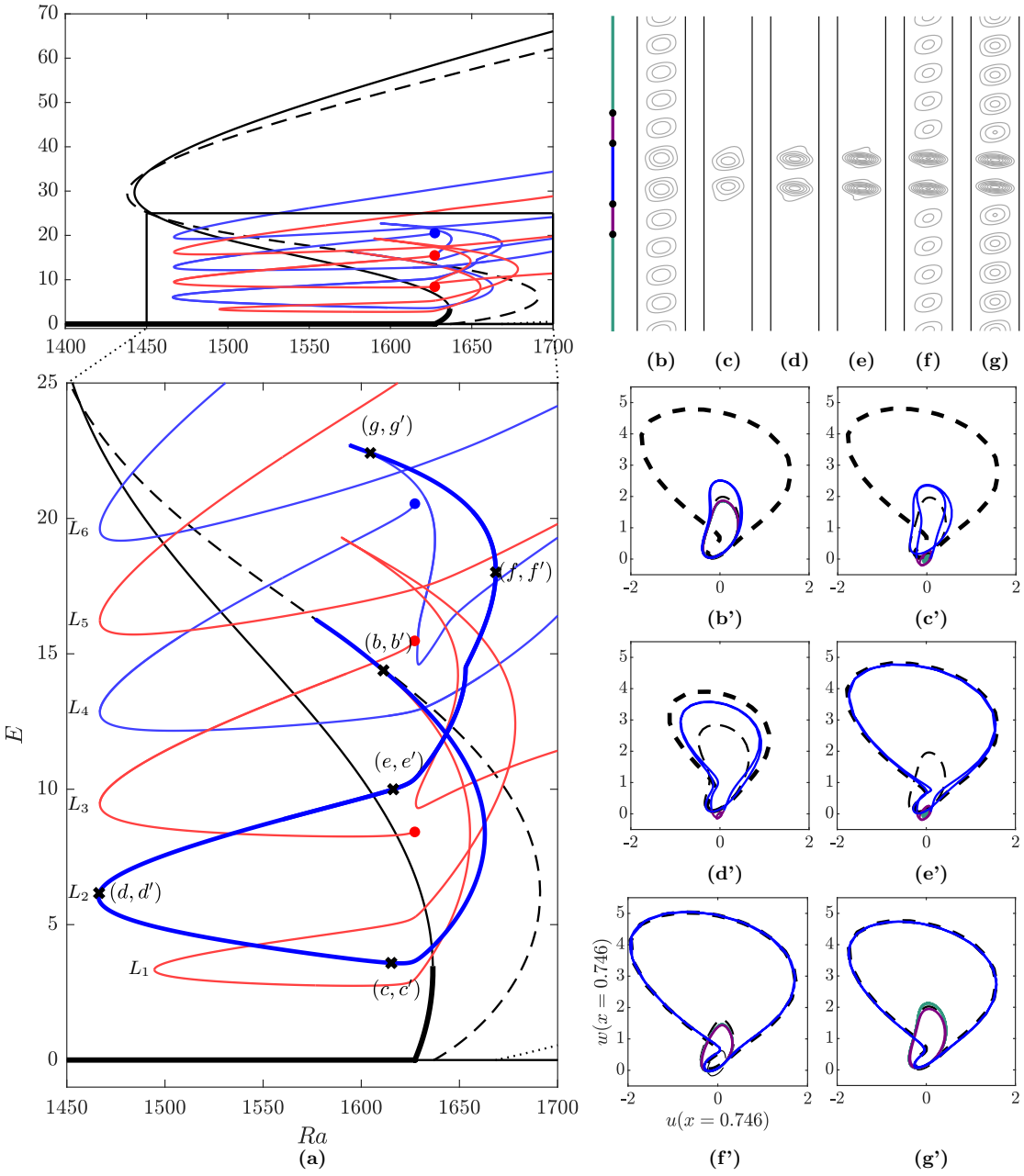

Figure 5.18: (a) Bifurcation diagrams when $Pr = 0.06$, showing: the conduction state, P12 (black solid), P11 (black dashed) and L_i, branch of convectons with i rolls (blue (red) when i is even (odd)). The branches L_i have been terminated either at $Ra = 1700$, or at the marked points, for clarity. (b)–(g) Streamfunction profiles of the labelled states of L_2 and (b′)–(g′) corresponding phase-space representations of these states. The phase-space plots show orbits representing the convectons on L_2 (blue), states on the upper (thick black dashed) and middle (thin black dashed) branch segments of P11 at the same value of the Rayleigh number.

in the cubic-quintic-septic Swift–Hohenberg equation [100] (cf. figure 3.11). The background rolls increase in amplitude as the Rayleigh number increases and ultimately resemble rolls in states on the unstable middle segment of the P11 branch, which can also be seen by the purple and green trajectories in the phase-space plots (f′) and (g′), which represent these background rolls, following the thin black dashed trajectory, which represent states on the P11 branch. The branch L_2 continues after the saddle node near (g); however, the subsequent behaviour is not considered here as the background rolls become non-uniform. This can lead to states, for example, becoming two-pulsed, where they consist of two distinct regions of strong convection rolls that are separated either by weak rolls or conduction state.

States on L_1 display analogous behaviour across the branch segment shown in figure 5.18(a), except with a single central roll instead of a pair of rolls. In contrast, on the other convecton branches (L_i for $i = 3, ..., 6$), only the outer two rolls adjust their shape along segments analogous to (c,c′)–(e,e′) on L_2, while the interior rolls continue to follow the form of states on the upper P11 branch. The background conduction state continues to fill with rolls as the branches cross into supercritical Rayleigh numbers ($Ra > Ra_c$), which may be deduced from figure 5.18(a) as the branches change gradient when they cross $Ra = Ra_c$.

There remains the outstanding question as to what happens to these convectons and the branches on which they lie as the Prandtl number decreases beyond $Pr = 0.06$. We were unable to address this here owing to the numerical difficulties associated with thin viscous boundary layers at small Prandtl numbers, but we will briefly speculate on the anticipated behaviour. The primary bifurcation will become increasingly supercritical and the large-amplitude subcritical saddle nodes of P11 and P12 will move towards higher Rayleigh numbers. These saddle nodes will ultimately move beyond the primary bifurcation at $Ra = Ra_c$ so that the primary branches lie entirely within the supercritical regime $Ra > Ra_c$, as we found for parameter values in Region 4 in Chapter 4 (cf. figure 4.11). We suspect that the organised structure of the disconnected convecton branches will persist during this change, but will shift towards larger Rayleigh numbers

so that these branches continue to lie to the right of the large-amplitude saddle nodes of the primary branches. This would mean that, within Region 4, the convecton branches will also entirely lie within supercritical Rayleigh numbers and convectons might appear as domain-filling patterned states where large-amplitude rolls lie within a background of small-amplitude rolls, as in figure 5.18(f) for $Pr = 0.06$.

5.4 DISCUSSION

In this chapter, we characterised how the structure of snaking secondary branches of convectons in a system of natural doubly diffusive convection changed as the Prandtl number was varied. We found that the typical snaking found by Bergeon and Knobloch [24] persists over a range of large Prandtl numbers. However, this snaking can become more complicated at lower Prandtl numbers. We attributed much of the complexity to the transition between convectons containing buoyancy-driven rolls (R1 rolls) and those containing a second type of roll driven by a balance between inertia and buoyancy (R2 rolls). Spatially periodic states with both types of rolls coexist with the stable conduction states over a small range of Prandtl numbers and thus our results may be of interest to other systems that exhibit tristability [67, 100].

Decreasing the Prandtl number below $Pr = 0.11$, we found that the snaking branches undergo a series of disconnections that separates convectons with R1 rolls, which now lie on isolas, from those with R2 rolls, which continue to lie on the main snaking branch. The isolas later reconnect with others and a pair of secondary branches from P12 to produce a pair of branches that exhibit snaking at small-amplitude. These snaking branches persist until just prior to the codimension-two point where the criticality of the primary bifurcation changes. Meanwhile, the main snaking branches were found to break up into a series of disconnected branch segments. These maintained an organised stacked structure within subcritical Rayleigh numbers as the Prandtl number decreased and the primary bifurcation becomes supercritical. Hence, natural doubly diffusive convection provides an example of a non-variational system that admits localised states

when the primary bifurcation is supercritical, which is a property that has only recently been observed in one-dimensional systems without a conserved quantity in the simpler variational cubic-quintic-septic Swift–Hohenberg equation [100].

While we have not discussed the stability of the primary and secondary branches in much detail here, we should emphasise that each primary branch destabilises in a drift-pitchfork bifurcation, which notably occurs on the lower segments of the primary branches when $Pr < 0.11$. Thus, we found that convectons can exist in low Prandtl number regimes despite the lack of bistability between the conduction state and large-amplitude periodic states. While this observation can be explained by restricting to the centro-symmetric subspace, where the primary branches cannot destabilise to drift and the system exhibits bistability, it raises the interesting question about whether convectons inherit this drift instability and, if so, what the properties of the instability are.

6 | UNBALANCED BUOYANCY EFFECTS

So far in this thesis, we have only considered systems where the horizontal thermal and solutal gradients imposed via the sidewall boundary conditions provide equal but opposite effects on the total fluid density. This has been achieved by fixing the value of the buoyancy ratio, defined

$$N = \frac{\rho_C \Delta C}{\rho_T \Delta T}, \tag{6.1}$$

where ρ_C (ρ_T) is the solutal (thermal) expansion coefficient and ΔC (ΔT) is the concentration (temperature) difference between sidewalls, to be $N = -1$. While this choice has important dynamical implications, most notably in the existence of a steady quiescent conduction state for all Rayleigh numbers, this balance is unlikely to be achieved in physical or experimental systems where, for example, the imposed solutal concentration may be hard to control (e.g., [92]). It is therefore compelling to understand how sensitive convectons are to changes in the buoyancy ratio and the absence of the conduction state, particularly since convectons have only been studied in balanced systems of natural doubly diffusive convection [9, 12, 14, 23, 24, 120], where the motionless conduction state forms the background of these localised states.

In this chapter, we will study the effects that breaking the balance has on the natural doubly diffusive convection in a closed vertical cavity. This configuration will be introduced in section 6.1. We will summarise the key results of the balanced system ($N = -1$) in section 6.2 since they differ from those with periodic boundary conditions. This summary is followed by discussing four aspects of the unbalanced systems with $N \neq -1$: the large-scale flow that develops (section 6.3.1); the small-amplitude unfolding of primary bifurcations (section 6.3.2); the form of convectons in both thermally and

solutally dominated regimes (section 6.3.3); and how the structure of anticonvectons changes and its impact on the existence of convectons in thermally dominated regimes (section 6.3.4).

6.1 DOUBLY DIFFUSIVE CONVECTION IN A CLOSED CAVITY

6.1.1 MOTIVATION FOR BOUNDARY CONDITIONS

We have so far considered domains with periodic boundary conditions in the vertical direction and systems where the imposed horizontal temperature and solutal gradients provide exactly balancing effects on the total fluid density ($N = -1$). These conditions allow a motionless conduction state to exist for all Rayleigh numbers and for this trivial base state to destabilise in pitchfork bifurcations that lead to primary branches of periodic states, as has been discussed in the previous chapters.

However, when the buoyancy ratio is varied away from the balanced case, the imposed horizontal temperature and solute gradients generate a vertical shear flow of the form (e.g., modified from [163]):

$$w = \frac{1}{6}Ra(1+N)x(1-x^2) \quad \text{for} \quad 0 \leqslant x \leqslant 1, \tag{6.2}$$

which replaces the motionless conduction state as the base state for the system. This base flow clearly breaks the reflection symmetry about the centre of the domain and we consequently expect for the steady states to drift vertically. For example, we find that branches of periodic convection when $N = -1$ become branches of periodic travelling waves when $N \neq -1$, while steady convectons become pulses of convection that travel vertically in the base shear flow. However, accurate study of these travelling states proved to be numerically challenging because time-stepping only allows us to obtain stable states and extending the numerical continuation code to follow travelling states and periodic orbits (e.g., [120, 182]) would have been difficult in the limited time frame for this project.

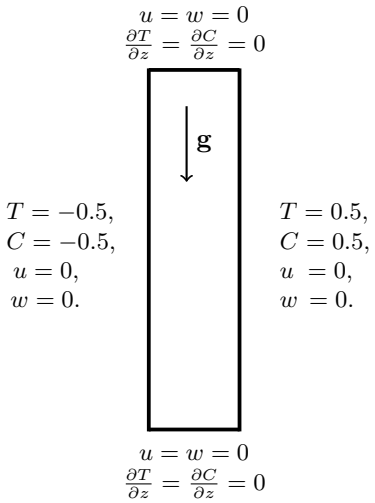

Figure 6.1: Representation of the non-dimensional closed cavity with no-slip boundary conditions.

6.1.2 NO-SLIP BOUNDARY CONDITIONS

Hence, for this chapter, we decided to study the effects of the buoyancy ratio in a closed domain with no-slip boundary conditions on each wall. With this choice, the base flow is a large-scale recirculating flow for $N \neq -1$ and stationary convectons exist and can be numerically continued. The governing equations for the system of doubly diffusive convection remain as

$$\frac{1}{Pr}\left(\frac{\partial \mathbf{u}}{\partial t} + \mathbf{u}\cdot\nabla\mathbf{u}\right) = -\nabla p + \nabla^2\mathbf{u} + Ra\,(T + NC)\,\hat{\mathbf{z}}, \tag{6.3}$$

$$\nabla\cdot\mathbf{u} = 0, \tag{6.4}$$

$$\frac{\partial T}{\partial t} + \mathbf{u}\cdot\nabla T = \nabla^2 T, \tag{6.5}$$

$$\frac{\partial C}{\partial t} + \mathbf{u}\cdot\nabla C = \frac{1}{Le}\nabla^2 C, \tag{6.6}$$

where we fix $Le = 5$ and $Pr = 1$, allow the buoyancy ratio N to vary and treat the Rayleigh number Ra as a bifurcation parameter. The system (6.3)–(6.6) is now considered in the closed cavity that is bounded by the vertical sidewalls at $x = \pm 0.5$ and horizontal end walls at $z = 0, L_z$, as depicted in figure 6.1. Here, L_z is the vertical length of the

domain and assumes one of $L_z = 4\lambda_c$, $5\lambda_c$ or $12\lambda_c$, where λ_c is the critical wavelength of the primary bifurcation with periodic boundary conditions. The following boundary conditions are imposed on the sidewalls:

$$u = 0, \quad w = 0, \quad -\frac{\partial p}{\partial x} + \frac{\partial^2 u}{\partial x^2} = 0, \quad T = -0.5, \quad C = -0.5 \quad \text{on} \quad x = -0.5, \tag{6.7}$$

$$u = 0, \quad w = 0, \quad -\frac{\partial p}{\partial x} + \frac{\partial^2 u}{\partial x^2} = 0, \quad T = \ 0.5, \quad C = \ 0.5 \quad \text{on} \quad x = 0.5, \tag{6.8}$$

$$u = 0, \quad w = 0, \quad -\frac{\partial p}{\partial x} + \frac{\partial^2 u}{\partial x^2} = 0, \quad \frac{\partial T}{\partial z} = \ 0, \quad \frac{\partial C}{\partial z} = \ 0 \quad \text{on} \quad z = 0, L_z, \tag{6.9}$$

where, in addition to the fluid velocity vanishing on the four sidewalls owing to the no-slip boundary conditions, the domain allows no thermal or solutal flux through the horizontal end walls.

This choice of domain removes the translational symmetry that was seen with the periodic boundary conditions and thereby also removes the possibility of the conduction state when $N = -1$ undergoing a circle of pitchfork bifurcations, found by Xin et al. [191], and the presence of domain-filling periodic states. These effects thus influence both where the branches of convectons bifurcate from and where they terminate, as will be seen in sections 6.2.1 and 6.2.2. The reflection symmetry about the centre of the domain is preserved, however, and may be expressed as

$$S_\Delta : (x, z) \mapsto (-x, -z), \quad (u, w, T, C) \mapsto -(u, w, T, C). \tag{6.10}$$

While this system admits states that break this reflection symmetry (for example, the two-dimensional equivalent to the two-roll wall-attached state found by Beaume et al. [14]), in this initial study, we will only consider states that preserve this symmetry.

Again, the results in this chapter were obtained via numerical continuation of branches using a spectral element numerical method based on a Gauss–Lobatto–Legendre discretisation and supplemented by Stokes preconditioning. Each element of the numerical domain was discretised using 25 nodes in both the x and z directions, while the number of spectral elements depends upon the vertical extent of the cavity and are detailed in

L_z	ne_x	n_x	n_z
$4\lambda_c$	8	25	25
$5\lambda_c$	10	25	25
$12\lambda_c$	24	25	25

Table 6.1: Discretisations used in the spectral element code for the numerical continuation of the system of doubly diffusive convection for the three domain sizes considered. The domain is discretised using ne_x spectral elements, with each element containing n_x nodes in the $x-$direction and n_z nodes in the $z-$direction.

table 6.1. Results are typically presented using bifurcation diagrams that, unless otherwise stated, present the total kinetic energy:

$$E = \int_0^1 \int_0^{L_z} \left(\frac{1}{2} \left(u^2 + w^2 \right) \right) dz\, dx, \tag{6.11}$$

of the steady state as a function of the Rayleigh number, or using streamfunctions of the steady states. In contrast to the previous notation for plotting streamfunctions, two scales will be used to depict both weak and strong flows in the same figure. A logarithmic scale is shown using black (clockwise flow) and grey (anticlockwise flow) streamlines, while a linear scale is shown using red (clockwise flow) and blue (anticlockwise flow) streamlines.

6.2 BALANCED SYSTEM WHEN $N = -1$

We begin by detailing key properties of the balanced system with no-slip boundary conditions in a bounded domain as there are some differences compared to applying periodic boundary conditions. The system is reviewed in three parts: initially, we consider primary bifurcations of the conduction state; then, we consider the structure of the convecton branches; finally, we introduce some of the anticonvectons that are found.

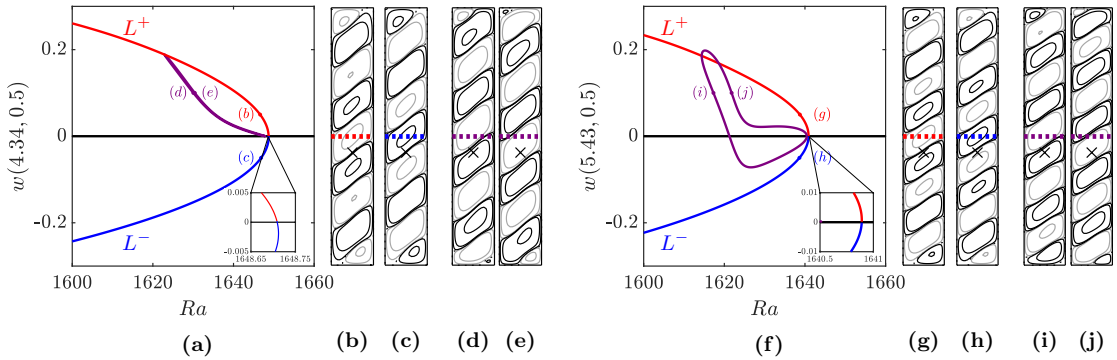

Figure 6.2: First primary pitchfork and transcritical bifurcations of the conduction state in domains with vertical extent: (a)–(e) $L_z = 4\lambda_c$ and (f)–(j) $L_z = 5\lambda_c$. The bifurcation diagrams (a) and (f) show the vertical velocity of states at the point marked by the black crosses in the streamfunction plots against the Rayleigh number. The following branches are shown: conduction state (black), L^+ (red), L^- (blue) and branches of asymmetric states that bifurcate from the pitchfork bifurcation (purple). The insets provide a magnification of the first transcritical bifurcation. The remaining panels present the streamfunction of states marked in the bifurcation diagrams using contour values: $[-10^{-3}, -10^{-2}, -10^{-1}]$ (grey); and $[10^{-3}, 10^{-2}, 10^{-1}]$ (black).

6.2.1 PRIMARY BIFURCATIONS OF THE CONDUCTION STATE

With these no-slip boundary conditions in the balanced case ($N = -1$), the conduction state can destabilise in either transcritical or pitchfork bifurcations [70, 191] when the buoyancy force driven by the sidewall heating overcomes the viscous dissipation associated with fluid motion. Transcritical bifurcations arise when centro-symmetric eigenmodes, which have a roll centred in the middle of the domain, destabilise, while pitchfork bifurcations arise when anti-centro-symmetric eigenmodes destabilise. By varying the size of the domain, Ghorayeb and Mojtabi [70] found that the ordering of the first set of transcritical and pitchfork bifurcations switches and that the two bifurcations occur in quicker succession in larger domains. Thus, we start by illustrating these primary bifurcations in small domains ($L_z = 4\lambda_c \approx 9.93$ and $L_z = 5\lambda_c \approx 12.4$), before considering them in the larger domain with $L_z = 12\lambda_c \approx 29.8$, which will later be used to investigate the effects of taking $N \neq -1$ on spatially localised states.

Figure 6.2 presents the bifurcation diagrams showing the first two bifurcations of

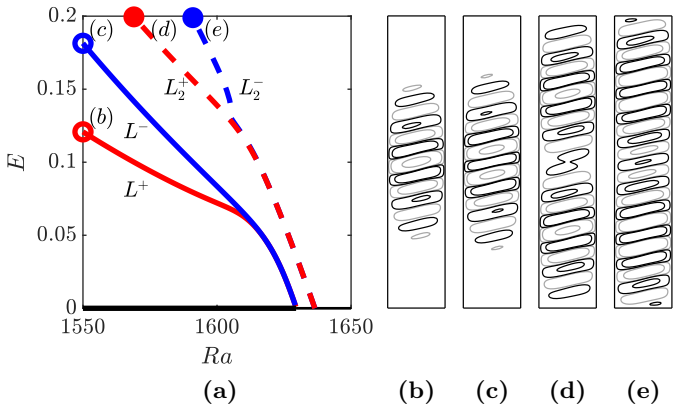

Figure 6.3: First two transcritical bifurcations for $N = -1$, $Le = 5$ and $Pr = 1$ in a domain with $L_z = 12\lambda_c$ and no-slip boundary conditions. (a) Bifurcation diagram showing the branches that originate from these bifurcations. (b)–(e) Streamfunctions along the four main branches: (b) L^+, (c) L^-, (d) L_2^+ and (e) L_2^-. The contour values used were: $[-10^{-3}, -10^{-2}, -10^{-1}]$ (grey); and $[10^{-3}, 10^{-2}, 10^{-1}]$ (black).

the conduction state when $L_z = 4\lambda_c$ (figure 6.2(a)–(e)) and $L_z = 5\lambda_c$ $L_z = 4\lambda_c$ (figure 6.2(f)–(j)). In both of these domains, the conduction state first destabilises in a pitchfork bifurcation and the resulting pair of branches consist of asymmetric states like those shown in figures 6.2(d), (e), (i) and (j). These branches terminate on L^+ (red), the branch containing spatially modulated states with an anticlockwise central roll that bifurcates from the following transcritical bifurcation, together with L^- (blue), the branch containing spatially modulated states with a clockwise central roll. The insets in figures 6.2(a) and (f) highlight the transcritical nature of this primary bifurcation and how the supercritical branch undergoes a saddle-node bifurcation shortly after onset, in an analogous manner to the three-dimensional behaviour observed by Beaume et al. [14]. The initially supercritical branch then proceeds to head towards lower Rayleigh numbers so that the behaviour on a larger scale resembles that of a pitchfork bifurcation. Which of the primary branches L^+ and L^- is initially supercritical depends on the domain size and we find that L^- (blue) bifurcates supercritically when $L_z = 4\lambda_c$ while L^+ (red) bifurcates supercritically when $L_z = 5\lambda_c$. The streamfunction panels (c) and (g) indicate that such dependence arises because states on these branches have clockwise rolls in the top left and bottom right of the domain, whereas the corresponding rolls are

anticlockwise in states on the subcritical branch (see panels (b) and (h)).

Figure 6.3 presents the branches bifurcating from the first two transcritical bifurcations of the conduction state in the larger domain with $L_z = 12\lambda_c \approx 29.8$. The conduction state first destabilises in a pitchfork bifurcation (not shown owing to the short extent of the bifurcating branches) and shortly after in a transcritical bifurcation at $Ra \approx 1629.6$, where the branches L^+ and L^- bifurcate subcritically and supercritically, respectively. These branches remain indistinguishable at small amplitude on the scale shown in figure 6.3(a) owing to the supercritical branch turning around at a saddle node shortly after onset.

Since the no-slip boundary conditions on the horizontal end walls lead to enhanced viscous dissipation, the critical eigenmodes associated with this transcritical bifurcation weaken towards the ends of the domain. They also differ through the flow direction of the central convection roll in that the roll is anticlockwise on L^+ (figure 6.3(b)) and clockwise on L^- (figure 6.3(c)). Thus, owing to both the amplitude modulation and the nonlinear mechanism that favours anticlockwise convection rolls as the branches are followed towards lower Rayleigh numbers and larger amplitudes, this difference leads to convectons with an odd number of localised rolls lying on L^+ and those with an even number of localised rolls lying on L^-, as was previously found with periodic boundary conditions [24].

Beyond this first transcritical bifurcation, the conduction state undergoes further bifurcations associated with modes of different wavelengths destabilising. For example, the conduction state undergoes a further transcritical bifurcation at $Ra \approx 1636.5$, where the branches of two-pulse states (L_2^+ and L_2^-) bifurcate. Like their single-pulse counterparts, states on these branches become amplitude modulated as each branch is followed towards larger amplitudes (see figures 6.3(d) and (e)). However, the primary bifurcation of the conduction state at $Ra \approx 1629.6$ means that these multi-pulse states are more unstable than the single pulse states on L^+ or L^-.

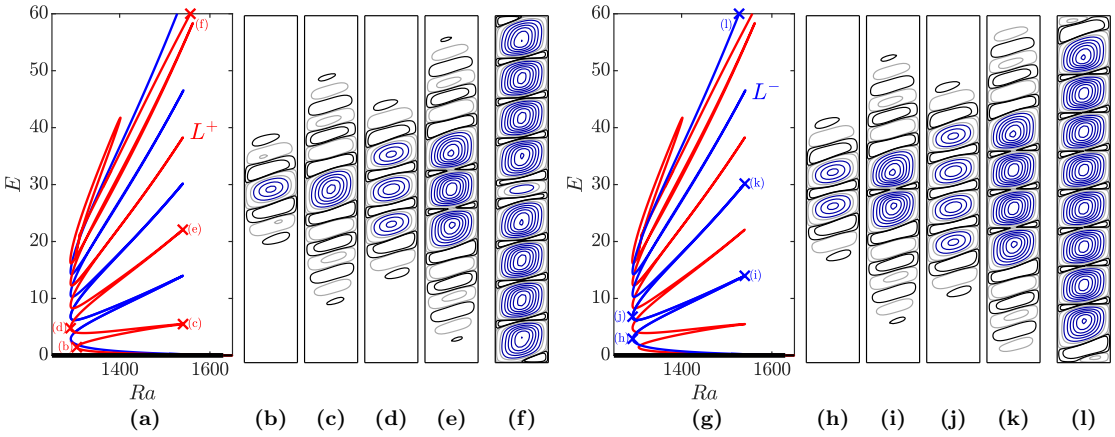

Figure 6.4: Convecton branches and streamfunction profiles for $N = -1$, $Pr = 1$ and $Le = 5$. (a) and (g) Bifurcation diagram showing branches corresponding to convectons with an odd (L^+) and even (L^-) number of strong anticlockwise central rolls, which are shown in red and blue, respectively. (b)–(e) Streamfunction profiles of the first four saddle nodes along L_1^-. (f) Streamfunction profile of large-amplitude state on L^+. (h)–(k) Streamfunction profiles of the first four saddle nodes along L_1^+. (l) Streamfunction profile of large-amplitude state on L^-. Contours are shown using linear (blue) and logarithmic (black and grey) scales and take the values: $[-10^{-3}, -10^{-2}, -10^{-1}]$ (grey); $[10^{-3}, 10^{-2}, 10^{-1}]$ (black); $[-0.2, -0.4, -0.6, ...]$ (blue).

6.2.2 CONVECTONS

The convecton branches, L^+ and L^-, head away from the primary transcritical bifurcation of the conduction state and towards lower Rayleigh numbers before first turning around at a left saddle node located at $Ra \approx 1305$ for L^+ (figure 6.4(b)) or $Ra \approx 1292$ for L^- (figure 6.4(h)). The amplitude modulation of the states increases along these branch segments, which results in the convective motion occupying a smaller proportion of the domain, as may be seen by comparing figures 6.3(b) and (c) with figures 6.4(b) and (h), respectively. The central anticlockwise rolls also strengthen faster than the clockwise rolls, which maintain flow with a similar order of magnitude along these low-energy branch segments.

After the first left saddle nodes, the two convecton branches proceed to undergo homoclinic snaking over the interval $1291 < Ra < 1540$, as seen in figures 6.4(a) and (g), which is the same pinning region as when periodic boundary conditions are imposed in the

vertical direction with the same Prandtl and Lewis numbers. The convecton rolls also exhibit similar strengthening and nucleation behaviour as the branches are followed to large amplitude, as shown by the changes in the streamfunction plots between convectons at the first four saddle nodes on L^+ (figures 6.4(b)–(e)) and L^- (figures 6.4(h)–(k)). Between the left and right saddle nodes, the anticlockwise rolls strengthen and become larger. This reduces the distance between adjacent anticlockwise rolls as the dividing weak clockwise rolls are squashed so that by the right saddle node they split into two smaller rolls, which are pushed towards either sidewall. Outside of these central rolls, weak counterrotating rolls strengthen with increasing Rayleigh number, but since the growth occurs in an amplitude-modulated manner, fluid velocities near the end walls remain small. Only the anticlockwise rolls adjacent to the strong central rolls strengthen as the convecton branches proceed towards the following left saddle node, with both the strong central rolls and the weak counterrotating rolls decaying, which results in the number of strong central anticlockwise rolls increasing by two between successive left saddle nodes.

This type of snaking behaviour continues until anticlockwise rolls almost fill the domain, as was also previously found with periodic boundary conditions. In this case, however, there are no domain-filling spatially periodic states that the convecton branches can terminate on and they instead extend towards large amplitudes as defect states [26, 80], like those in figures 6.4(f) and (l). For example, on L^+, after reaching a nine-roll state at a left saddle node around $Ra \approx 1302$ and $E \approx 17.4$, the central roll decays as the branch continues towards higher Rayleigh numbers while the remaining eight anticlockwise rolls strengthen, as seen in figure 6.4(f). The other convecton branch, L^-, exhibits alternative behaviour, where an eight-roll state, like figure 6.4(l), strengthens with increasing Rayleigh number until $Ra \approx 2210$, where the end anticlockwise rolls split into two pairs of anticlockwise rolls and the branch returns to lower Rayleigh numbers as a ten-roll state (not shown). The specific details of this large-amplitude behaviour depends on the domain size, so will not be considered any further here, although we will note that behaviour in systems with non-periodic boundary conditions is typically more compli-

cated than with periodic boundary conditions. Indeed, Houghton and Knobloch [80] found complex behaviour in the Swift–Hohenberg equation in a finite domain, where branches repeatedly snaked up and down the pinning region with what they called "far" from Neumann boundary conditions.

6.2.3 ANTICONVECTONS

Branches of anticonvectons—localised states where rolls are attached to both end walls and separated by a void region—are a distinguishing feature of the system with no-slip boundary conditions. Mercader et al. [130] first found these states in binary fluid convection and attributed their presence to the breaking of the translational invariance associated with periodic boundary conditions, thereby separating branches that correspond to convectons centred half a domain apart. Owing to this similarity, branches of anticonvectons also undergo homoclinic snaking within the same pinning region as the convectons. Anticonvectons also exist in this system of natural doubly diffusive convection but their properties tend to be more complex than those in binary fluid convection because of the nonlinear mechanism that favours anticlockwise rolls.

Figure 6.5 shows two types of anticonvectons that lie on snaking branches that we refer to as A (shown in black) and $\tilde{A}$ (shown in purple). These branches appear to connect on the lowest branch segment, although this could not be confirmed owing to numerical difficulties that most likely arose because of the multitude of anticonvectons with similar roll positions in close proximity to each other. Nevertheless, we believe the two branches to connect since the corresponding branches when $N \neq -1$ do connect and could be numerically continued without difficulty (see figure 6.16). Both anticonvecton branches proceed to snake upwards within the interval $1291 < Ra < 1541$, with both types of anticonvectons extending by a pair of anticlockwise rolls on the interior side of the existing rolls over a single snaking oscillation (e.g., compare panels (b), (d) and (f) or (h), (j) and (l)). The oscillations continue until 6-roll states (shown in figures 6.5(f) and (l)) are obtained and the oscillations are subsequently affected by finite domain effects, as was seen for the convecton branches in figure 6.4.

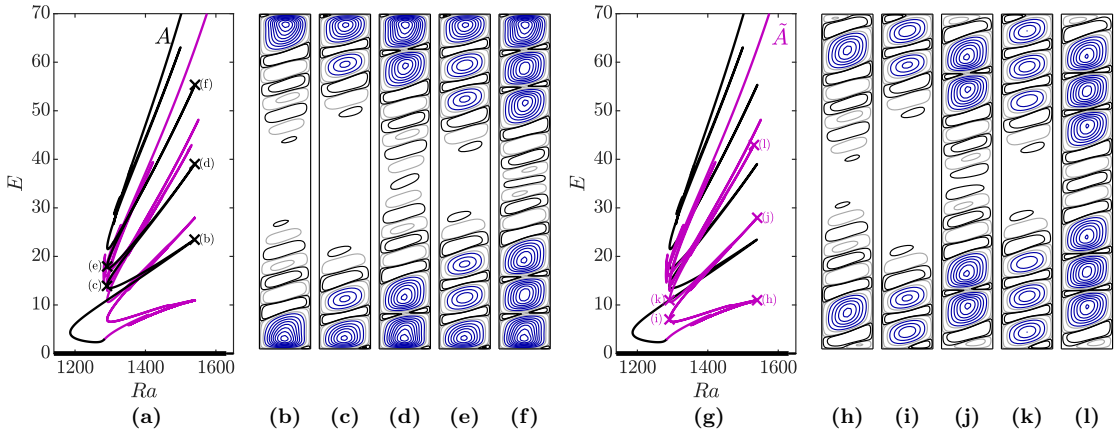

Figure 6.5: Anticonvecton branches and streamfunction profiles for $N = -1$, $Pr = 1$ and $Le = 5$. (a) and (g) Bifurcation diagrams corresponding to branches with two types of anticonvectons A (black) and $\tilde{A}$ (purple) when $N = -1$. (b)–(f) Streamfunctions of steady states at the saddle nodes of the snaking anticonvecton branch A. (h)–(l) Streamfunctions of steady states at the saddle nodes of the snaking anticonvecton branch $\tilde{A}$. Contours are shown using linear (blue) and logarithmic (black and grey) scales and take the values: $[-10^{-3}, -10^{-2}, -10^{-1}]$ (grey); $[10^{-3}, 10^{-2}, 10^{-1}]$ (black); $[-0.2, -0.4, -0.6, ...]$ (blue).

The form of the anticonvectons differ between the two branches. In states lying on the branch A (figures 6.5(b)–(f)), the anticlockwise rolls attached to the end walls are not elliptical like those in convectons, but rather appear to be squashed towards either the top or the bottom wall, with the flow being nearly horizontal along these end walls. The end rolls weaken as the branch A passes from the right saddle nodes (e.g., (b), (d) and (f)) to the following left saddle node (e.g., (c) and (e)). This pushes the anticlockwise rolls away from the top left and bottom right corners of the domain, thereby leaving space for the weak clockwise rolls in these corners to strengthen and grow. The anticlockwise rolls that strengthen within the interior of the domain are not affected by the horizontal end walls, however, and display similar forms to the rolls that nucleate in the convectons seen in figure 6.4.

Anticonvectons along the second branch, $\tilde{A}$, similarly extend by anticlockwise rolls strengthening on the interior side of the state between right and left saddle nodes. However, this branch additionally exhibits a more complex series of changes than those

along the first anticonvecton branch, A. The strong anticlockwise end rolls are no longer squashed against the horizontal walls, but rather separated from them by weaker rolls. These weak rolls exhibit new behaviour that is responsible for the vertical translation of the strong anticlockwise rolls that occurs over a single snaking oscillation of $\tilde{A}$, as seen in figures 6.5(h)–(l). Following $\tilde{A}$ between a right saddle node and the next left saddle node, we see how the small, weak anticlockwise corner rolls weaken and disappear (e.g., between (h) and (i)). The clockwise rolls between each weak corner roll and the adjacent strong anticlockwise roll also weaken as the Rayleigh number decreases and become smaller to occupy only a small triangular region in the top left and bottom right corners of the domain instead of the full horizontal extent of the domain as they do at the right saddle nodes. The weakening of this pair of rolls results in the strong anticlockwise rolls translating towards the end walls as seen in figure 6.5. This process occurs in reverse between each left saddle node and the following right saddle node, which leads to the weak end rolls strengthening and the strong anticlockwise rolls translating back towards the centre of the domain.

6.3 UNBALANCED SYSTEMS

6.3.1 LARGE-SCALE FLOW

We now turn our attention to considering what happens to these states and branches as the buoyancy ratio varies away from $N = -1$ and we enter unbalanced regimes. The first notable difference that we find in these systems is that they do not admit the conduction state as a steady solution. Instead, the basic state consists of a large-scale recirculating flow that develops from low Rayleigh numbers. Basic properties of this large-scale flow can be ascertained by considering a parallel flow approximation similar to those applied in natural convection (e.g., [6]) or binary fluid convection in porous media (e.g., [4]).

To achieve this, we consider the centre of a sufficiently long domain and assume that the horizontal end walls have negligible impact on the flow and that there is purely

conductive heat and solute transport between the sidewalls, i.e., $T = C = x$. The latter assumption means that the fluid density, generally defined

$$\rho = \rho_0 + \rho_T \Delta T (T + NC), \tag{6.12}$$

where ρ_0 is the reference density of the fluid at $x = 0$, is approximated by

$$\rho \approx \rho_0 + \rho_T \Delta T (1 + N) x. \tag{6.13}$$

Thus, the fluid density is uniform when $N = -1$, but exhibits linear horizontal dependence when $N \neq -1$. Noting that $\rho_T < 0$, i.e., that density decreases with increasing temperature, this approximate density profile shows that when $N > -1$ ($N < -1$), fluid at the right sidewall is less dense (more dense) than fluid at the left sidewall and that this density difference increases with increasingly imbalanced systems.

These horizontal density gradients are a source of vorticity, which may be seen from the vorticity equation:

$$\frac{1}{Pr}\left(\frac{\partial \omega}{\partial t} + \mathbf{u} \cdot \nabla \omega\right) = \nabla^2 \omega - Ra\left(\frac{\partial \Theta}{\partial x} + N\frac{\partial \Phi}{\partial x}\right) - Ra(1 + N), \tag{6.14}$$

where $\omega = \hat{\mathbf{y}} \cdot \nabla \times \mathbf{u}$ is the vorticity and $\Theta = T - x$, $\Phi = C - x$ are the deviations from the linear profiles for temperature and solutal concentration. Assuming steady unidirectional flow in the vertical direction with $\Theta = \Phi = 0$, we find that the vorticity satisfies

$$\nabla^2 \omega = Ra(1 + N), \tag{6.15}$$

and that the vertical velocity profile may be approximated by

$$w(x, z) \approx -\frac{1}{24} Ra(1 + N)\, x(2x - 1)(2x + 1), \tag{6.16}$$

which we see resembles that found in natural convection [6], except with a Rayleigh number that has been modified by the deviation of the buoyancy ratio away from

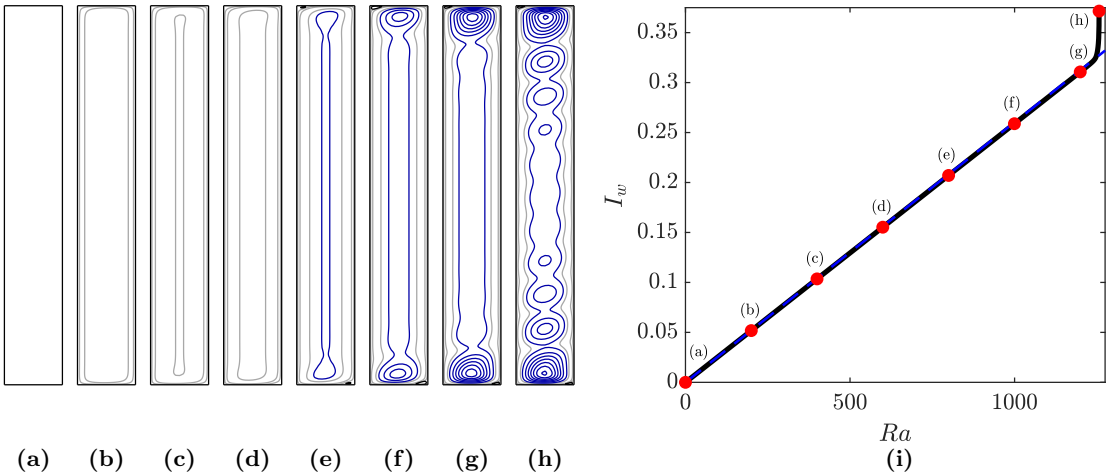

Figure 6.6: Development of the anticlockwise large-scale flow with Ra until the first right saddle node at $Ra \approx 1257$ when $N = -0.9$. (a)–(h) Streamfunctions of the large-scale flow at the Rayleigh numbers marked in (i). Contours are shown using linear (blue) and logarithmic (black and grey) scales and take the values: $[-10^{-3}, -10^{-2}, -10^{-1}]$ (grey); $[10^{-3}, 10^{-2}, 10^{-1}]$ (black); $[-0.2, -0.4, -0.6, ...]$ (blue). (i) Plot showing I_w (6.17) for the large-scale flow at different Rayleigh numbers. The blue dashed line indicates the relationship $I_w = \frac{1}{384} Ra(1+N)$, obtained from the analytical approximation (6.16).

$N = -1$.

Figures 6.6(a)–(h) illustrate this vertical shear flow within the centre of the domain at low Rayleigh numbers for $N = -0.9$. We see that the strength of the flow increases with Rayleigh number, as is expected from the approximation (6.16). This is further evidenced by panel (i), which shows that the quantity

$$I_w = \int_0^{0.5} w\left(x, z = \frac{L_z}{2}\right) dx, \tag{6.17}$$

initially increases linearly with Rayleigh number, which is in agreement with the analytical approximation (6.16) where $I_w = \frac{1}{384} Ra(1+N)$.

The approximation given in (6.16) is not valid near the horizontal end walls of the domain since the vertical shear flow is incompatible with the associated no-slip boundary conditions. Instead, we find that the vertical flow is forced sideways near the end walls to generate a domain-filling recirculating flow with anticlockwise circulation in ther-

mally dominated flows ($N > -1$) or clockwise circulation in solutally dominated flows ($N < -1$).

The approximation (6.16) further breaks down towards larger Rayleigh numbers, but the manner in which this occurs depends on the value of the buoyancy ratio as we will see throughout the remainder of this chapter. When $N = -0.9$, for example, we see that this breakdown first occurs via the formation of secondary rolls near the horizontal end walls, as seen in figures 6.6(d)–(g). The origin of these rolls is doubly diffusive in nature, which can be seen through the following argument in weakly thermally dominated flows. As the fluid flows in an anticlockwise direction alongside the horizontal end walls, hotter and solute-rich fluid is drawn from the top right corner of the domain to the left. This leftward moving flow is denser than the ambient fluid owing to the higher solute concentration, so will sink and flow down the left sidewall according to (6.16). This fluid motion enhances the horizontal density gradient between sidewalls and generates negative vorticity, which, when sufficiently large, leads to an anticlockwise secondary roll at the top of the domain. An analogous secondary roll forms in the bottom left corner of the domain owing to the large-scale flow preserves the S_Δ symmetry. These rolls strengthen with increasing Rayleigh number and we see the formation of further secondary rolls near the first right saddle node of the branch (figure 6.5(h)). These rolls influence the vertical velocity profile along the horizontal midline and explain the deviation of I_w away from the linear relationship when $Ra > 1230$.

We finally note that the formation of these secondary rolls, via doubly diffusive effects, differs from the initial formation of secondary rolls in natural convection [185], which occur via inertial effects. We also found inertia-driven secondary rolls in this system; however, these were at considerably higher Rayleigh numbers so will not be discussed in this thesis.

6.3.2 SMALL-AMPLITUDE UNFOLDING

In the balanced system we saw that the two branches of convectons, L^+ and L^-, bifurcate from a primary transcritical bifurcation of the conduction state at $Ra \approx 1629.6$ in figure 6.3. This does not occur in the unbalanced systems as the primary transcritical bifurcation unfolds when $N \neq -1$ since the large-scale flow enhances one of the eigenmodes of the transcritical bifurcation, while diminishing the other. To understand what happens to convectons at large amplitude, we therefore start by exploring this unfolding at small amplitude and extend earlier results by Bardan et al. [5], who considered the unfolding for two choices of N in small domains.

SMALL DOMAINS

As in the balanced case with $N = -1$, we first investigate the unfolding in smaller domains whose vertical extent is either $L_z = 4\lambda_c \approx 9.93$ (left set of columns in figure 6.7) or $L_z = 5\lambda_c \approx 12.4$ (right set of columns in figure 6.7), both for the simplicity of interpreting the results and to determine how the branches bifurcating from the first pitchfork bifurcation change under small variations to N. Regardless of the buoyancy ratio and domain size, the branches containing states with a clockwise central roll (black in the streamfunction plots in figure 6.7) extend to large amplitude as the L^- branch (blue), while those with an anticlockwise central roll extend to larger amplitudes as L^+ (red).

Figure 6.7 indicates how the unfolding of the primary transcritical bifurcation varies with both domain size and buoyancy ratio. In particular, when $N = -0.9999$, we find that the branch of large-scale flow developing from $Ra = 0$ connects to the branch initially associated with the states containing weak clockwise rolls in the top left and bottom right corners of the domain, i.e., L^- when $L_z = 4\lambda_c$ (figure 6.7(b)) and L^+ when $L_z = 5\lambda_c$ (figure 6.7(e)). Such behaviour likely arises because the anticlockwise roll inclined downwards from the top right corner of the domain (or the symmetry-related roll in the bottom left corner) reinforces the large-scale flow with the same sense of rotation, while the weaker clockwise corner rolls form via viscous effects. Since the number

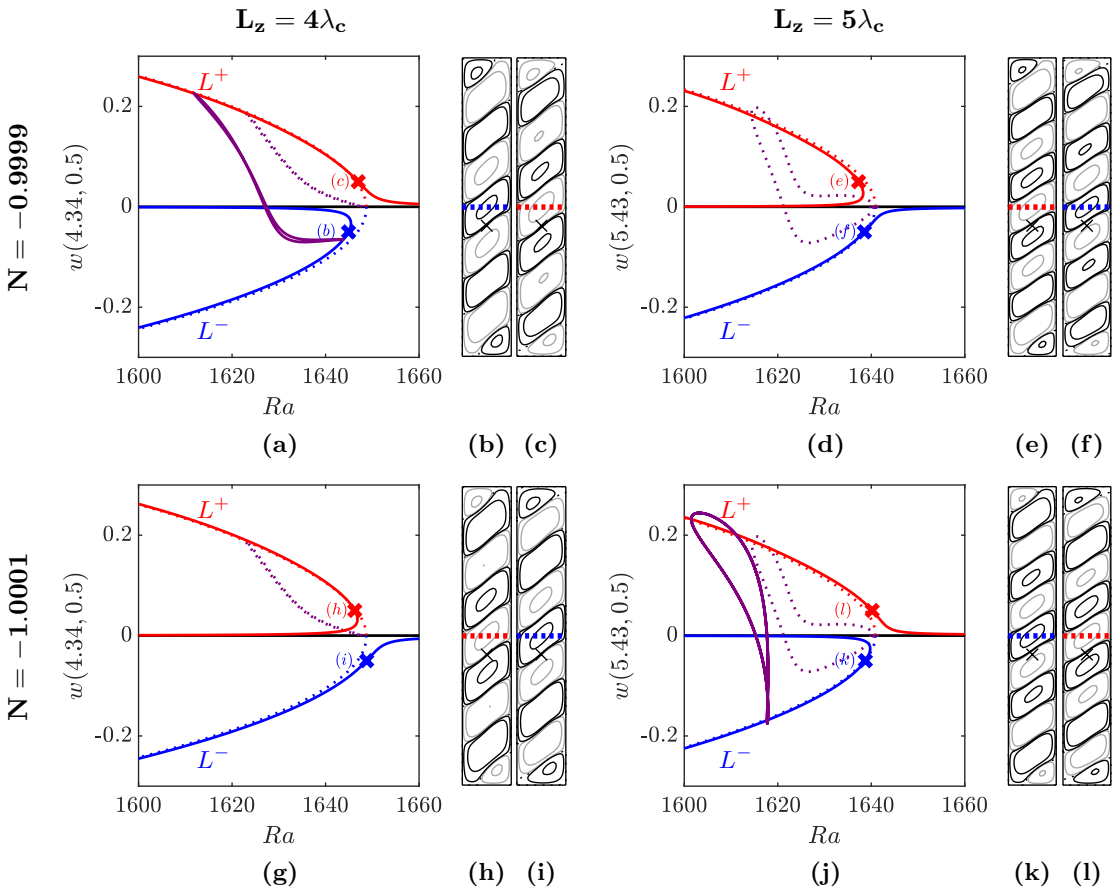

Figure 6.7: Unfolding of the primary transcritical bifurcation in small domains of length $L_z = 4\lambda_c \approx 9.93$ (left set of panels) and $L_z = 5\lambda_c \approx 12.4$ (right set of panels) for $N = -0.9999$ (top row) and $N = -1.0001$ (bottom row). (a), (d), (g), (j) Bifurcation diagrams showing the vertical velocity of states at the point marked by black crosses in the streamfunction plots against Rayleigh number for branches with $N = -1$ (dotted lines) and either (a), (d) $N = -0.9999$ or (g), (j) $N = -1.0001$ (solid lines). The colours red, blue and purple indicate L^+, L^- and branches of asymmetric states, respectively. The streamfunction plots are shown at the marked points in the bifurcation diagrams. The horizontal midline is shown using a red or blue dotted line to indicate whether the state lies on L^- (blue) or L^+ (red). The contour values used were: $[-10^{-3}, -10^{-2}, -10^{-1}]$ (grey); and $[10^{-3}, 10^{-2}, 10^{-1}]$ (black).

of pairs of rolls in the eigenmode associated with the transcritical bifurcation when $N = -1$ varies with the domain size, the branch containing states with these clockwise corner rolls also changes and consequently so does the unfolding of the transcritical bifurcation. The results when $N = -1.0001$ are analogous and we find that the branch of large-scale flow developing from $Ra = 0$ now connects to the branch initially associated with states containing weak anticlockwise rolls in the top left and bottom right corners of the domain, i.e., L^+ when $L_z = 4\lambda_c$ (figure 6.7(h)) and L^- when $L_z = 5\lambda_c$ (figure 6.7(k)).

In figure 6.2, we saw that when $N = -1$ the conduction state undergoes a pitchfork bifurcation prior to the transcritical bifurcation and the resulting branches (purple dotted lines in figure 6.7) terminate at a pitchfork bifurcation on L^+ (red) for both $L_z \approx 4\lambda_c$ and $L_z \approx 5\lambda_c$. Unlike the transcritical bifurcation considered above, this pitchfork bifurcation does not unfold as the buoyancy ratio varies away from $N = -1$ because the large-scale flow preserves the S_Δ symmetry of the system [5]. Nevertheless, this bifurcation and the bifurcating branches are affected both by the buoyancy ratio and the domain size, as illustrated by the presence or absence of purple lines in figure 6.7.

Under small variations in N, the destabilising pitchfork bifurcation of the conduction state instead occurs on the branch that originates from $Ra = 0$ (i.e., L^- (blue) when $L_z = 4\lambda_c$, $N > -1$ or $L_z = 5\lambda_c$, $N < -1$ and L^+ (red) when $L_z = 4\lambda_c$, $N < -1$ or $L_z = 5\lambda_c$, $N > -1$), but the bifurcating branches continue to terminate on L^+ for both domain sizes. This leads to short branch segments that either connect L^- to L^+ or connect L^+ to itself. The former connections persist as N is varied away from the balanced case, as evidenced in figures 6.7(a) and (j). Whereas in the latter case, the two pitchfork bifurcations approach each other on L^+ and ultimately collide (at $N \approx -0.999902$ when $L_z = 5\lambda_c$ or $N \approx -1.0009$ when $L_z = 4\lambda_c$), so that the connections are not found in the bifurcation diagrams presented in figures 6.7(d) and (g).

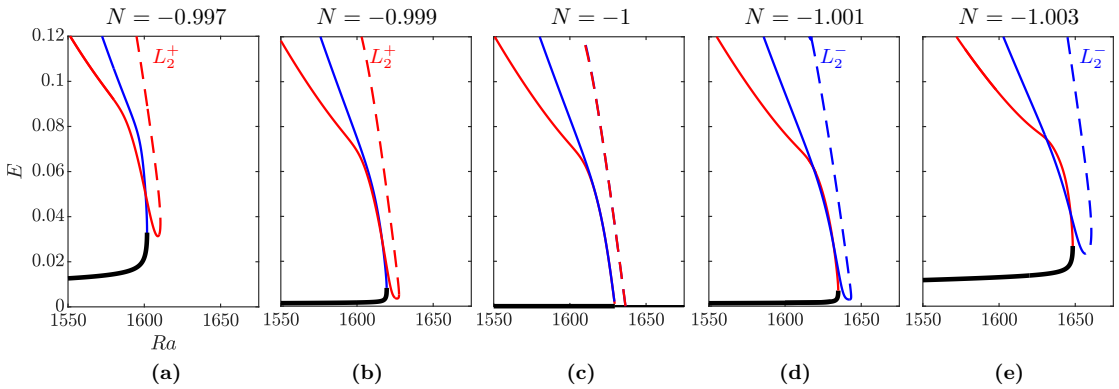

Figure 6.8: Unfolding of the primary bifurcation in a domain with $L_z \approx 29.8$ for N between (a) $N = -0.997$ and (e) $N = -1.003$. The branch segments shown include the conduction state or large-scale flow (black), L^- (blue), L^+ (red) and the branch of two-pulse states, L_2^+ (red dashed) or L_2^- (blue dashed), that connects to one of the convecton branches.

LARGE DOMAINS

Since we are primarily interested in how convectons are affected by variations in the buoyancy ratio, we proceed by determining the unfolding of the primary transcritical bifurcation in a larger domain of $L_z = 12\lambda_c \approx 29.8$, as this will indicate the origin of these localised states. This unfolding is illustrated in figure 6.8, where we see similarities to the unfolding in the smaller domain with $L_z = 4\lambda_c \approx 9.93$ (figures 6.7(a) and(g)). In particular, we find that the branch of large-scale flow originating from low Rayleigh numbers connects to L^- when $N > -1$ and to L^+ when $N < -1$. As with the smaller domains, the second convecton branch connects at small amplitude to the branch of large-scale flow states following the primary transcritical bifurcation. However, this behaviour is only clearly seen over a small range of Rayleigh numbers in figure 6.8 since this branch segment proceeds to connect to a branch of two-pulse convectons after the unfolding of the second transcritical bifurcation. Here, we find that L^+ connects to L_2^+ when $N > -1$, while L^- connects to L_2^- when $N < -1$. We should note that this result is likely to be sensitive to the domain size, however.

Details of the unfolding are further seen in figure 6.9, which shows an enlargement of

the bifurcation diagram for $N = -0.999$ (figure 6.8(b)), together with streamfunctions of a small amplitude along each branch segment. As the branch of weak anticlockwise base flow states (e.g., figure 6.9(b)) is followed towards larger Rayleigh numbers, the single large roll breaks up into a series of weak counterrotating rolls with a clockwise roll in the centre of the domain (figure 6.9(c)). The central rolls proceed to strengthen along L^-, while the outer rolls weaken and are replaced by a pair of weak anticlockwise flows that extend vertically from the central rolls to either vertical end of the domain (figure 6.9(d)).

Convectons on L^+ at small amplitude assume a similar form with a central anticlockwise roll being immediately surrounded by weak counterrotating rolls and then by a pair of large anticlockwise rolls that fill the remainder of the domain (figure 6.9(e)). The large outer rolls break up as the branch is followed towards states with lower kinetic energy that originated from the conduction state (figure 6.9(f)). The central rolls weaken during this period and continue to do so while other interior rolls strengthen to give multi-pulse states on L_2^+ as this branch turns back towards lower Rayleigh numbers (figure 6.9(g)). The subsequent behaviour of this two-pulse convecton branch appears to be sensitive to the domain size considered here since we find that the branch turns back on itself and re-enters the parameter regime depicted in figure 6.9(a), before leaving by following the branch segment associated with the second two-pulse convecton branch, L_2^-, (figure 6.9(h)). This process is associated with repositioning of rolls within the states and occurs several times, as can be seen from the three saddle-nodes within the range $1590 < Ra < 1600$ in figure 6.9. The branch finally exits this small-amplitude region and snakes towards larger amplitude states at lower Rayleigh numbers following L_2^-.

6.3.3 CONVECTONS WITH VARYING BUOYANCY RATIO

In these weakly unbalanced systems, the branches involved in the above unfolding (figure 6.8) proceed to undergo homoclinic snaking as they extend towards larger amplitudes. This behaviour is illustrated in figure 6.10 for $N = -0.999$, where we see the close resemblance of the snaking branches to those in the balanced system for $N = -1$

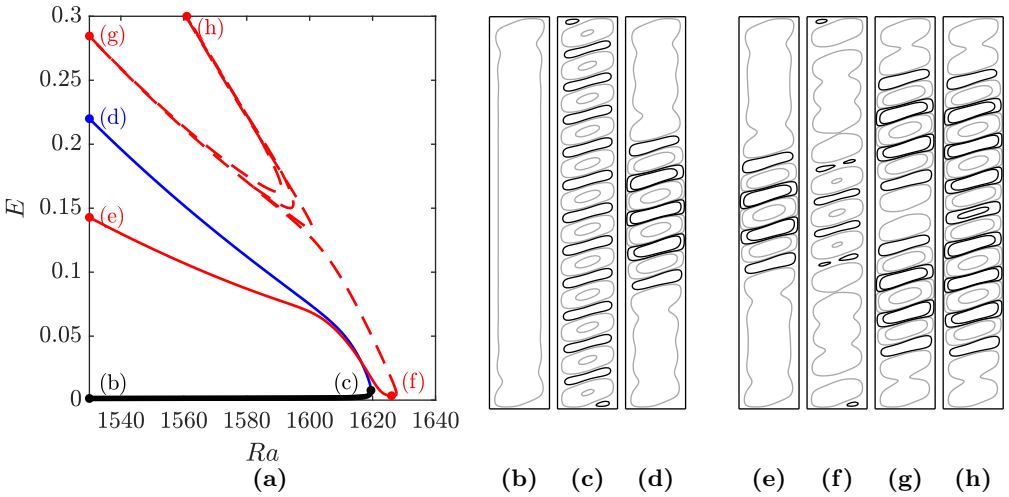

Figure 6.9: (a) Extension of the bifurcation diagram for $N = -0.999$ in a domain with $L_z = 12\lambda_c \approx 29.8$ shown in figure 6.8(b). (b)–(h) Streamfunctions of the small-amplitude profiles along the different branch segments. The contour values used were: $[-10^{-3}, -10^{-2}, -10^{-1}]$ (grey); and $[10^{-3}, 10^{-2}, 10^{-1}]$ (black).

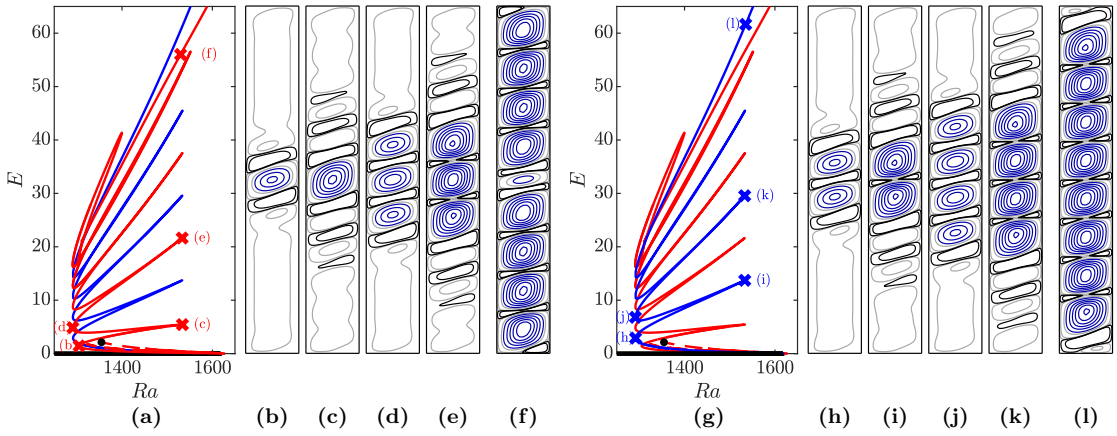

Figure 6.10: Convecton branches and streamfunction profiles for $N = -0.999$, $Pr = 1$ and $Le = 5$. (a) and (g) Bifurcation diagram showing the convecton branches L^+ (red) and L^- (blue) and a branch of two-pulse states (red dashed) that is terminated at small-amplitude at the black dot. (b)–(f), (h)–(l) Streamfunctions of: (b)–(e) convectons at four saddle nodes of L^+ that are marked in (a); (f) the domain-filling state on L^+ marked in (a); (h)–(k) convectons at four saddle nodes of L^- marked in (g); (l) the domain-filling state on L^- marked in (g). Contours are shown using linear (blue) and logarithmic (black and grey) scales and take the values: $[-10^{-3}, -10^{-2}, -10^{-1}]$ (grey); $[10^{-3}, 10^{-2}, 10^{-1}]$ (black); $[-0.2, -0.4, -0.6, ...]$ (blue).

(figure 6.4). The strong central anticlockwise rolls in the convectons (figures 6.10(b)–(e), 6.10(h)–(k)) and the domain-filling states (figures 6.10(f), (l)) that lie on these branches are also minimally affected by the small change to the buoyancy ratio.

The imbalance in the system can, however, be seen in the large, weak rolls that fill the domain outside of the central rolls. Their origin is similar to the large-scale flow considered in section 6.3.1, in that they are driven by the horizontal density gradient imposed by the boundary conditions. These rolls are sensitive to increases in the Rayleigh number, with each of them breaking up into smaller counterrotating rolls between successive left and right saddle nodes (e.g., compare figures 6.10(d) and (e)) as they cannot overcome the strengthening of the rolls that contribute to the front of the convecton with increasing Rayleigh number. This breakup allows the pair of weak anticlockwise rolls closest to the central rolls to strengthen between right and left saddle nodes (e.g., figures 6.10(c)–(d) and (i)–(j)), which increases the number of strong anticlockwise rolls by two over each snaking oscillation.

The background rolls also strengthen as the buoyancy ratio varies further away from $N = -1$ and the form of convectons undergo significant changes, particularly as N is decreased into the solutally dominated regime $N < -1$. To explore these changes, we tracked a four-roll convecton at $Ra = 1350$ from $N = -1$ into both the thermally and solutally dominated regimes and present the streamfunctions of these states from $N = -0.98$ to $N = -1.2$ in figure 6.11. The changes that the convectons exhibit differ between regimes, which may be expected since the large-scale recirculating flow either opposes the anticlockwise flow of the central convecton rolls when $N < -1$, or has the same sense of circulation as these central rolls when $N > -1$. We will therefore consider the two regimes separately.

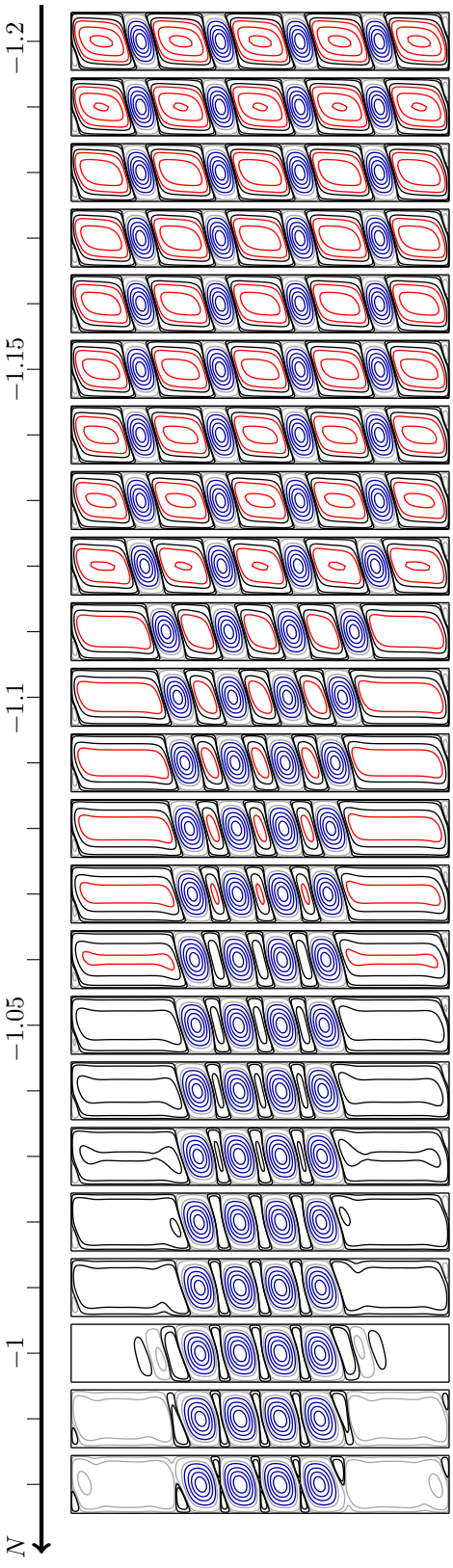

Figure 6.11: Convectons at $Ra = 1350$ and $Pr = 1$, with the buoyancy ratio varying in intervals of $N = -0.01$ from $N = -0.98$ to $N = -1.2$. Contours are shown using linear (blue) and logarithmic (black and grey) scales and take the values: $[-10^{-3}, -10^{-2}, -10^{-1}]$ (grey); $[10^{-3}, 10^{-2}, 10^{-1}]$ (black); $[-0.2, -0.4, -0.6, ...]$ (blue); $[0.2, 0.4, 0.6, ...]$ (red).

Upon increasing N into the thermally dominated regime, we find that the central convecton rolls undergo similar changes to when the Rayleigh number was increased in the balanced (figure 6.4) and weakly imbalanced (figure 6.10) regimes. Starting from the balanced case $N = -1$ (third panel of figure 6.11) and increasing N, the weak clockwise rolls that separate the four strong anticlockwise rolls weaken. These rolls additionally narrow in the centre and develop a stagnation point by $N = -0.98$ (first panel), which splits each clockwise roll into two smaller rolls and reduces the distance between adjacent anticlockwise rolls. The other clockwise rolls that separate the four central rolls from the background state (conduction state or large weak anticlockwise rolls) also weaken with increasing N and become smaller so that, by $N = -0.98$, a single streamline encircles one of the background rolls together with the adjacent anticlockwise convecton roll on both sides of the domain.

The four-roll convecton at $Ra = 1350$ could not be tracked to $N = -0.97$. We instead use the state found for $N = -0.98$ (first panel in figure 6.11) as an initial condition for time-stepping to gain insight into why this steady localised state stops being found. The temporal evolution is depicted in figure 6.12, where we observe two main changes before the time-dependent state converges. Firstly, we notice that as the rolls in each pair of weak central clockwise rolls separate onto their respective sidewall by $t = 2$ (figure 6.12(c)), a single streamline is able to extend across the entire domain and encircle all of the anticlockwise rolls. Secondly, we find that the secondary anticlockwise rolls at the ends of the domain strengthen over time to ultimately resemble the end rolls on anticonvectons on branch A by $t = 20$ (figure 6.12(e)). This latter observation motivates using anticonvectons in explaining why we cease finding convectons in the thermally dominated regime in the following section.

Upon decreasing N into the solutally dominated regime from $N = -1$ (third panel of figure 6.11), a pair of weak clockwise rolls develop and occupy the domain to either side of the central convecton rolls (fourth panel of figure 6.11). Both these large outer rolls and the weak clockwise rolls between strong anticlockwise rolls strengthen as N decreases. The strengthening of the central clockwise rolls forces the adjacent strong

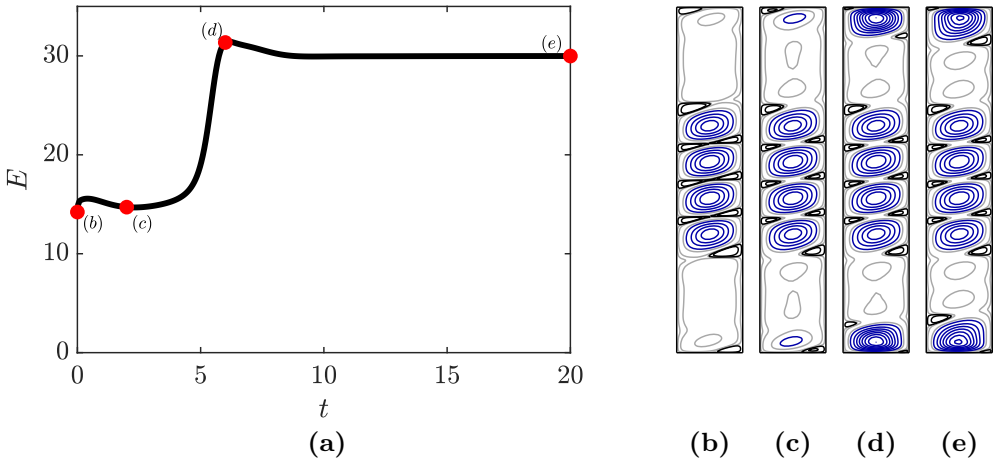

Figure 6.12: Temporal evolution of four-roll convecton at $Ra = 1350$ when $N = -0.97$ using the convecton at $Ra = 1350$ and $N = -0.98$ (first panel of figure 6.11) as the initial condition. (a) Energy-time plot for the temporal dynamics. (b)–(e) Streamfunctions of the states at (b) $t = 0$, (c) $t = 2$, (d) $t = 6$ and (e) $t = 20$. Contours are shown using linear (blue) and logarithmic (black and grey) scales and take the values: $[-10^{-3}, -10^{-2}, -10^{-1}]$ (grey); $[10^{-3}, 10^{-2}, 10^{-1}]$ (black); $[-0.2, -0.4, -0.6, ...]$ (blue).

anticlockwise rolls to move further apart, which reduces the vertical extent of the outermost clockwise rolls. This process continues until $N \approx -1.13$, when the state consists of five strong clockwise rolls that are approximately uniform and separated by four anticlockwise rolls of comparable magnitude. The nine rolls maintain these positions as N decreases to $N = -1.2$, despite the clockwise rolls continuing to strengthen. A similar transition to domain-filling patterned states with alternating clockwise and anticlockwise rolls is also observed as N decreases into the solutally dominated regime starting from convectons with different numbers of central rolls. However, the rates of these transitions depend on the number of anticlockwise rolls as patterned states with more (fewer) anticlockwise rolls are first identified at larger (smaller) values of the buoyancy ratio.

Despite the state at $Ra = 1350$ changing from a localised state when $N = -0.98$ to a domain-filling patterned state when $N = -1.2$, the four strong anticlockwise rolls maintain a similar amplitude throughout. This observation is quantified in figure 6.13, which highlights how the total kinetic energy (black) of the steady states in figure 6.11 and

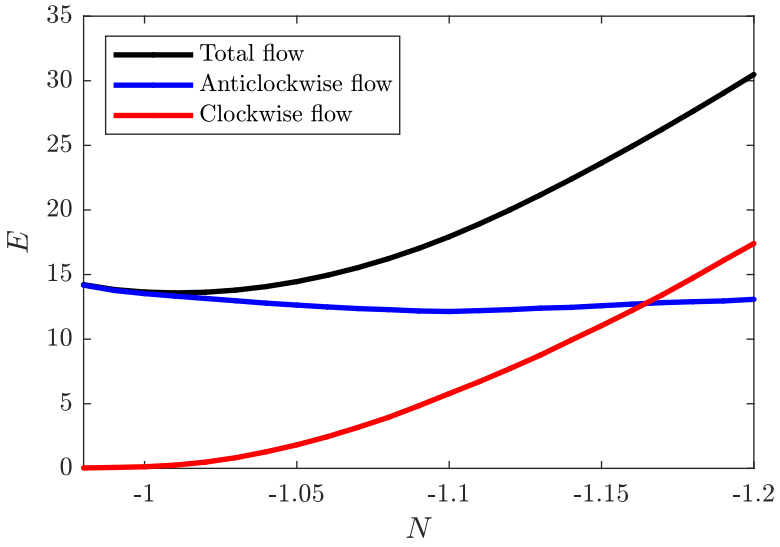

Figure 6.13: Total kinetic energy (black) of the states shown in figure 6.11 from $N = -0.98$ to $N = -1.2$, together with contributions from the clockwise flow (red) and the anticlockwise flow (blue).

contributions from both clockwise (red) and anticlockwise flow (blue) vary with N. At $N = -0.98$, the total kinetic energy ($E \approx 14.2$) is dominated by the anticlockwise flow of the four central rolls and the two background rolls, which contributes to 99.8% of the total kinetic energy. The contribution from anticlockwise flow decreases to a minimum of $E \approx 12.1$ at $N \approx -1.1$, which may be explained by the competition between anticlockwise rolls and the opposing sense of circulation that is driven by the horizontal density gradient, which weakens the anticlockwise background flow for $-0.98 > N > -1$. The contribution from anticlockwise flow proceeds to increase to $E \approx 13.1$ at $N = -1.2$, which likely arises from the shear between counterrotating rolls strengthening anticlockwise rolls. Meanwhile, we find that the clockwise flow strengthens monotonically with decreasing N and forms the dominant sense of circulation for $N \leqslant -1.17$.

6.3.4 EFFECT OF ANTICONVECTON BRANCH ON CONVECTONS

The results of the previous section naturally lead to asking the question: why do we stop finding convectons in the thermally dominated regime? The answer to this ques-

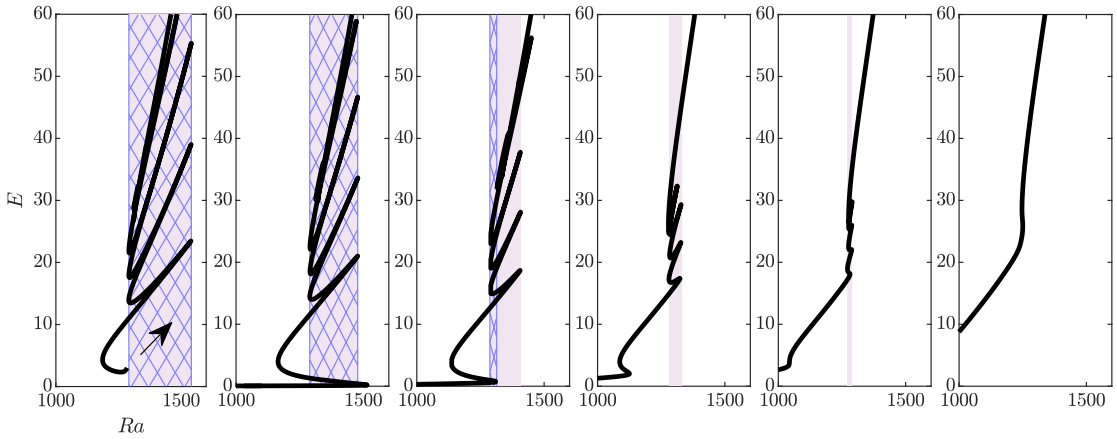

(a) $N = -1$ **(b)** $N = -0.99$ **(c)** $N = -0.975$ **(d)** $N = -0.95$ **(e)** $N = -0.93$ **(f)** $N = -0.89$

Figure 6.14: The anticonvecton branch for: (a) $N = -1$, (b) $N - 0.99$, (c) $N = -0.975$, (d) $N = -0.95$, (e) $N = -0.93$ and (f) $N = -0.89$. The anticonvecton pinning region is shaded in light purple, while the convecton pinning region is hatched in blue when it exists. The black arrow in (a) indicates the direction in which the anticonvecton branch continues when $N = -1$ (cf. figure 6.5).

tion relates to how the convecton pinning region depends upon the structure of the anticonvecton branch. This dependence is illustrated in figure 6.14, where the bifurcation diagrams for selected N show the anticonvecton branch (black) and the pinning region associated with its large-amplitude snaking (light purple), together with the convecton pinning region (blue hatched). This figure shows that the convecton pinning region, when it exists, is always bounded on the left by the lower edge of the anticonvecton pinning region. In contrast, the right edge of the convecton pinning region changes with increasing N, owing to the formation of a small-amplitude right saddle node at $N \approx -0.9904$, when the anticonvecton branch connects to the branch of large-scale flow originating from $Ra = 0$, and its subsequent motion towards lower Rayleigh numbers. Initially, the right edge of the convecton pinning region coincides with the upper edge of the anticonvecton pinning region (figures 6.14(a) and (b)), but changes to being bounded by the first right saddle node of the anticonvecton branch when this saddle node is located within the anticonvecton pinning region (figure 6.14(c)). Consequently, the convecton pinning region disappears (e.g., figures 6.14(d)–(f)) when this right saddle node passes through the left edge of the anticonvecton pinning region.

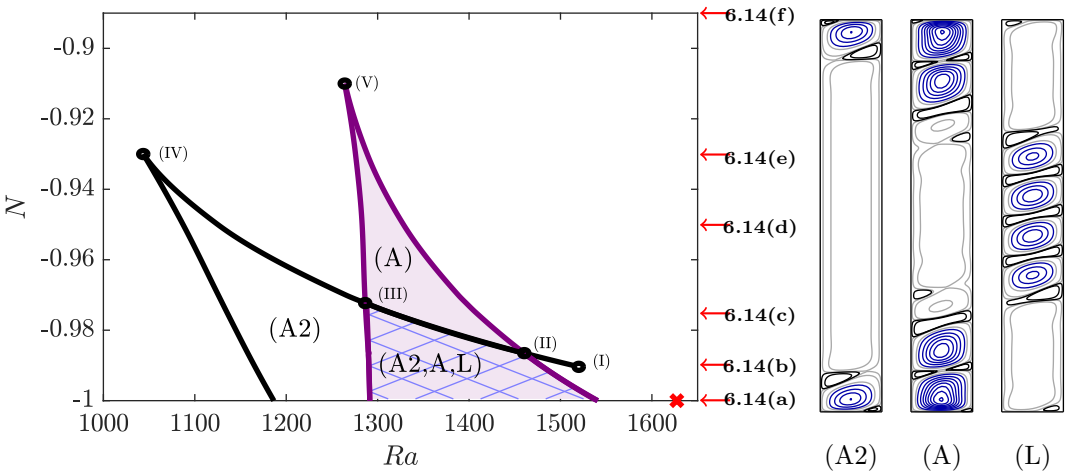

Figure 6.15: Regions of (Ra, N) parameter space in which two-roll anticonvectons (A2), snaking anticonvectons (A), shaded in light purple, and convectons (L), hatched in blue, can be found. The boundaries between regions are given by: the first left and right saddle nodes of the anticonvecton branch (black) and the pinning region of the snaking anticonvectons (purple). Five codimension-two points where the boundaries intersect are labelled and marked by the black circles. The red cross marks the primary bifurcation of the conduction state when $N = -1$. The three panels on the right give representative examples of the three types of states. Arrows indicate the values of N used to produce the bifurcation diagrams in figure 6.14.

Figure 6.15 summarises the above changes in (Ra, N) parameter space by tracking the following over a range of N: the convecton pinning region (blue hatched), in which convectons (L) exist; the anticonvecton pinning region (light purple), in which anticonvectons (A) exist; the first left saddle node of the anticonvecton branch and, when it exists, the first right saddle node of the anticonvecton branch, which together bound the region where two-roll anticonvectons (A2) exist. From this figure, we identify five codimension-two points where saddle nodes corresponding to the boundaries either originate (I), cross through each other (II) and (III) or collide and disappear (IV) and (V). The qualitative structure of the bifurcation diagrams change near these points, as seen in figure 6.14, and these changes will be discussed in the remainder of this section.

(I): CHANGES AT SMALL-AMPLITUDE

The small-amplitude structure of the bifurcation diagrams is the first to change as the buoyancy ratio is increased into the thermally dominated regime. We find that the behaviour changes from the unfolding discussed in figure 6.8, where the branch of large-scale flow originating from the origin connects to L^- before extending towards larger amplitudes, to involve branches of states with weak anticlockwise rolls at both ends of the domain. This occurs in several stages and involves intermediate branches of states that we will not consider in detail. Hence, for simplicity, we focus on two aspects of the small-amplitude reconnections around $N \approx -0.9904$ (point (I) in figure 6.15): firstly, how the anticonvecton branch connects to the branch of large-scale flow (figure 6.16) and, secondly, which branch L^- connects to instead (figure 6.17).

Figure 6.16 depicts how the lower sections of the anticonvecton branches change when N is increased from $N = -1$ (figure 6.16(a)) to $N = -0.99$ (figure 6.16(e)). This branch segment undergoes a cusp bifurcation near where A (black) and $\tilde{A}$ (pink) connect when $N \approx -0.996$, which leads to the two new saddle nodes seen in figure 6.16(c) when $N = -0.994$. The right saddle node of this pair extends towards lower energies and larger Rayleigh numbers as N increases and approaches the left saddle node that an intermediate branch (grey in figure 6.16(d)) undergoes before snaking towards larger am-

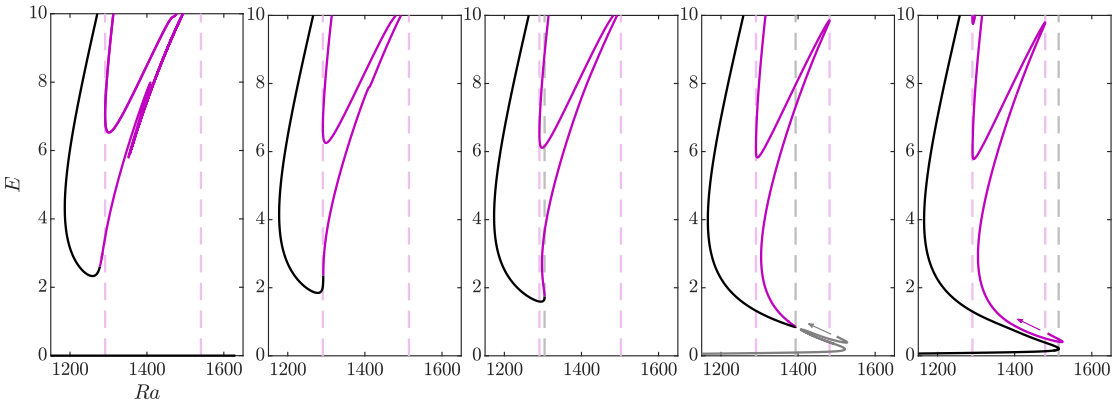

(a) $N = -1$ (b) $N = -0.996$ (c) $N = -0.994$ (d) $N = -0.99045$ (e) $N = -0.99$

Figure 6.16: Bifurcation diagrams showing how the anticonvecton branch A (black) disconnects from $\tilde{A}$ (purple) and instead connects to the branch of base flow between $N = -1$ and $N = -0.99$. Arrows indicate the direction in which the branches continue. The purple vertical dashed lines indicate the limits of the anticonvecton pinning region. The grey vertical dashed lines in (c)–(e) indicate the location of the lower right saddle node of the anticonvecton branch.

plitudes, which is indicated by the upward-pointing grey arrow. The two saddle nodes connect in a transcritical bifurcation around $N \approx -0.9904$ and the two branches of anticonvectons separate as this bifurcation unfolds. This results in the branch of large-scale flow connecting to A when $N = -0.99$, while $\tilde{A}$ connects with the intermediate branch and continues towards larger amplitudes (figure 6.16(e)).

Other branches also extend towards smaller amplitudes as the buoyancy ratio increases, including branches of hybrid convectons that consist of states containing central rolls (like convectons) and an anticlockwise roll at either end of the domain (see figures 6.18(b.ii)–(b.v) and (c.ii)–(c.v) for examples). Figure 6.17 illustrates this behaviour for the branch of even hybrid convectons $\tilde{L}^-$ (green dotted) and how this leads to the branch connecting with L^- (blue) by $N = -0.99$ (figure 6.17(e)). In the balanced system with $N = -1$ (figure 6.17(a)), this branch of hybrid convectons snakes upwards in both directions from the left saddle node at $E \approx 6$, as indicated by the thick and thin green dotted lines. As N increases, this lower left saddle node moves towards lower energies and each of the adjacent branch segments undergoes a cusp bifurcation around $N \approx -0.996$, which leads to the additional saddle nodes seen on the lower part of $\tilde{L}^-$ by

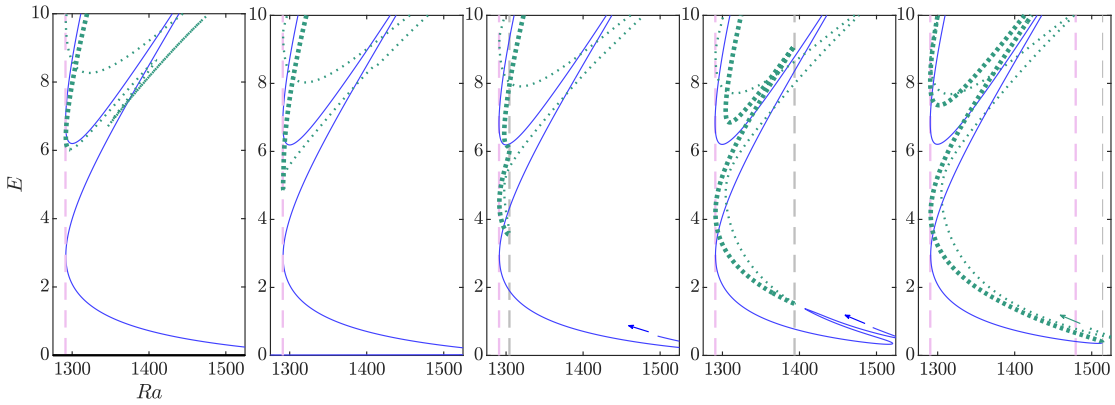

(a) $N = -1$ **(b)** $N = -0.996$ **(c)** $N = -0.994$ **(d)** $N = -0.99045$ **(e)** $N = -0.99$

Figure 6.17: Bifurcation diagrams showing how the convecton branch L^- (blue) connects to the branch of hybrid convectons $\tilde{L}^-$ (green dotted) between $N = -1$ and $N = -0.99$. Arrows indicate the direction in which the branches continue. As in figure 6.16, the purple vertical dashed lines indicate the limits of the anticonvecton pinning region, while the grey vertical dashed lines in (c)–(e) indicate the location of the lower right saddle node of the anticonvecton branch.

$N = -0.994$ (figure 6.17(c)). The newly formed right saddle nodes are located at similar values of the Rayleigh number as the right saddle node that forms on the anticonvecton branch in figure 6.16, as evidenced by the dashed vertical grey lines in both figures, and this continues to be the case as N increases to $N = -0.99045$ (figure 6.17(d)). Meanwhile, we find that L^- disconnects from the branch of large-scale flow between $N = -0.996$ and $N = -0.994$ and instead continues by snaking upwards (see blue arrows in figure 6.17). Similarly to the intermediate branch previously discussed, L^- exhibits a left saddle node that approaches the right saddle node of $\tilde{L}^-$ when $N = -0.99045$ (figure 6.17(d)), before they connect around $N \approx -0.9904$. This leads to the convecton branch L^- smoothly connecting to the branch of even hybrid convectons $\tilde{L}^-$ by $N = -0.99$ (figure 6.17(e)). The branch of odd hybrid convectons $\tilde{L}^+$ exhibits analogous changes and connects to L^+ by $N = -0.99$.

Figure 6.18 depicts sections of the bifurcation diagrams and streamfunctions of states along the branches for $N = -0.99$ after these reconnections have occurred and the branch of anticonvectons connects to the branch of large-scale flow (top row), while each branch of convectons connects to the corresponding branch of hybrid convec-

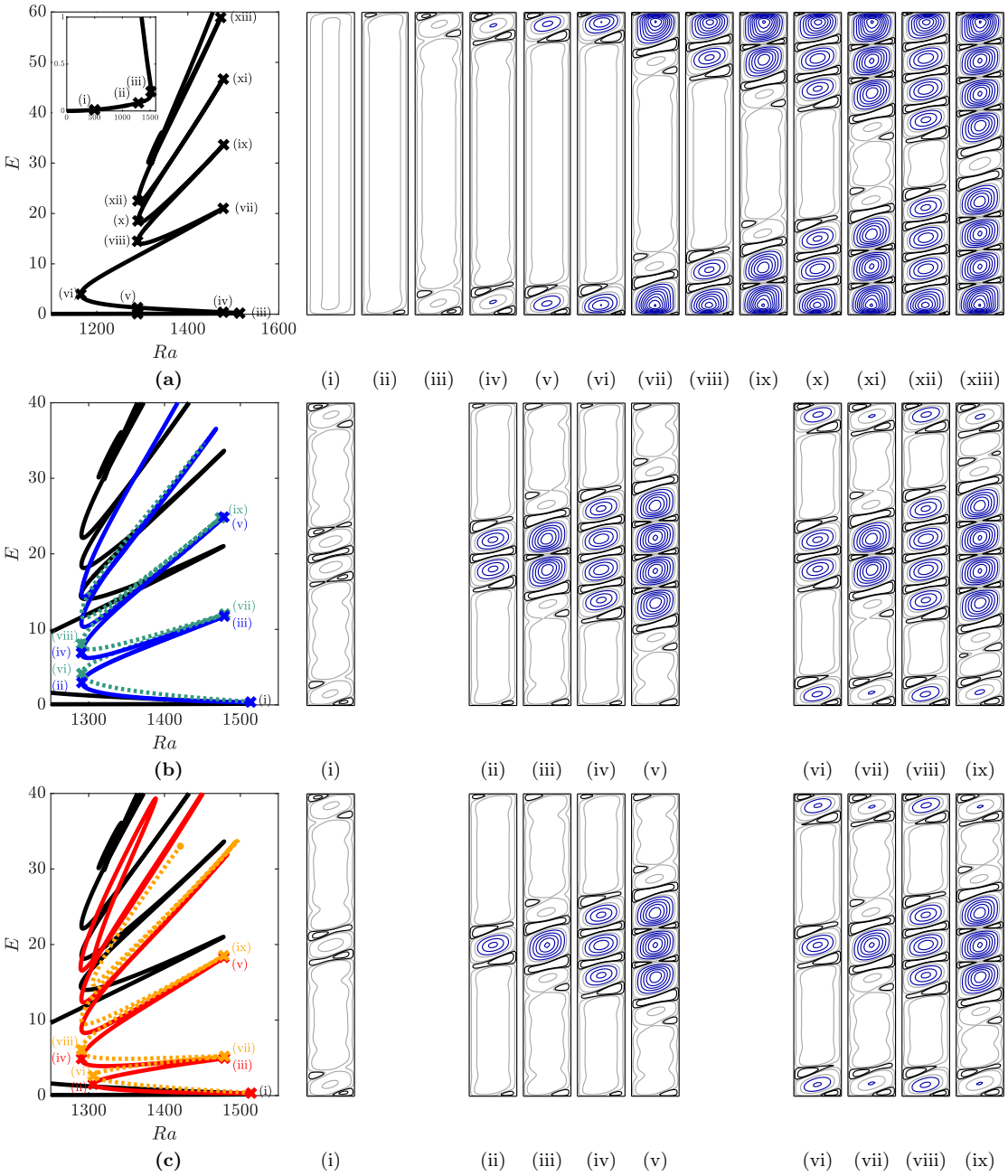

Figure 6.18: Bifurcation diagrams and streamfunctions for steady states when $N = -0.99$. Top row: (a) Branch of anticonvectons A (black) and (i)–(xiii) selected profiles of anticonvectons. Middle row: (b) Branch of even convectons L^- (blue) and even hybrid convectons $\tilde{L}^-$ (green); (i) State at the saddle node where L^- and $\tilde{L}^-$ join; States at the first four saddle nodes of (ii)–(v) L^- and (vi)–(ix) $\tilde{L}^-$ Bottom row: (b) Branch of odd convectons L^+ (red) and odd hybrid convectons $\tilde{L}^+$ (orange); (i) State at the saddle node where L^+ and $\tilde{L}^+$ join; States at the first four saddle nodes of (ii)–(v) L^+ and (vi)–(ix) $\tilde{L}^+$. Contours are shown using linear (blue) and logarithmic (black and grey) scales and take the values: $[-10^{-3}, -10^{-2}, -10^{-1}]$ (grey); $[10^{-3}, 10^{-2}, 10^{-1}]$ (black); $[-0.2, -0.4, -0.6, ...]$ (blue).

tons (bottom two rows). The initial behaviour of the anticonvecton branch is similar to that previously seen when $N = -0.9$ (figure 6.6), as a domain-filling anticlockwise flow develops across the domain and strengthens with increasing Rayleigh number (figures 6.18(a.i) and (a.ii)). This branch turns around at the right saddle node marked (iii), where the state has a pair of secondary anticlockwise rolls at either end of the domain. These rolls strengthen as the branch is followed towards the following left saddle node marked (vi) and separate from the weak domain-filling flow as the small clockwise rolls, first seen in (a.iii), strengthen and extend across the full horizontal extent of the domain (figures 6.18(a.iii)–(a.vi)). The subsequent behaviour of this anticonvecton branch closely resembles that when $N = -1$ (figure 6.5), where the anticonvectons extend by a pair of strong anticlockwise rolls across each oscillation as the branch snakes upwards until the domain has nearly filled (a.xiii). The main difference, however, is the presence of the weak anticlockwise flow that fills the region between the two sets of stronger rolls.

As a result of the reconnection process illustrated in figure 6.17 and the corresponding one for L^+ and $\tilde{L}^+$, we find that each branch of convectons (blue and red solid lines) connects with the corresponding branch of hybrid convectons (green and orange dotted lines) at a small-amplitude right saddle node, as shown in figures 6.18(b) and (c). Figures 6.18(b.i) and (c.i) depict the associated state, which we see contain either one (c.i) or two (b.i) weak central anticlockwise roll(s) separated by a pair of weak clockwise rolls from the larger anticlockwise rolls, which each contain a secondary anticlockwise end roll with amplitude comparable to the central roll(s).

After these right saddle nodes, each of the convecton and hybrid convecton branches proceed to snake upwards within the anticonvecton pinning region before finite domain effects become important at large amplitudes. During this upwards snaking process, the central rolls of both types of states develop in similar ways (compare figures 6.18(b.ii)–(b.v) to (b.vi)–(b.ix) and (c.ii)–(c.v) to (c.vi)–(c.ix)). As the branches are followed between successive left and right saddle nodes, the central anticlockwise rolls strengthen and a secondary roll develops on the interior side of each of the large, weak anticlockwise rolls. The central rolls proceed to weaken while the secondary rolls con-

tinue to strengthen and disconnect from the background flow as each branch is followed towards the following left saddle node. This process therefore increases the number of central rolls by two over a single snaking oscillation in both types of states.

Differences between convectons and hybrid convectons, however, are observed by the presence or absence of strong anticlockwise rolls located at either end of the domain. Starting from the right saddle nodes where the corresponding branches meet ((i) in figures 6.18(b) and (c)) and heading towards lower Rayleigh numbers along either convecton branch, the pair of anticlockwise end rolls seen in figures 6.18(b.i) and (c.i) weaken. This leads to each of the large background rolls extending from the central rolls to one end of the domain and the absence of stronger anticlockwise end rolls in convectons. In contrast, as each hybrid convecton branch is followed from its small-amplitude right saddle node, marked (i) in figures 6.18(b) and (c), towards lower Rayleigh numbers, the secondary anticlockwise end rolls strengthen and separate from the large background rolls, as seen in figures 6.18(b.vi) and (c.vi). The strength of these end rolls are governed by the segment (iv)–(v) on the anticonvecton branch, as can be seen by comparing these end rolls at the left saddle nodes ((b.vi), (b.viii), (c.vi) and (c.viii)) to (a.v) and those at the right saddle nodes ((b.vii), (b.ix), (c.vii) and (c.ix)) to (a.iv). Thus, in contrast to the central rolls of both convectons and hybrid convectons that strengthen (weaken) with increasing (decreasing) Rayleigh number, the end rolls in the hybrid convectons weaken (strengthen) with increasing (decreasing) Rayleigh number.

(II): FROM SNAKING TO ISOLAS

The snaking of the connected branches of convectons and hybrid convectons seen in figure 6.18 persists until $N \approx -0.9866$ (point (II) in figure 6.15), when the first right saddle node of the anticonvecton branch (figure 6.18(a.iii)) coincides with the right edge of the convecton and anticonvecton pinning regions. As this right saddle node passes into the anticonvecton pinning region for larger values of the buoyancy ratio, the snaking branches break up into a set of vertically stacked isolas that are bounded between this saddle node and the left edge of the anticonvecton pinning region, as exemplified in

figures 6.20(a) and (b). This is the same process that was termed 'Snake death II: Isola formation' by Yulin and Champneys [194], who first observed it in a model of a discrete optical cavity with detuning and a linear loss term. Champneys et al. [44] later presented a theoretical argument explaining how such behaviour can arise from the unfolding of a saddle-centre bifurcation when a fold in a branch of homogeneous states coincides with an edge of the pinning region. This appears to also be the case here in the doubly diffusive system, where the anticonvecton branch at small amplitude acts as the branch of homogeneous states.

The manner in which the snaking branches break up into a set of vertically stacked isolas can be understood by considering the unfolding of transcritical bifurcations that occur between the convecton and hybrid convecton branches. Figure 6.19 depicts one such example near the right saddle nodes associated with convectons and hybrid convectons with four central rolls. The right saddle nodes of L^- and $\tilde{L}^-$ approach as the buoyancy ratio increases between $N = -0.98664$ (figure 6.19(a)) and $N = -0.98663$ (figure 6.19(b)), before connecting in a transcritical bifurcation between $N = -0.98663$ and $N = -0.98662$ (figure 6.19(c)). As this bifurcation unfolds upon further increase of the buoyancy ratio, the upper and lower branch segments of L^- separate and respectively connect to the upper and lower branch segments of $\tilde{L}^-$, as seen in figures 6.19(c) and (d). This leads to a pair of branches on which states transition between convectons and hybrid convectons as the branches are traversed. While it has not been confirmed here, it is likely that right saddle nodes associated with convectons with different number of central rolls reconnect over a small range of buoyancy ratios, which would result in an intermediate combination of isolas and snaking, similar to behaviour that Yulin and Champneys [194] found.

Figures 6.20(a) and (b) present the bifurcation diagram for $N = -0.975$ after the breakup process has finished and all convectons lie on one of the vertically stacked isolas. Each isola is 'C-shaped' and most are bounded between the left edge of the anticonvecton pinning region at $Ra \approx 1288$ and the first right saddle node of the anticonvecton branch at $Ra \approx 1314$. We find that exceptions arise, however, both for the isolas containing

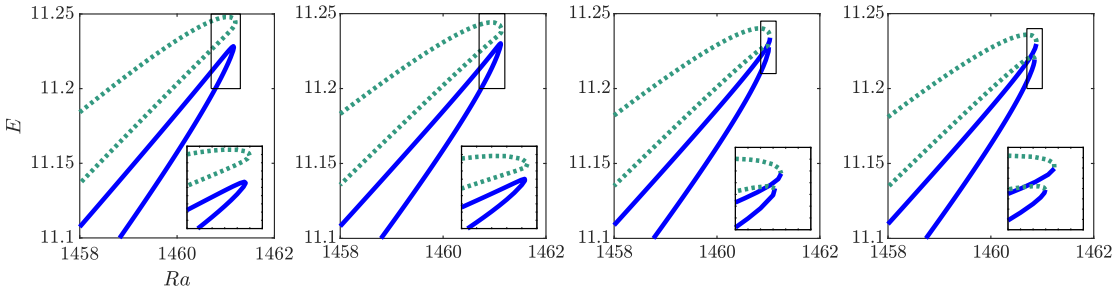

(a) $N = -0.98664$ (b) $N = -0.98663$ (c) $N = -0.98662$ (d) $N = -0.98661$

Figure 6.19: Bifurcation diagrams showing the unfolding around a transcritical bifurcation between L^- (blue solid) and $\tilde{L}^-$ (green dotted) at $N \approx -0.98662$ (near (II) in figure 6.15). The branch segments show convectons and hybrid convectons with four central rolls close to the right edge of the pinning region.

convectons with one or two central rolls and those containing nearly domain-filling states, which are found to lie within different ranges of Rayleigh numbers, but note that this may be anticipated as the saddle nodes of the original snaking branches can differ from the edges of the pinning region at both small and large amplitudes (see figure 6.18).

Figures 6.20(c)–(j) illustrate the typical manner in which the form of convectons changes as a single isola is traversed. Starting at the lower right saddle node (c) and following the lower branch segment (originally L^-, blue) towards the following left saddle node, the pair of outer central rolls strengthen, while the inner central rolls and end rolls weaken (figures 6.20(c)–(e)). All six rolls of the convecton proceed to strengthen as this branch segment is followed to the upper right saddle node (figures 6.20(e)–(g)). The remaining two segments of the isola (green dotted) originated from the hybrid convecton branch, $\tilde{L}^-$ and, as such, we see that the end rolls of the convectons are stronger on these branch segments and have maximal strength at the left saddle node (i). Following these hybrid branch segments from right saddle node (g) back to (c), we see how the central rolls vary in the reverse order to that just described, with the four central rolls first weakening towards the left saddle node (i). The outer pair of central rolls continue to weaken from the left saddle node (i) towards the right saddle node (c), while the inner central rolls strengthen again. This behaviour is expected as in figure 6.18 we previously saw that the central rolls within a hybrid state varied over a single snaking oscillation in the same

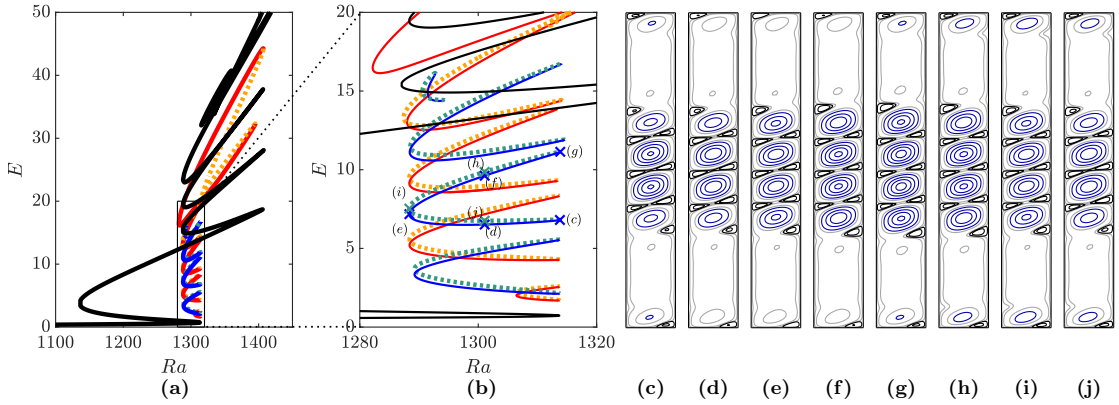

Figure 6.20: (a), (b) Bifurcation diagram for $N = -0.975$ showing the branch of anticonvectons (black) and stacked isolas of convectons (red/orange dotted and blue/green dotted). (b) Magnification of the vertically stacked isolas. (c)–(j) Streamfunctions of selected convectons along the isola with four central rolls. Contours are shown using linear (blue) and logarithmic (black and grey) scales and take the values: $[-10^{-3}, -10^{-2}, -10^{-1}]$ (grey); $[10^{-3}, 10^{-2}, 10^{-1}]$ (black); $[-0.2, -0.4, -0.6, ...]$ (blue).

way as convecton rolls.

(III): END OF CONVECTONS

The first right saddle node of the anticonvecton branch continues towards lower Rayleigh numbers as the buoyancy ratio increases and ultimately passes through the left edge of the anticonvecton pinning region, as seen in figure 6.14. The isolas of convectons are bounded by this saddle node and the left edge of the anticonvecton pinning region, as evidenced in figure 6.21. Thus, as the buoyancy ratio increases between $N \approx -0.9866$ (II) and $N \approx -0.972$ (III), the right saddle nodes of the isolas move towards lower Rayleigh numbers. Meanwhile, the left saddle nodes only undergo small changes in location, as seen in the left panel of figure 6.21. The isolas therefore become smaller until they disappear around $N \approx -0.972$ (III), when the first right saddle node of the anticonvecton branch coincides with the left edge of the anticonvecton pinning region. This behaviour explains why we were unable to track the four-roll convecton in figure 6.11 to $N = -0.97$.

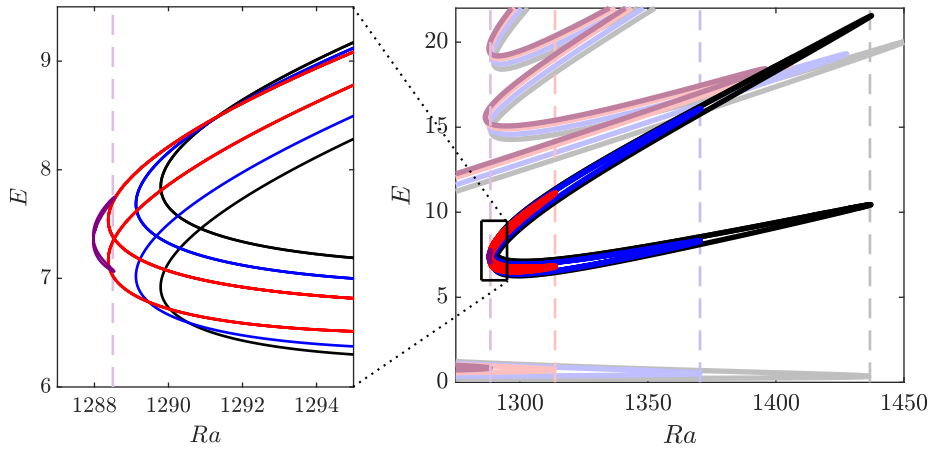

Figure 6.21: Isolas of convectons with four central rolls as N increases to point (III) in figure 6.15 showing $N = -0.985$ (black), $N = -0.98$ (blue), $N = -0.975$ (red) and $N = -0.9725$ (purple). The faint solid lines present the anticonvecton branch at the corresponding parameter values, while the vertical dashed lines mark the Rayleigh numbers of the first right saddle node of each branch. The panel on the left shows a magnification of the region near the left saddle nodes of the isolas.

(IV) AND (V): END OF ANTICONVECTONS

The snaking structure of the anticonvecton branch persists over a wider range of buoyancy ratios; its existence, however, still depends upon there being competition between thermal and solutal buoyancy effects and we cease to find anticonvectons when $N > -0.91$ (point (V) in figure 6.15).

The two-roll anticonvectons (A2) are the first anticonvectons to stop existing. This occurs by the first right saddle node of the anticonvecton branch moving towards lower Rayleigh numbers at a faster rate than the following left saddle node, as seen in figure 6.15. The two saddle nodes then coincide and disappear in a cusp bifurcation around $N \approx -0.93$ (point (IV)). Figure 6.22(a) depicts the anticonvecton branch for $N = -0.93$, shortly after the cusp bifurcation, where we see that states on this branch increase monotonically in both energy and Rayleigh number until the start of the snaking around $Ra \approx 1281$. This branch segment corresponds to the large-scale anticlockwise flow strengthening and developing stronger secondary rolls at both ends of the domain (figures 6.22(b)–(d)). Since these end rolls remain as secondary rolls of the domain-filling

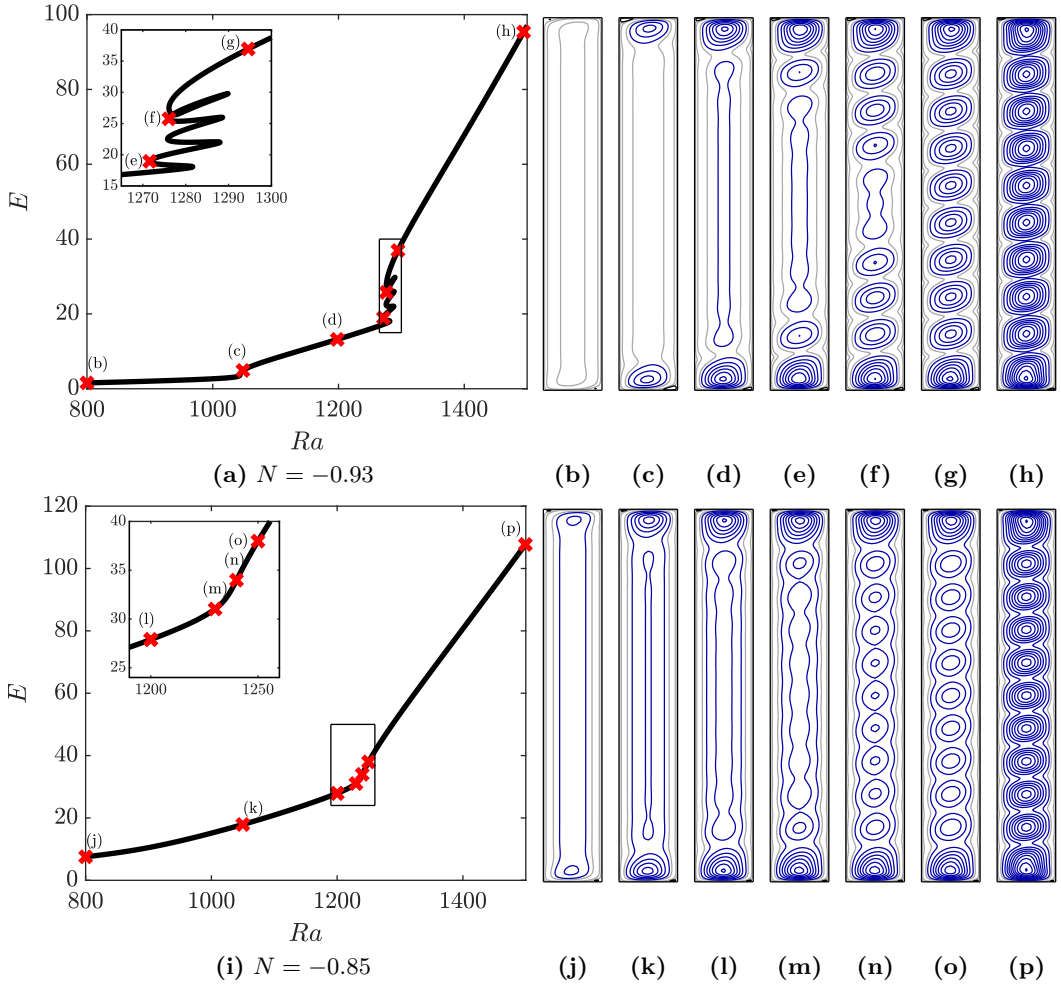

Figure 6.22: Anticonvecton branches and streamfunctions for selected states along the branch when $N = -0.93$ (top row) and $N = -0.85$ (bottom row). These represent the behaviour either side of point (V) in figure 6.15, where the anticonvecton branch snakes for $N < -0.91$ and does not snake for $N > -0.91$. Contours are shown using linear (blue) and logarithmic (black and grey) scales and take the values: $[-10^{-3}, -10^{-2}, -10^{-1}]$ (grey); $[10^{-3}, 10^{-2}, 10^{-1}]$ (black); $[-0.2, -0.4, -0.6, ...]$ (blue).

flow, rather than separating from the weaker flow, these states differ from the two-roll anticonvectons (A2) illustrated in figure 6.15.

The anticonvecton pinning region becomes smaller as the buoyancy ratio increases, as evidenced in figures 6.14 and 6.15. This continues until $N \approx -0.91$ (point (V) in figure 6.15), when the anticonvecton branch stops snaking. This transition occurs via left and right saddle nodes of the snaking branch disappearing in successive cusp bifurcations, which is similar to how localised states in the quadratic-cubic Swift–Hohenberg equation disappear in the approach to the codimension-two point where the criticality of the primary bifurcation changes [37].

Figure 6.22 illustrates the differences in how states transition along the snaking anticonvecton branch when $N = -0.93$ (top row) and how they transition along the non-snaking branch when $N = -0.85$ (bottom row). In both cases, states first change by a roll adjacent to each end wall strengthening and later by rolls nucleating and strengthening within the interior of the domain. When $N = -0.93$, this nucleation occurs pairwise inwards from the ends of the domain between successive left saddle nodes (figures 6.22(d)–(f)). This continues until a domain-filling ten-roll state is reached (figure 6.22(g)), whose rolls proceed to strengthen with increasing Rayleigh number (figure 6.22(h)). However, when $N = -0.85$, while we see initial strengthening of rolls adjacent to the end rolls (figure 6.22(m)), further interior rolls proceed to strengthen in a spatially modulated manner to reach an eleven-roll domain-filling state (figure 6.22(n)). Again, the interior rolls strengthen with Rayleigh number to achieve nearly uniform amplitude by $Ra = 1500$ (figures 6.22(o) and (p)).

A weak anticlockwise flow surrounds each of the domain-filling states in figure 6.22. This flow strengthens with increasing N, as can be seen by comparing figures 6.22(h) and (p), while the secondary interior rolls weaken. While we have not studied these states further into the thermally dominated regime, we would expect the trend to continue until a single domain-filling anticlockwise roll, driven primarily by thermal buoyancy force, is achieved at these relatively low Rayleigh numbers.

6.4 DISCUSSION

In this chapter, we have considered how breaking the balance between opposing thermal and solutal gradients affects the natural doubly diffusive convection within a closed vertical cavity. These imbalanced systems do not admit the steady conduction state, which is instead replaced at low Rayleigh numbers by a large-scale recirculating flow that strengthens with both increasing Rayleigh number and variation of N away from $N = -1$. The primary bifurcations of the conduction state, from which branches of convectons bifurcate when $N = -1$, unfold as a result of this large-scale flow. These small-amplitude changes are found to be the main structural differences between the bifurcation diagrams for the balanced and weakly imbalanced systems.

Further differences developed as the buoyancy ratio increased into the thermally dominated regime as anticlockwise rolls at the ends of the domain tend to strengthen. This strengthening enabled the branch of anticonvectons to connect with the branch of large-scale flow originating from $Ra = 0$ by $N \approx -0.9904$. The subsequent positioning of the first right saddle node of this branch was found to be critical both in understanding why the snaking branches of convectons and hybrid convectons broke up into a stack of isolas and when we ceased to find these isolas containing convectons. The branches maintain an organised structure despite variations in the buoyancy ratio since the centro-symmetry was preserved. This differs from related systems with a broken symmetry, including [120, 131], where the structure of the snaking branches become increasingly complex as the degree of symmetry breaking increases.

Anticonvectons persist over a wider range of buoyancy ratios with $N > -1$ than convectons. We found their existence to be limited by a value of the buoyancy ratio for which the anticonvecton branch stopped snaking. This separates states where interior rolls grow successively inwards from the ends of the domain (with snaking), from those where interior rolls strengthen simultaneously (without snaking). This resembles the transition from successive to simultaneous roll formation found in laterally heated stably stratified systems of doubly diffusive convection, where Lee et al. [107] used exper-

imental data to divide (Ra_T, Ra_S) parameter space into regimes corresponding to these two types of behaviour together with stagnant and unicellular flows. They found that the boundaries between regimes occurred at approximately constant buoyancy ratios between $N \approx 10$ and $N \approx 55$, which Lee and Hyun [109] later validated numerically and Dijkstra and Kranenborg [61] related to paths of bifurcation points. We should note, however, that in these studies, the buoyancy ratio was defined using the initial vertical solutal stratification for ΔC and hence we should not try to directly compare the numerical values.

We obtained contrasting behaviour when the buoyancy ratio decreased into the solutally dominated regime compared to increasing the buoyancy ratio into the thermally dominated regime. Instead of convectons ceasing to exist, we found that convectons smoothly transitioned into domain-filling patterned states consisting of alternating clockwise and anticlockwise convection rolls. We have not yet considered these states in detail; however, investigating further details about these states, including where they are found and the structure of the branches on which they lie could be considered in future work.

7 | CONCLUSIONS

7.1 OVERVIEW

Motivated by the wide variety of physical fluids that undergo doubly diffusive convection, the primary aim of this thesis was to determine how the four physical parameters—the Rayleigh number (Ra), the Prandtl number (Pr), the Lewis number (Le) and the buoyancy ratio (N)—affect properties of states in this system, including spatially localised states known as convectons, and the structure of the branches on which they lie.

We began by investigating the Prandtl and Lewis number dependence of natural doubly diffusive convection in Chapter 4. This involved first performing a weakly nonlinear analysis to determine the criticality of the primary bifurcation of the conduction state, during which we showed that inertial effects, which are enhanced at low Prandtl numbers, increase the supercriticality of the bifurcation. We then numerically continued a selection of both subcritical and supercritical primary branches towards larger amplitudes. Of particular note is that we found that the supercritical branches exhibited an 'S'-shaped structure, where large-amplitude steady convection states coexist with either the stable conduction state or small-amplitude states. These states do not exhibit bistability, however, as we showed that the large-amplitude states are unstable to drift at low Prandtl numbers.

In Chapter 5, we considered how the coexistence between steady states allows convectons in large-aspect-ratio domains, even when the primary bifurcation is supercritical.

In particular, we focussed on understanding the transition from the typical subcritical snaking behaviour at large Prandtl numbers [24] to a stack of disconnected branches of convectons at low Prandtl numbers. This transition involved a number of complex steps, including branches breaking up into isolas or disconnected branch segments, which we interpreted, using phase-space representations of convecton rolls, as the inertial contributions to the rolls change from being subdominant at high Prandtl numbers to becoming significant at low Prandtl numbers.

In Chapter 6, we investigated the effects of varying the buoyancy ratio away from the balanced case $N = -1$. Relaxing this condition introduces a horizontal density gradient from the imposed sidewall boundary conditions, which tends to drive anticlockwise flows in thermally dominated regimes ($N > -1$) and clockwise flows in solutally dominated regimes ($N < -1$). We found that this difference in preferred circulation leads to contrasting behaviour in what happens to convectons as the buoyancy ratio is varied into the two regimes. While convectons smoothly transitioned into domain-filling patterned states consisting of counterrotating rolls in solutally dominated regimes, convectons ceased to exist in sufficiently thermally dominated regimes, which we related to the manner in which the snaking branch of anticonvectons changed structure with increasing buoyancy ratio.

In summary, we were able to show that convectons persist over a range of parameter values, including those for which the horizontally imposed thermal and solutal concentration gradients do not exactly balance. This robustness of convectons to changes in parameter values suggests that it may not be infeasible to find evidence of localised states within experiments performed in vertically extended domains, particularly since experimentally relevant parameter values all lie within the regime in which the primary bifurcation is subcritical (see figure 4.8), where coexistence between the stable conduction state and periodic convection states is predicted.

Our results also provide further insight into spatially localised states. Most notably, we have demonstrated that natural doubly diffusive convection is a non-variational system that admits localised states even when the primary bifurcation is supercritical. We found

that the transition towards this behaviour from the typical snaking in the subcritical regime was more complicated than in the variational Swift–Hohenberg equation (see figure 3.10), which we attributed to the periodic state associated with localised states changing when the physical parameters in the fluids system were varied. Thus, the results presented in Chapter 5 may be of interest when studying other systems that admit tristability.

Breaking the balance between thermal and solutal buoyancy contributions in Chapter 6 allowed us to consider ways in which localised states are affected by non-trivial background states. In thermally dominated systems, we saw that snaking branches of convectons and hybrid convectons connected to form a vertical stack of C-shaped isolas when a fold in the branch of weak background flow entered the pinning region. This differs from similar previously observed transitions, which occurred when a fold in the patterned branch entered the pinning region [44, 194].

7.2 DIRECTIONS FOR FURTHER RESEARCH

The results presented in this thesis suggest a number of potential future research directions, both to improve our understanding of localised states and fundamental properties of doubly diffusive convection. We end by discussing two potential areas.

7.2.1 CONVECTON STABILITY AND TEMPORAL DYNAMICS

One important consideration that we have not discussed is the stability of the spatially localised states that we identified in Chapters 5 and 6. Such an analysis could help determine whether it would be possible to observe convectons experimentally and would further help understand the temporal dynamics of the system at large Rayleigh numbers. Previous analyses of this kind have been undertaken by Beaume [9], who was able to explain how the spatio-temporal chaos for supercritical Rayleigh numbers in three-dimensional natural doubly diffusive convection [14] arises after undergoing twist

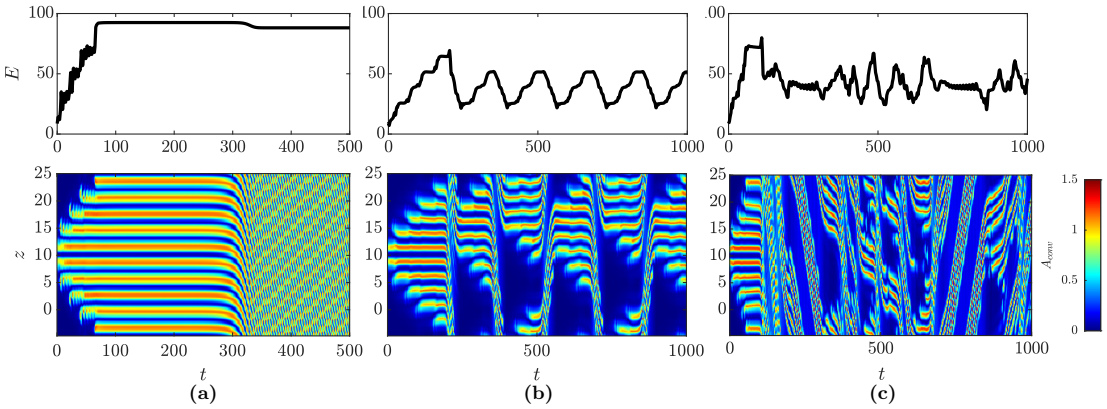

Figure 7.1: Selected depinning behaviour starting from a two-roll convecton with (a) $Pr = 0.2$ and $Ra = 1650$, (b) $Pr = 0.12$ and $Ra = 1600$ and (c) $Pr = 0.12$ and $Ra = 1650$. The top row shows energy-time plots, while the bottom row shows space-time plots of the convective amplitude, A_{conv} (7.1), where red indicates the centre of a roll and dark blue represents the conduction state.

instabilities [12], and by Watanabe et al. [187], who determined the ultimate trajectory of a time-dependent state from the underlying connections between stable and unstable manifolds of steady localised states in binary fluid convection, and indicate the potential value of such a study.

Bergeon and Knobloch [24] previously showed that the snaking secondary branches of convectons for large Prandtl numbers and $N = -1$ exhibited similar stability properties to the branches in the Swift–Hohenberg equation [37]: namely, that the branch segments stabilise (destabilise) near the left (right) saddle nodes. While we might expect this behaviour to persist over a wide range of Lewis numbers and large Prandtl numbers when inertia is subdominant in the dynamics, the stability of convectons at lower Prandtl numbers is less obvious. For example, they may exhibit oscillatory and chaotic temporal behaviour as was found in similar systems of natural convection [91, 127] or binary fluid convection [126] at low Prandtl numbers. Alternatively, we may find that, like the primary branches of periodic states (cf. Chapter 4), the secondary branches of convectons destabilise in a drift instability, which would lead to branches of localised travelling pulses, similar to those found in related studies [120, 186, 187].

The drift instability of the primary branch will impact the temporal dynamics when the

system is initialised with a localised state at a Rayleigh number that lies to the right of the pinning region and allowed to evolve in time, in a process known as depinning. At large Prandtl numbers, when the steady domain-filling periodic states are stable to drift, pairs of rolls successively nucleate on the outside of existing convecton rolls until the domain is full and the time-dependent state converges on this stable state [24]. However, convergence to a steady periodic state will not always be possible when these states are unstable to drift and we would instead expect different dynamics. Figure 7.1 depicts some of the preliminary results from investigations into this depinning behaviour by presenting energy-time plots on the top row, together with space-time plots of the convective amplitude:

$$A_{\text{conv}} = \sqrt{\int_0^1 w^2 dx}, \tag{7.1}$$

on the bottom row, for three sets of parameter values. These initial simulations have indicated a variety of complex dynamics including: convergence to stable domain-filling drifting states (figure 7.1(a)) when the drift instability occurs on the upper segment of the corresponding primary branch; and convergence to periodic orbits (figure 7.1(b)) or chaotic attractors (figure 7.1(c)) when the drift instabilities occur on lower segments of the primary branches. Characterising parameter regimes in which we find each type of depinning dynamics would help us to understand the combined impact of the drift instability and localised states on the temporal dynamics of this system. Further, modelling the results using a simple Swift–Hohenberg-like equation could prove insightful into understanding temporal dynamics associated with other systems admitting localised states that undergo an instability on the primary branch.

A further avenue for future research concerns the temporal dynamics associated with varying the buoyancy ratio. Previous studies on this matter have observed a range of steady, periodic, quasi-periodic or chaotic behaviour [113, 114, 135, 162], but have typically been limited to high Rayleigh numbers and within domains of small vertical extent. We might therefore be interested in determining whether this range of complex dynamics persists at lower Rayleigh numbers and whether they are affected, in any way, by the presence of convectons or anticonvectons.

7.2.2 DOUBLY DIFFUSIVE CONVECTION

The configuration of natural doubly diffusive convection that we considered in this study—a two-dimensional domain with laterally imposed thermal and solutal concentration gradients on the sidewalls—is highly idealised. Thus, a natural extension to this research would be to extend the model by incorporating more physically realistic aspects of the phenomenon.

Firstly, we would want to extend the results into a three-dimensional domain since using a two-dimensional domain suppresses any transverse fluid motion that might develop owing to buoyancy ratios with $N \neq -1$ [162, 193], low Prandtl numbers [42] or rolls twisting in small- [22] or large- [12] aspect-ratio domains. Thus, in a three-dimensional domain, we would anticipate finding a wider variety of localised states and more complex temporal behaviour owing to these additional instabilities.

A second extension would be to consider the effects of the buoyancy force not being parallel to the driving thermal or solutal gradients. The first way that this could be achieved would be to incline the domain, similarly to the studies [25, 137, 138, 172]. When this inclination is combined with variations in the buoyancy ratio, we would expect that the inclination will either enhance or oppose the base flow and we might observe similar trends to those seen in Chapter 6, except with adjusted values of the Rayleigh number and buoyancy ratio. This type of study would also allow us to make a connection between convectons that we have considered here with those found in a horizontal layer, where thermal and solutal gradients are parallel with the buoyancy force [10]. Alternatively, we could consider lateral heating with stable solutal stratification, which has previously been shown to exhibit a multiplicity of steady states, including some that are localised, lying on a single branch with numerous saddle nodes [175, 176]. It could be of interest to explore the connection between this second configuration and that considered in Chapter 6 by introducing a homotopy between them.

Finally, while we were able to make progress in understanding the effects of breaking the symmetry between the roles of temperature and solutal concentration by varying the

buoyancy ratio in Chapter 6, the system maintained a centro-symmetry. This symmetry preserves the snaking structure of branches of convectons, which raises the compelling question about what the complexity of the branches is when this symmetry is broken. Such an analysis could be achieved, for example, by using periodic boundary conditions with $N \neq -1$, or adapting the sidewall boundary conditions like Lo Jacono et al. [120], and would likely make this model system of localised states in natural doubly diffusive convection more realistic.

BIBLIOGRAPHY

[1] E. L. Allgower and K. Georg. *Numerical continuation methods: an introduction*, volume 13. Springer Science & Business Media, 2012.

[2] W. E. Arnoldi. The principle of minimized iterations in the solution of the matrix eigenvalue problem. *Quarterly of Applied Mathematics*, 9(1):17–29, 1951.

[3] D. Avitabile, D. J. B. Lloyd, J. Burke, E. Knobloch, and B. Sandstede. To snake or not to snake in the planar Swift–Hohenberg equation. *SIAM Journal on Applied Dynamical Systems*, 9(3):704–733, 2010.

[4] A. Bahloul, N. Boutana, and P. Vasseur. Double-diffusive and Soret-induced convection in a shallow horizontal porous layer. *Journal of Fluid Mechanics*, 491:325–352, 2003.

[5] G. Bardan, A. Bergeon, E. Knobloch, and A. Mojtabi. Nonlinear doubly diffusive convection in vertical enclosures. *Physica D: Nonlinear Phenomena*, 138(1-2):91–113, 2000.

[6] G. K. Batchelor. Heat transfer by free convection across a closed cavity between vertical boundaries at different temperatures. *Quarterly of Applied Mathematics*, 12 (3):209–233, 1954.

[7] O. Batiste, E. Knobloch, A. Alonso, and I. Mercader. Spatially localized binary-fluid convection. *Journal of Fluid Mechanics*, 560:149–158, 2006.

[8] C. Beaume. Adaptive Stokes preconditioning for steady incompressible flows. *Communications in Computational Physics*, 22(2):494–516, 2017.

[9] C. Beaume. Transition to doubly diffusive chaos. *Physical Review Fluids*, 5(10): 103903, 2020.

[10] C. Beaume, A. Bergeon, and E. Knobloch. Homoclinic snaking of localized states in doubly diffusive convection. *Physics of Fluids*, 23(9):094102, 2011.

[11] C. Beaume, A. Bergeon, H.-C. Kao, and E. Knobloch. Convectons in a rotating fluid layer. *Journal of Fluid Mechanics*, 717:417–448, 2013.

[12] C. Beaume, A. Bergeon, and E. Knobloch. Convectons and secondary snaking in three-dimensional natural doubly diffusive convection. *Physics of Fluids*, 25(2): 024105, 2013.

[13] C. Beaume, E. Knobloch, and A. Bergeon. Nonsnaking doubly diffusive convectons and the twist instability. *Physics of Fluids*, 25(11):114102, 2013.

[14] C. Beaume, A. Bergeon, and E. Knobloch. Three-dimensional doubly diffusive convectons: instability and transition to complex dynamics. *Journal of Fluid Mechanics*, 840:74–105, 2018.

[15] C. Beaume, A. M. Rucklidge, and J. Tumelty. Near-onset dynamics in natural doubly diffusive convection. *Journal of Fluid Mechanics*, 934:A42, 2022.

[16] M. Beck, J. Knobloch, D. J. B. Lloyd, B. Sandstede, and T. Wagenknecht. Snakes, ladders, and isolas of localized patterns. *SIAM Journal on Mathematical Analysis*, 41 (3):936–972, 2009.

[17] C. Beckermann and R. Viskanta. Double-diffusive convection during dendritic solidification of a binary mixture. *PhysicoChemical Hydrodynamics*, 10(2):195–213, 1988.

[18] C. Beckermann and R. Viskanta. An experimental study of solidification of binary mixtures with double-diffusive convection in the liquid. *Chemical Engineering Communications*, 85(1):135–156, 1989.

[19] C. Beghein, F. Haghighat, and F. Allard. Numerical study of double-diffusive natural convection in a square cavity. *International Journal of Heat and Mass Transfer*, 35(4):833–846, 1992.

[20] R. Bennacer and D. Gobin. Cooperating thermosolutal convection in enclosures-i. Scale analysis and mass transfer. *International Journal of Heat and Mass Transfer*, 39 (13):2671–2681, 1996.

[21] M. Benzi. Preconditioning techniques for large linear systems: a survey. *Journal of Computational Physics*, 182(2):418–477, 2002.

[22] A. Bergeon and E. Knobloch. Natural doubly diffusive convection in three-dimensional enclosures. *Physics of Fluids*, 14(9):3233–3250, 2002.

[23] A. Bergeon and E. Knobloch. Periodic and localized states in natural doubly diffusive convection. *Physica D: Nonlinear Phenomena*, 237(8):1139–1150, 2008.

[24] A. Bergeon and E. Knobloch. Spatially localized states in natural doubly diffusive convection. *Physics of Fluids*, 20(3):034102, 2008.

[25] A. Bergeon, K. Ghorayeb, and A. Mojtabi. Double diffusive convection in an inclined cavity. *Physics of Fluids*, 11:549–559, 1999.

[26] A. Bergeon, J. Burke, E. Knobloch, and I. Mercader. Eckhaus instability and homoclinic snaking. *Physical Review E*, 78(4):046201, 2008.

[27] T. L. Bergman and M. T. Hyun. Simulation of two-dimensional thermosolutal convection in liquid metals induced by horizontal temperature and species gradients. *International Journal of Heat and Mass Transfer*, 39(14):2883–2894, 1996.

[28] M. Bestehorn and H. Haken. Transient patterns of the convection instability: A model-calculation. *Zeitschrift für Physik B Condensed Matter*, 57(4):329–333, 1984.

[29] G. Beylkin, J. M. Keiser, and L. Vozovoi. A new class of time discretization schemes for the solution of nonlinear PDEs. *Journal of Computational Physics*, 147(2):362–387, 1998.

[30] S. Blanchflower. Magnetohydrodynamic convectons. *Physics Letters A*, 261(1-2): 74–81, 1999.

[31] L. J. Bloomfield and H. E. Huppert. Solidification and convection of a ternary solution cooled from the side. *Journal of Fluid Mechanics*, 489:269–299, 2003.

[32] U. Bortolozzo, L. Pastur, P. L. Ramazza, M. Tlidi, and G. Kozyreff. Bistability between different localized structures in nonlinear optics. *Physical Review Letters*, 93(25):253901, 2004.

[33] J. P. Boyd. *Chebyshev and Fourier spectral methods*. Courier Corporation, 2001.

[34] P. N. Brown and H. F. Walker. GMRES on (nearly) singular systems. *SIAM Journal on Matrix Analysis and Applications*, 18(1):37–51, 1997.

[35] J. Burguete and H. Mancini. Localized structures in convective experiments. *The European Physical Journal Special Topics*, 223(1):9–20, 2014.

[36] J. Burke and J. H. P. Dawes. Localized states in an extended Swift–Hohenberg equation. *SIAM Journal on Applied Dynamical Systems*, 11(1):261–284, 2012.

[37] J. Burke and E. Knobloch. Localized states in the generalized Swift–Hohenberg equation. *Physical Review E*, 73(5):056211, 2006.

[38] J. Burke and E. Knobloch. Homoclinic snaking: structure and stability. *Chaos: An Interdisciplinary Journal of Nonlinear Science*, 17(3):037102, 2007.

[39] J. Burke and E. Knobloch. Snakes and ladders: localized states in the Swift–Hohenberg equation. *Physics Letters A*, 360(6):681–688, 2007.

[40] J. Burke and E. Knobloch. Multipulse states in the Swift-Hohenberg equation. In *Conference Publications*, volume 2009, page 109. American Institute of Mathematical Sciences, 2009.

[41] J. Burke, S. M. Houghton, and E. Knobloch. Swift-Hohenberg equation with broken reflection symmetry. *Physical Review E*, 80(3):036202, 2009.

[42] F. H. Busse. The oscillatory instability of convection rolls in a low Prandtl number fluid. *Journal of Fluid Mechanics*, 52(1):97–112, 1972.

[43] G. F. Carey, K. C. Wang, and W. D. Joubert. Performance of iterative methods for Newtonian and generalized Newtonian flows. *International Journal for Numerical Methods in Fluids*, 9(2):127–150, 1989.

[44] A. R. Champneys, E. Knobloch, Y.-P. Ma, and T. Wagenknecht. Homoclinic snakes bounded by a saddle-center periodic orbit. *SIAM Journal on Applied Dynamical Systems*, 11(4):1583–1613, 2012.

[45] A. R. Champneys, F. Al Saadi, V. F. Breña–Medina, V. A. Grieneisen, A. F. M. Marée, N. Verschueren, and B. Wuyts. Bistability, wave pinning and localisation in natural reaction–diffusion systems. *Physica D: Nonlinear Phenomena*, 416:132735, 2021.

[46] S. J. Chapman and G. Kozyreff. Exponential asymptotics of localised patterns and snaking bifurcation diagrams. *Physica D: Nonlinear Phenomena*, 238(3):319–354, 2009.

[47] R. M. Clever and F. H. Busse. Low-Prandtl-number convection in a layer heated from below. *Journal of Fluid Mechanics*, 102:61–74, 1981.

[48] S. M. Copley, A. F. Giamei, S. M. Johnson, and M. F. Hornbecker. The origin of freckles in unidirectionally solidified castings. *Metallurgical transactions*, 1(8): 2193–2204, 1970.

[49] P. Coullet, C. Riera, and C. Tresser. A new approach to data storage using localized structures. *Chaos: An Interdisciplinary Journal of Nonlinear Science*, 14(1):193–198, 2004.

[50] S. M. Cox and P. C. Matthews. New instabilities in two-dimensional rotating convection and magnetoconvection. *Physica D: Nonlinear Phenomena*, 149(3):210–229, 2001.

[51] S. M. Cox and P. C. Matthews. Exponential time differencing for stiff systems. *Journal of Computational Physics*, 176(2):430–455, 2002.

[52] J. D. Crawford and E. Knobloch. Symmetry and symmetry-breaking bifurcations in fluid dynamics. *Annual Review of Fluid Mechanics*, 23(1):341–387, 1991.

[53] M. C. Cross, P. G. Daniels, P. C. Hohenberg, and E. D. Siggia. Phase-winding solutions in a finite container above the convective threshold. *Journal of Fluid Mechanics*, 127:155–183, 1983.

[54] J. H. P. Dawes. Localized pattern formation with a large-scale mode: slanted snaking. *SIAM Journal on Applied Dynamical Systems*, 7(1):186–206, 2008.

[55] J. H. P. Dawes. Modulated and localized states in a finite domain. *SIAM Journal on Applied Dynamical Systems*, 8(3):909–930, 2009.

[56] J. H. P. Dawes. The emergence of a coherent structure for coherent structures: localized states in nonlinear systems. *Philosophical Transactions of the Royal Society A: Mathematical, Physical and Engineering Sciences*, 368(1924):3519–3534, 2010.

[57] J. H. P. Dawes and S. Lilley. Localized states in a model of pattern formation in a vertically vibrated layer. *SIAM Journal on Applied Dynamical Systems*, 9(1):238–260, 2010.

[58] J. H. P. Dawes and J. L. M. Williams. Localised pattern formation in a model for dryland vegetation. *Journal of Mathematical Biology*, 73(1):63–90, 2016.

[59] A. D. Dean, P. C. Matthews, S. M. Cox, and J. R. King. Exponential asymptotics of homoclinic snaking. *Nonlinearity*, 24(12):3323, 2011.

[60] F. Dias and G. Iooss. Capillary-gravity interfacial waves in infinite depth. *European Journal of Mechanics. B, Fluids*, 15(3):367–393, 1996.

[61] H. A. Dijkstra and E. J. Kranenborg. A bifurcation study of double diffusive flows in a laterally heated stably stratified liquid layer. *International Journal of Heat and Mass Transfer*, 39(13):2699–2710, 1996.

[62] H. A. Dijkstra, F. W. Wubs, A. K. Cliffe, E. Doedel, I. F. Dragomirescu, B. Eckhardt, A. Y. Gelfgat, A. L. Hazel, V. Lucarini, A. G. Salinger, et al. Numerical bifurcation methods and their application to fluid dynamics: analysis beyond simulation. *Communications in Computational Physics*, 15(1):1–45, 2014.

[63] E. Doedel, H. B. Keller, and J. P. Kernevez. Numerical analysis and control of bifurcation problems (I): Bifurcation in finite dimensions. *International Journal of Bifurcation and Chaos*, 1(03):493–520, 1991.

[64] T. A. Driscoll, N. Hale, and L. N. Trefethen. Chebfun Guide, 2014.

[65] S. Durante, K. Schroeder, L. Mazzei, .S Pierini, M. Borghini, and S. Sparnocchia. Permanent thermohaline staircases in the Tyrrhenian Sea. *Geophysical Research Letters*, 46(3):1562–1570, 2019.

[66] W. J. Firth, L. Columbo, and T. Maggipinto. On homoclinic snaking in optical systems. *Chaos: An Interdisciplinary Journal of Nonlinear Science*, 17(3):037115, 2007.

[67] P. Gandhi, Y. R. Zelnik, and E. Knobloch. Spatially localized structures in the Gray–Scott model. *Philosophical Transactions of the Royal Society A: Mathematical, Physical and Engineering Sciences*, 376(2135):20170375, 2018.

[68] P. Garaud. Double-diffusive convection at low Prandtl number. *Annual Review of Fluid Mechanics*, 50:275–298, 2018.

[69] P. Garaud. Double-diffusive processes in stellar astrophysics. In M. Rieutord, I. Baraffe, and Y. Lebreton, editors, *Multi-Dimensional Processes in Stellar Physics*, pages 13–60. EDP Sciences, 2021.

[70] K. Ghorayeb and A. Mojtabi. Double diffusive convection in a vertical rectangular cavity. *Physics of Fluids*, 9(8):2339–2348, 1997.

[71] J. F. Gibson and T. M. Schneider. Homoclinic snaking in plane Couette flow: bending, skewing and finite-size effects. *Journal of Fluid Mechanics*, 794:530–551, 2016.

[72] D. Gobin and R. Bennacer. Cooperating thermosolutal convection in enclosures—II. Heat transfer and flow structure. *International Journal of Heat and Mass Transfer*, 39(13):2683–2697, 1996.

[73] J. Guckenheimer and P. Holmes. *Nonlinear Oscillations, Dynamical Systems and Bifurcations of Vector Fields*. Springer, New York, 1983.

[74] J. M. Hamilton, M. R. Lewis, and B. R. Ruddick. Vertical fluxes of nitrate associated with salt fingers in the world's oceans. *Journal of Geophysical Research: Oceans*, 94 (C2):2137–2145, 1989.

[75] H. Han and T. H. Kuehn. Double diffusive natural convection in a vertical rectangular enclosure—I. Experimental study. *International Journal of Heat and Mass Transfer*, 34(2):449–459, 1991.

[76] H. Han and T. H. Kuehn. Double diffusive natural convection in a vertical rectangular enclosure—II. numerical study. *International Journal of Heat and Mass Transfer*, 34(2):461–471, 1991.

[77] U. Hansen and D. A. Yuen. Numerical simulations of thermal-chemical instabilities at the core–mantle boundary. *Nature*, 334(6179):237, 1988.

[78] U. Hansen and D. A. Yuen. Subcritical double-diffusive convection at infinite Prandtl number. *Geophysical & Astrophysical Fluid Dynamics*, 47(1-4):199–224, 1989.

[79] M. F. Hilali, S. Métens, P. Borckmans, and G. Dewel. Pattern selection in the generalized Swift-Hohenberg model. *Physical Review E*, 51(3):2046, 1995.

[80] S. M. Houghton and E. Knobloch. Homoclinic snaking in bounded domains. *Physical Review E*, 80(2):026210, 2009.

[81] G. W. Hunt, G. J. Lord, and A. R. Champneys. Homoclinic and heteroclinic orbits underlying the post-buckling of axially-compressed cylindrical shells. *Computer Methods in Applied Mechanics and Engineering*, 170(3-4):239–251, 1999.

[82] G. W. Hunt, G. J. Lord, and M. A. Peletier. Cylindrical shell buckling: a characterization of localization and periodicity. *Discrete and Continuous Dynamical Systems Series B*, 3(4):505–518, 2003.

[83] H. E. Huppert. The fluid mechanics of solidification. *Journal of Fluid Mechanics*, 212:209–240, 1990.

[84] H. E. Huppert and E. G. Josberger. The melting of ice in cold stratified water. *Journal of Physical Oceanography*, 10(6):953–960, 1980.

[85] H. E. Huppert and R. S. J. Sparks. Double-diffusive convection due to crystallization in magmas. *Annual Review of Earth and Planetary Sciences*, 12(1):11–37, 1984.

[86] H. E. Huppert and J. S. Turner. Ice blocks melting into a salinity gradient. *Journal of Fluid Mechanics*, 100(2):367–384, 1980.

[87] H. E. Huppert and J. S. Turner. Double-diffusive convection. *Journal of Fluid Mechanics*, 106:299–329, 1981.

[88] J. M. Hyun and J. W. Lee. Double-diffusive convection in a rectangle with cooperating horizontal gradients of temperature and concentration. *International Journal of Heat and Mass Transfer*, 33(8):1605–1617, 1990.

[89] G. Iooss and M. Pérouème. Perturbed homoclinic solutions in reversible 1:1 resonance vector fields. *Journal of Differential Equations*, 102(1):62–88, 1993.

[90] H. D. Jiang, S. Ostrach, and Y. Kamotani. Unsteady thermosolutal transport phenomena due to opposed buoyancy forces in shallow enclosures. *Journal of Heat Transfer*, 113:135–140, 1991.

[91] K. Kamakura and H. Ozoe. Oscillatory phenomena of low-Prandtl-number fluids in a rectangular cavity. *Numerical Heat Transfer, Part A Applications*, 30(5):427–437, 1996.

[92] Y. Kamotani, L. W. Wang, S. Ostrach, and H. D. Jiang. Experimental study of natural convection in shallow enclosures with horizontal temperature and concentration gradients. *International Journal of Heat and Mass Transfer*, 28(1):165–173, 1985.

[93] H. C. Kao and E. Knobloch. Weakly subcritical stationary patterns: Eckhaus instability and homoclinic snaking. *Physical Review E*, 85(2):026211, 2012.

[94] G. E. Karniadakis, M. Israeli, and S. A. Orszag. High-order splitting methods for the incompressible Navier-Stokes equations. *Journal of Computational Physics*, 97 (2):414–443, 1991.

[95] H. B. Keller. Numerical solution of bifurcation and nonlinear eigenvalue problems. *Application of Bifurcation Theory*, pages 359–384, 1977.

[96] C. T. Kelley. *Solving nonlinear equations with Newton's method*, volume 1. SIAM, 2003.

[97] D. E. Kelley, H. J. S. Fernando, A. E. Gargett, J. Tanny, and E. Özsoy. The diffusive regime of double diffusive convection. *Progress in Oceanography*, 56:461–481, 2003.

[98] E. Knobloch. Convection in binary fluids. *The Physics of Fluids*, 23(9):1918–1920, 1980.

[99] E. Knobloch. Spatial localization in dissipative systems. *Annual Review of Condensed Matter Physics*, 6(1):325–359, 2015.

[100] E. Knobloch, H. Uecker, and D. Wetzel. Defectlike structures and localized patterns in the cubic-quintic-septic Swift–Hohenberg equation. *Physical Review E*, 100 (1):012204, 2019.

[101] P. Kolodner, D. Bensimon, and C. M. Surko. Traveling-wave convection in an annulus. *Physical Review Letters*, 60(17):1723, 1988.

[102] B. Krauskopf, H. M. Osinga, and J. Galán-Vioque. *Numerical continuation methods for dynamical systems*, volume 2. Springer, 2007.

[103] Y. A. Kuznetsov. *Elements of applied bifurcation theory*, volume 112. Springer Science & Business Media, 2013.

[104] T. Lay, J. Hernlund, and B. A. Buffett. Core–mantle boundary heat flow. *Nature Geoscience*, 1(1):25, 2008.

[105] J. Leconte and G. Chabrier. A new vision of giant planet interiors: Impact of double diffusive convection. *Astronomy & Astrophysics*, 540:A20, 2012.

[106] J. Lee, M. T. Hyun, and K. W. Kim. Natural convection in confined fluids with combined horizontal temperature and concentration gradients. *International Journal of Heat and Mass Transfer*, 31(10):1969–1977, 1988.

[107] J. Lee, M. T. Hyun, and Y. S. Kang. Confined natural convection due to lateral heating in a stably stratified solution. *International Journal of Heat and Mass Transfer*, 33(5):869–875, 1990.

[108] J. W. Lee and J. M. Hyun. Double-diffusive convection in a rectangle with opposing horizontal temperature and concentration gradients. *International Journal of Heat and Mass Transfer*, 33(8):1619–1632, 1990.

[109] J. W. Lee and J. M. Hyun. Double diffusive convection in a cavity under a vertical solutal gradient and a horizontal temperature gradient. *International Journal of Heat and Mass Transfer*, 34(9):2423–2427, 1991.

[110] R. B. Lehoucq, D. C. Sorensen, and C. Yang. *ARPACK users' guide: solution of large-scale eigenvalue problems with implicitly restarted Arnoldi methods*. SIAM, 1998.

[111] S. Levitus and T. P. Boyer. World Ocean Atlas 1994. Volume 4. Temperature. 1994.

[112] S. Levitus, R. Burgett, and T. P. Boyer. World Ocean Atlas 1994. Volume 3. Salinity. 1994.

[113] X. Liang, X. Li, D. Fu, and Y. Ma. Complex Transition of Double-Diffusive Convection in a Rectangular Enclosure with Height to-Length Ratio Equal to 4: Part I. *Communications in Computational Physics*, 6(2):247, 2009.

[114] X. Liang, B. Peng, and Z. F. Tian. Complex transition of double-diffusive convection in a rectangular enclosure with height-to-length ratio equal to 4: Part II. *International Journal of Heat and Mass Transfer*, 135:247–261, 2019.

[115] D. J. B. Lloyd, B. Sandstede, D. Avitabile, and A. R. Champneys. Localized hexagon patterns of the planar Swift–Hohenberg equation. *SIAM Journal on Applied Dynamical Systems*, 7(3):1049–1100, 2008.

[116] D. Lo Jacono, A. Bergeon, and E. Knobloch. Spatially localized binary fluid convection in a porous medium. *Physics of Fluids*, 22(7):909, 2010.

[117] D. Lo Jacono, A. Bergeon, and E. Knobloch. Magnetohydrodynamic convectons. *Journal of Fluid Mechanics*, 687:595–605, 2011.

[118] D. Lo Jacono, A. Bergeon, and E. Knobloch. Spatially localized magnetoconvection. *Fluid Dynamics Research*, 44(3):031411, 2012.

[119] D. Lo Jacono, A. Bergeon, and E. Knobloch. Three-dimensional spatially localized binary-fluid convection in a porous medium. *Journal of Fluid Mechanics*, 730:R2, 2013.

[120] D. Lo Jacono, A. Bergeon, and E. Knobloch. Localized traveling pulses in natural doubly diffusive convection. *Physical Review Fluids*, 2(9):093501, 2017.

[121] E. Makrides and B. Sandstede. Predicting the bifurcation structure of localized snaking patterns. *Physica D: Nonlinear Phenomena*, 268:59–78, 2014.

[122] M. Mamou, P. Vasseur, and E. Bilgen. Double-diffusive convection instability in a vertical porous enclosure. *Journal of Fluid Mechanics*, 368:263–289, 1998.

[123] C. K. Mamun and L. S. Tuckerman. Asymmetry and Hopf bifurcation in spherical Couette flow. *Physics of Fluids*, 7(1):80–91, 1995.

[124] P. C. Matthews and H. Susanto. Variational approximations to homoclinic snaking in continuous and discrete systems. *Physical Review E*, 84:066207, Dec 2011.

[125] P. C. Matthews, M. R. E. Proctor, A. M. Rucklidge, and N. O. Weiss. Pulsating waves in nonlinear magnetoconvection. *Physics Letters A*, 183(1):69–75, 1993.

[126] E Meca, I. Mercader, O. Batiste, and L. Ramirez-Piscina. Blue sky catastrophe in double-diffusive convection. *Physical Review Letters*, 92(23):234501, 2004.

[127] I. Mercader, O. Batiste, L. Ramírez-Piscina, X. Ruiz, S. Rüdiger, and J. Casademunt. Bifurcations and chaos in single-roll natural convection with low Prandtl number. *Physics of Fluids*, 17(10):104108, 2005.

[128] I. Mercader, O. Batiste, A. Alonso, and E. Knobloch. Convectons in periodic and bounded domains. *Fluid Dynamics Research*, 42(2):025505, 2009.

[129] I. Mercader, O. Batiste, A. Alonso, and E. Knobloch. Localized pinning states in closed containers: homoclinic snaking without bistability. *Physical Review E*, 80(2): 025201, 2009.

[130] I. Mercader, O. Batiste, A. Alonso, and E. Knobloch. Convectons, anticonvectons and multiconvectons in binary fluid convection. *Journal of Fluid Mechanics*, 667: 586–606, 2011.

[131] I. Mercader, O. Batiste, A. Alonso, and E. Knobloch. Effect of small inclination on binary convection in elongated rectangular cells. *Physical Review E*, 99(2):023113, 2019.

[132] W. J. Merryfield, G. Holloway, and A. E. Gargett. A global ocean model with double-diffusive mixing. *Journal of Physical Oceanography*, 29(6):1124–1142, 1999.

[133] V. T. Neal, S. Neshyba, and W. Denner. Thermal stratification in the Arctic Ocean. *Science*, 166(3903):373–374, 1969.

[134] J. J. Niemela, G. Ahlers, and D. S. Cannell. Localized traveling-wave states in binary-fluid convection. *Physical Review Letters*, 64(12):1365, 1990.

[135] T. Nishimura, M. Wakamatsu, and A. M. Morega. Oscillatory double-diffusive convection in a rectangular enclosure with combined horizontal temperature and concentration gradients. *International Journal of Heat and Mass Transfer*, 41(11):1601–1611, 1998.

[136] L. Padman and T. M. Dillon. Vertical heat fluxes through the Beaufort Sea thermohaline staircase. *Journal of Geophysical Research: Oceans*, 92(C10):10799–10806, 1987.

[137] R. C. Paliwal and C. F. Chen. Double-diffusive instability in an inclined fluid layer. Part 1. Experimental investigation. *Journal of Fluid Mechanics*, 98:755–768, 1980.

[138] R. C. Paliwal and C. F. Chen. Double-diffusive instability in an inclined fluid layer. Part 2. Stability analysis. *Journal of Fluid Mechanics*, 98:769–785, 1980.

[139] J. W. Pearson and J. Pestana. Preconditioners for Krylov subspace methods: An overview. *GAMM-Mitteilungen*, 43(4):e202000015, 2020.

[140] I. Pérez-Santos, J. Garcés-Vargas, W. Schneider, L. Ross, S. Parra, and A. Valle-Levinson. Double-diffusive layering and mixing in Patagonian fjords. *Progress in Oceanography*, 129:35–49, 2014.

[141] Y. Pomeau. Front motion, metastability and subcritical bifurcations in hydrodynamics. *Physica D: Nonlinear Phenomena*, 23(1-3):3–11, 1986.

[142] B. Pradenas, I. Araya, M. G. Clerc, C. Falcón, P. Gandhi, and E. Knobloch. Slanted snaking of localized Faraday waves. *Physical Review Fluids*, 2(6):064401, 2017.

[143] T. Radko. *Double-diffusive convection*. Cambridge University Press, 2013.

[144] Y. Requilé, S. C. Hirata, M. N. Ouarzazi, and A. Barletta. Weakly nonlinear analysis of viscous dissipation thermal instability in plane Poiseuille and plane Couette flows. *Journal of Fluid Mechanics*, 886:A26, 2020.

[145] M. J. Robbins, A. J. Archer, U. Thiele, and E. Knobloch. Modeling the structure of liquids and crystals using one-and two-component modified phase-field crystal models. *Physical Review E*, 85(6):061408, 2012.

[146] B. Ruddick and K. Richards. Oceanic thermohaline intrusions: observations. *Progress in Oceanography*, 56(3-4):499–527, 2003.

[147] B. R. Ruddick and J. S. Turner. The vertical length scale of double-diffusive intrusions. *Deep-Sea Research Part A. Oceanographic Research Papers*, 26(8):903–913, 1979.

[148] B. R. Ruddick, O. M. Phillips, and J. S. Turner. A laboratory and quantitative model of finite-amplitude thermohaline intrusions. *Dynamics of Atmospheres and Oceans*, 30(2-4):71–99, 1999.

[149] Y. Saad. *Iterative methods for sparse linear systems*, volume 82. SIAM, 2003.

[150] Y. Saad. *Numerical methods for large eigenvalue problems: revised edition*. SIAM, 2011.

[151] Y. Saad and M. H. Schultz. GMRES: A generalized minimal residual algorithm for solving nonsymmetric linear systems. *SIAM Journal on Scientific and Statistical Computing*, 7(3):856–869, 1986.

[152] H. Sakaguchi. Standing wave patterns for the complex Swift-Hohenberg equation. *Progress of Theoretical Physics*, 98(3):577–585, 1997.

[153] H. Sakaguchi. Herringbone Pattern for an anisotropic complex Swift-Hohenberg equation. *Physical Review E*, 58(6):8021, 1998.

[154] H. Sakaguchi and H. R. Brand. Stable localized solutions of arbitrary length for the quintic Swift-Hohenberg equation. *Physica D: Nonlinear Phenomena*, 97(1-3): 274–285, 1996.

[155] H. Sakaguchi and H. R. Brand. Standing wave localized squares in pattern-forming nonequilibrium systems. *Journal de Physique II*, 7(10):1325–1330, 1997.

[156] R. W. Schmitt. Form of the temperature-salinity relationship in the central water: Evidence for double-diffusive mixing. *Journal of Physical Oceanography*, 11(7):1015–1026, 1981.

[157] R. W. Schmitt. The characteristics of salt fingers in a variety of fluid systems, including stellar interiors, liquid metals, oceans, and magmas. *Physics of Fluids*, 26 (9):2373–2377, 1983.

[158] R. W. Schmitt. Double diffusion in oceanography. *Annual Review of Fluid Mechanics*, 26(1):255–285, 1994.

[159] R. W. Schmitt, H. Perkins, J. D. Boyd, and M. C. Stalcup. C-SALT: An investigation of the thermohaline staircase in the western tropical North Atlantic. *Deep-Sea Research Part A. Oceanographic Research Papers*, 34(10):1655–1665, 1987.

[160] R. W. Schmitt, J. R. Ledwell, E. T. Montgomery, K. L. Polzin, and J. M. Toole. Enhanced diapycnal mixing by salt fingers in the thermocline of the tropical Atlantic. *Science*, 308(5722):685–688, 2005.

[161] T. M. Schneider, J. F. Gibson, and J. Burke. Snakes and ladders: localized solutions of plane Couette flow. *Physical Review Letters*, 104(10):104501, 2010.

[162] I. Sezai and A. A. Mohamad. Double diffusive convection in a cubic enclosure with opposing temperature and concentration gradients. *Physics of Fluids*, 12(9): 2210–2223, 2000.

[163] B. M. Shankar, J. Kumar, and I. S. Shivakumara. Stability of double-diffusive natural convection in a vertical fluid layer. *Physics of Fluids*, 33(9):094113, 2021.

[164] N. C. Shibley and M.-L. Timmermans. The formation of double-diffusive layers in a weakly turbulent environment. *Journal of Geophysical Research: Oceans*, 124(3): 1445–1458, 2019.

[165] E. D. Siggia. High Rayleigh number convection. *Annual Review of Fluid Mechanics*, 26(1):137–168, 1994.

[166] G. L. G. Sleijpen, H. A. Van der Vorst, and D. R. Fokkema. BiCGstab (l) and other hybrid Bi-CG methods. *Numerical Algorithms*, 7(1):75–109, 1994.

[167] P. Sonneveld and M. B. Van Gijzen. IDR (s): A family of simple and fast algorithms for solving large nonsymmetric systems of linear equations. *SIAM Journal on Scientific Computing*, 31(2):1035–1062, 2009.

[168] E. A. Spiegel. Semiconvection. *Comments on Astrophysics and Space Physics*, 1:57, 1969.

[169] K. Staliunas and V. J. Sanchez-Morcillo. Dynamics of phase domains in the Swift-Hohenberg equation. *Physics Letters A*, 241(1-2):28–34, 1998.

[170] J. Swift and P. C. Hohenberg. Hydrodynamic fluctuations at the convective instability. *Physical Review A*, 15(1):319, 1977.

[171] R. I. Tait and M. R. Howe. Thermohaline staircase. *Nature*, 231(5299):178–179, 1971.

[172] S. Thangam, A. Zebib, and C. F. Chen. Double-diffusive convection in an inclined fluid layer. *Journal of Fluid Mechanics*, 116:363–378, 1982.

[173] U. Thiele, A. J. Archer, M. J. Robbins, H. Gomez, and E. Knobloch. Localized states in the conserved Swift-Hohenberg equation with cubic nonlinearity. *Physical Review E*, 87(4):042915, 2013.

[174] L. N. Trefethen. *Spectral Methods in MATLAB*. SIAM, 2000.

[175] N. Tsitverblit. Bifurcation phenomena in confined thermosolutal convection with lateral heating: Commencement of the double-diffusive region. *Physics of Fluids*, 7 (4):718–736, 1995.

[176] N. Tsitverblit and E. Kit. The multiplicity of steady flows in confined double-diffusive convection with lateral heating. *Physics of Fluids A*, 5(4):1062–1064, 1993.

[177] L. S. Tuckerman and D. Barkley. Bifurcation analysis for timesteppers. In *Numerical methods for bifurcation problems and large-scale dynamical systems*, pages 453–466. Springer, 2000.

[178] J. S. Turner. Double-diffusive phenomena. *Annual Review of Fluid Mechanics*, 6(1): 37–54, 1974.

[179] J. S. Turner. Multicomponent convection. *Annual Review of Fluid Mechanics*, 17(1): 11–44, 1985.

[180] J. S. Turner. The melting of ice in the Arctic Ocean: The influence of double-diffusive transport of heat from below. *Journal of Physical Oceanography*, 40(1): 249–256, 2010.

[181] J. S. Turner and L. B. Gustafson. Fluid motions and compositional gradients produced by crystallization or melting at vertical boundaries. *Journal of Volcanology and Geothermal Research*, 11(2-4):93–125, 1981.

[182] J. S. Umbría and M. Net. Stationary Flows and Periodic Dynamics of Binary Mixtures in Tall Laterally Heated Slots. In Gelfgat. A., editor, *Computational Modelling of Bifurcations and Instabilities in Fluid Dynamics*, pages 171–216. Springer, 2019.

[183] C. G. van der Boog, H. A. Dijkstra, J. D. Pietrzak, and C. A. Katsman. Double-diffusive mixing makes a small contribution to the global ocean circulation. *Communications Earth & Environment*, 2(1):1–9, 2021.

[184] M. B. Van Gijzen and P. Sonneveld. Algorithm 913: An elegant IDR (s) variant that efficiently exploits biorthogonality properties. *ACM Transactions on Mathematical Software (TOMS)*, 38(1):1–19, 2011.

[185] C. M. Vest and V. S. Arpaci. Stability of natural convection in a vertical slot. *Journal of Fluid Mechanics*, 36(1):1–15, 1969.

[186] T. Watanabe, M. Iima, and Y. Nishiura. Spontaneous formation of travelling localized structures and their asymptotic behaviour in binary fluid convection. *Journal of Fluid Mechanics*, 712:219–243, 2012.

[187] T. Watanabe, M. Iima, and Y. Nishiura. A skeleton of collision dynamics: Hierarchical network structure among even-symmetric steady pulses in binary fluid convection. *SIAM Journal on Applied Dynamical Systems*, 15(2):789–806, 2016.

[188] A. J. Wathen. Preconditioning. *Acta Numerica*, 24:329–376, 2015.

[189] J. A. Weaver and R. Viskanta. Natural convection in binary gases due to horizontal thermal and solutal gradients. *Journal of Heat Transfer*, 113:141–147, 1991.

[190] P. D. Woods and A. R. Champneys. Heteroclinic tangles and homoclinic snaking in the unfolding of a degenerate reversible Hamiltonian–Hopf bifurcation. *Physica D: Nonlinear Phenomena*, 129(3-4):147–170, 1999.

[191] S. Xin, P. Le Quéré, and L. S. Tuckerman. Bifurcation analysis of double-diffusive convection with opposing horizontal thermal and solutal gradients. *Physics of Fluids*, 10(4):850–858, 1998.

[192] Y. You. A global ocean climatological atlas of the Turner angle: Implications for double-diffusion and water-mass structure. *Deep-Sea Research*, 49:2075–2093, 2002.

[193] L. B. Younis, A. A. Mohamad, and A. K. Mojtabi. Double diffusion natural convection in open lid enclosure filled with binary fluids. *International Journal of Thermal Sciences*, 46(2):112–117, 2007.

[194] A. V. Yulin and A. R. Champneys. Discrete snaking: multiple cavity solitons in saturable media. *SIAM Journal on Applied Dynamical Systems*, 9(2):391–431, 2010.

[195] Y. R. Zelnik, S. Kinast, H. Yizhaq, G. Bel, and E. Meron. Regime shifts in models of dryland vegetation. *Philosophical Transactions of the Royal Society A: Mathematical, Physical and Engineering Sciences*, 371(2004):20120358, 2013.

[196] B.-X. Zhao and J.-Q. Yang. Numerical investigation of 2D double-diffusive convection in rectangular cavities with different aspect ratios: Heat and mass transfer and flow characteristics. *Physics of Fluids*, 34(3):034120, 2022. doi: 10.1063/5.0084537.

[197] G. Zodiatis and G. P. Gasparini. Thermohaline staircase formations in the Tyrrhenian Sea. *Deep-Sea Research Part I: Oceanographic Research Papers*, 43(5):655–678, 1996.